UNIVERSIDADE DE LISBOA,
FACULDADE DE CIÊNCIAS

UNIVERSITY OF SAINT JOSEPH,
INSTITUTE OF SCIENCE AND ENVIRONMENT

PETROLOGY AND GEOCHEMISTRY OF THE IGNEOUS ROCKS FROM MACAO (SOUTH CHINA): TECTONO-MAGMATIC IMPLICATIONS

"Documento Definitivo"

PhD in Science

Doutoramento em Geologia

Especialidade em Geoquímica

Pedro Moniz Quelhas

Tese orientada por:

Ágata Alveirinho Dias
João Mata

Documento especialmente elaborado para a obtenção do grau de doutor

2019

UNIVERSIDADE DE LISBOA,
FACULDADE DE CIÊNCIAS

UNIVERSITY OF SAINT JOSEPH,
INSTITUTE OF SCIENCE AND ENVIRONMENT

PETROLOGY AND GEOCHEMISTRY OF THE IGNEOUS ROCKS FROM MACAO (SOUTH CHINA): TECTONO-MAGMATIC IMPLICATIONS

PhD in Science

Doutoramento em Geologia

Especialidade em Geoquímica

Pedro Moniz Quelhas

Tese orientada por:

Ágata Alveirinho Dias

João Mata

Júri:

Presidente:

● Doutor Peter Stilwell, Associate Professor, University of Saint Joseph, Macao

Vogais:

● Doutor Mei-Fu Zhou, Full Professor, University of Hong Kong;

● Doutor Lung Sang Chan, Full Professor, HKUSPACE Community College, Hong Kong;

● Doutora Ágata Alveirinho Dias, Professora Associada, University of Saint Joseph, Macao;

● Doutor João Mata, Professor Associado com Agregação, Faculdade de Ciências da Universidade de Lisboa.

Fundo para o Desenvolvimento das Ciências e da Tecnologia de Macau

Documento especialmente elaborado para a obtenção do grau de doutor

2019

Acknowledgements

There are many people who deserve my deepest appreciation because, one way or another, they helped me reach the end of my PhD journey. I apologize in advance in case somebody is missing from this list.

First, I have to thank my supervisors, Prof. Ágata Dias and Prof. João Mata, for their availability, patience and wise advices. More specifically, I want to thank Ágata for always being available to help me in every matter related to my research and personal life. More than a supervisor she became a true friend and made everything she could to ensure I was motivated and happy with my academic and personal life during the PhD period. To João Mata I want to thank for always making sure my research was progressing in the right direction and for the countless hours that he spent listening and discussing topics related to my research, trusting my decisions, suggesting new paths and giving me freedom to explore new ideas. To Ágata and João I will always be grateful for helping me to become, not only a better scientist, but mostly important a better person.

I would like to express my thanks to FDCT (Fundo para o Desenvolvimento das Ciências e da Tecnologia, Macau) for funding my PhD scholarship (043/2014/A1) during three years. I thank Bank of China for their funding in the first year of my PhD. I thank FCiências.ID for the scholarship within the project "Serviços de mineralogia, petrologia e geoquímica", cc 309. I also thank IDL (Instituto Don Luiz), FCUL (Faculdade de Ciências da Universidade de Lisboa) for supporting my research.

I thank Dra. Luísa Ribeiro for sharing her knowledge about the geology of Macao, especially during my first field trips. I also thank LNEG (Laborátorio Nacional de Energia e Geologia) through Dra. Luísa Ribeiro for giving access to samples collected in Macao during the 90's.

I am very grateful to Varon Lou for all the help during fieldwork and preparation of the samples for whole-rock chemical analyses. I also thank Ricardo Borges for his help during fieldwork and for his skilled assistance in doing the geological map of Macao.

I want to thank Dr. Rod Sewell (Hong Kong Geological Survey) and Professor Chan (University of Hong Kong), who revised my PhD research proposal and gave me important advice on how to achieve my research aims. I also want to thank them for going on field trips with me in Macao and sharing their geological knowledge about the region.

I am thankful to Prof. David Gonçalves, Dean of the ISE (Institute of Science and Environment) at USJ (University of Saint Joseph), for his friendship and support and for following up my research with keen interest.

I thank Prof. Isabel Costa and Prof. Telmo Bento dos Santos (FCUL) for their friendship and availability to discuss topics related to my research.

I want to thank to Prof. Línia Martins (FCUL) for her words of encouragement and motivation which were crucial to my decision of undertaking this PhD journey.

This work could not have been completed without the excellent thin sections prepared by Dr. Cyntia Mourão and without the microprobe analysis made under the guidance of Dr. Pedro dos Reis Rodrigues, to whom I am thankful.

I thank Dr. Jean Wong who guided me through the LA-MC-ICPMS zircon U–Pb analysis at the Department of Earth Sciences of the University of Hong Kong. I thank Dr. Don Davis who performed the U–Pb zircon ID-TIMS dating at Jack Satterly Geochronology Laboratory, Department of Geology, University of Toronto, Canada, and always showed availability to discuss the data with me.

I am also indebted to the Departamento de Geologia staff (FCUL), especially to Dina Gouveia and Marta Antunes, for their sympathy and precious help on bureaucratic matters.

I thank all the professors and students in the ISE (USJ) and Departamento de Geologia (FCUL) for providing me with a healthy and productive research environment during my PhD research.

In the ISE (USJ) I want to specifically thank to Andreia Ramos, Pedro Vieira, Muhammad Saidu Bashir, Alexandre Lebel, Lúcia Gonzalez, Rafael Ayala Lara and Lukas Breitzler, who shared the office with me during my stay in Macao. I appreciate their friendship, useful advices and support that kept me motivated through tough times. In FCUL, I want to specifically thank to Joana Ferreira, Inês Pereira, Alexa Gomez, Diogo Carvalho, Pedro Cachapuz and Ana Rita Rosa for their friendship, cheerful mood, and useful discussions on topics related with my thesis.

At last, I thank to my mother Gisela Moniz and my father Vítor Quelhas for all their love, support and encouragement given me over the years, always making sure I had all the conditions I needed to finish my PhD.

Abstract

The territory of Macao is composed of several granitic intrusions belonging to one of the biggest granite provinces in the world, the Southeast China Magmatic Belt (SCMB), located in the southeast (SE) area of the Cathaysia Block. The SCMB is known by the occurrence of large volumes of Mesozoic magmatic rocks (over 90% are granitic rocks and equivalent volcanic rocks with minor basalts), occupying a total outcrop area of nearly 200.000 km^2. The geology of Macao (~30 Km^2) is dominated by granitic rocks displaying a wide range of textural, mineralogical and chemical features, making it an ideal region to study these rocks and the petrogenetic processes responsible for their diversity.

This study employed a wide range of research methodologies, namely field studies, petrography, zircon geochronology, mineral chemistry, whole-rock elemental and isotopic geochemistry to determine the nature of the source, the petrogenetic processes and the tectonic regimes of the Mesozoic magmatism in this region. Thus, the data collected along this study aims to provide new knowledge on the tectono-magmatic evolution of Macao, in particular, and of SE China, in general.

The results obtained from the high-precision U–Pb zircon geochronology, acquired through isotope dilution thermal ionization mass spectrometry (ID-TIMS) and *in-situ* laser ablation multi-collector inductively coupled mass spectrometry (LA-MC-ICPMS), revealed different ages for Macao granites. Despite its relatively small area, the determined ages tightly constrain the Macao granitic magmatism to two periods, ranging from 164.5 ± 0.6 to 162.9 ± 0.7 Ma (MGI – Macao Group I granites) and 156.6 ± 0.2 to 155.5 ± 0.8 Ma (MGII – Macao Group II granites). In addition, younger dacitic rocks were dated at 150.6 ± 0.6 Ma and <120 Ma. The existence of two proximal but distinct granitic pulses, spanning for a time of about 9 Ma and separated by ca. 6 Ma, in the Macao granitic suite suggests that it was incrementally assembled. This hypothesis is also extendable to the neighbouring Hong Kong region, where the magmatic activity occurred in four major pulses spanning for about 24 Ma. However, the MGII granites indicate the occurrence, on the Pearl River Delta region, of a magmatic pulse between those defined in Hong Kong at the origin of Lamma Suite (165–160 Ma) and the Kwai Chung Suite (148–146 Ma). In addition, Rare Element Earth (REE) ratios suggest that this pulse may only occur in Macao area, while MGI granites show evolving trends of REE ratios similar to those of Jurassic granites outcropping in vast areas of the

Cathaysia Block (SE China). Inheritance patterns in the zircon U–Pb data indicate the presence of a population of antecrysts (165–180 Ma) crystallized from earlier magmatic pulses and a population of inherited zircons, from Precambrian to Phanerozoic sources, incorporated into the magmas during melting and/or ascent/emplacement at crustal levels. The oldest inherited ages (2.4 Ga and possibly 2.9 Ga) suggest contribution of Proterozoic and possibly of late Archaean crustal sources for the Macao magmatism.

The granitic rocks of Macao are mainly high-K calc-alkaline metaluminous to weakly peraluminous I-type granites with variable degrees of fractionation. Fractional crystallization played an important role in the evolution of these granites, though the fractionation paths differ for the highly fractionated facies of both groups mainly due to distinct accessory fractionating phases. Such difference is evident by distinct REE evolution trends: while MGI magmas seem to have evolved by gradual enrichment in heavy REE relatively to light REE, originating progressively flatter REE patterns, magmas from MGII are marked by depletion of middle REE, leading to progressively concave upward REE patterns. However, while most of the geochemical variation of the MGII granites can be explained by fractional crystallization, the same is not true for MGI granites. The MGI highly fractionated granites show evidence for the REE tetrad effect and are characterized by non-CHArge-and-RAdius-Controlled (non-CHARAC) behaviour of trace elements, suggesting late-stage melt/fluid interactions involving F-rich fluids. The stage of evolution represented by the MGI highly fractionated granites corresponds to the onset of fluid/melt interaction in a highly evolved granitic system, which may have led to enhanced hydrothermal activity in more evolved stages, as those represented in neighbouring areas in SE China. Significant differences in isotopic composition were also observed, with the MGII being characterized by a much narrow range of initial $^{87}Sr/^{86}Sr$ ratios and $\varepsilon_{Nd}(t)$ and $\varepsilon_{Hf}(t)$ values than MGI. Based on these differences, the MGII granites are considered to be part of a comagmatic suite that has evolved in closed system, contrasting with what can be inferred for MGI. The increase in initial $^{87}Sr/^{86}Sr$ ratios with degree of evolution, the presence of metasedimentary enclaves and the high percentage of inherited zircon with Paleozoic ages in MGI, suggest the occurrence of an assimilation fractionation crystallization (AFC) process. The AFC processes were a major cause for the I-S transitional characteristics of the MGI highly fractionated granites and possibly of the other similar Jurassic biotite granites in SE China. The observed decoupling of Sr, Nd and Hf isotope systems might have resulted from magma mixing between the granitic and more mafic

magmas, which caused the homogenization of Sr isotope ratios but not of the Nd and Hf ones. Such process is also supported by the occurrence of Microgranular Mafic Enclaves (MME) hosted by the granites.

Isotope and major element compositions together with model ages strongly suggest that Macao granitic magmas were generated by partial melting of infracrustal medium-to-high K basaltic Paleo-Proterozoic to Mesoproterozoic protoliths heated by, and mixed to some degree with mantle-derived magmas. The temporal and spatial association of Macao and SE China Jurassic I-type granites with basaltic/gabbroic rocks, syenites and A-type granites, displaying typical intraplate chemical features, indicates an extensional regime rather than an active margin for the origin of these rocks. It also points to an important role of mantle-derived magmas in the production of SE China Jurassic granites. Adiabatic decompression melting of the asthenospheric mantle produced mafic magmas, which underplated at the base of the crust (Moho), subsequently triggering partial melting of the lower crust to generate the granitic magmas. The Jurassic Macao granites are interpreted as being produced in an intraplate extensional setting related to the break-off and foundering of a previously flat-slab (Paleo-Pacific plate) beneath the Eurasian plate.

The boundary between east and west Cathaysia blocks is roughly along the Zhenghe-Dapu Fault (ZDF), which intersects the SE China coast near Hong Kong and is thought to have played a major role for the Mesozoic magmatic activity in this region. The stronger isotopic affinities of Macao granites with the other granitic rocks and lower crustal xenoliths from the western Cathaysia Block suggest that the ZDF is likely to pass south of Macao, a fact that has not been mentioned before.

In addition to the Early Yanshanian (Jurassic) granitic magmatism in Macao, the younger ages obtained for the dacite dykes indicate that the territory was also affected, to a lesser degree, by Late Yanshanian (Cretaceous) magmatism. The transition from granitic to dacitic magmatism most likely corresponds to a change in the regional tectonic regime, which induced a significant change in the magma genesis processes. In contrast with the intraplate features of Macao and SE China Jurassic granites and coeval mafic rocks, the geochemical features of the Macao dacite dykes (e.g. high LILE/HFSE ratios and negative anomalies of Nb, Ta and Ti) are identical to those characterizing arc-like subduction-related magmas. These dacites are most likely evolved products

of arc-like magmatism and may testify the reestablishment of a normal subduction system in this area of SE China.

Keywords: I-type granites; U–Pb zircon geochronology; Yanshanian Orogeny; Macao (SE China); Cathaysia Block.

Resumo

O território de Macau é composto por várias intrusões graníticas que se integram numa das maiores províncias graníticas da Terra, a Faixa Magmática do Sudeste da China (FMSC), localizada na parte sudeste (SE) do bloco Cathaysia. A FMSC é conhecida pela ocorrência de grandes volumes de rochas magmáticas mesozóicas (mais de 90% são rochas graníticas e equivalentes vulcânicas com basaltos em quantidades subordinadas), ocupando uma área total de aproximadamente 220.000 km^2. A geologia de Macau (~30 Km^2) é dominada por rochas graníticas apresentando ampla gama de características texturais, mineralógicas e químicas, fazendo desta uma região ideal para estudar este tipo de rochas, bem como os processos petrogenéticos responsáveis pela sua diversidade.

Este estudo utilizou uma vasta gama de técnicas de investigação, nomedamente estudos de campo, petrografia, geocronologia U–Pb em zircões, química mineral e geoquímica elementar e isotópica de rocha-total, de modo a determinar a natureza da fonte, os processos petrogenéticos e os regimes tectónicos do magmatismo Mesozóico nesta região. A integração dos dados recolhidos permitiu obter novos conhecimentos sobre a evolução tectono-magmática de Macau, em particular, e do SE da China, em geral.

Os dados de geocronologia de U–Pb de alta precisão em zircões, adquiridos através de espectrometria de massa por ionização térmica (ID-TIMS) e espectrometria de massa com acoplamento indutivo de múltiplos coletores a laser (LA-MC-ICPMS) *in-situ*, permitiram determinar idades distintas para o magmatismo de Macau. Apesar da sua área relativamente pequena, as novas idades restringem o magmatismo granítico de Macau a dois períodos que variam de 164.5 ± 0.6 a 162.9 ± 0.7 Ma (MGI – granitos do grupo I) e 156.6 ± 0.2 a 155.5 ± 0.8 Ma (MGII – granitos do grupo II). Além dos granitos, rochas dacíticas mais recentes foram datadas em 150.6 ± 0.6 Ma e <120 Ma. A existência de dois distintos pulsos graníticos espacial e temporalmente próximos, abrangendo um período de cerca de 9 Ma e separados por cerca de 6 Ma, sugere que a suíte granítica de Macau tenha resultado de um crescimento incremental. Esta hipótese é também extensível à região vizinha de Hong Kong, onde a atividade magmática ocorreu em quatro pulsos principais ao longo de um período de cerca de 24 Ma. No entanto, os granitos do MGII indicam a ocorrência, na região do Delta do Rio as Pérolas, de um pulso magmático entre aqueles que, em Hong Kong, estiveram na origem do "Lamma Suite" (165-160 Ma) e do "Kwai Chung Suite" (148-

146 Ma). Além disso, a evolução das razões de Elementos das Terras Raras (ETR) sugere que este pulso poderá apenas ter ocorrido na área de Macau, enquanto que os granitos do MGI apresentam tendências de evolução de razões de ETR semelhantes às dos granitos jurássicos que afloram em vastas áreas do bloco Cathaysia (no SE da China). O padrão de distribuição das idades dos zirões herdados sugere a presença de uma população de antecristais (165-180 Ma) cristalizados em pulsos magmáticos anteriores e outra de zircões herdados de fontes pré-câmbricas a fanerozóicas, incorporados nos magmas durante a fusão e/ou ascensão/intrusão em níveis crustais mais superficiais. As idades herdadas mais antigas (2.4 Ga e 2.9 Ga) sugerem a contribuição de fontes crustais proterozóicas e, possivelmente, arcaicas para o magmatismo de Macau.

As rochas graníticas de Macau correspondem, na sua maioria, a granitos metaluminosos a fracamente hiperaluminosos, calco-alcalinos com alto teor em K, de tipo-I e com graus de fracionação variáveis. A cristalização fracionada desempenhou um papel importante na evolução deste granitos, embora as trajectórias de fracionação tenham diferido para as fácies altamente fracionadas em ambos os grupos, sobretudo devido à cristalização de fases minerais acessórias distintas. Tal diferença é evidente nas diferentes tendências de evolução dos ETR destes granitos: enquanto que os magmas que deram origem aos granitos MGI parecem ter evoluído através de um enriquecimento progressivo em Elementos das Terras Raras Leves (ETRL) relativamente aos Elementos das Terras Raras Pesadas (ETRP), originando padrões de ETR progressivamente mais planos, os magmas dos granitos MGII caracterizam-se por um empobrecimento em Elementos das Terras Raras Médias (ETRM), originando padrões de ETR progressivamente mais côncavos.

Enquanto que a maior parte da variação geoquímica dos granitos do MGII é explicada por cristalização fracionada, tal não se verifica para os granitos do MGI. Os granitos altamente fracionados do MGI mostram evidências do efeito tétrade nos padrões de ETR, bem como elementos traço caracterizados por um comportamento químico não controlado pela carga e raio iónico (non-CHARAC), sugerindo a ocorrência de interações entre o magma granítico e um fluído rico em F em estágios tardios da evolução magmática. O estágio de evolução representado pelos granitos altamente fracionados do MGI corresponde ao início da interação entre o magma e o fluído, num sistema granítico altamente evoluído, que pode ter levado a uma maior atividade hidrotermal em estágios tardios, como aqueles que estão representados em áreas vizinhas no SE da China. Foram também observadas diferenças significativas na composição isotópica entre os dois tipos de granitos. Os do MGII são caracterizados por uma variação muito mais estreita das razões

iniciais de $^{87}Sr/^{86}Sr$ e dos valores de $\varepsilon_{Nd}(t)$ e $\varepsilon_{Hf}(t)$ do que os do MGI, sugerindo que os granitos do MGII possam corresponder a uma suíte comagmática que terá evoluído em sistema fechado, contrastando com o que pode ser inferido para o MGI. O aumento das razões iniciais de $^{87}Sr/^{86}Sr$ com o grau de evolução magmática, a presença de encraves metassedimentares e a elevada percentagem de zircões herdados com idades paleozóicas no MGI, apontam para a ocorrência de um processo de assimilação-cristalização fracionada (ACF). Os processos de ACF terão sido a causa das características transicionais I-S dos granitos altamente fracionados do MGI e, possivelmente, de granitos biotíticos jurássicos com características semelhantes aflorantes em outras áreas do SE da China. O desacoplamento dos sistemas isotópicos de Sr, Nd e Hf poderá ter sido consequência da mistura entre o magma granítico e magmas mais máficos, o que causou a homogeneização das razões isotópicas de Sr, mas não das dos isótopos de Nd e Hf. Tal processo é também suportado pela presença de abundantes encraves microgranulares máficos (EMM) nos granitos.

As composições isotópicas e a geoquímica de elementos maiores, juntamente com as idades modelo dos granitos, sugerem que os magmas graníticos de Macau terão sido gerados pela fusão parcial de protólitos infracrustais basálticos (elevado teor em K) paleoproterozóicos a mesoproterozóicos aquecidos pela intrusão contemporânea de magmas máficos de origem mantélica, estacionados na base da crosta inferior. A associação temporal e espacial dos granitos tipo-I jurássicos com rochas basálticas/gabróicas, sienitos e granitos tipo-A com características químicas intra-placa, sugere a ocorrência de um regime extensional na origem destas rochas, ao invés de uma margem continental ativa. Tal associação aponta também para um papel importante dos magmas mantélicos na geração dos granitos jurássicos do SE da China. A fusão parcial por descompressão adiabática do manto astenosférico terá produzido magmas máficos, que ao estacionarem na base da crosta (Moho), terão induzido a fusão parcial desta, gerando assim os magmas graníticos. Os granitos jurássicos de Macau são interpretados como tendo sido produzidos num ambiente extensional intra-placa, consequência do rompimento ("break-off") e afundamento de uma placa plana previamente subductada (placa Paleo-Pacífica) sob a placa Eurasiática.

A fronteira entre os blocos este e oeste do Cathaysia situa-se aproximadamente ao longo da falha Zhenghe-Dapu, que intersecta a costa do sudeste da China perto de Hong Kong e que é consdierada como tendo desempenhado um papel importante na actividade magmática regional durante o Mesozóico. As fortes afinidades isotópicas dos granitos de Macau com rochas graníticas

e xenólitos da crosta inferior pertencentes ao bloco oeste do Cathaysia sugerem que a falha Zhenghe-Dapu deverá passar a sul de Macau, facto que não terá sido sugerido anteriormente.

Além do magmatismo granítico em Macau, gerado no período inicial da orogenia Yanshaniana (Jurássico), as idades mais recentes obtidas para os filões dacíticos indicam que o território terá sido também afectado, em menor grau, pelo magmatismo do período tardio da orogenia Yashaniana (Cretácico). A transição de magmatismo granítico para dacítico, deverá ter correspondido a uma mudança no regime tectónico regional, induzindo alterações significativas nos processos de génese magmática. Em contraste com as características intra-placa dos granitos jurássicos de Macau e do SE da China, assim como das rochas máficas coevas, as características geoquímicas dos filões dacíticos de Macau (ex. elevadas razões entre elementos litófilos de grande raio iónico e elementos de elevado potencial iónico, bem como anomalias negativas de Nb, Ta e Ti) são idênticas às que caracterizam os magmas de arcos magmáticos associados a zonas de subducção. Estas rochas dacíticas representam provavelmente produtos mais evoluídos de magmatismo do tipo arco magmático e poderão testemunhar o restabelecimento de um sistema de subducção normal nesta área do SE da China.

Palavras-chave: granitos tipo-I; geocronologia U–Pb em zircão; Orogenia Yanshaniana; Macau (Sul da China); bloco Cathaysia.

Publications arising from this thesis

Journal articles

Published publications

Quelhas, P., Dias, Á A., Mata, J., Don, D., Ribeiro, L. (2019) High-precision geochronology of Mesozoic magmatism in Macao, Southeast China: evidence for multistage granite emplacement. Geoscience Frontiers. In press. https://doi.org/10.1016/j.gsf.2019.04.011

Submitted publications

Quelhas, P., Dias, Á A., Mata, J. (2019) Evidence for mixed contribution of mantle, lower and upper crust to the genesis of Jurassic I-type granites from Macao, SE China. Lithos. Submitted.

Conference abstracts

Poster presentations

Quelhas P., Dias Á. A., Mata, J., Don, D. W., 2019. Geochronological, geochemical and petrographic constraints on incremental pluton growth: the case of Macao granitic suite, SE China. Goldschmidt Conference, 18–23 August 2019, Barcelona, Spain.

Quelhas, P., Mata, J., Lou, U. T., Ribeiro, M. L., Borges, R., Dias, Á. A., 2018. A origem e evolução dos magmas graníticos de Macau à luz de dados de geoquímica elementar e isotópica / Source and evolution of Macao granitic magmas: insights from whole-rock geochemistry and isotopic signatures. XIV Congresso de Geoquímica dos Países de Língua Portuguesa e XIX Semana de Geoquímica (XIV CGPLP/XIX SG, international conference). 25–29 March 2018, Trás-os-Montes e Alto Douro, Portugal.

Quelhas, P., Mata, J., Lou, U. T., Ribeiro, M. L., Borges, R., Dias Á. A., 2017. New Geochemical Constraints on I-Type Granites of Macao: Petrogenesis and Geodynamic Implications. Goldschmidt Conference, 13–18 August 2017, Paris, France.

Quelhas, P., Mata, J., Lou, U. T., Ribeiro, M. L., Dias, Á. A., 2016. Mesozoic Granitic Magmatism in Macao, Southeast China. AGU Fall Meeting, 12–16 December 2016, San Francisco, USA.

Dias, Á. A., Quelhas, P., Lou, U. T., Mata, J., Ribeiro, M. L., 2016. Petrology and Geochemistry of Granitic Rocks from Macao. Goldschmidt Conference, 26 June–1 July 2016, Yokohama, Japan.

Table of Contents

List of Figures

Chapter 2

Chapter 4

Chapter 5

List of Tables

Glossary of acronyms and abbreviations

The following acronyms and abbreviations are used throughout this thesis:

Δ – range

A/CNK – molar ratio $Al_2O_3/(CaO + Na_2O + K_2O)$

A/NK – molar ratio $Al_2O_3/(Na_2O + K_2O)$

AFC – Assimilation Fractionation Crystallization

BSE – Backscattered Electron

BSE – Bulk Silicate Earth

CHARAC – CHArge-and-RAdius-Controlled

CL – Cathodoluminescence

D – Partition coefficient

DM – Depleted Mantle

EM – Enriched Mantle

EPMA – Electron Probe Micro-Analysis

FC – Fractional Crystallization

HFSE – High Field Strength Elements

HIMU – High "μ", or high $^{238}U/^{204}Pb$

HREE – Heavy Rare Erath Elements

ID-TIMS – Isotopic Dilution - Thermal Ionization Mass Spectrometry

IUGS – International Union of Geological Sciences

LA-MC-ICPMS – Laser Ablation-Multiple Collector-Inductively Coupled Plasma Mass Spectrometry

LC – Lower Crust

LCC – Lower Continental Crust

LFZ – Lianhuashan Fault Zone

M – Mantle

MGI – Macao Group I

MGII – Macao Group II

MME – Microgranular Mafic Enclaves

MORB – Mid-Ocean Ridge Basalts

MREE – Middle Rare Earth Elements

MSWD - Mean Square Weighted Deviation

NCB – North China Block

NHRL – Northern Hemisphere Reference Line

NNO – Nickel-Nickel Oxide (buffer)

OIB – Ocean Island Basalts

OR – Orogene

PM – Primitive Mantle

PPM – Parts Per Million

REE – Rare Earth Elements

SCB – South China Block

SCCFB – South China Caledonian Fold Belt

SCMB – Southeast China Magmatic Belt

SE – Southeast

SJPF – Shaoxing-Jiangshan-Pingxiang Fault Zone

TAS – Total Alkalis-Silica

T_{DM2} – two-stage depleted mantle model ages

$TE_{1,3}$ – Tetrad effect

T_{Zr} – Zircon saturation temperature (ºC)

UC – Upper Crust

UCC – Upper Continental Crust

wt% – Weight percent

ZDF – Zhenghe-Dapu Fault

Chapter 1. Introduction

1.1. Research background

The average composition of the continental crust is granitic (Wedepohl, 1995; Rudnick and Gao, 2003) and, in some orogenic belts, granites form most of the rock exposures. Understanding the geology of the lithosphere requires a deep understanding of the granitic rocks. This can be achieved by studying granitic rocks in a regional way (e.g. magmatic belts) or at a more local scale (e.g. plutons). Although they occur in large belts, which commonly extend for hundreds or even thousands of kilometres, each belt is made up of several individual bodies with variable size and variable degrees of complexity. The petrological diversity of these rocks expected within a single granite belt is almost the same as that between the belts themselves (Cobbing, 2000). The causes for this remain enigmatic and should be addressed by studying the individual granitic intrusions within the belt and frame their variability in the regional context. Those differences might result from a complex combination of variables including source composition/processes, the relative importance of distinct magmatic evolution processes, varying degrees of mantle – crust interaction and, in many cases, associated with structural factors related to different stages of the Wilson Cycle.

One of these examples is the SCMB (Southeast China Magmatic Belt), located in SE China. It is characterized by the occurrence of large volumes of Mesozoic magmatic rocks (over 90% are granitic rocks and equivalent volcanic rocks with minor basalts), occupying a total outcrop area of nearly 218,090 km^2 (Zhou et al., 2006). This makes SCMB, where Macao is included, one of the biggest granitic belts in the world (Li et al., 2009). At a more local scale, the geology of Macao is dominated by granitic rocks with a wide range of textural, mineralogical and chemical features, making it an ideal region to study these rocks and the petrogenetic processes responsible for their diversity. Since every magmatic belt is composed of many distinct plutons, each of them providing a different window into the past crustal history, the current study aims to provide providing important insights into the evolution of the crustal segment associated with Macao granitic rocks.

Despite the existence of many petrological studies on the SE China Mesozoic magmatism (e.g. Campbell and Sewell, 1997; Sewell and Campbell, 1997; Li, 2000; Zhou and Li, 2000; Zhou et al., 2006; Li et al., 2007; Guo et al., 2012; Huang et al., 2012; Huang et al., 2015; Li et al., 2015; Y. Zhang et al., 2015; Zhou et al., 2016; Gao et al., 2017; Qiu et al., 2017; Xiang et al., 2017; Zhang et al., 2017; Jiang et al., 2018), there are still several intrusions lacking detailed studies. Macao is one of these examples, where only petrographic, structural analysis, restricted elemental

geochemistry and K-Ar dating on biotite were done before this study (Neiva, 1944; Ribeiro et al., 1992; Ribeiro et al., 2010). In addition, the majority of studies on the Mesozoic magmatic rocks of SE China China were conducted in a larger scale, lacking the detail needed to adequately represent the small scale compositional and age variation of individual plutons. Thus, in addition to investigating the sequence of magmatic events in the Macao granitic suite, this research offers an opportunity to examine the evolution of the Yanshanian event in a localized context and provides a window open to a better knowledge of the variability of the large SCMB granite province. Though it is generally accepted that the SCMB formed as a result of intense magmatic activity related to the subduction of the Paleo-Pacific plate under the Eurasian plate (e.g. Lan et al., 1996; Lapierre et al., 1997; Zhou and Li, 2000; Zhou et al., 2006; Li et al., 2007; Chen et al., 2016; Xia et al., 2016), the nature of the sources, petrogenetic processes and tectonic setting(s) involved in this magmatic event are still enigmatic and highly debated. Therefore, the research behind this thesis aims to contribute with new petrological, geochronological and geochemical data to assist in the current understanding of the SE China Mesozoic tectono-magmatic evolution, providing useful clues to better clarify the existing controversies. Since granites are a major component of the continental crust, and given that these rocks form deep in this crust, it is possible, through their isotopic compositions, to understand the variability and nature of the source regions from which the granites derived.

A great deal of personal research on the subject of the complexity of granitic rocks was done during the course of this thesis, including the definition of granitic rocks, classification schemes, genetic processes, causes of chemical variability (e.g. source constraints and magma evolution processes). In order to share the acquired knowledge with those who want to start in the study of granites, the Appendix A consists of a review of the above-mentioned topics.

1.2. Research questions

The research presented in this thesis consists in a petrological, geochemical and geochronological study of the magmatic rocks from Macao (China), aiming to unravel the geological evolution of the Macao territory within the tectono-magmatic evolution of Southeast (SE) China during the Mesozoic.

The main questions to be solved in this thesis are listed below, together with the subjects addressed in the quest of the respective answers.

A. How are magmatic events in Macao related to each other?

The steps to answer this question include:

(1) Identifying the different lithotypes outcropping in Macao and understanding the spatial relationships between them;

(2) Characterizing the textural, mineralogical and geochemical features of the different magmatic rocks outcropping in the territory to better constrain the previously defined facies by Ribeiro et al. (1992);

(3) Determining the absolute age, with U–Pb zircon geochronology, of the different magmatic rocks in Macao;

(4) Recognizing individual magmatic events occurring in Macao.

B. What were the source, petrogenetic processes and tectonic setting of Macao magmatism?

The steps to answer this question include:

(1) Unravelling the source of Macao magmatism regarding to its composition and age;

(2) Identifying and describing the different petrogenetic processes responsible for the genesis and evolution of the magmas;

(3) Understanding the tectonic setting(s) operating in each magmatic event;

(4) Constraining the mechanisms behind magma emplacement in the upper crust and, consequently, the evolution of the continental crust in this region of SE China.

C. Are there, in Macao, petrological and geochemical evidences that can help to better constrain the Yanshanian Orogeny?

The steps to answer this question include:

(1) Determining if, in Macao, there were magmatic events belonging to the two main periods of the Yanshanian Orogeny (Early Yanshanian and Late Yanshanian periods) and what implications does this have for the regional geodynamic evolution;

(2) Identifying the petrogenetic type of Macao granites, contributing to the debate about the petrogenetic type of coeval granites in other areas of SE China, and thus

providing clues on the source (e.g. infracrustal or supracrustal) of granitic magmas during this stage of the Yanshanian Orogeny;

(3) Comparing the petrological, elemental and isotopic characteristics between Macao granitic rocks and coeval magmatic rocks from surrounding areas, in order to understand their temporal, spatial and chemical variation, in an integrated vision on the nature of the magmatic activity at the regional scale;

(4) Constraining the source of the granitic magmatism during the Mesozoic in Macao and SE China through elemental and isotopic geochemistry of the Macao granites and, in particular, through the calculation of model ages.

D. How can the study of the Macao granites contribute to the knowledge on the genesis and evolution of granitic rocks?

Due to the variability of granitic textures and mineralogy found in the Macao suite, these granites provide important clues on the genesis and evolution processes responsible for certain types of textural and mineralogical features that may be found in other granitic suites worldwide. Moreover, the variable geochemical features of the Macao granites can better constrain the causes of chemical variability in granitic rocks in general, and in particular those belonging to the I-type.

1.3. Thesis outline

This thesis consists of seven chapters, which address the above questions:

Chapter 1 defines the research background, questions and objectives of the thesis.

Chapter 2 incorporates an overview of the geological background of SE China, since the formation of the South China Block. It also addresses the nature of the Yanshanian Orogeny and its role in the formation of the South China Magmatic Belt, then focusing on the regional geological context of Macao.

Chapter 3 presents the results of field studies and provides a detailed petrographic and mineralogical description of the magmatic rocks in Macao, including the different granitic facies, microgranular mafic enclaves (MME) and dacite dykes.

Chapter 4 presents a study entitled “High-precision geochronology of Mesozoic magmatism in Macao, Southeast China: evidence for multistage granite emplacement”, where the geochronological data are presented and interpreted in the light of other petrographic and

geochemical data. This chapter has been published in the Geoscience Frontiers journal (Quelhas et al., 2019).

Chapter 5 presents a study entitled "Petrogenesis of Macao I-type granites: evidence for mixed contribution of mantle, lower and upper crust", which presents mineral chemistry, whole-rock elemental and isotopic data to interpret the petrogenesis of Macao granites in the context of SE China tectono-magmatic evolution. This chapter has been submitted to Lithos journal (Quelhas et al. submitted), and is currently under revision.

Chapter 6 presents a brief description and interpretation of the geochemical data of the dacite dykes from a petrogenetic point of view.

Chapter 7 summarizes the key findings of this research and discusses their implications towards answering the research questions. Further research opportunities identified on the basis of this research are also presented.

Chapter 2. Geological setting

2.1. Geological background of South China

Although the magmatic rocks of Macao are part of the SCMB, formed during the Mesozoic Era, the crustal block to which they belong, i.e. the South China Block (SCB) and in particular the Cathaysia Block (Fig. 2.1), had a complex pre-Mesozoic history. In order to understand how these blocks were formed, how they evolved and shaped the geology of South China and their regional tectono-magmatic features, a detailed description of the main orogenic events is given below.

2.1.1. South China Block

The Asian continent was formed during the Phanerozoic by the welding of several continental blocks including Siberia, Tarim, North China, South China, Indochina, India, and several small-sized microcontinents (e.g. Chen et al., 1993; Charvet and Faure, 1996; Charvet, 2013; Faure et al., 2014). China, in particular, resulted from the collage of three main blocks - North China Block (NCB), South China Block (SCB) and Tarim Block - and a number of smaller blocks (Fig. 2.1; Huang, 1978; Ma and Wu, 1981; Zhao et al., 2001; Zhao and Guo, 2012; Huang and Opdyke, 2016). These blocks are thought to have originally rifted from Gondwana during the Paleozoic, subsequently drifting across the Tethys and finally accreting to Eurasia during the Mesozoic (Cai and Zhang, 2009; Faure et al., 2014). The SCB and NCB sutured during the late Middle Triassic to Middle Jurassic interval along the Qinling-Dabie and Sulu Orogeny (Fig. 2.1; Li, 1998; Grimmer et al., 2003). However, the SCB had a more complex tectonic history than the NCB (Xu et al., 2005). The precise location of the SCB within Gondwana is still debated, though there is a general consensus that it was a part of East Gondwana and occupied a position near western Australia and the Lhasa and Qiangtang blocks adjacent to northern Greater India (Duan et al., 2011; Cawood et al., 2013; Cocks and Torsvik, 2013).

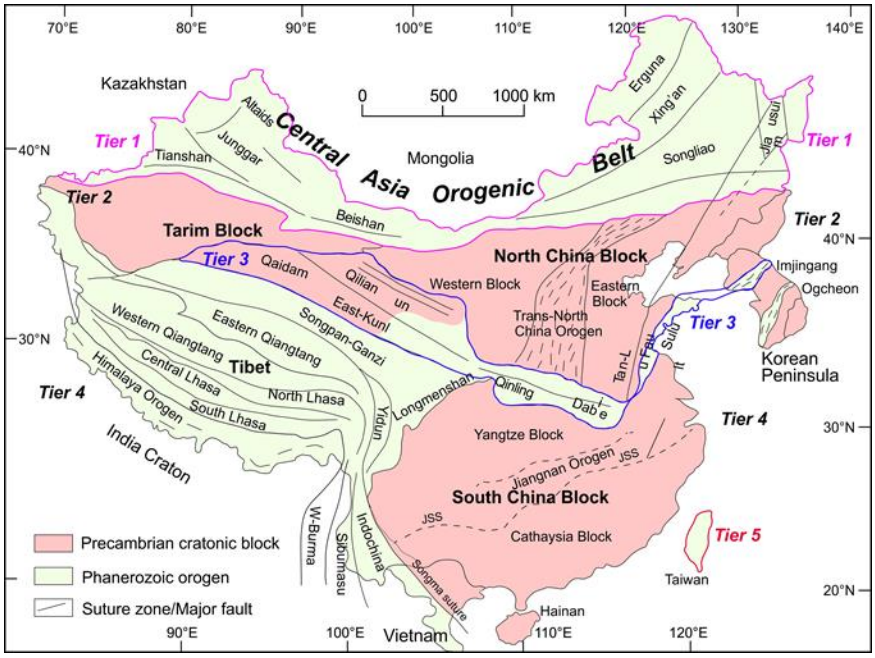

Fig. 2.1. Simplified tectonic map of China with the major Precambrian blocks and Late Neoproterozoic and Paleozoic fold belts. Tier 1 is defined by the Central Asian Orogenic Belt (CAOB) along the northern margin of China, which consists of the Xing'an-Mongolia orogenic belt in the NE and the Tianshan Orogen; Tier 2 includes the North China Block (NCB) to the east and Tarim Block to the west; Tier 3, also known as the Central China Orogen, is composed of the Sulu-Dabie-Qinling-Kunlun Orogen in the NW; Tier 4 contains blocks rifted from Gondwana, which include the Songpan-Ganzi, Qiangtang, and Lhasa terranes of Tibet in the west and the South China Block in the east; Tier 5 is represented by the island of Taiwan on the SE margin of China and marks where China crust continues to grow; JSS – Jiangshan-Shaoxing suture. Modified after Stern et al. (2018).

SCB maintained a position off western Australia and northeast India from the beginning of the Neoproterozoic to the end of the Paleozoic, along the periphery of both the Rodinian and Gondwanan supercontinents (Figs. 2.2a and 2.2b). In the late Paleozoic, it separated from Pangea and started drifting across the Tethys Ocean (Fig. 2.2c) prior to accretion onto the NCB and establishment near its current location within Asia (see Cawood et al., 2013).

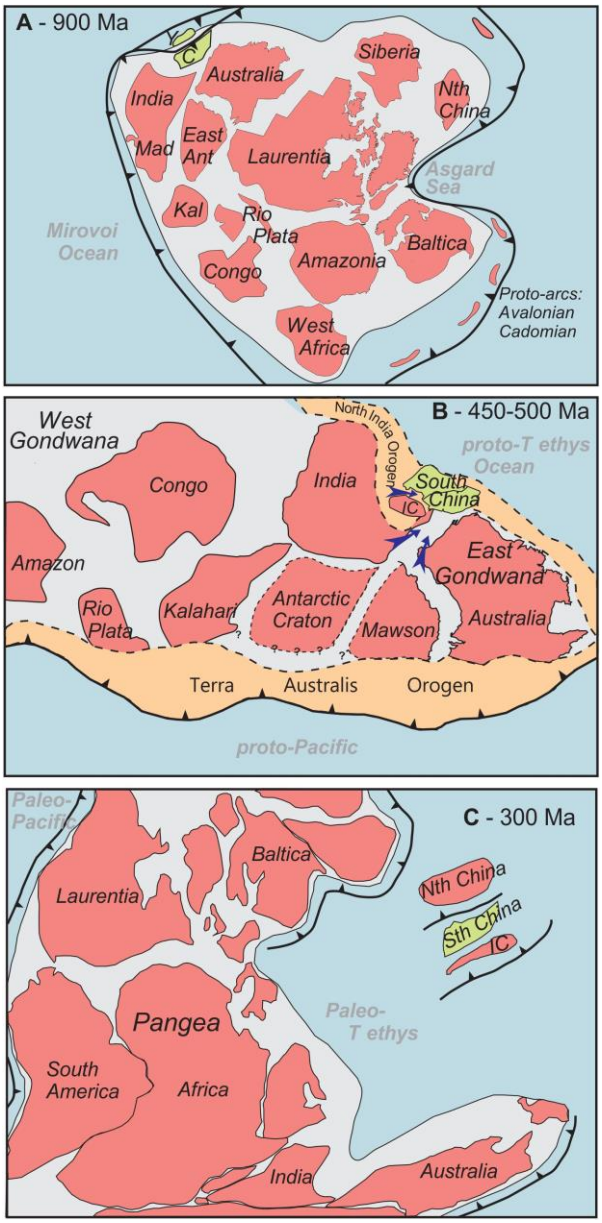

Fig. 2.2. Schematic paleogeographic reconstructions showing position of South (Sth) China and North (Nth) China blocks. A) Rodinia ca. 900 Ma. Mad–Madagascar; Kal–Kalahari; Ant–Antarctica; C - Cathaysia; B) Gondwana ca. 500–450 Ma. IC–Indochina; C) Pangea ca. 300 Ma. From Cawood et al. (2013).

The SCB is presently located in the west Pacific plate margin, bounded to the north by the Qinling-Dabie orogenic belt (which separates SCB from NCB), and to the west and southwest by the Tibetan terrains and Indochina Block, respectively (Fig. 2.1). It is composed of two main Precambrian tectonic units: the Yangtze Block to the northwest and the Cathaysia Block to the southeast (Fig. 2.1). Each of these unites had a different geological history as evidenced by different

basement composition and ages (e.g. Yu et al., 2012; Xia et al., 2015). The Yangtze Block is widely recognized as a cratonic shield area whereas the Cathaysia Block is made up of several Phanerozoic mobile belts, including a broad (~400 km) NE-trending belt of Mesozoic intrusions, extending through the maritime provinces of Guangdong, Fujian and Zhejiang and the Cenozoic mountain ranges of Taiwan (e.g. Chen and Jahn, 1998; Sewell et al., 2000b).

Yangtze and Cathaysia blocks were welded during the early Neoproterozoic time through the Jiangnan (also known as Jinning, Sibao or Grenvillian) Orogeny to form the unified SCB (Fig. 2.3; Guo et al., 1989; Shu and Charvet, 1996; Li, 1998; Zhao and Cawood, 1999; Li et al., 2002; Greentree et al., 2006; Wang et al., 2006; X.-L. Wang et al., 2007; Ye et al., 2007; Li et al., 2008; X.-L. Wang et al., 2008; Zheng et al., 2008; Li et al., 2009a; Zhou et al., 2009). The respective suture zone is coincident with the NE-trending Jiangshang–Shaoxing fault (Fig. 2.1; Zhao and Cawood, 1999). Several evidences record the development of the Jiangnan Orogeny: a Neoproterozoic magmatic arc suggesting a subduction beneath the SE border of the Yangtze block (Cheng, 1993; Zhou et al., 2002; Wang et al., 2006; Ye et al., 2007; Zhao and Zhou, 2007; Li et al., 2009a); an ophiolitic mélange in the NE Jiangnan area (Xu and Qiao, 1989; Zhou et al., 1989; Chen et al., 1991; Li et al., 1994; Liu et al., 1995; Gao et al., 2009); high-pressure metamorphism represented by glaucophane schists in an amphibolite facies metamorphic belt of Xiwan area, in Jiangxi Province, SE China (Zhou, 1989; Shu et al., 1994; Shu and Charvet, 1996; Zhou and Zou, 1996); and ductile deformation associated with widespread greenschist metamorphism along the NE Jiangxi shear zone and Jiangshan–Shaoxing zone (Wang and Mo, 1995; Shu and Charvet, 1996).

The evolution of the Jiangnan Orogeny occurred in four main stages (Fig. 2.4; Charvet and Faure, 1996; Charvet, 2013): (1) at 1–0.9 Ga, the Yangtze and Cathaysia blocks were separated by the South China Ocean, which was consumed by a north-westward subduction beneath the Yangtze block, leading to the Ganzhewan island arc and the Huaiyu back-arc basin; (2) at ca. 870–860 Ma, the subsequent collision led to the closure of the South China Ocean and the Huaiyu back-arc basin, leading to the emplacement of thrust sheets of ophiolitic mélange (~900 Ma) and blueschists (900–870 Ma); (3) between 840 and 800 Ma, late- to post-collisional granitic plutonism took place, the final compressive deformation was partly accommodated by sinistral ductile strike-slip shear and rifting-related mafic magmatism began and; (4) around 750 Ma, the rift basin was created and began to be filled with the sedimentary sequence starting with the Nanhua system.

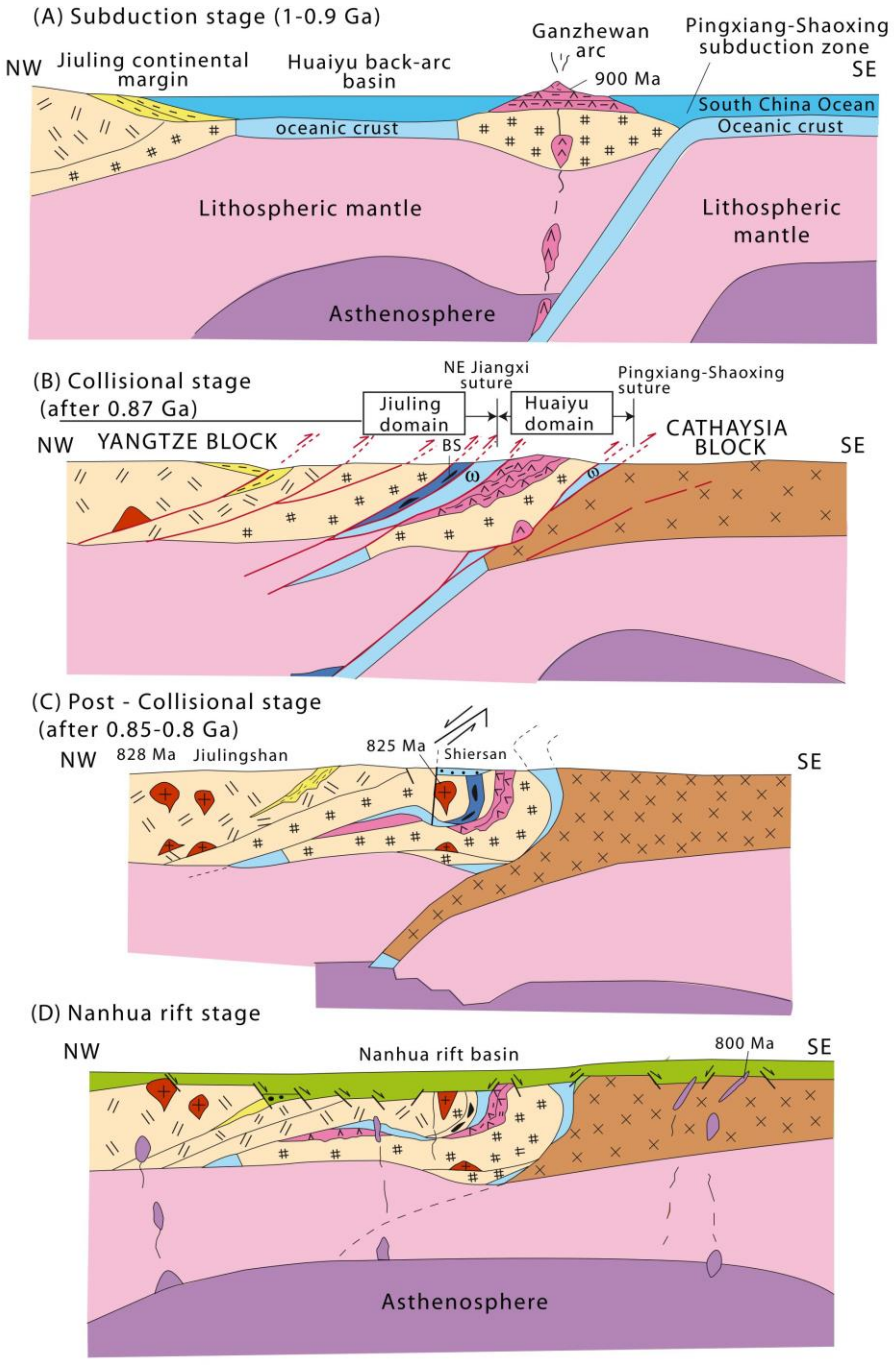

Fig. 2.3. Tectonic evolutionary model of the SCB during the Neoproterozoic. From Charvet (2013).

2.1.2. Cathaysia Block

The concept of the Cathaysia Block, named after the ‘‘Cathaysia old continent’’ of Grabau (1924), comes from the observation that its basement is unconformably overlain by Devonian

sediments. Initially, Cathaysia was considered to be a single block of Precambrian age, composed of intensely folded and faulted metamorphic basement rocks and intruded by large volumes of Mesozoic granitic magmas and mantled by vast areas of Jurassic to Cretaceous acid volcanic rocks, particularly in the coastal region (Grabau, 1924). Huang (1978) later described Cathaysia as including a vast "Southeast China Caledonian foldbelt" to the west and a much smaller tectonic unit of "Southeast maritime foldbelt" along the southeastern coastal region, which was intensely transformed by Mesozoic tectonism and magmatism. Others considered it as having resulted from a complex collage of suture-bounded terranes, only assembled during the Mesozoic (Hsu et al., 1990; Chen and Jahn, 1998).

While the Yangtze Block is characterized by Meso-Neoarchean crystalline basement represented by the Kongling complex and widespread Neoproterozoic magmatic rocks in the periphery of the block (Fig. 2.4; Li, 1999; Qiu et al., 2000; Z.-X. Li et al., 2003; Wang et al., 2006; Zheng et al., 2006; Zheng et al., 2007; Zheng et al., 2008; Gao et al., 2011), the Cathaysia Block is dominated by voluminous Phanerozoic magmatic rocks, particularly Mesozoic granitic rocks, with only sparse exposed Precambrian basement rocks (Fig. 2.4). The basement is overlain by Protorezoic metasediments and a Sinian (Chinese equivalent of Ediacaran, 630–542 Ma; e.g. Zhu et al., 2007) to Mesozoic sedimentary and volcanic cover (Fig. 2.4; Chen and Jahn, 1998; Shen et al., 2000).

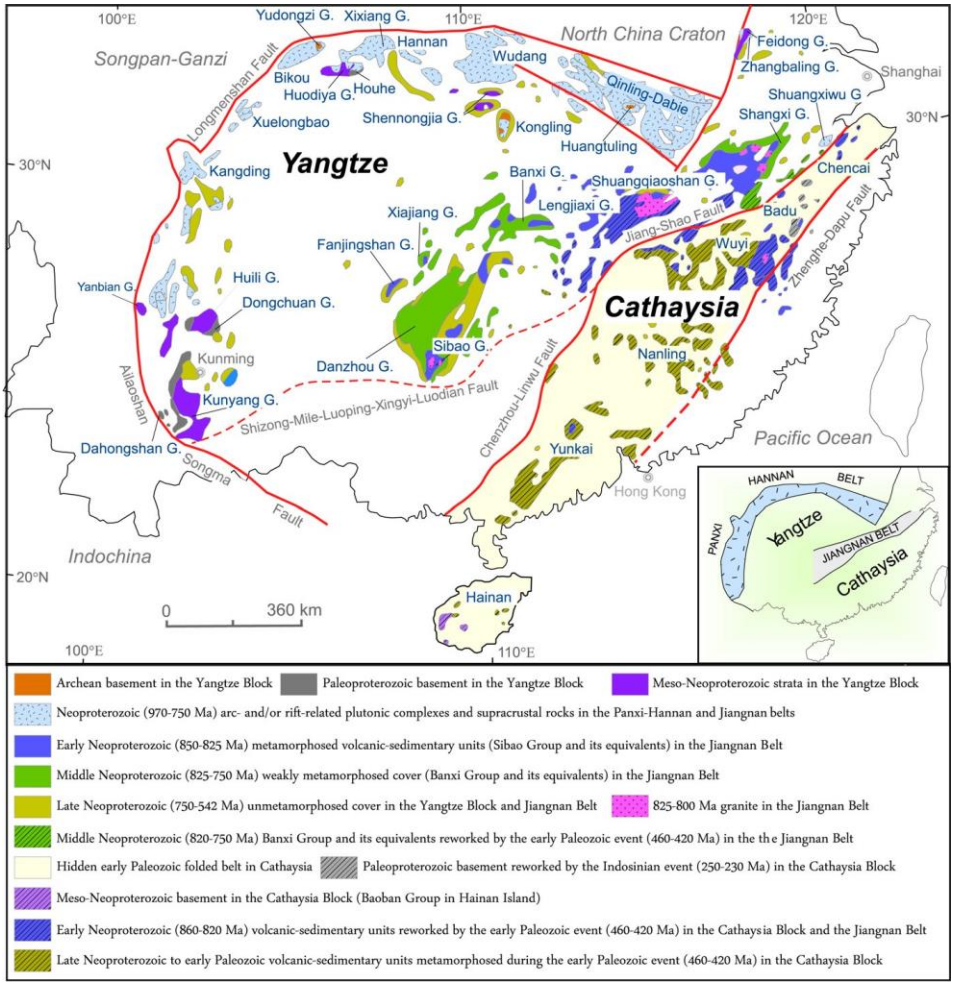

Fig. 2.4. Geological map of South China Block showing the distribution of Precambrian rocks in the Yangtze and Cathaysia Blocks separated by the Jiangnan Belt. The inset shows the spatial distribution of the Jiangnan Belt and Panxi-Hannan Belt in the Yangtze Block. Abbreviations: G - Group. From Zhao & Guo (2012).

Based on the types of magmatic rocks and the episodic growth patterns of the Precambrian crust, more recent studies have divided the Cathaysia Block into the Wuyishan terrane (Zhejiang and Fujian Provinces) to the northeast and the Nanling-Yunkai terrane to the southwest (Yu et al., 2010), or the eastern Cathaysia and western Cathaysia blocks, respectively (Xu et al., 2007b). The absence of the Paleozoic and Triassic magmatic overprints in the eastern Cathaysia Block has been taken as an evidence that the two terranes were separated before Triassic, or at least Paleozoic time, and may only have been juxtaposed by strike-slip movement during the Mesozoic (Xu et al., 2007b). The suture boundary separating these two terrains is thought to be coincident with the

NNE-NE trending Zhenghe–Dapu fault (Fig. 2.4; Chen and Jahn, 1998; Zheng et al., 2011; H.-T. Cai et al., 2015; Shu et al., 2015; Sewell et al., 2016).

Precambrian rocks in the northeastern part of Cathaysia include Paleoproterozoic S-, I- and A-type and high-grade metamorphic rocks (Chen and Jahn, 1998; R. Liu et al., 2009; Yu et al., 2009; Yu et al., 2012), suggesting the occurrence of a Paleoproterozoic Orogeny in the Cathaysia, probably related to the assembly of the supercontinent Columbia (Yu et al., 2009; Yu et al., 2012). Minor Neoproterozoic magmatic rocks also outcrop in this area (Li et al., 2005; Wan et al., 2007; Shu et al., 2011). The surface Precambrian rocks in the western Cathaysia consist only of Neoproterozoic igneous rocks and sedimentary strata (Zhang and Zheng, 2013; Li et al., 2014). Despite no Archean to Paleoproterozoic basement outcrops have been found in the western Cathaysia, the central Nanling area (western Cathaysia) contains abundant Neoarchean, Grenvillian and Neoproterozoic zircons with fewer Mesoproterozoic and Meso- to Paleo-Archean ages (Yu et al., 2010; Charvet, 2013). Studies on crustal xenoliths and zircon xenocrysts entrained in Mesozoic and Cenozoic volcanic rocks from neighbouring areas of Macao also suggest the existence of a highly evolved Archean-Paleoproterozoic basement beneath the western Cathaysia Block (Guo et al., 1997; Zheng et al., 2004; Dai et al., 2008; Li et al., 2018)

In southern Guangdong Province, where Macao is located, the isotopic signatures of Mesozoic granitic rocks indicate a strong heterogeneity in the basement, characterized by Paleoproterozoic- and Mesoproterozoic-dominated crustal domains interspersed with a few narrow belts displaying mantle-derived features, whose boundaries coincide with major Mesoproterozoic fault zones that controlled the subsequent geological evolution in SE China (e.g. Campbell and Sewell, 1997; Darbyshire and Sewell, 1997; Sewell et al., 2000b; Shen et al., 2000; Y. Zhang et al., 2015).

2.1.2.1. Paleozoic

The Cathaysia Block comprises a NE–SW trending orogen stretching for ~2000 km (Fig. 2.5; Ren et al., 1999; Charvet, 2013) known as the South China Caledonian Fold Belt (SCCFB; Huang, 1978), Early Paleozoic Orogen of the SCB (Faure et al., 2009) or Wuyi–Yunkai Orogen (Li et al., 2010). It has been recognized as Early Paleozoic in age based on the existence of an angular unconformity separating pre-Devonian deformed rocks and Devonian strata, and the occurrence of widespread high-grade metamorphic rocks, migmatites and granitoids (Grabau, 1924; Ren, 1964; Ren, 1991; Zhao et al., 1996). Due to the absence of early Paleozoic ophiolitic rocks, accretionary

complexes and magmatic arc, and because early Paleozoic magmatic rocks are mainly confined to the inland area of the SCB with only a few along the plate margins, the Wuyi–Yunkai orogen has been regarded as an intraplate orogeny (Fig. 2.5; Faure et al., 2009; Charvet et al., 2010; Li et al., 2010; Charvet, 2013). Both sedimentary and magmatic records indicate that the SCB was in an intracontinental setting as a consequence of a rift closure from the Late Ordovician to Early Silurian (Ren, 1991; Charvet et al., 2010; Li et al., 2010; Charvet, 2013; D. Wang et al., 2013; Xu and Xu, 2015).

Stratigraphically, a two-stage stable depositional environment has been proposed for the Paleozoic: a sandy-muddy sequence that accumulated in the Cambrian to Late Ordovician, and a carbonate sequence formed between the Carboniferous and Early Triassic (Shu et al., 2006; Shu et al., 2008b; Wang et al., 2010; Zhang and Zheng, 2013; Shu et al., 2014; Shu et al., 2015). A large stable depositional environment (>1000 km) was formed by the Cambrian to Ordovician successions, which comprise carbonate sequences in the Yangtze Block, carbonate-siliceous sequences in the region of the Jiangnan orogen and graptolite-bearing sandy-muddy sequences in the Cathaysia Block (e.g. Chen et al., 1995; L. Shu et al., 2008; Wang et al., 2010; X. Chen et al., 2012; Rong et al., 2012; Shu et al., 2014).

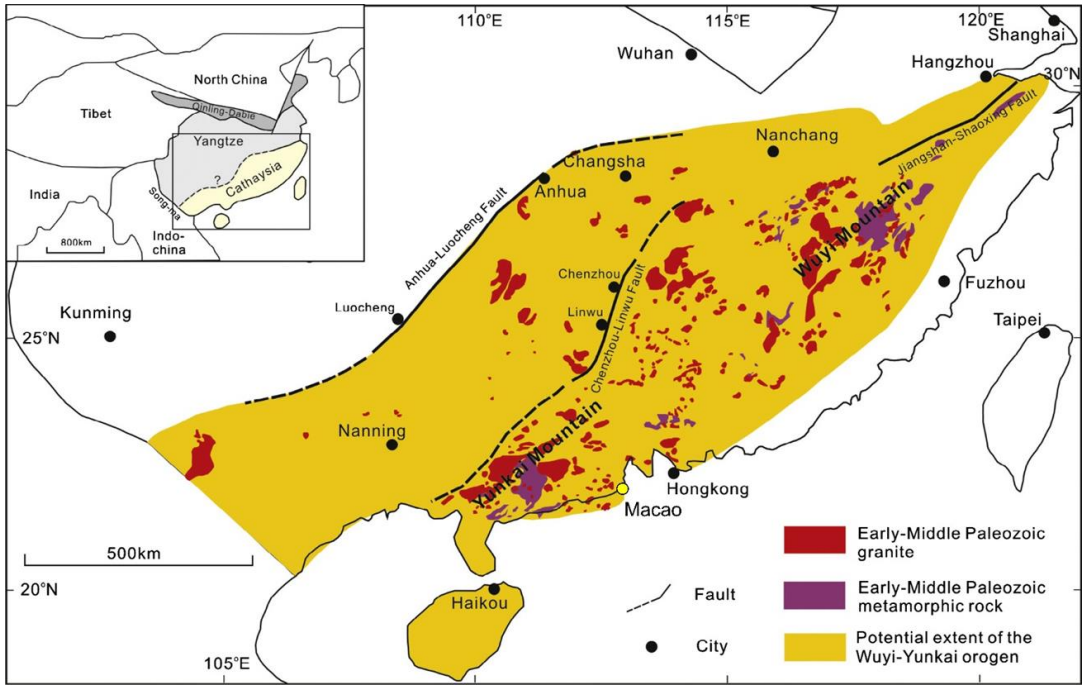

Fig. 2.5. Simplified geological map showing the distribution of the Paleozoic granites and high grade metamorphic rocks in the Cathaysia Block. Modified after Feng et al. (2014).

During the Silurian, a major tectonomagmatic event occurred in the SCB resulting in folding, thrusting and large-scale crustal anatexis, leading to emplacement of granites and lower greenschist facies metamorphism (Ren, 1991; Li et al., 2010; Xu et al., 2011; Zhang and Zheng, 2013; Shu et al., 2015). The Paleozoic granites are widespread in the eastern SCB (Fig. 2.5), occurring as laccoliths and batholiths with a total exposure area of over 20,000 km^2. Geochronological studies have defined a wide age-span of ca. 381–467 Ma for these granites (e.g. Wan et al., 2007; Y. Wang et al., 2007b; Li et al., 2010; Wan et al., 2010; Wang et al., 2011; Zhang et al., 2012; Zhao et al., 2013; Feng et al., 2014; Xia et al., 2014; Peng et al., 2015; Q. Zhang et al., 2015; Xu et al., 2016; Cai et al., 2017; C. Yan et al., 2017). Most of these granites are peraluminous S-type granites, with minor amphibole bearing I-type granites, and their origin has been interpreted as a result of syn-orogenic to late orogenic anatexis of the orogenically thickened crust (Li et al., 2010; Zhao et al., 2013; Xia et al., 2014; Peng et al., 2015; C. Yan et al., 2017). Some A-type granites have also been reported, suggesting strongly post-collisional extension environment in the Wuyi-Yunkai orogen at least since 410 Ma (Feng et al., 2014; Cai et al., 2017).

From the Middle to Late Devonian, the south China region evolved into a more stable littoral-neritic depositional environment (Zhang et al., 2013), characterized by Brachiopoda-, coral-, and Fusulina-bearing carbonate depositional platform containing limestone, dolomite, black chert, and minor sandstone and mudstone (Shu et al., 2008a). During the Triassic, further tectonomism and magmatism affected the region. Pre-Mesozoic deformation structures are unconformably overlain by Late Triassic coarse-grained clastic rocks (Shu et al., 2015), suggesting that the Cathaysia Block was intensely reworked by Early Mesozoic tectono-magmatic activity.

2.1.2.2. Mesozoic

The Mesozoic Era was characterized by intense and widespread magmatic activity in the SCB, resulting in the formation of large volumes of magmatic rocks mostly concentrated in the southeast region of the block, with its density increasing towards the ocean (Fig. 2.6). The Mesozoic magmatic rocks in the SE part of SCB are mainly distributed in Zhejiang, Fujian, Jiangxi, Guangdong and Hunan Provinces with a total outcrop area of nearly 218,090 km^2 (Zhou et al., 2006). Over 90% of these rocks are granites and equivalent volcanic rocks with minor basalts.

Two periods of tectono-magmatism are recognized during Mesozoic (Zhou et al., 2006): (1) the Indosinian period [Early (251–234 Ma) and Late (234–205 Ma) sub-periods] and; (2) the Yanshanian period [Early (180–142 Ma) and Late (142–67 Ma) sub-periods].

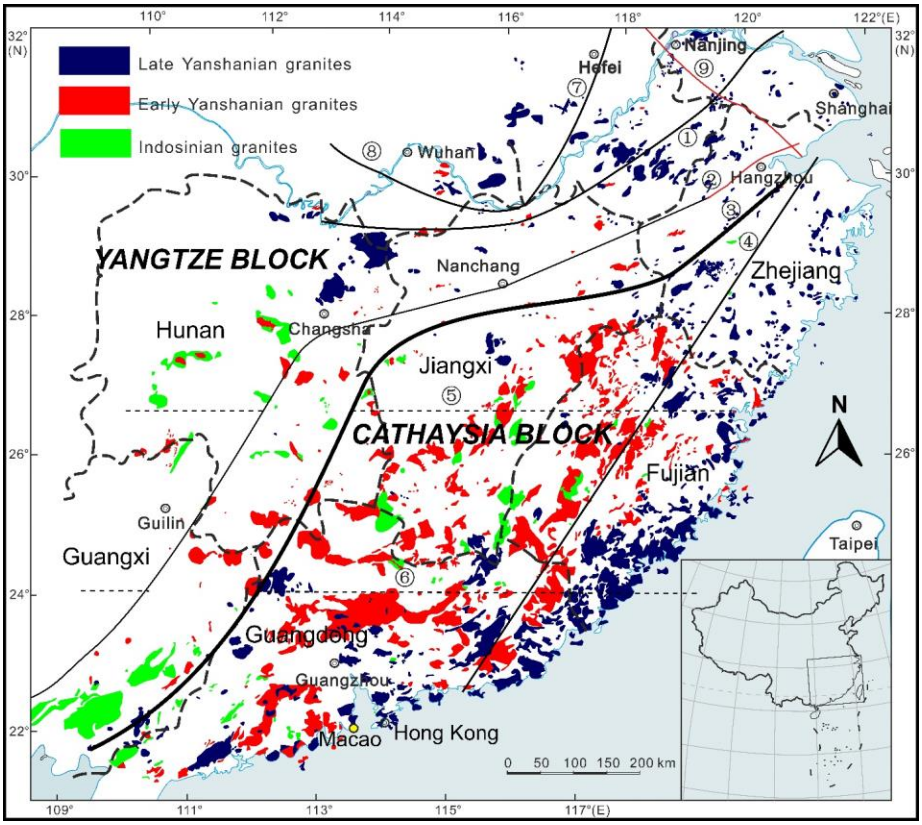

Fig. 2.6. Geological map showing the distribution of the Mesozoic granitic rocks in SE China: Triassic (Indosinian), Jurassic (Early Yanshanian) and Cretaceous (Late Yanshanian). ① Nantong-Liyang-South Lushan-Ruichang-Chongyang fault, ② Hangzhou-Xiangtan-Jinxiu-Pingxiang fault (northwestern margin of Qin-Hang belt, ③ Shaoxing-Jiangshan-Pingxiang-Wuzhou-Hepu fault (southeastern margin of Qin-Hangbelt), ④ Yuyao-Zhenhe-Dapu fault, ⑤ Qiyang-Ninggang-Guangchang-Nanping fault (north Nanling Mountain), ⑥ Jinxiu-Xinfeng-Xinning-Yunxiao fault (south Nanling Mountain),⑦Tancheng-Lujiang fault, ⑧ South Dabie fault, ⑨ Chuzhou-Jiaxing fault. Modified after Mao et al. (2014).

2.1.2.2.1 Early Mesozoic (251-205 Ma)

Although the bulk of magmatic rocks in SCB has been attributed to the Late Mesozoic magmatism (180-67 Ma), the Triassic magmatism also played a significant role during the early Mesozoic period, as a result of continental collisions related to the closure of the Paleo-Tethys Ocean (e.g. Lepvrier et al., 2004; Mao et al., 2011; Faure et al., 2014). Two main collisions occurred: between the Indochina and South China blocks at ca. 243 Ma along the southern margins (Lepvrier et al., 2004) and between the South China and North China blocks at ca. 240 to 211 Ma

in the north (Jiang et al., 2011). Extensive tectonism developed in this period, including stratigraphic unconformities, metamorphism, and magmatism (Zhou et al., 2006; Li and Li, 2007; Y. Wang et al., 2013; Gao et al., 2017). The tectonic events that occurred in this period were named the Indosinian Orogeny (Huang et al., 1987; Chen and Jahn, 1998; Zhou et al., 2006).

The Triassic magmatic rocks in South China mainly consist of granite, with only minor syenite (e.g. Wang et al., 2005; Xie et al., 2005; Jianren Mao et al., 2013), diabase (e.g. Tang et al., 2013; K.-X. Wang et al., 2013) and rare MME (e.g. Chen et al., 2007; Dai et al., 2008; Xu et al., 2014). These magmatic rocks occur in the interior of South China, far from the continental margins, mainly to the west of the Zhenghe-Dapu Fault (Fig. 2.6; Huang et al., 1987; Chen and Jahn, 1998; Zhao et al., 2013). The Triassic granitic rocks in the southeastern part of the SCB occur as plutons with a total outcrop area of 21,000 km^2, equivalent to 12.3% of the outcrop area of granitic rocks in South China (Mao et al., 2011). The majority of these rocks are strongly peraluminous, S-type granites, with high aluminous minerals like muscovite, garnet, cordierite and tourmaline (Sun, 2005; Y. Wang et al., 2007a; Yu et al., 2007), the remaining being calc-alkaline I-type biotite granites, with or without amphiboles (Y. Wang et al., 2007a; Xu et al., 2014; Gao et al., 2017). Recent works have also confirmed the presence of Indosinian alkaline A-type granites in some provinces of South China (e.g. Sun et al., 2011; Jianren Mao et al., 2013; Zhao et al., 2013; Y. Cai et al., 2015).

Two periods of Indosinian magmatic activity can be distinguished according to their different geodynamic genetic processes (Zhou et al., 2006; Y. Wang et al., 2007a; Mao et al., 2011; Jianren Mao et al., 2013): (1) early Indosinian granites (251–234 Ma) make up about 90% of all the Indosinian granitoids, emplaced in a compressional setting related to the collision between the SCB and the Indochina Block; (2) late Indosinian granites (234–205 Ma) emplaced in an intraplate extensional regime during the late-collisional phase.

The early Indosinian granitic rocks are well exposed along and around the Songma suture (where the Indochina Block and SCB collided; see Fig. 2.1), corresponding to the peak period of collision-related magmatism which took place between 258 ± 6 Ma and 243 ± 5 Ma (Carter et al., 2001). Features such as deformation fabrics (e.g. schistocity, gneissic or mylonitized structures) and magmatic foliation are observed in early Indosinian syn-collision granites, but absent in late

Indosinian post-collision granites (Zhou et al., 2006; Mao et al., 2011; Jianren Mao et al., 2013), indicating a compressive regime operating in the early Indosinian period.

The late Indosinian granitoids occur as dispersed medium grain size massive plutons (about 90% of all the Indosinian granitoids). Indeed, a wide extensional tectonic regime dominated in the Cathaysia Block between 254 to 225 Ma (late Permian–Triassic) as evidenced by the occurrence of Triassic A-type granites and alkaline syenites in the SCB Ma (Wang et al., 2005; Sun et al., 2011).

The Late Triassic NE-trending A-type granite belt (consistent with main NE-trending strike-slip faults) has been interpreted by some authors as being formed in an extensional setting induced by subduction of the Paleo-Pacific plate beneath the SCB (Wang et al., 2005; Sun et al., 2011; K.-X. Wang et al., 2013; Y. Cai et al., 2015). According to this model, the Paleo-Pacific slab was subducted northwestward beneath the SCB since the Permian, and this subduction would have caused a broad occurrence of deformation and granitic magmatism with a width up to 1300 km from coastal to internal South China and from late Paleozoic to early Mesozoic (Li et al., 2006; Li and Li, 2007; Li et al., 2012).

However, according to other authors, the absence of early Mesozoic ophiolite suites, oceanic basins and arc magmatism in the SCB, plus the planar-shaped distribution of these granites, does not agree with the interpretation of Indosinian oceanic/arc-continental subduction (Y. Wang et al., 2007a; Zhao et al., 2013). Zhao et al. (2013) argued that the overall tectonic regime of the SCB at the late Permian–middle Triassic was compressional and the transtensional environment, evidenced by the Indosinian alkaline syenites and A-type granites, was a result of local NE-trending extensional zones. These local extensions, which followed folding-napping and thickening of crust during the Indosinian collision, led to the formation of para-foreland type basins and associated strongly peraluminous S-type granites (Sun, 2005; Zhou et al., 2006). Since about 225 Ma, the SCB entered the within-plate post-collisional environment (Zhao et al., 2013), where underplating of small amounts of magma provided enough heat to induce dehydrated melting of the country rocks to generate late-Indosinian peraluminous granites (Wang et al., 2007). This model emphasizes that the Triassic intracontinental orogenesis of South China was a response to the far-field stress due to the continental collision between Indochina and South China in the south and

between North China and South China in the north (Zhou et al., 2006; Y. Wang et al., 2007a; K.-X. Wang et al., 2013).

2.1.2.2.2 Late Mesozoic (180-67 Ma)

A major change in the geodynamic setting in the SCB occurred during the Mesozoic, from the eastern Tethyan tectonic regime in the early Mesozoic to the Paleo-Pacific tectonic regime in the late Mesozoic. This transition was marked by a period of magmatic quiescence between 205 and 180 Ma (Zhou et al., 2006).

Although different views on the Mesozoic petrogenesis in SCB have been proposed through the years, nowadays it is generally accepted that subduction of the Paleo-Pacific plate under the Eurasian plate was the key engine for the Late Mesozoic magmatic activity (Zhou and Li, 2000; Zhou et al., 2006; Li and Li, 2007; Jiang et al., 2009; Jiang et al., 2015; Y. Zhang et al., 2015). This tectono-magmatic event is commonly known as the Yanshanian Orogeny. The paleo-suture of the subduction is thought to be located in the east flank of the Central Range, Taiwan (Zhou & Li, 2000). Nevertheless, the style of subduction has remained controversial, leading to the proposition of different models (see below). The onset of this Mesozoic subduction also varies: Early Triassic (e.g. Li et al., 2007), Middle Jurassic (e.g. Zhou & Li, 2000; Zhou et al, 2006; Jiang et al., 2009) and Early Cretaceous (C.-H. Chen et al., 2008b). In addition, the evolution of the subduction process was marked by multiple tectonic regimes during the Early Yanshanian and Late Yanshanian periods (e.g. Li and Li, 2007; Meng et al., 2012; Jiang et al., 2015). The questions of how and when the transitions between different tectonic settings occurred and the relationship between the tectonic shifts and the change in characteristics and distribution of magmatism are still not clear.

An active continental margin, associated with subduction of the Paleo-Pacific Plate beneath the Eurasian Plate, is commonly considered as the origin for extensive silicic magmatism in SE China during the late Mesozoic (Jahn, 1974; Jahn et al., 1990; Charvet et al., 1994; Lapierre et al., 1997). Alternatively, a continental rifting model involving lithospheric extension, caused by the collision between Indochina and SCB or crustal extension post-dating the Triassic Indosinian Orogeny, has also been proposed (Gilder et al., 1991; Li, 2000).

Zhou & Li (2000) states that during the early period of the Middle Jurassic (180-170 Ma), some small-scale magmatism was reactivated and became progressively more intensive; low-angle

and high speed subduction of the Paleo-Pacific plate during the Middle-Late Jurassic was responsible for the formation of the Late Mesozoic broad magmatic arc in SE China (Zhou and Li, 2000; Geng and Xu, 2006). From Middle Jurassic to Cretaceous (ca. 100 Ma), magmatism gradually migrated oceanward due to the change from low to high subduction angle (Zhou and Li, 2000; Geng and Xu, 2006).

Li and Li (2007) pointed out several reasons as why the above-mentioned models, i.e. those invoking a continental arc, cannot adequately explain the Late Mesozoic magmatism in SE China: (1) many Jurassic rocks do not have arc geochemistry; rather, they are bimodal and many are intraplate alkalic rocks (X.-H. Li et al., 2003; Li et al., 2004); (2) development of a system of sub-parallel NE-trending grabens formed simultaneously with regional magmatism in SE China, considered to be analogous to the present-day Basin and Range Province in the western USA (Gilder et al., 1991); (3) the magmatic province stretched ~1000 km from the continental margin, not just along the coastal region; and (4) the temporal-spatial distribution of the magmatism was not the result of a simple coastward migration, as suggested by the of Zhou and Li (2000). Instead, Li and Li (2007) proposed a flat-slab subduction model to account for formation of a broad intracontinental magmatic belt, which involved the subduction of a flat oceanic plateau of ~1000 km diameter beneath the Eurasian plate, between ca. 250 Ma and ca. 190 Ma, and slab foundering between ca. 190 Ma and ca. 150 Ma to account for the bimodal alkaline basaltic-rhyolitic magmatism in SE China. According to the authors, the Jurassic-Cretaceous coastward migration of both extensional and arc-related magmatism can best be explained by a rollback of the arc system.

The model of Li and Li (2007) suggested that by the late Triassic (ca. 210 Ma) the subducted Paleo-Pacific plate reached the Yangtze Block and that the early Mesozoic magmatism in SE China was the result of the Paleo-Pacific plate subduction. However, several authors argued that there is no evidence for subduction in SE China in the Triassic and that magmatism during this period was instead related to collision between Indochina and SCB during the Indosinian Orogeny (Y. Wang et al., 2007a; Zhao et al., 2013). Taking this into account, Jiang et al. (2009) suggested that during the middle Jurassic time (180-160 Ma) SE China was a continental arc coupled with the subduction of the Paleo-Pacific plate and since the beginning of late Jurassic time (160-140 Ma) an intra-arc rift has been formed as a consequence of slab roll-back. More recently, the same authors proposed

a more complex model involving repeated slab–advance–retreat of the Paleo-Pacific plate (Jiang et al., 2015).

A non-subduction related intracontinental orogeny model has also been proposed by Chen et al. (2008). The authors argued that the mantle beneath the Cathaysia Interior and Cathaysia Folded Belt is characterized by a homogeneous domain, which remained undisturbed during the Jurassic, distinctly different from the Southeast Coast Magmatic Belt that has been modified by the Paleo-Pacific subduction. Therefore, the east-west basalt array in SE China represents an eastward trace of continental extension through time, probably related to the progressive Triassic continent–continent collision between the Indochina and SCB. The Jurassic granitoids in SE China are thus interpreted as products of post-orogenic (Indosinian) magmatism.

Independently of the tectonic setting, the Late Mesozoic tectono-magmatic activity was responsible for the formation of large volumes of magmatic rocks (e.g. Sun et al., 2012). The majority of these rocks are granites associated with minor rhyolites and subordinate mafic intrusive and volcanic rocks (e.g. Zhou and Li, 2000; Zhou et al., 2006; Li et al., 2007). In general, Jurassic granitic and volcanic rocks occur mostly in the interior part of the Cathaysia Block, whereas Cretaceous granitoids and volcanic rocks tend to concentrate along the coastal area of SE China (Fig. 2.7; Chen and Jahn, 1998; Zhou and Li, 2000).

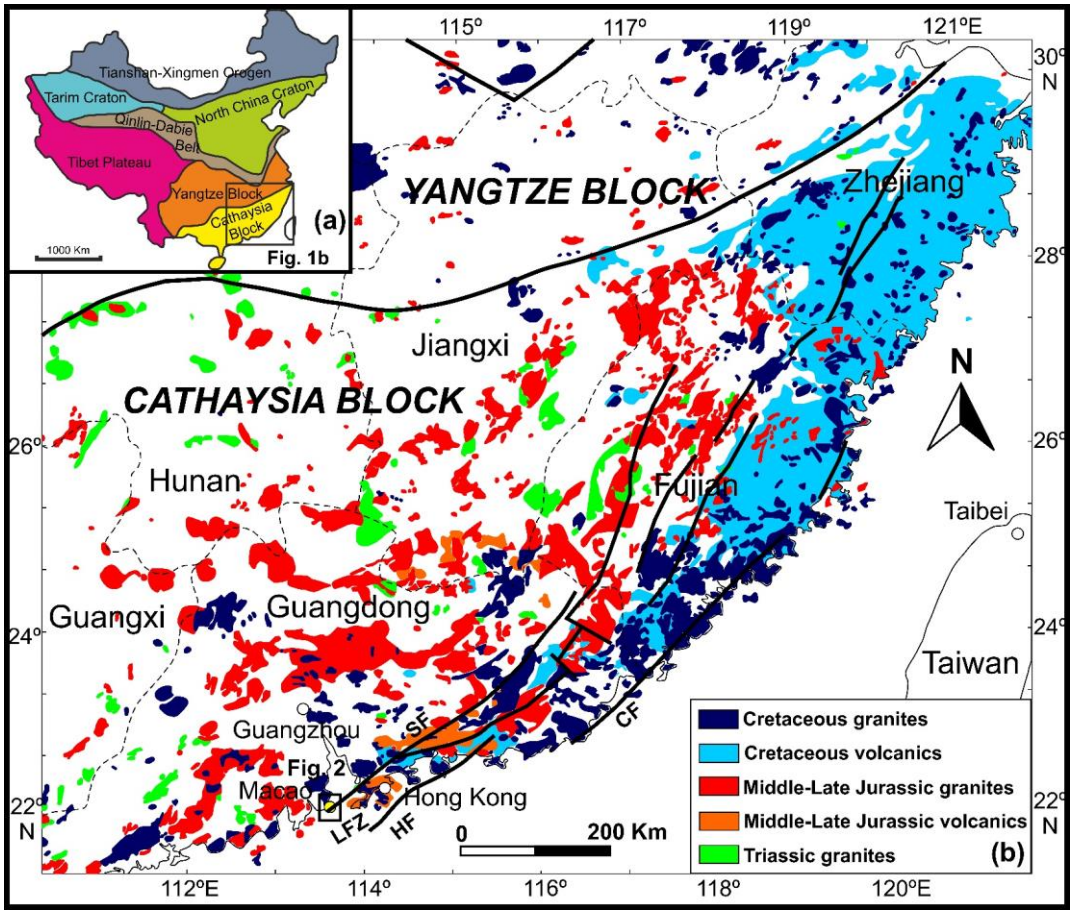

Fig. 2.7. (a) Simplified tectonic sketch of China; (b) Geological map of SE China, showing the distribution of Mesozoic granitic and volcanic rocks on the Cathaysia Block. The Lianhuashan Fault Zone (LFZ), Shenzhen Fault (SF), Haifeng Fault (HF) and Changle–Na'nao Fault (CF) are also represented. Fig. adapted from Davis et al. (1997) and Zhou et al. (2006).

The Early Yanshanian granitoid-volcanic rocks were emplaced in the mid- and late- Jurassic (180–142 Ma), and are mainly distributed in the interior of the Cathaysia Block, in zones parallel to the coastline of SE China, with a total outcrop area of 75.000 Km^2 (Fig. 2.7; Zhou et al., 2006; Li et al., 2007). The Yanshanian granitic rocks are associated with large-scale tungsten, tin, molybdenum, copper, gold, and other rare metal mineralization (Jingwen Mao et al., 2013; Cao et al., 2018). A great part of these granitic rocks are metaluminous to weakly peraluminous calc-alkaline I-type granodiorites and biotite granites with minor MME and variable degrees of fractionation (e.g. Sewell et al., 1992; Li et al., 2007; Huang et al., 2012; Y. Zhang et al., 2015; Xiang et al., 2017; Zhang et al., 2017). They are often spatially and temporally associated with minor gabbro, syenite, diorite, A-type granite and two-mica granite (e.g. X.-H. Li et al., 2003; Li

et al., 2004; Li et al., 2007; Xu et al., 2007a; Y. Wang et al., 2008; He et al., 2010; Meng et al., 2012; Zhang et al., 2017).

The Late Yanshanian granitic and volcanic rocks occupy about 139,920 km^2 in the SCB and are divided into two main stages: early Late Yanshanian (Early Cretaceous) granitic-volcanic rocks genetically associated with active continental margin magmatism and the late Late Yanshanian (Late Cretaceous) tholeiitic basalt volcanism recorded in red beds of back-arc basins (Chen et al., 2000; Zhou et al., 2006). Granites and rhyolites often coexist, forming volcano-subvolcano-intrusion assemblages, whereas mafic rocks (gabbros and basalts) are volumetrically minor (<10%) to absent (Zhou et al., 2006). The Late Yanshanian granitic rocks are dominantly high-K I-type and A-type granites formed in four major magmatic episodes between 136–146 Ma, 122–129 Ma, 101–109 Ma and 87-97 Ma (Chen et al., 2000; Li, 2000).

2.2. Geological background of Macao

2.2.1. Previous studies

The first known study on the geology of Macao was published by Costa (1944) and provides the first geological map of this territory. In the same year, Neiva (1944) made a petrographic study of the eruptive rocks (term used back then for the igneous rocks) outcropping in Macao. Later, Lemos (1963) produced the first geological map of the Macao territory at a scale of 1:25000, which was subsequently included in a more detailed report (Carrington da Costa and Lemos, 1964) where five main geological units were defined: sediments currently in deposition - beach sands; landfills; sand dunes; consolidated clay-sandy sediments; eruptive rocks. Despite the fact that nowadays many research approaches and classification terms used in these first studies are considered outdated, they provided the basis for further research and even contain some information that is no longer available due to the increasing urbanization of Macao since that time. As an example, Neiva (1944) identified a basaltic dyke intruding the granitic rocks in the Macao Peninsula, which was not found in subsequent studies. Some years later, Rocha and Torquato (1967) studied the mineralogical and micro fauna composition of sands from Taipa and Coloane beachs. Marques (1988) gave a major contribution to the existing cartography and produced three geological/geotechnical letters (1:10000) in which stratigraphic units were addressed in detail. Two years later, based on geotechnical reports performed on the territory, studies were made on the

geotechnical features of the muds and alluvial deposits of Macao (Marques and Silva, 1990b; Marques and Silva, 1990a).

The most complete and detailed geological study in Macao was carried out by Ribeiro et al. (1992). This study includes not only a more detailed geological map of Macao, Taipa and Coloane at a 1:5000 scale, comprising its different lithologies and structures, but also detailed explanatory notes with a comprehensive description of the stratigraphy, mineralogy, tectonics, chemistry and magmatism of the rocks outcropping in Macao territory. In addition, Ribeiro et al. (1992) provided the first ages of the Macao granites based on K-Ar dating of biotite, with most samples dated between 154 ± 5 and 168 ± 4 Ma, plus a significantly younger date of 94 ± 2 Ma (see also Ribeiro et al., 2010). Some of these reports were also published as summaries (So and Ribeiro, 1997; Ribeiro et al., 2010).

After the above-mentioned studies, no other significant geological works have been published for the region up until 2015, when a new research project on the geology of Macao was initiated. The project on the "Petrology and Geochemistry of Igneous Rocks from Macao: Implications for the Crustal Evolution of Southern China" (Ma.G.I.C.; 2015), funded by the Macao Science and Technology Development Fund (FDCT), aimed to contribute towards a deeper understanding of the petrology and geochemistry of the igneous rocks of Macao and its implications for the geodynamic evolution of the territory. This doctoral thesis, as well as the publications arising from it, were developed within the context of this project.

2.2.2. Regional geological context

Macao is located in southern Guangdong province, along the coast of SE China, ca. 50 Km to the west of Hong Kong, on the western margin of the Pearl River Delta (Fig. 2.8). In this region, there is a predominance of granitic intrusions belonging to the ~ 3500 km long and ~ 800 km wide NE-trending Mesozoic SCMB (Figs. 2.6 and 2.7).

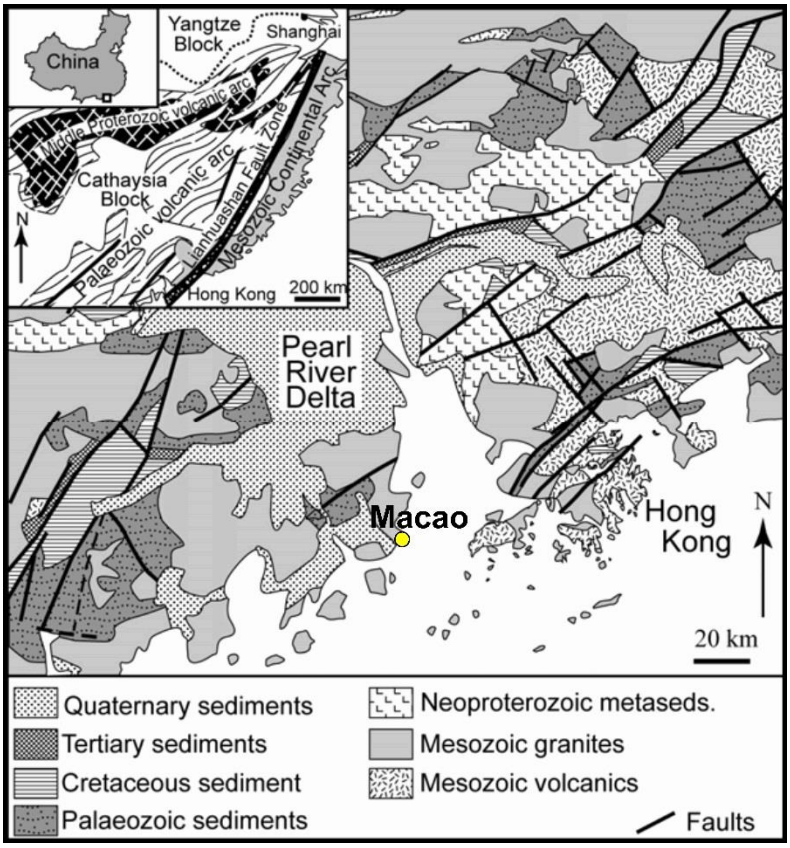

Fig. 2.8. Geological Map of the Pearl River Delta, southern Guangdong Province. Modified after Shaw et al. (2010).

The Mesozoic volcanic rocks in the region crop out on the east side of the Pearl River delta, Hong Kong (Fig. 2.8), where Late Mesozoic magmatic rocks compose around 85% of this territory. Despite no Archean and Proterozoic basement rocks outcrop in Hong Kong, geochemical, isotopic and geophysical studies strongly suggest their existence beneath the Yanshanian magmatic rocks exposed at the surface (Darbyshire and Sewell, 1997; Sewell and Campbell, 1997; Sewell et al., 2000b). The Mesozoic volcanic-plutonic rocks intruded Late Paleozoic and Younger Early to Middle Jurassic sedimentary successions of deformed and metamorphosed by several tectonic events (Sewell et al., 1992; Sewell et al., 2000a).

The Yanshanian magmatic rocks in Hong Kong consist of dacitic to rhyolitic ignimbrites and lavas with intercalated tuffaceous sedimentary units, as well as plutonic rocks such as granodiorite, granite, quartz monzonite and minor dykes of diverse compositions (Sewell et al., 2000a; Sewell et al., 2012). The Jurassic-Early Cretaceous magmatism is considered to have occurred in four

distinct magmatic episodes constrained by detailed field work (Sewell and Campbell, 1997) and high-precision zircon U–Pb data (Davis et al., 1997; Campbell et al., 2007; Sewell et al., 2012): 165-160 Ma (Lamma Suite), 148-146 Ma (Kwai Chung Suite), 143 Ma (Cheung Chau Suite) and 141 Ma (Lion Rock Suite). These volcanic-plutonic assemblages are representatives of ancient caldera-related large-scale silicic magmatic systems (Fig. 2.9; Campbell and Sewell, 1997).

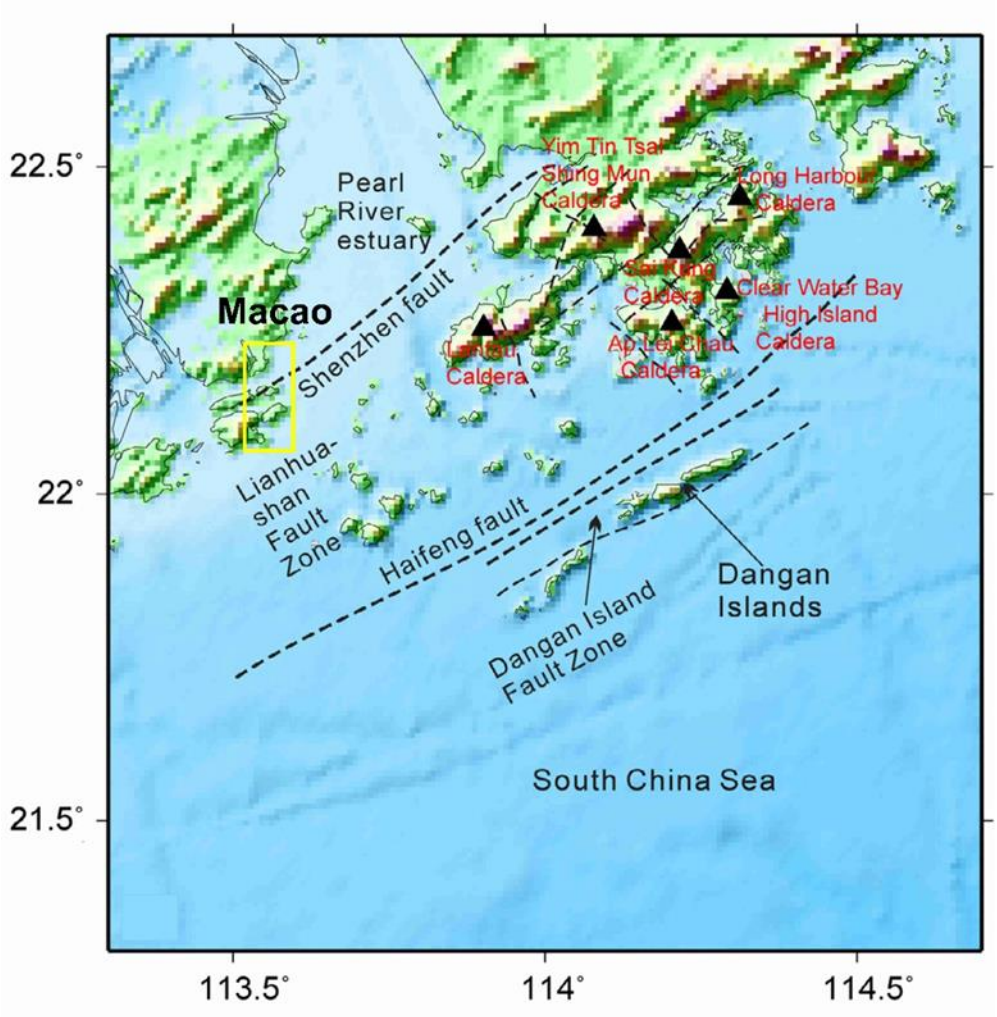

Fig. 2.9. Distribution of faults and Late Mesozoic calderas in Hong Kong. The triangles show the locations of identified calderas. The dashed lines represent the faults that are closely associated with the calderas and magmatism. Modified after Xia and Zhao (2014).

To the west of Macao, along the southern coastal region of the Guangdong Province, a few amphibole-bearing granites occur as stocks/small plutons (Huang et al., 2012), intruding the Paleozoic strata to the southeast of the Wuchuan–Sihui fault (Fig. 2.10). They were formed in the

Late Jurassic and are temporally and spatially associated with high-K, shoshonitic basic-intermediate rocks in the region (X.-H. Li et al., 2000b; X. H. Li et al., 2000; Wang et al., 2003). In contrast, most of the other granites in this region were emplaced to the east into pre-Devonian strata (Fig. 2.10) and form larger plutons or batholiths. They are composed of biotite granites (rarely containing amphibole) spatially associated with volumetrically minor tourmaline-, muscovite- and garnet-bearing granites. Zircon U–Pb geochronological data show that these granites were emplaced at 166–159 Ma (Fig. 2.10; Huang et al., 2012).

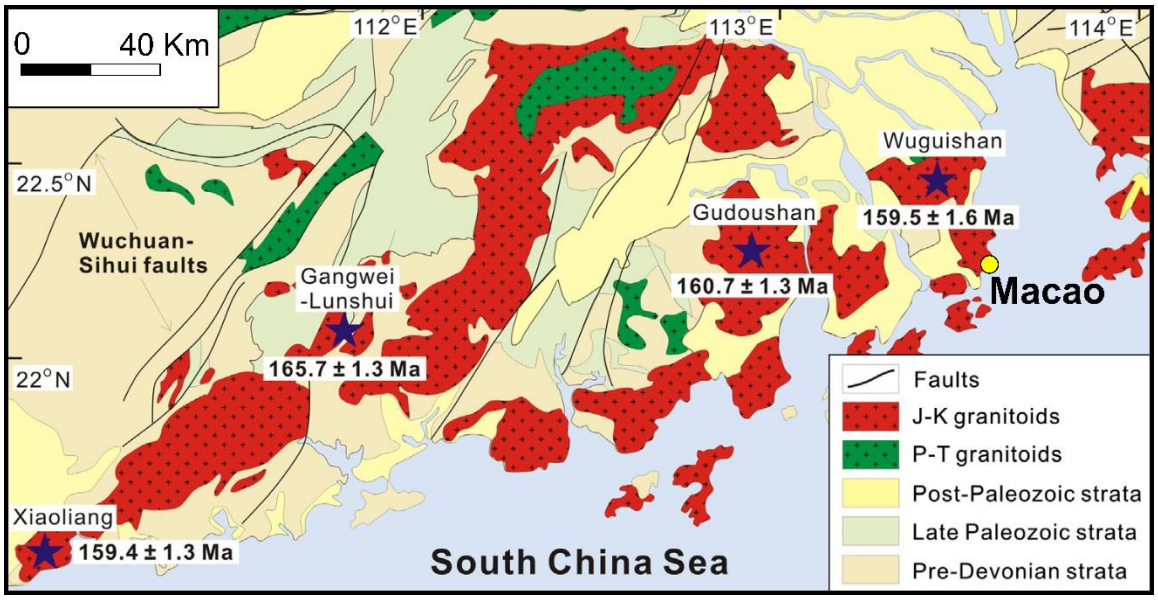

Fig. 2.10. Geological map showing the distribution of Mesozoic granites along the southern coastal region of the Guangdong Province, SE China. Modified after Huang et al. (2012).

The emplacement of granitic rocks in the region was controlled by several large-scale regional NE-trending fault zones (Fig. 2.9; Ribeiro et al., 1992; Xia and Zhao, 2014; Zhou et al., 2006). Some of these regional structures are well documented in Hong Kong (Xia and Zhao, 2014) and are considered to have been major conduits for the magmas involved in the regional plutonism and volcanism. One of the most important tectonic structures in the coastal region of SE China is the NE-trending Lianhuashan Fault Zone (LFZ; also known as Zhenghe-Dapu Fault), which can be traced for over 400 km through the coastal provinces of SE China (Figs. 2.7 and 2.9; Chen, 1987; Ding and Lai, 1997). Near Macao and Hong Kong, the LFZ comprises a 30 km wide zone limited to the North by the Shenzhen Fault and to the south by the Haifeng fault (Fig. 2.7; Chen, 1987; Huang and Zhang, 1990). Several volcanic centres and plutonic assemblages occur associated with

the LFZ, suggesting that it was a major locus of magmatic activity during the Late Mesozoic (Campbell and Sewell, 1997; Davis et al., 1997; Sewell and Campbell, 1997; Xia and Zhao, 2014).

2.2.3. Geology of Macao

The Macao territory (~30 km²) is composed by several granitic intrusions belonging to a batholith extending about 50 km to the north (Ribeiro et al., 1992). The northernmost and most representative intrusion is the Wuguishan pluton (~500 Km^2), dated at 159.5 ± 1.6 Ma (Fig. 2.10; Huang et al., 2012). The geology of Macao is dominated by magmatic rocks, among which biotite granites, with variable textural and mineralogical characteristics, predominate. They commonly contain MME, of variable size and shape, and are intruded by a relatively diversified swarm of granitic, dacite dykes and quartz veins (Fig. 2.11). The granitic dykes gene really have more irregular contours and diffuse contacts with the host granite, while the contacts between dacite dykes are always sharp.

The granitic rocks intrude strongly altered supracrustal Devonic metasediments (Ribeiro et al., 1992; Huang et al., 2012), which outcrop in Coloane as metasedimentary meter-wide enclaves within the granites. These enclaves show slaty cleavage with variable direction and, in some cases, being discordant with the direction of the contacts with the host granite (which are sharp and parallel). Thus, the country rock seems to have been foliated and folded prior to the emplacement of the granites. These rocks consist of metasediments, with textural and mineralogical features indicative of both low-grade regional and contact metamorphism (Ribeiro et al., 1992).

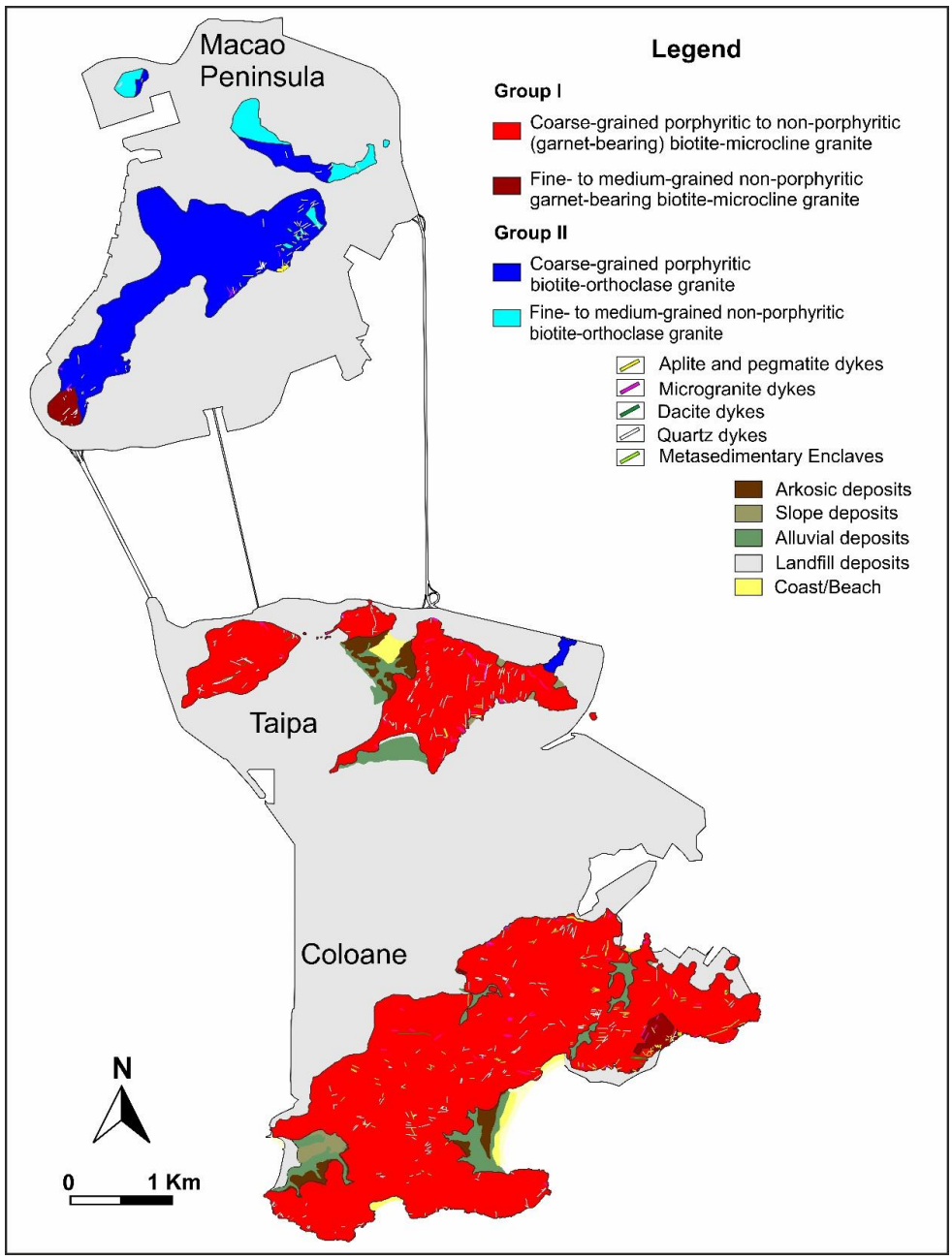

Fig. 2.11. Simplified geological map of Macao showing the distribution of the different facies outcropping in the territory.

Since the emplacement of the granitic plutons, the region underwent tectonic stress fields. Ribeiro et al. (1992) has assigned some of the fracturing and faulting systems affecting the granites to one cycle of deformation related to the Yanshanian Orogeny; however, the authors also emphasize a possible subsequent influence of the still active Shenzhen fault zone (Fig. 2.9), which is concordant with one of the main fracturing systems (ENE-WSW) in Macao. The Shenzhen fault

formed during the late Paleozoic and is thought to have controlled the subsequent regional magmatism (Zhang and Wu, 1994).

The most recent lithologies in Macao are sedimentary deposits of marine, river and continental nature, accumulated in basins created by the fracturing of the granitoids since the late Mesozoic (Fig. 2.11; Ribeiro et al., 1992). Through lithological correlations with surrounding areas, a Holocene-Pleistocene age was proposed for these sediments (Marques, 1988) which comprise sandy and silty fluvial-marine deposits and few arkosic and conglomeratic alluvial formations, found in the lowland areas of Taipa and Coloane and covering the older rocks (So and Ribeiro, 1997).

Chapter 3. Lithofacies of Macao

3.1. Granitic rocks

Granitic rocks outcropping in Macao are mainly biotite granites. In the field, they have massive structure, often occurring as metric-wide rounded boulders, either isolated or in chaotic groups of blocks. Most of the surface area of the granitic intrusions is covered by dense and sub-tropical vegetation, leaving poor and weathered exposures. The freshest samples were thus obtained from outcrops along the coastline, from road cuts and core drillings.

As was mentioned in the previous chapter (section 2.3.3), the granites can be divided into microline-bearing (Group I or MGI) and orthoclase-bearing (Group II or MGII) granites (Fig. 2.11). However, regardless of the structure, the alkali feldspar is perthitic in both groups, suggesting that cooling was slow enough to allow sub-solidus ex-solution, involving splitting of the feldspars into Na-rich lamellae by internal diffusion of ions.

Though most of the mineralogical components are common in both groups, there are significant differences in the occurrence and abundance of specific accessory phases in the two groups. The following sections will describe the main textural and mineralogical features of the granitic rocks from Macao. Additionally, detailed description of other facies such as the clinopyroxene-garnet-bearing tonalite, MME and dacitic dykes will be provided.

3.1.1. MGI granitic rocks

The MGI granites outcrop predominantly in Taipa and Coloane areas, although a small outcrop in the southernmost tip of Macao Peninsula has been also identified (Fig. 2.11). Metasedimentary enclaves are frequently hosted by these granites. This group can be further divided into two sub-groups according to textural and mineralogical features: (1) coarse-grained porphyritic to non-porphyritic (garnet-bearing) biotite-microcline granite (Fig. 3.1) and; (2) fine- to medium-grained non-porphyritic garnet-bearing biotite-microcline granite (Fig. 3.2). Detailed descriptions of each subfacies are given below.

The porphyritic varieties vary from very coarse-grained in Coloane (Fig. 3.1a) to medium- to coarse-grained in Taipa (Fig. 3.1e). In Taipa, the transition from porphyritic to non-porphyritic facies in the field is not clear, but seems to be gradual in many cases. Also, due to the fact that the surface of hills is mostly covered by soil and vegetation, it was not possible to define the limits between those two facies. For this reason, and because an identical age was obtained for these

facies (see chapter 4), they were mapped as a single unit. The distinction is mainly based on textural and mineralogical criteria. Comparing to porphyritic varieties, the non-porphyritic ones are characterized by comparatively smaller grain size, xenomorphic texture and by the occurrence of garnet as accessory phase.

The MGI granites are gray to whitish in colour. Their modal composition consists mainly of quartz (30–35 vol%), alkali feldspar (35–40 vol%) and plagioclase (20–25 vol%), with minor amount of biotite (10–15 vol%). With decreasing abundance of biotite, the granitic rocks change from monzogranite, through syenogranite to alkali feldspar granite, suggesting different degrees of evolution. Both facies are intruded by microgranite, aplite and pegmatite dykes (see descriptions bellow) showing irregular contours and mostly diffuse, more rarely sharp, contacts with the host granite.

Deformation in this group is evidenced by several features such as strong undulatory extinction, subgranulation, sutured crystal boundaries and bands of crushed minerals (e.g. quartz and alkali feldspar).

3.1.1.1. Coarse-grained porphyritic to non-porphyritic (garnet-bearing) biotite-microcline granite

The coarse-grained porphyritic to non-porphyritic (garnet-bearing) biotite-microcline granites are characterized by hypidiomorphic texture. Alkali feldspar occurs as euhedral to subhedral megacrysts or as heterogranular subhedral to anhedral crystals in the groundmass and it can range up to 8 cm long in the more coarse-grained varieties (Fig. 3.1a) and it consists of perthite with poikilitc texture (Fig. 3.1b), hosting small inclusions of plagioclase and quartz and more rarely of alkali feldspar and biotite. In terms of its structure, the alkali feldspar is microcline, evidenced in hand specimen by the grey whitish colour and under microscope by tartan pattern (albite/pericline twins; Fig. 3.1b). The tartan pattern is clearer in Coloane granites and less evident in Taipa granites, suggesting different degrees of symmetry between microclines of these two areas. Plagioclase occurs as subhedral tabular crystals (< 1cm) with polysynthetic albite twinning, showing normal and oscillatory zoning under the microscope. Quartz is anhedral and heterogranular (< 0.7 cm; Fig. 3.1b), in some cases forming graphic and myrmekitic intergrowths with alkali feldspar and plagioclase, respectively. Quartz grains often show evidences for significant deformation such as pervasive strong undulatory extinction, subgranulation and sutured grain boundaries (see Fig. 3.1b

and Fig. 5.3b in chapter 5). Biotite is anhedral to subhedral, occurring as interstitial isolated slab-flake crystals or in mineral clusters (Fig. 3.1c), often hosting a wide variety of accessory minerals. Accessory minerals include ilmenite, magnetite, rutile, titanite, thorite, zircon, allanite (Fig. 3.1d), epidote, apatite, monazite, xenotime, garnet (only in the non-porphyritic varieties; Fig. 3.1e and f), fluorite and sulphides.

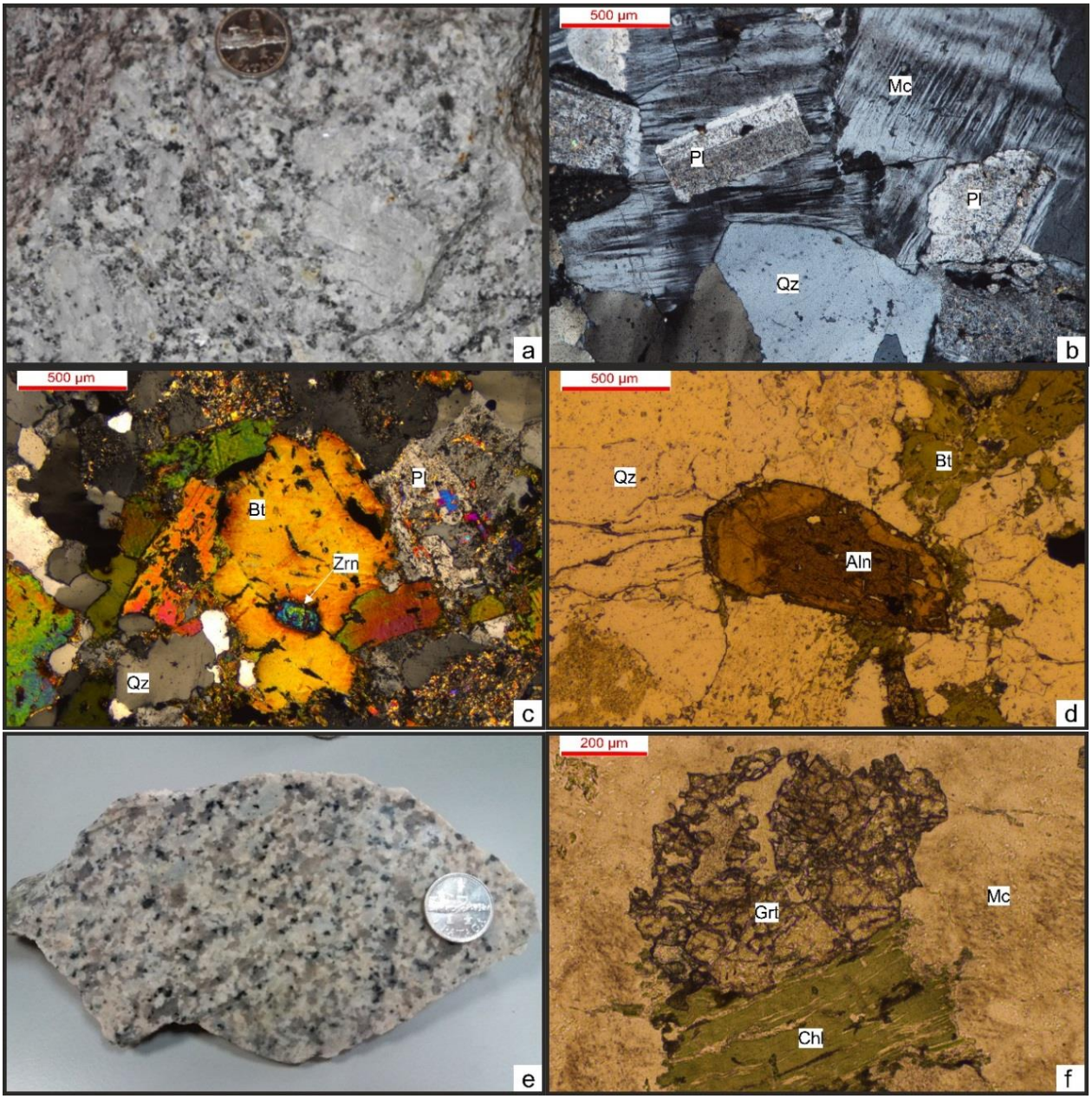

Fig. 3.1. Representative images of the MGI coarse-grained granitic facies: (a) whitish coarse-grained porphyritic biotite-microcline granite with large microcline megacrysts (hand specimen); (b) microcline megacrysts with poikilitic texture, containing tabular plagioclase, and quartz with strong undulatory extinction; (c) biotite aggregate with a zircon inclusion (thin section; crossed nicols); (d) well-developed allanite crystal with compositional zoning (thin section; crossed nicols); (e) coarse-grained non-porphyritic biotite-microcline garnet-bearing granite (hand specimen); (f) desegregated garnet crystal in a non-porphyritic coarse-grained granite (thin section; crossed nicols). Qz—quartz; Mc – microcline; Pl – plagioclase; Aln - allanite; Grt – garnet; Bt – biotite; Zrn – zircon; Chl – chlorite.

3.1.1.2. Fine- to medium-grained non-porphyritic garnet-bearing biotite-microcline granite

The fine- to medium-grained non-porphyritic garnet-bearing biotite-microcline granites (Fig. 3.2a) occur as small intrusions in Macao Peninsula and in Coloane (Fig. 2.11) and it is characterized

by the presence of large crystals of garnet (Fig. 3.2a and b) and blade-shaped biotite (Fig. 3.2c). Under the microscope, the texture is xenomorphic (Fig. 3.2d). Alkali feldspar is present as anhedral perthite grains (<0.5 cm), showing Carlsbad twinning and weak undulatory extinction. Sodic feldspar blebs are usually weakly developed, with irregular contours, rarely showing polysynthetic twins. It is often poikilitic, including fine crystals of anhedral quartz and subhedral tabular zoned plagioclase. Plagioclase is less abundant than alkali feldspar, occurring as anhedral to subhedral tabular weakly sericitized grains (<0.5 mm), with polysynthetic twinning (rarely combined with Carlsbad twins) and occasionally showing continuous normal zoning. Quartz is represented by inequigranular anhedral grains (<0.5 mm; Fig. 3.2d), with irregular to sutured boundaries and strong undulatory extinction. The grains are frequently fractured and sub-granulated. Biotite occurs as fine-grained subhedral needle-shaped crystals (Fig. 3.2c), pleochroic between pale yellow and green and moderately chloritized. Some crystals have abundant pleochroic haloes. Accessory minerals include: garnet, ilmenite, magnetite, fluorite, apatite, allanite, thorite, tantalo-niobate, sulphides.

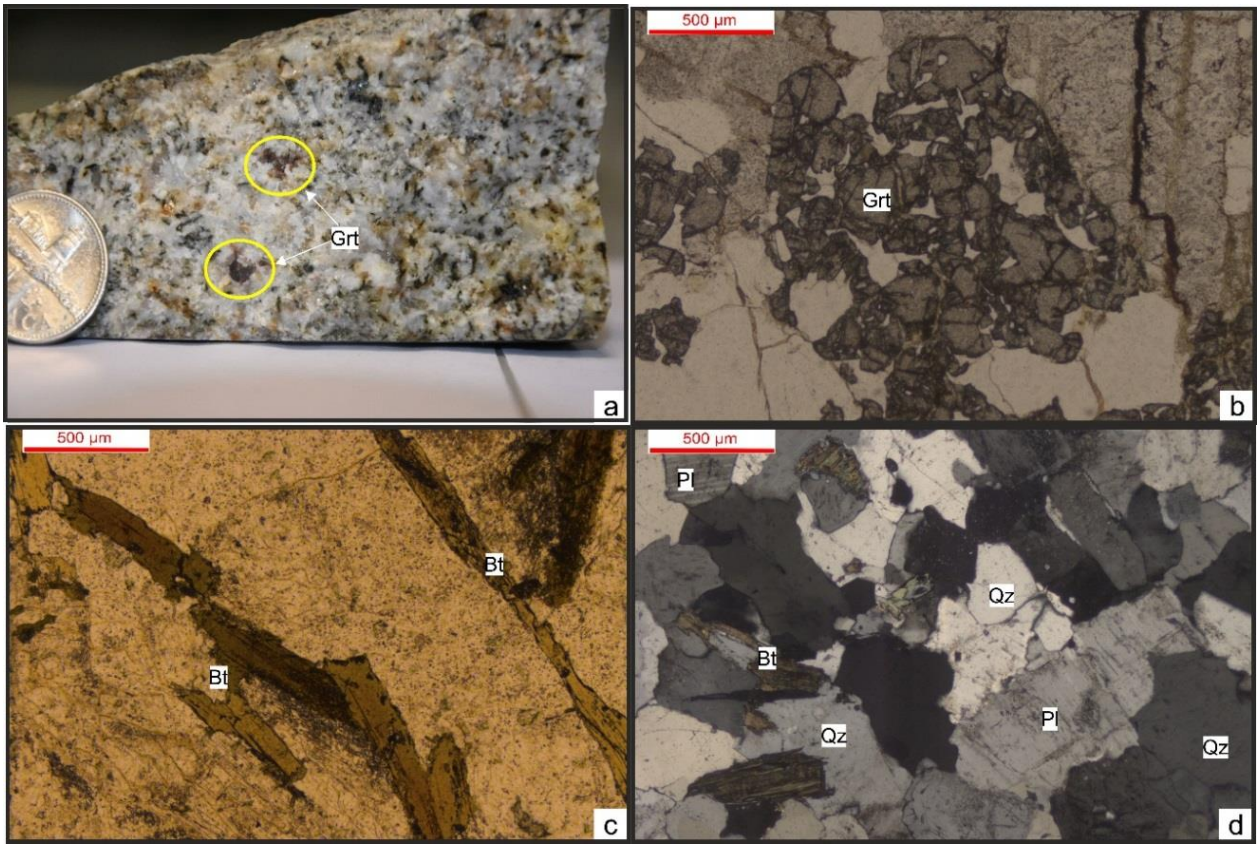

Fig. 3.2. Representative images of the MGI fine-grained granitic facies: (a) whitish fine-grained moderately equigranular biotite-microcline garnet-bearing granite (hand specimen); (b) large garnet crystal disaggregated and corroded, suggesting disequilibrium (thin section; parallel nicols); (c) blade-shaped biotite, common in the fine-grained granitic facies (thin section; parallel nicols); (d) fine-grained anhedral quartz, plagioclase and biotite (thin section; crossed nicols). Grt – garnet; Bt – biotite; Qz – quartz; Pl – plagioclase.

3.1.1.3. Microgranite dykes

Microgranite dykes tend to be more abundant in some specific areas (e.g. northeastern areas of Taipa main intrusions; Fig. 2.11) and display a wide range of diameters (from centimetre to meter-wide; Fig. 3.3a). They are leucocratic (in some cases slightly pinkish due to K-feldpsar alteration; Fig. 3.3b) and have a fine-grained (<0.1 cm), moderately equigranular xenomorphic texture (Fig. 3.3c and d). Alkali feldspar is represented by fine-grained anhedral microperthite with weak undulatory extinction (Fig. 3.3d) and, in some cases, with poikilitic texture, hosting inclusions of quartz and plagioclase. Sodic blebs are rarely well-developed to the point of showing polysynthetic twinning. Plagioclase is less abundant than alkali feldspar, occurring as fine-grained subhedral tabular crystals with polysynthetic twinning. Quartz is present as fine-grained

intergranular anhedral grains with undulatory extinction and as worm-like intergrowths with alkali feldspar, producing abundant graphic textures (Fig. 3.3d). Biotite is present as rare green to light yellow pleochroic fine-grained anhedral to subhedral blade-shaped flakes. The plates are weakly to strongly chloritized and often show deformation features such as broken crystals and bent cleavages. Accessory minerals include: Fe-Ti oxides, sulphides, garnet and fluorite.

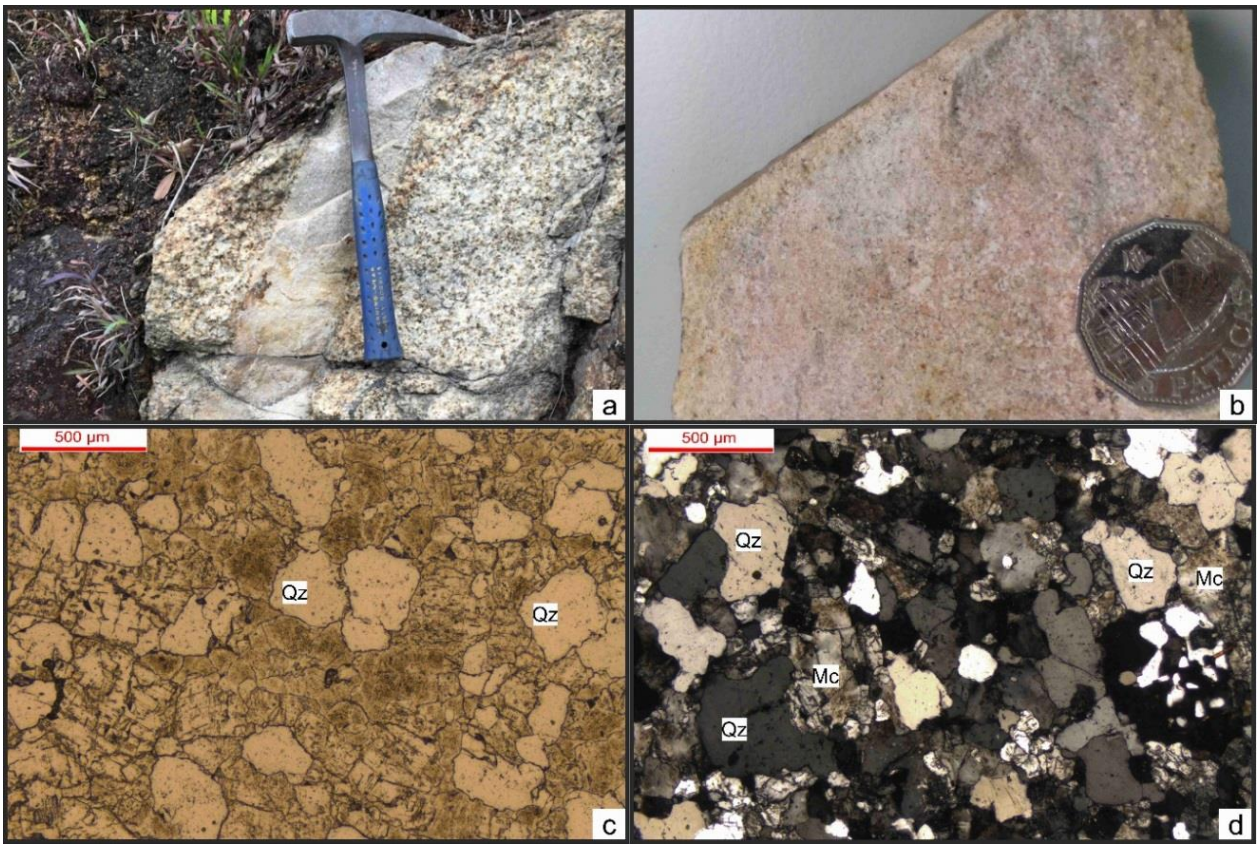

Fig. 3.3. Representative images of the MGI microgranite dykes: (a) mcirogranite dyke cutting the coarse-grained porphyritic biotite-microcline granite (hand specimen); (b) fine-grained equigranular texture of the microgranite dyke (hand specimens); (c) fine-grained anhedral quartz and feldspar grains (thin section; parallel nicols); (d) xenomorphic texture formed by anhedral quartz and microcline, in some cases with incipient development of graphic texture (thin section; crossed nicols). Qz – quartz; Mc – microcline.

3.1.1.4. Aplite-pegmatite dykes

Pegmatites occur essentially as dykes cutting fine-grained granitic facies forming, in some cases, pod-shaped bodies (up to 1 meter in diameter; see Fig. 5.3f in chapter 5). Alternation between aplite and pegmatite textures is common in these dykes (Fig. 3.4a).

Aplites dykes have centimetre- to decimetre-wide dimensions (Fig. 3.4a and b) and are characterized by a very fine-grained (<0.1 cm) moderately equigranular xenomorphic texture with of abundant garnet crystals as accessory mineral (Fig. 3.4c). The major mineral components in the mineralogy of aplites are: alkali feldspar, represented by anhedral microperthitic microcline crystals, rarely poikilitic (hosting smaller plagioclase and quartz grains), with weak undulatory extinction and weakly to well-developed sodic blebs; subhedral tabular plagioclase crystals with frequent polysynthetic twinning (Fig. 3.4d), and; (3) anhedral crystals of quartz (Fig. 3.4d) with moderate to strong undulatory extinction and irregular to slightly sutured boundaries. Biotite is also present as a minor component. It has weakly to strongly chloritized anhedral to subhedral flakes (Fig. 3.4d) showing strong pleochroism between pale yellow and brownish green, with a few pleochroic haloes. Garnet (light brown anhedral to subhedral octogonal-shaped crystals; Fig. 3.4c) often occur associated with biotite. Other accessory minerals include Fe-Ti oxides, sulphides, fluorite and sulphides.

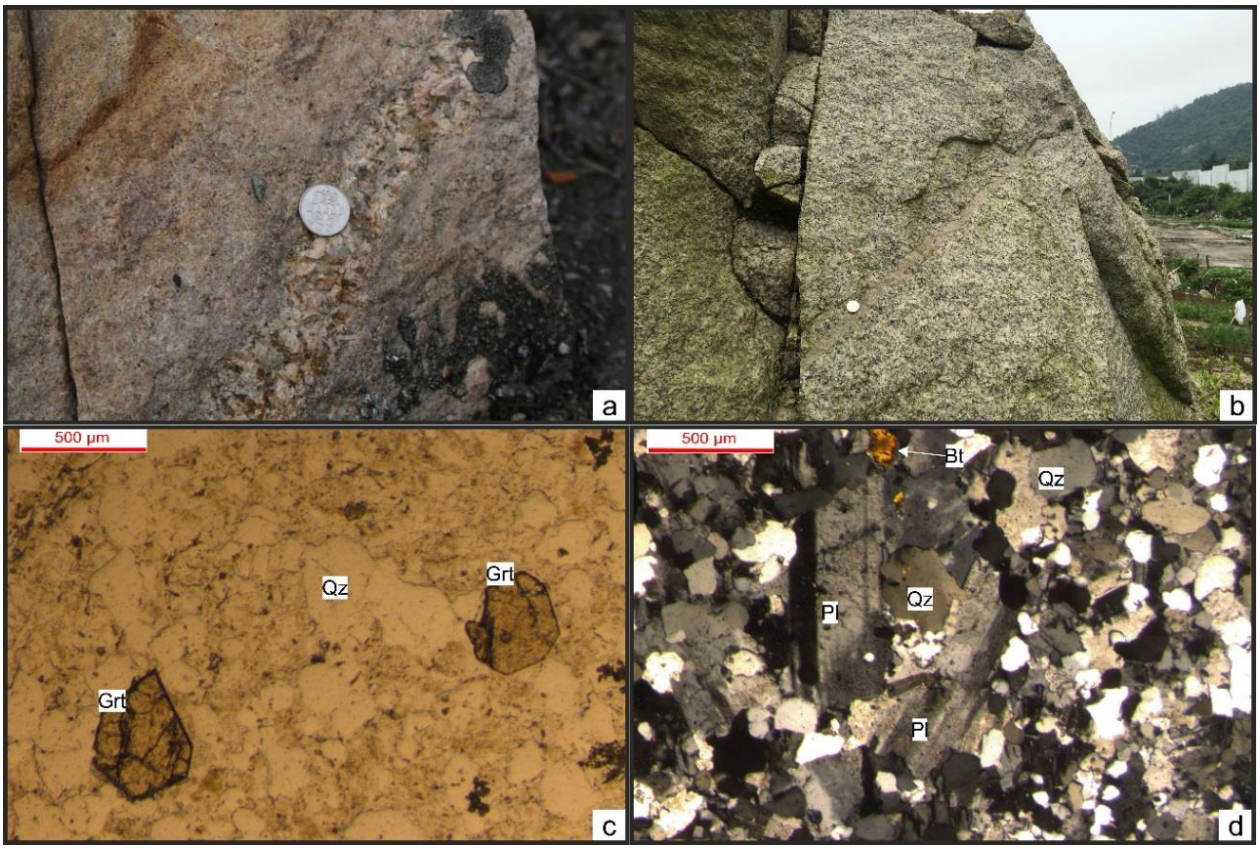

Fig. 3.4. Representative images of the MGI aplite and pegmatite dykes: (a) pegmatite vein within an aplite dyke (hand specimen); (b) aplite dyke cutting a coarse-grained porphyritic biotite-microcline granite (hand specimen); (c) euhedral to subhedral garnet grains (thin section; parallel nicols); (d) fine-grained texture with sub-equal amounts of feldspar and quartz, with rare and poorly developed biotite flakes (thin sections; crossed nicols). Qz – quartz; Grt – garnet; Bt – biotite; Pl – plagioclase.

3.1.2. MGII granitic rocks

The MGII granites mainly outcrop in Macao Peninsula area, with a small outcrop in the easternmost tip of Taipa (Fig. 2.11). They occupy a much smaller outcrop area than MGI granites, being mostly restricted to the northern part of the Macao territory. No metasedimentary enclaves were found in this group. According to textural and mineralogical features, this group can be further divided into two sub-groups: (1) coarse-grained porphyritic biotite-orthoclase granite and; (2) fine- to medium-grained non-porphyritic biotite-orthoclase granite. With decreasing amount of biotite, the granitic rocks change from monzogranite to syenogranite, suggesting different degrees of evolution. Detailed descriptions of each subfacies can be found below.

This group of granites is usually pinkish in colour (Fig. 3.5a) and is mainly composed of quartz (30–35 vol%), alkali feldspar (35–40 vol%), plagioclase (20–25 vol%) and biotite (10–15 vol%). No garnet has been identified in this group and, contrasting with MGI granites, euhedral titanite is particularly abundant and well-developed.

3.1.2.1. Coarse-grained porphyritic biotite-orthoclase granite

Coarse-grained porphyritic biotite-orthoclase granites are characterized by hypidiomorphic texture. Alkali feldspar consists of subhedral to euhedral tabular perthitic orthoclase megacrysts (up to 5 cm long; Fig. 3.5a and b) and microperthite subhedral to anhedral crystals in the groundmass, often showing Carlsbad twinning. Sodic feldspar blebs are usually weakly developed; however, well-developed megacrysts with irregular contours and showing polysynthetic twins are also present. The alkali feldspar megacrysts are poikilitic, containing small inclusions of plagioclase and quartz and more rarely of alkali feldspar and biotite (Fig. 3.5b). Frequently, it has reaction rims (locally embayed rims) against plagioclase producing myrmekitic textures. Plagioclase occurs as tabular subhedral crystals (~0.5 cm, ranging from 0.1 to 1 cm) and generally has compositional zoning and polysynthetic twinning (Fig. 3.5c). The cores are moderately to strongly sericitized, in some cases almost covering the whole crystal. Quartz occurs as heterogranular (coarse- to fine-grained) anhedral grains with sharp to irregular boundaries and showing weak to moderate undulatory extinction. Biotite is euhedral to subhedral occurring either as isolated slab-flake crystals or as mafic clots including and/or associated with a wide variety of accessory minerals Fig. 3.5b and c). Titanite is an abundant accessory mineral, occurring as well-

developed fine-grained euhedral rhomb-shape crystals (Fig. 3.5d). Other accessory minerals include: zircon, apatite, fluorite, allanite, monazite, xenotime, Fe-Ti oxides and sulphides.

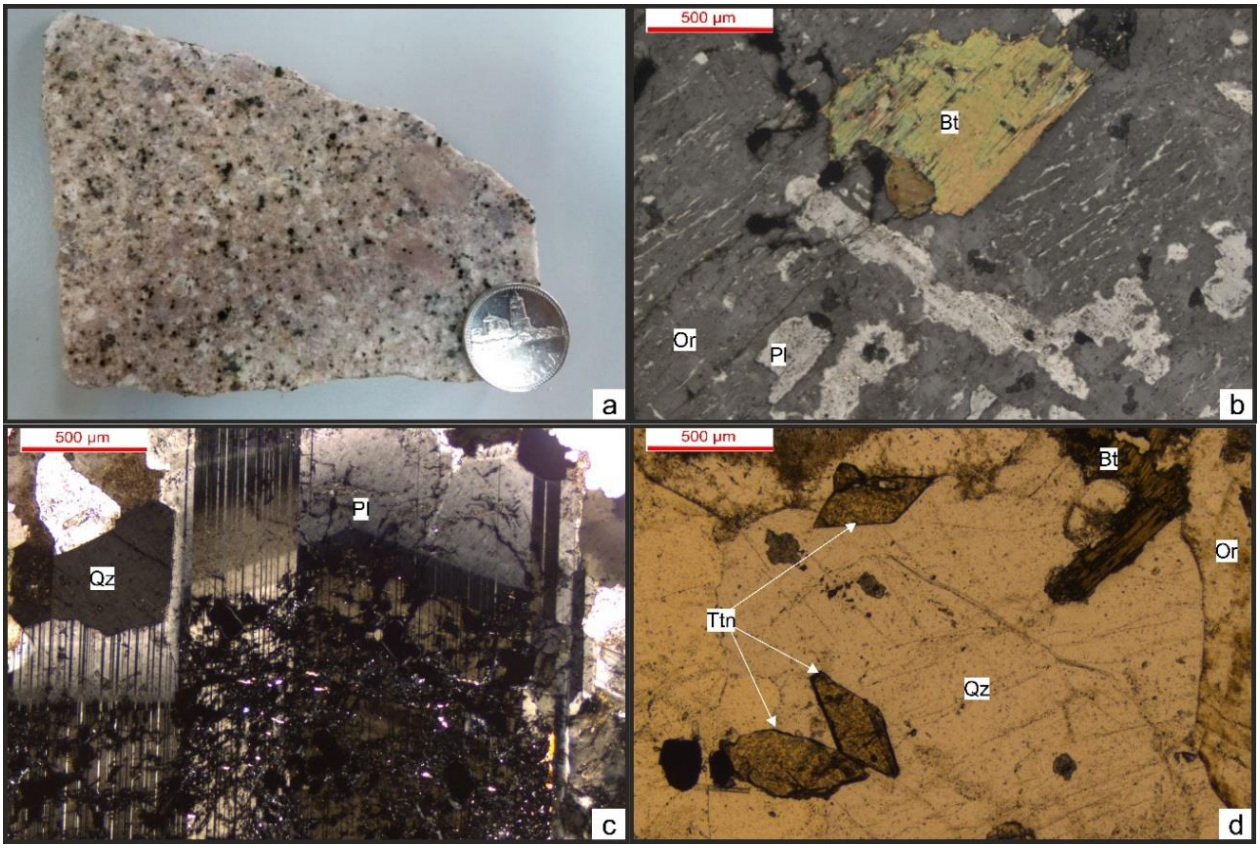

Fig. 3.5. Representative images of the MGII coarse-grained granitic facies: (a) pinkish coarse-grained porphyritic biotite-orthoclase granite with large orthoclase megacrysts (hand specimen); (b) orthoclase megacrysts with poikilitic texture, hosting smaller subhedral plagioclase and biotite flakes (thin section; crossed nicols); (c) large tabular plagioclase crystal showing optical zoning (thin section; crossed nicols); (d) euhedral elongated rhomb-shaped titanite crystals (thin section; parallel nicols). Qz – quartz; Pl – plagioclase; Or – orthoclase; Bt – biotite; Ttn - titanite.

3.1.2.2. Fine- to medium-grained non-porphyritic biotite-orthoclase granite

Fine-grained non-porphyritic varieties (Fig. 3.6a) have a similar mineralogy as the porphyritic facies but with different modal proportions. Feldspar and quartz tend to occur in sub-equal amounts while the amount of biotite and accessory minerals is comparatively lower. In some of these samples no biotite has been found.

Alkali feldspars occurs as anhedral to subhedral tabular microperthite crystals (Fig. 3.6b). Plagioclase is present as anhedral to subhedral tabular crystals with polysynthetic twinning and compositional zoning (Fig. 3.6b). Quartz occurs as heterogranular (<0.5 cm) anhedral crystals with

irregular borders and weak undulatory extinction; graphic textures are abundant (Fig. 3.6d). Biotite occurs as sparse highly chloritized anhedral flakes often contained other accessory minerals and in some cases altering to epidote. Accessory minerals include: apatite, zircon, allanite (Fig. 3.6d), epidote, ilmenite, magnetite, sulphides.

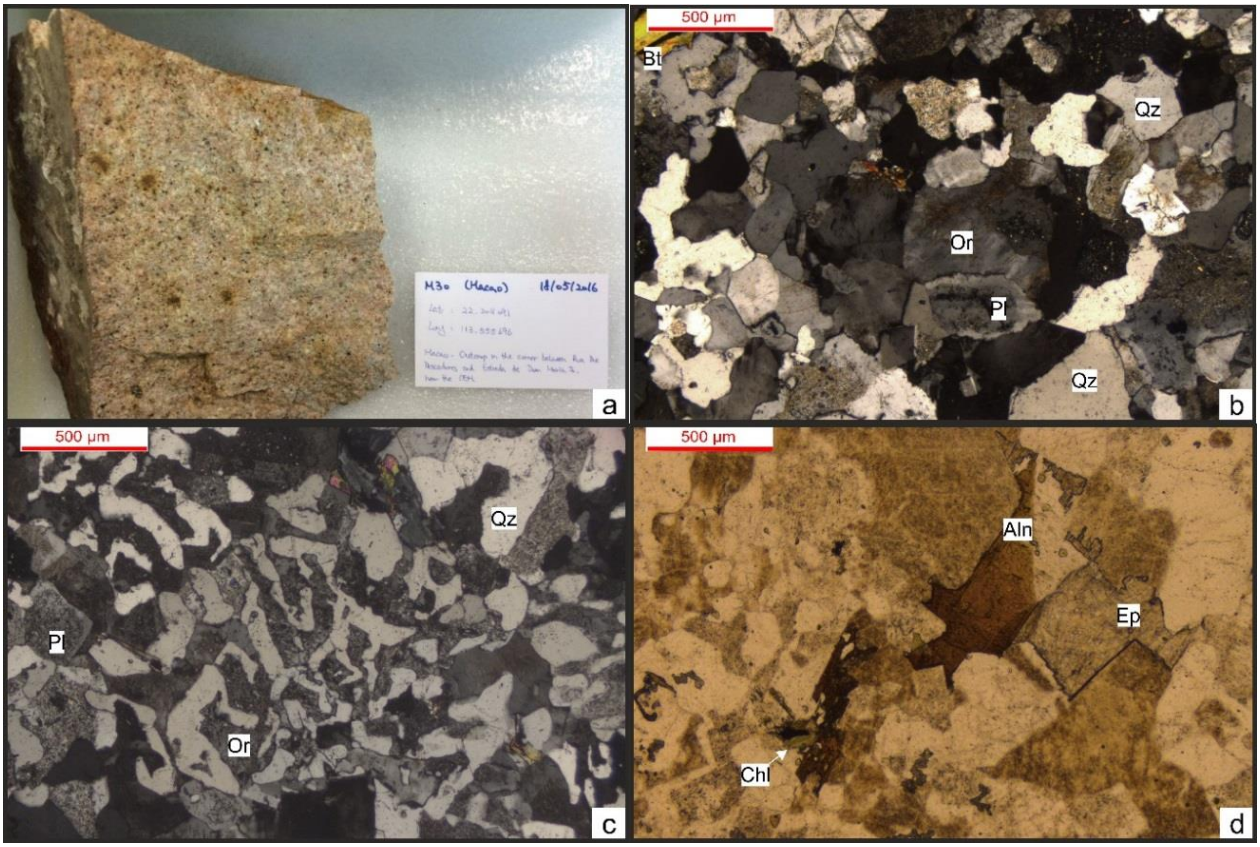

Fig. 3.6. Representative images of the MGII fine-grained granitic facies: (a) slightly pinkish fine-grained moderately equigranular biotite-orthoclase granite (hand specimen); (b) fine-grained equigranular texture with anhedral quartz, alkali feldspar and subhedral tabular plagioclase crystals (thin-section; crosses nicols); (c) intergrowth between quartz and alkali feldspar (orthoclase) producing graphic textures (thin-section; crosses nicols); (d) epidote showing a change in composition from allanite (brown) to another epidote variety (pale yellow; thin-section; parallel nicols). Qz – quartz; Pl – plagioclase; Or – orthoclase; Bt – biotite; Ttn - titanite.

3.1.2.3. Aplite-pegmatite dykes

Aplites and pegmatites (Fig. 3.7a) intrude all granitic facies in Macao Peninsula, showing diffuse irregular contacts with the host granite. The aplitic facies have a fine- to medium-grained inequigranular xenomorphic texture (Fig. 3.7b–d). Alkali feldspar is present as anhedral to subhedral tabular perthite (<1 cm; Fig. 3.7c), often poikilitc, hosting a few inclusions of anhedral quartz and subhedral tabular plagioclase. Sodic blebs are weakly developed, rarely showing

polysynthetic twinning (Fig. 3.7c). Plagioclase is represented by anhedral to subhedral tabular weakly to strongly sericitized crystals (<0.5 cm; Fig. 3.7d), in some cases normally zoned. Quartz occurs as anhedral grains (<0.5 cm; Fig. 3.7b–d) with irregular to sutured boundaries, often subgranulated and showing weak undulatory extinction. It also occurs as wormy and skeletal crystals producing granophyric texture (Fig. 3.7d). Biotite is rare, weakly developed and chloritized (Fig. 3.7b). Accessory phases include: zircon, Ti-Fe oxides, sulphides and thorite.

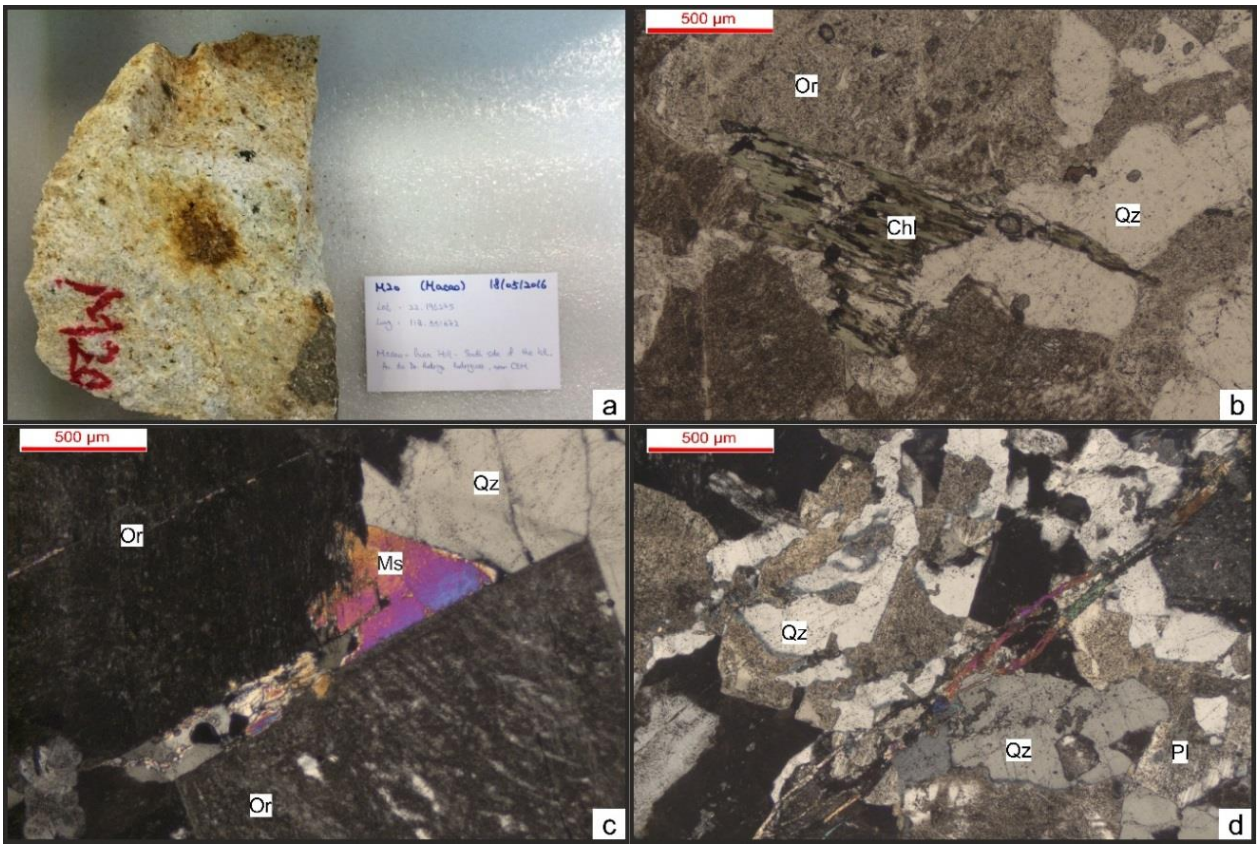

Fig. 3.7. Representative images of the MGII aplite-pegmatite dykes: (a) fine- to coarse-grained biotite-orthoclase aplite-pegmatite dyke (hand specimen); (b) alteration of primary biotite formed chlorite (thin-section; parallel nicols); (c) secondary muscovite formed in the intergranular space between orthoclase and quartz (thin section; crossed nicols); (d) intergrowth between quartz and alkali feldspar (orthoclase) producing graphic textures (thin section; crossed nicols). Qz – quartz; Or – orthoclase; Chl – chlorite; Ms – muscovite; Pl – plagioclase.

3.1.3. Clinopyroxene-garnet-bearing tonalite

The clinopyroxene-garnet-bearing tonalite was obtained by core drilling in the Coloane area and does not outcrop in Macao. This granitoid is a leucocratic (whitish) medium- to coarse-grained porphyritic clinopyroxene-andradite-bearing tonalite (Fig. 3.8a and b), with plagioclase megacrysts

(<3 cm) in a medium-grained (0.1–0.5 cm) moderately equigranular hypidiomorphic groundmass. Alkali feldspar is rare, occurring as coarse-grained anhedral to subhedral tabular poikilitic perthite crystals, hosting fine-grained anhedral quartz and subhedral tabular plagioclase. Plagioclase is abundant, occurring as medium to coarse-grained subhedral tabular megacrysts and smaller tabular crystals, showing polysynthetic twinning (Fig. 3.8b). Some crystals are normally zoned and the majority is weakly sericitized. Quartz occurs as fine to medium-grained aggregates of subhedral crystals (~0.5–1 cm; Fig. 3.8b) with sharp to slightly sutured boundaries. Clinopyroxene appears as green pleochroic fine to medium-grained anhedral to subhedral prismatic crystals (Fig. 3.8a and b), often associated with garnet and titanite. Fibrous aggregates of amphibole, with strong pleochroism and low relief, occur as a replacement product in the borders of clinopyroxene crystals (Fig. 3.8a). Garnet exists as brown fine-grained anhedral to subhedral grains (Fig. 3.8a), often zoned and usually associated with titanite and clinopyroxene. Titanite occurs as brown fine-grained anhedral to subhedral rhomb-shaped crystals. In this facies, biotite is absent and the accessory minerals include: sulphides, Fe-Ti oxides, apatite, allanite, monazite and zircon.

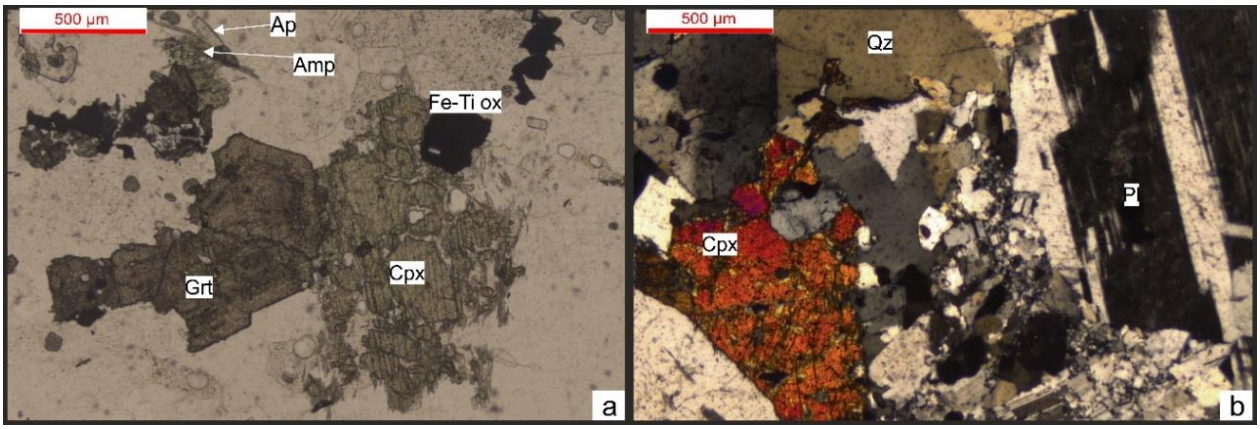

Fig. 3.8. Representative images of the clinopyroxene-garnet-bearing tonalite: (a) subhedral zoned garnet crystal in contact with anhedral clinopyroxene (parallel nicols); (b) anhedral clinopyroxene, quartz and subhedral tabular plagioclase crystals separated by a band of crushed minerals due to deformation (crossed nicols). Ap – apatite; Anf – amphibole; Fe-Ti Ox – Fe-Ti oxides; Grn – garnet; Cpx – clinopyroxene; Qz – quartz; Pl – plagioclase.

This facies was dated and its age is addressed in chapter 4. However, the mineral assemblage of this granitoid is enigmatic, as it has not been found in the literature. In addition, only one sample is available, making it difficult to make an accurate petrogenetic interpretation. For this reason and because this sample was obtained by core drilling and does not outcrop in Macao, its petrogenesis is not addressed in this thesis.

3.2. Microgranular mafic enclaves

MME are mainly hosted by the porphyritic coarse-grained granitic facies in both groups. They are easily recognized in the field by their dark colour contrasting with the lighter tone of the host granites. Compared with the host granite, MME generally contain a similar mineral assemblage, but with higher contents of biotite and plagioclase, and lower contents of quartz and alkali feldspar.

In MGI granites, MME have varied dimensions (centimetre to decimetre-wide, in some cases reaching up to 1 meter in diameter; Fig. 3.9a and b). Their compositions vary from monzogranite to granodiorite containing acicular biotite and no accessory titanite. In the field, they commonly occur as irregular blobs, oval and elongated in shape, with sharp contacts with the host granite (Fig. 3.9a). Textures vary from slightly porphyritic with alkali feldspar megacrysts to fine-grained equigranular hypidiomorphic. Alkali feldspar occurs as sparse perthitic microcline megacrysts that probably crystallized from the granitic magma and were later incorporated into the MME. Plagioclase occurs as subhedral tabular crystals with polysynthetic twinning, occasionally combined with Carlsbad twinning; the crystals show clear compositional zoning (normal and oscillatory; Fig. 3.9b) and are moderately sericitized, especially in the core area. Quartz is present as anhedral to subhedral subgranulated crystals with sharp to irregular boundaries and strong undulatory extinction (Fig. 3.9b). Biotite exists as a mesh of abundant (50%) green to light yellow pleochroic acicular to lamellar flakes without pleochroic haloes (Fig. 3.9b). The most common accessory minerals include allanite, zircon and apatite.

In MGII granites, MME are distinguished from MGI MME for their comparatively smaller size. They are mostly quartz monzodioritic in composition and have abundant titanite and in some cases hornblende (Fig. 3.9c–d; see also Fig. 5.3i in chapter 5). In the field, they commonly have sharp to diffusive contacts with their host and occur as centimetre to decimetre-wide round-shaped blobs and more rarely as dike-like trails. The texture is fine- to medium-grained slightly porphyritic to fine-grained moderately equigranular hypidiomorphic (Fig. 3.9d). Alkali feldspar occurs as pertithic orthoclase megacrysts with reaction borders, suggesting that it may be a foreign crystal from the granitic magma that reacted with a more mafic liquid. It is absent in the groundmass. Those K-feldpsar megacrysts are poikilitic, hosting a wide variety of minerals such as quartz, plagioclase and biotite. Plagioclase is present as subhedral to euhedral tabular crystals with polysynthetic twinning and compositional zoning in the groundmass (Fig. 3.9d) and also as larger

subhedral megacrysts strongly sericitized and with reaction borders, suggesting that they crystallized from the granitic liquid and interacted with the more mafic liquid. Quartz is abundant occurring as anhedral grains with sharp to irregular boundaries showing weak undulatory extinction (Fig. 3.9d). Biotite occurs as abundant highly chloritized flakes (Fig. 3.9d). In some MME, hornblende occurs as green prismatic crystals more or less preserved (see Fig. 5.3i in chapter 5). Titanite is common, occurring as isolated or in mineral aggregations of lozenge-shaped crystals often associated with biotite (see Fig. 4.3k in chapter 4). Accessory minerals include: Ti-Fe oxides, allanite, zircon and fluorite.

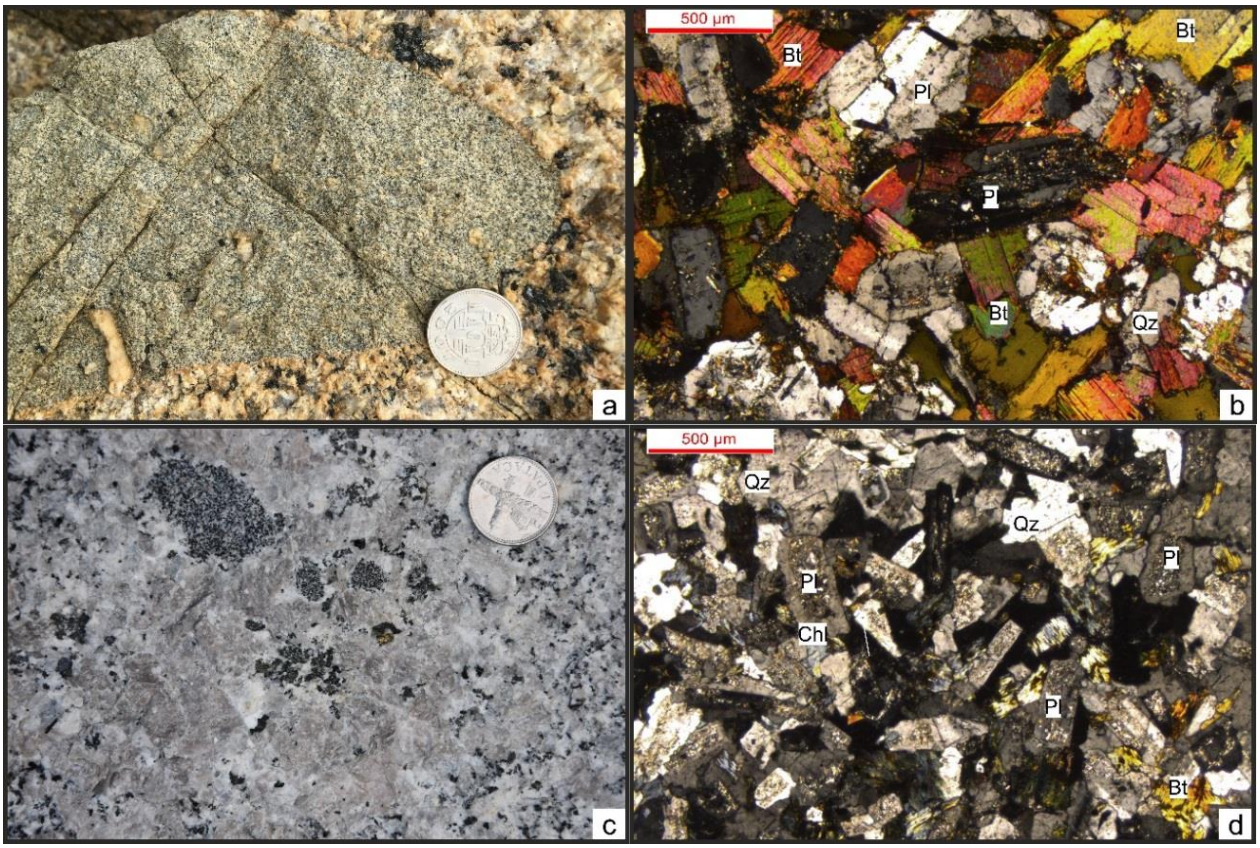

Fig. 3.9. Representative images of the microgranular mafic enclaves (MME) from Macao: (a) MME from MGI, with an alkali feldspar megacryst straddling the boundary between MME and host granite (hand specimen); (b) fine-grained moderately equigranular texture of the MGI MME, with high concentrations of biotite (thin sections; crossed nicols); (c) MME from MGII associated with a concentration of pinkish orthoclase megacrysts(hand specimen); (d) fine-grained moderately equigranular texture of the MGII MME, showing a mesh of tabular plagioclase, anhedral quartz and highly chloritized biotite (thin sections; crossed nicols). Bt – biotite; Qz – quartz; Pl – plagioclase; Chl – chlorite.

3.3. Dacite dykes

Dacite dykes are a minor lithology in Macao, outcropping in Coloane and Taipa (Fig. 2.11), which cross-cut all the granitic facies.

In Coloane, dacite dykes usually occur with lenticular shape and relatively well-defined regular contours. Their texture is slightly porphyritic. Plagioclase occurs as fine-grained anhedral to subhedral tabular phenocrysts (<0.5 cm) with polysynthetic twinning and compositional zoning (Fig. 3.10b). Hornblende occurs as brown fine-grained heterogranular prismatic crystals (<0.1 cm; Fig. 3.10b and c). Biotite is a minor component present as totally chloritized anhedral flakes. Alteration of feldspars produces pervasive sericite (Fig. 3.10c). The aphanitic groundmass is mainly composed of alkali feldspar and microcrystalline quartz with minor Fe-Ti oxides and sulphides (abundant dispersed anhedral to subhedral square crystals in the groundmass), allanite (brown very fine-grained anhedral zoned fragments), zircon and apatite (present as abundant fine-grained prismatic crystals in the groundmass).

In Taipa, dacite dykes occur with variable dimensions (decimetric to metric), with sharp contacts with the host granite. They have an aphanitic texture. Quartz is rare, occurring as anhedral grains or small amygdule-shaped crystals, showing strong undulatory extinction and subgranulation. (Fig. 3.10d). Feldspar is strongly altered to sericite, showing anhedral grains (Fig. 3.10d). They also contain accessory amounts of Fe-Ti oxides.

Fig. 3.10. Representative images of the Macao dacite dykes: (a) Coloane dacite dyke, with a greenish colour due to chloritization (hand specimen); (b) Coloane dacite sample – euhedral amphibole and zoned plagioclase phenocrysts within a feldspatic groundmass (crossed nicols); (c) Coloane dacite samples – highly altered subhedral amphibole within a feldspatic groundmass (crossed nicols); (d) Taipa dacite – aphanitic, mainly composed by quartz and feldspar with no amphibole (crossed nicols). Qz – quartz; Or – orthoclase; Chl – chlorite; Ms – muscovite; Pl – plagioclase.

Chapter 4. High-precision geochronology of Mesozoic magmatism in Macao, Southeast China: evidence for multistage granite emplacement

---

Published as:

Quelhas, P., Dias, Á A., Mata, J., Don, D., Ribeiro, L. (2019) High-precision geochronology of Mesozoic magmatism in Macao, Southeast China: evidence for multistage granite emplacement. Geoscience Frontiers. *In press*. https://doi.org/10.1016/j.gsf.2019.04.011

Abstract

Six new high precision U–Pb zircon ID-TIMS ages plus thirteen in situ high spatial resolution U–Pb zircon LA-MC-ICPMS ages are reported from Jurassic plutonic (metaluminous to weakly peraluminous biotite granites) and Jurassic to Cretaceous hypabyssal (dacites) rocks from Macao. Despite its relatively small area (~30 km^2), the new ages tightly constrain the Macao granitic magmatism to two periods ranging from 164.5 ± 0.6 Ma to 162.9 ± 0.7 Ma and 156.6 ± 0.2 Ma to 155.5 ± 0.8 Ma, separated by ca. 6 Ma. Inherited zircons point to the existence of a basement with ages up to Paleo-Proterozoic and late Archean in the region. In addition, younger dacitic rocks were dated at 150.6 ± 0.6 Ma and <120 Ma. U–Pb zircon ages and whole-rock REE data of Macao granites indicate that the first pulse is also represented in Hong Kong and Southeast (SE) China, while magmatism with the chemical characteristics of the second pulse seems to not be represented outside Macao. The two granitic magmatic pulses have distinct mineralogical and geochemical features that support their discrete nature rather than a continuum of comagmatic activity and suggest that the Macao granitic suite was incrementally assembled during a period of ca. 9 Ma, a hypothesis also extendable to the neighbouring Hong Kong region for a time lapse of ca. 24 Ma. In Macao, the transition from granitic magmatism (Middle to Upper Jurassic) to the younger dacite dykes (Upper Jurassic to Lower Cretaceous) most likely corresponds to a change in the regional tectonic setting, from an extensional regime related with foundering of the subducting Paleo-Pacific plate during the Early Yanshanian period to the reestablishment of a normal subduction system in SE China during the Late Yanshanian period.

Keywords: Granites; U–Pb Geochronology; Zircon; Jurassic; Yanshanian Orogeny; Macao.

4.1. Introduction

Granitic rocks are a major component of the upper continental crust, which has an estimated "granitic" average composition (e.g. Rudnick and Gao, 2003). Slight distinctive differences in their mineralogy and chemical composition have potential implications for their origin, which is crucial to understand the tectono-thermal evolution of continents (Kemp and Hawkesworth, 2003; Arndt, 2013).

Mesozoic granitic rocks are widely distributed in the Cathaysia Block, Southeast (SE) China. Along the coast of SE China, where Macao and Hong Kong are located, magmatism associated with the Yanshanian Orogeny occurred in two main stages: Early Yanshanian (180–142 Ma) and Late Yanshanian (142–67 Ma; Zhou et al., 2006). In adjacent areas of Macao, different types of granites (I, S and A) occur with dominant Jurassic to Cretaceous ages (Li et al., 2007; Y. W. Chen et al., 2012; Huang et al., 2012; Huang et al., 2015; Li et al., 2015; Y. Zhang et al., 2015; Qiu et al., 2016; Zheng et al., 2016; Zhou et al., 2016; Zhang et al., 2017; Zheng et al., 2017). However, many of these studies dealt with large batholith areas where sampling cannot adequately represent the small-scale compositional variation of plutonic bodies. Thus, detailed geochemical and age variation information can have been missed, which may have potentially important implications for the magmatic evolution during the Yanshanian Orogeny. In contrast, more detailed work was done in the neighbouring region of Hong Kong, where high-precision U–Pb zircon geochronology constrained the Jurassic–Early Cretaceous magmatism (165–141 Ma) to four main pulses correlated with important tectonic events within the Yanshanian Orogeny (Sewell et al., 1992; Sewell et al., 2012a). Despite its relatively small area (~30 km^2), the Macao territory includes a wide range of granitic facies with different textures, mineralogy and compositions. The first dating of Macao granitic rocks was obtained on biotite using the Potassium (K)–Argon (Ar) method, with most samples dated between 154 ± 5 Ma and 168 ± 4 Ma. A significantly younger date of 94 ± 2 Ma was also reported (Ribeiro et al., 1992; Ribeiro et al., 2010). However, the number of samples analysed was not enough to encompass the variety of granitic facies outcropping in the territory and did not include the hypabyssal dykes intruding the granites. Besides, the K–Ar method has some inherent limitations resulting from post-magmatic Ar loss or gain, which may lead to erroneous ages (e.g. Cobbing, 2000; Gillot et al., 2006; Lee, 2014). U–Pb zircon dating is now the first choice for dating granites, providing the basis for accurate and precise age determination

given: (1) the lack of significant Pb incorporation during crystallization (Harley and Kelly, 2007; Scherer et al., 2007); (2) its high blocking temperature (>900 ºC; e.g. Scherer et al., 2007); and (3) extremely low Th, U and Pb diffusion rates (e.g. Cherniak et al., 1997b; Lee et al., 1997). For these reasons, zircon has been considered the best deep-time archive of Earth's continental crust (Davis et al., 2003; Roberts and Spencer, 2015).

In this study, a large number of zircon grains from the Macao granites were dated. Two methods were employed: isotope dilution thermal ionization mass spectrometry (ID-TIMS) and laser ablation multi-collector inductively coupled plasma mass spectrometry (LA-MC-ICPMS). While ID-TIMS is the most precise and most accurately calibrated method for the determination of crystallization ages of zircon, LA-MC-ICPMS is a fast, yet reasonably accurate and precise, technique, making it easy to obtain large numbers of analyses with a good spatial resolution (10–60 mm spot size, 5–20 mm depth) that allows better assessment of inheritance. Both methods combined provided a robust age data set for the Macao magmatic rocks. The new data set includes not only different granitic facies from each of the three main outcropping areas in Macao (Macao Peninsula, Taipa and Coloane), but also the post-granite dacite dykes. We use these data to verify the validity of the previous ages attributed to Macao granitic rocks, to know the age of a larger number of granitic facies and other magmatic rocks, to investigate the periodicity of magmatism in the territory and to contribute to a better knowledge of the tectono-thermal evolution of the Yanshanian Orogeny.

4.2. Geological background

The South China Block (SCB) was formed during the Early Neoproterozoic, by amalgamation of the Cathaysia Block in the southeast and the Yangtze Block in the northwest along the Jiangshan-Shaoxing suture zone (Fig. 4.1; e.g. Li et al., 2002; Ye et al., 2007; Charvet, 2013; Y. Wang et al., 2013). While the Yangtze Block has an Archean to Paleoproterozoic basement (Qiu et al., 2000; Zheng et al., 2006), the oldest basement of Cathaysia Block is represented by sporadic Paleoproterozoic rocks outcropping in the eastern part (e.g. Li, 1997; X.-H. Li et al., 2000a; Yu et al., 2012; Liu et al., 2014). In the western part, the outcropping Precambrian basement consists of Neoproterozoic igneous rocks and sedimentary strata (e.g. Zhang and Zheng, 2013; Li et al., 2014). The Cathaysia Block has been episodically reworked by the Jiangnan (Neoproterozoic), Wuyi–

Yunkai (Early Paleozoic), Indosinian (Triassic) and Yanshanian (Late Mesozoic) tectono-thermal events (e.g. Li, 1998; Y. Wang et al., 2013).

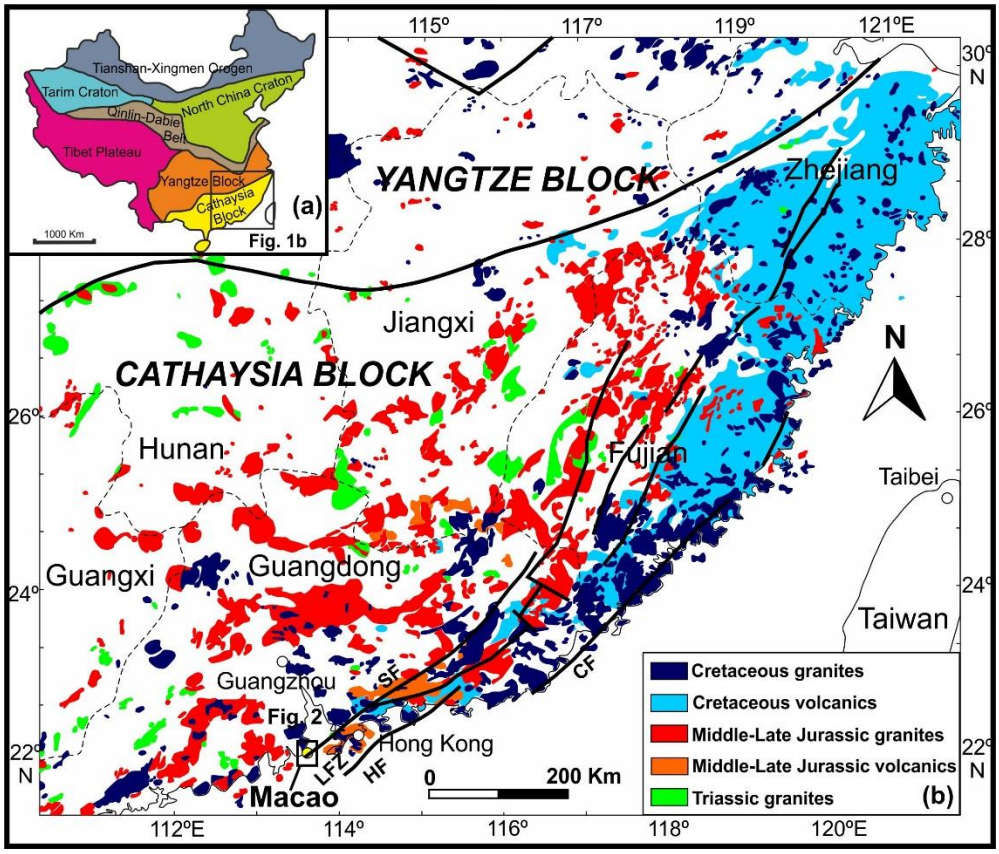

Fig. 4.1. (a) Simplified tectonic sketch of China; (b) geological map of SE China, showing the distribution of Mesozoic granitic and volcanic rocks on the Cathaysia Block. The Lianhuashan Fault Zone (LFZ), Shenzhen Fault (SF), Haifeng Fault (HF) and Changlee–Na'nao Fault (CF) are also represented. Figure adapted from Davis et al. (1997) and Zhou et al. (2006).

Macao is located on the SE China coast, south of Guangdong Province, about 50 km west of Hong Kong. In this area, there is a predominance of granitic intrusions that belong to a ~3500 km long and ~800 km wide NE-trending magmatic belt cropping out on the SE part of the Cathaysia Block (Fig. 4.1). Its origin has been associated with the Yanshanian Orogeny, related to the Late Mesozoic subduction of the Paleo-Pacific plate under the Eurasian plate (e.g. Lapierre et al., 1997; Zhou and Li, 2000; Zhou et al., 2006; Li and Li, 2007; Jiang et al., 2009; Jiang et al., 2015). In the neighbouring region of Hong Kong, the Jurassic–Early Cretaceous magmatism occurred in four main pulses constrained by high-precision zircon U–Pb geochronology: 165–160 Ma (Lamma Suite), 148–146 Ma (Kwai Chung Suite), 143 Ma (Cheung Chau Suite) and 141 Ma (Lion Rock Suite) (Sewell et al., 1992; Sewell et al., 2012a). These magmatic pulses record a temporal

evolution of magma compositions indicative of a transition from a compression-related to an extension-related tectonic regime (Sewell et al., 1992), consistent with the tectono-magmatic evolution of SE China (Zhou et al., 2006). Yanshanian magmatism probably continued in Hong Kong area until ca. 100–80 Ma, ceasing with the beginning of continental arc collapse, a consequence of the large-scale crustal extension in the region (Tang et al., 2014).

One of the most important tectonic structures in the coastal region of SE China is the NE-trending Lianhuashan Fault Zone, which can be traced for over 400 km through the coastal provinces of SE China (Chen, 1987; Ding and Lai, 1997). Near Macao and Hong Kong, the Lianhuashan Fault Zone comprises a 30 km wide zone limited to the North by the Shenzhen Fault and to the south by the Haifeng fault (Chen, 1987; Huang and Zhang, 1990; Fig. 4.1). Several volcanic centres and plutonic assemblages occur associated with the Lianhuashan Fault Zone, suggesting that it was a major locus of magmatic activity during the Late Mesozoic (Campbell and Sewell, 1997; Davis et al., 1997; Sewell and Campbell, 1997; Xia and Zhao, 2014).

In Macao, the plutonic rocks mainly consist of biotite granites with variable petrographic, mineralogical and geochemical features (Fig. 4.2). They intrude into the Paleozoic strata, of dominant Devonian age (Ribeiro et al., 1992). Some remnants of the wall rocks are found in the territory as sparse metasedimentary enclaves within the granites. In addition, microgranular mafic enclaves (MME) of variable size and shape are common within the granites.

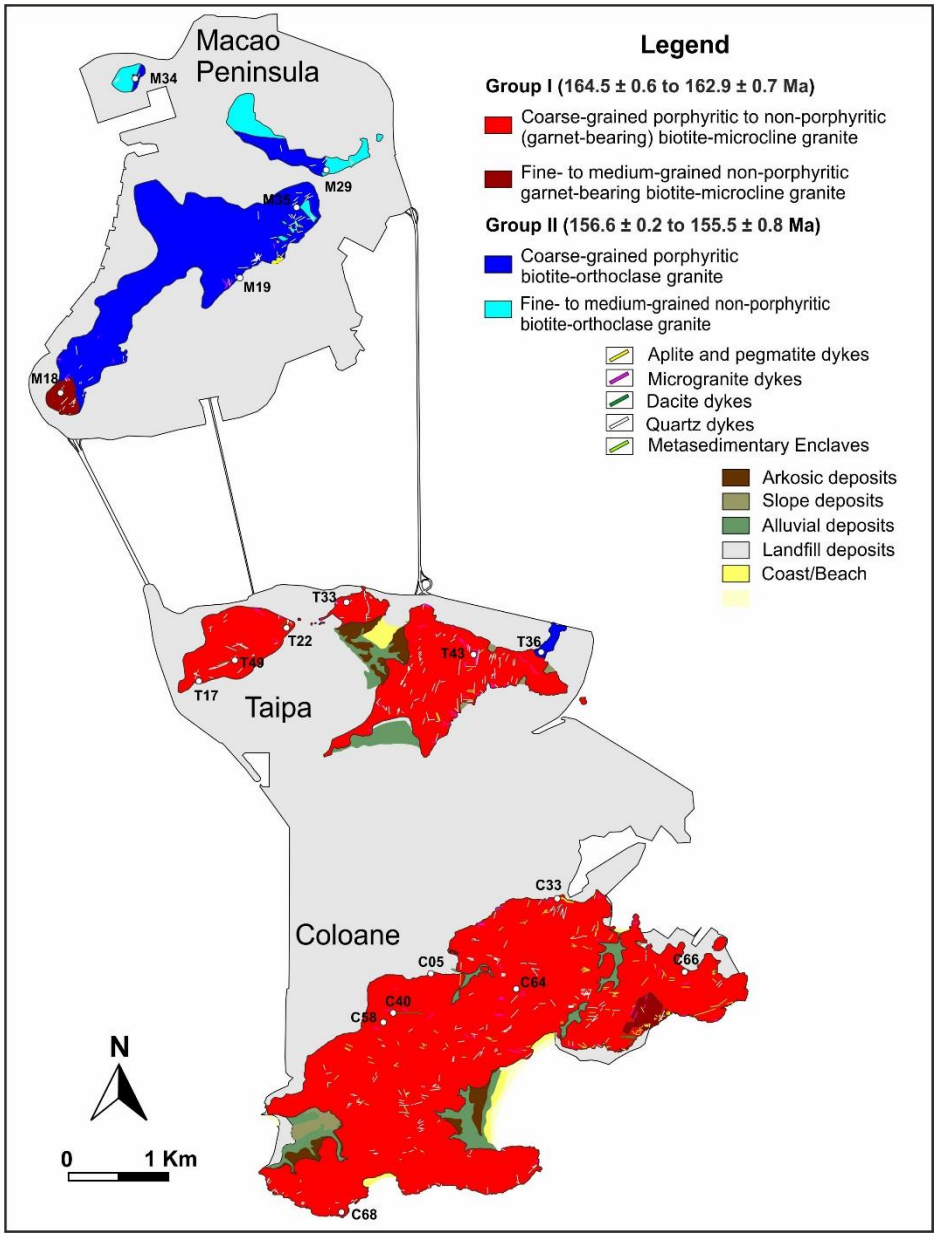

Fig. 4.2. Simplified geological map of Macao showing the distribution of the two groups of granites in the territory and the location of samples chosen for geochronology. Two main groups of granites are distinguished based on the determined ages and petrographic characteristics. See main text for details.

The granites are cut by a swarm of granitic dykes (microgranite, aplite and pegmatite) and dacite dykes. The former usually show irregular contours and diffuse contacts with the host granite, while the latter show sharp contacts.

4.3. Analytical methods

4.3.1. Mineral and whole-rock elemental chemistry

Mineral analyses were performed on carbon-coated polished thin sections using a JEOL SUPERPROBE™, model JXA-8200, in wavelength dispersive mode at the Departamento de Geologia da Faculdade de Ciências da Universidade de Lisboa (Portugal). Minerals were analysed with an acceleration voltage of 15 kV and a current of 25 nA, using a 5 mm wide beam. The analyses performed in each mineral phase were calibrated using the composition of reference materials, with reproducibility errors being lower than 2% and ordinarily around 1%. Matrix effects were corrected using the ZAF software provided by JEOL. Information about standards and detection limits are given in Supplementary File 1A.

Whole-rock major and trace element concentrations were obtained at Activation Laboratories, Ltd. (Ancaster, Ontario, Canada) using the geochemical analytical package 4E - Research - INAA, Total Digestion - ICP, Lithium Metaborate/Tetraborate Fusion - ICP, plus ICP-MS for some of the trace elements. Major oxide content was analysed by Inductively Coupled Plasma-Optical Emission Spectrometry (ICP-OES) using a Thermo Jarrell-Ash ENVIRO II ICP and/or Spectro Cirros ICP. Trace elements, including Rare Earth Elements (REE), were obtained using Inductively Coupled Plasma Mass-Spectrometry (ICP-MS) on a PerkinElmer SCIEX ELAN 6000, 6100 or 9000 ICP/MS and by Instrumental Neutron Activation Analysis (INAA). In-house standards and several certified reference materials of granitic to dioritic compositions (s.l.) from USGS (United States Geological Survey), GSJ (Geological Survey of Japan) and CCRMP (Canadian Certificate Reference Material Project) were used. Errors associated with the accuracy are 4% for major elements and better than 9% for the REE and the most widely used incompatible elements. Duplicate measurements of samples indicate that errors associated with reproducibility were generally lower than 5% for both major and trace elements. Information about detection limits is given in Supplementary File 1B. For detailed information regarding analytical and control procedures consult the Actlabs website (www.actlabs.com).

4.3.2. Geochronology

4.3.2.1. Zircon separation

Representative samples from the different magmatic facies identified through fieldwork and petrographic analysis were selected for zircon separation procedures. Samples were repeatedly crushed with a jaw crusher to obtain ca. 100 mm sized grains. Zircon grains were isolated using standard heavy liquids and magnetic techniques. Initial separation involved multiple passes of crushed rock over a Wilfley table to concentrate heavy minerals. Further zircon concentration was achieved by using heavy liquids (bromoform and methylene iodide) enabling density separation and a Frantz isodynamic magnetic separator. Final grains selection was made by hand picking under a binocular microscope, choosing the freshest, least-cracked zircon grains (see sections 4.3.2.2 and 4.3.2.3).

4.3.2.2. ID-TIMS

The isotope dilution (ID) - thermal ionization mass spectrometry (TIMS) analyses were performed at Jack Satterly Geochronology Laboratory, Department of Geology, University of Toronto, Toronto, Ont., Canada.

Zircon crystals were mounted in epoxy and polished to check for the possibility of xenocrystic cores. Grains were imaged with backscattered electrons (BSE) and cathodoluminescence (CL) using a JEOL JSM6610-Lv scanning electron microscope. Crystal domains that are high in U, and therefore relatively damaged by radiation, are bright under BSE and dark under CL, with the opposite for low U domains (Hanchat and Miller, 1993). Alteration shows as dark amorphous domains and is usually only seen in highly damaged zircon.

The freshest and least-cracked whole grains were hand-picked for analysis using an optical microscope. Chemical abrasion (CA; Mattinson, 2005) was used to remove any discordant domains. For CA treatment, zircon grains were annealed in quartz crucibles at 1000 ºC overnight. These crystals were then leached for 6 h in concentrated hydrofluoric acid (HF) at 200 ºC in Teflon bombs, the same conditions under which they are dissolved but for a shorter period, followed by leaching in 3N HCl overnight in Teflon bombs to dissolve any REE-rich fluoride phases that might inhibit equilibration with the spike. The annealing partially heals radiation damage in the zircon, rendering it more chemically inert and slowing its rate of dissolution in HF. Altered crystal

domains, which contain disturbed Pb and are responsible for discordance, dissolve faster than annealed unaltered zircon and are usually completely removed after a few hours of leaching. Relatively undamaged crystals such as these are attacked only slightly by the leaching process, in some cases showing surface etching and white colouration along cracks. Fragments were chosen to contain as little white discolouration as possible. In cases where there is noticeable etching, the presence of a small amount of discolouration does not seem to affect the results.

To minimize the possibility of inheritance, single zircon grains were analysed having characteristics typical of the igneous population, such as a euhedral shape and an abundance of melt or rod- like inclusions. Weights of zircon grains selected for ID-TIMS analyses were estimated from photomicrographs. Estimated weights should be accurate to about 30%. This affects only U and Pb concentrations, not age information, which depends only on isotope ratio measurements. Washed zircon was dissolved using concentrated HF in Teflon bombs at 200 ºC for 5 days (Krogh, 1973). Samples were subsequently redissolved in 3N HCl along with ^{205}Pb–^{233}U–^{235}U (ET535) spike. U and Pb were separated from the solutions using 50 mL anion exchange columns (Krogh, 1973). Mixed purified U and Pb solutions were loaded directly onto Re filaments using silica gel and analysed with a VG354 mass spectrometer in multi-collector static Faraday and single collector Daly mode. Dead time of the Daly measuring system is 16.5 ns. The mass discrimination correction for the Daly detector is constant at 0.06% per atomic mass unit (AMU). For samples that were large enough, U and Pb were analysed in static mode using multiple Faraday cups with mass 204 in the axial Daly. Smaller samples were analysed in peak jumping mode on the Daly collector. Faraday amplifiers were calibrated daily. Daly gains were calibrated at the beginning of each sample. $^{207}Pb/^{205}Pb$ ratios were measured in peak jumping mode on the Daly near the end of Pb emission to improve precision over static values, where the ^{207}Pb peak is too small for precise measurement using the Faraday collector. Isobaric interferences are monitored at mass 210 and typically show a gradual decrease throughout a run. They are only significant for the small 204 mass peak. Consequently, the $^{207}Pb/^{204}Pb$ ratio generally shows an increase with time. The $^{207}Pb/^{204}Pb$ ratio is measured by peak jumping on the Daly collector at the end of the Pb run when the mass 210 is at baseline. U isotopes are measured at higher temperature in static mode with the Faraday collectors. The $^{233}U/^{235}U$ ratio from the spike allows correction for analytical mass fractionation. Pb isotopes cannot be corrected for analytic mass fractionation, but silica loads are known to have a predictable Pb mass fractionation that begins at about 0.13% per AMU and decreases to about 0 as the load is

exhausted. The fractionation correction is taken to be 0.1% ± 0.04% per AMU. This sets a limit on age precision for precisely analysed samples.

4.3.2.3. LA-MC-ICPMS

The laser ablation (LA) multi-collector (MC) inductively coupled plasma source mass spectrometer (ICPMS) analyses were performed at the Department of Earth Sciences of the University of Hong Kong.

Individual zircon grains were hand-picked under a binocular microscope, then mounted in standard 1" epoxy mounts and polished. To characterize the internal structures of the zircons, BSE images were obtained using a JEOLJXA-8100 microprobe at the Department of Earth Sciences of the University of Hong Kong.

Zircon grains were analysed with a Nu Plasma HR MC-ICPMS (Nu Instruments, UK), coupled with a 193 nm excimer laser ablation system (RESOlution M-50, Resonetics LLC, USA). It combines rapid (<1.5 s for 99%) signal washout with full flexibility in sample size (50 mm 50 mm 25 mm) and high sensitivity (>10000 cps/ ppm for mid-high m/z, 55 mm, 5 Hz). The MC-ICPMS contains twelve F collectors and four ion counting detectors dispersed on the low mass side of the array, allowing simultaneous acquisition of ion signals ranging from mass ^{238}U, ^{232}Th, ^{208}Pb, ^{207}Pb, ^{206}Pb and ^{204}Pb. Instrument parameters and analytical details are described in Xia et al. (2011). In this study, beam diameter of 30 mm, repetition rate of 4 Hz and energy density of 5 J/cm^2 on sample surface were used. The machine measured the background signal around 15 s and ablation time 25 s, resulting in pits ~20 mm deep. The standard zircons 91500 (Wiedenbeck et al., 1995) and GJ-1 (Jackson et al., 2004) were measured every 10–15 unknown measurements for further calibration. The instrument configuration does not measure other elements, so no concentrations are given.

In most cases, the border of the crystals was analysed to ensure that a crystallization age was obtained, since the outermost part of zircon crystals usually corresponds to the more recent magmatic events. To avoid possible inheritance, the most internally homogenous grains were chosen for crystallization age determination. However, it must be considered that zircon grains often represent a continuum of crystallization ages and due to diameter of the laser (30 mm) some mixing cannot be totally avoided.

4.4. Analytical Results

4.4.1. Petrography

Overall, Macao biotite granites are mainly composed of quartz (30–35 vol%), K-feldspar (35–40 vol%), plagioclase (20–25 vol%) and biotite (5–10 vol%). According to the type of K-feldspar, they can be divided into microcline granites (Group I; Fig. 4.3a–d) and orthoclase granites (Group II; Fig. 4.3e–g), which are also distinct in age (see section 4.5.1; see also Fig. 4.2). In both groups, textures vary from medium- to coarse-grained porphyritic to fine-grained non- porphyritic moderately equigranular. K-feldspar occurs as euhedral to subhedral megacrysts (Fig. 4.3a, b and e) or heterogranular subhedral to anhedral crystals in the groundmass. It ranges up to 7 cm long and consists of perthite that commonly contains small inclusions of plagioclase and quartz. The K-rich phase portrays distinct structures, microcline in Group I granites and orthoclase in Group II, recognizable by the typical tartan pattern (albite/pericline twins; Fig. 4.3b) and Carlsbad twining, respectively. Plagioclase occurs as subhedral tabular crystals (<1 cm) with polysynthetic albite twinning, showing normal and oscillatory zoning under the microscope. Biotite is anhedral to subhedral, occurring as interstitial isolated slab-flake crystals or in mineral clusters, often containing a wide variety of accessory minerals. Its modal percentage tends to decrease from the porphyritic facies towards the fine-grained equigranular facies. Quartz is anhedral and heterogranular (<0.7 cm), in some cases forming graphic and myrmekitic intergrowths with K-feldspar and plagioclase, respectively. At odds with Group II granites, quartz grains from Group I show evidence for significant deformation such as pervasive undulatory extinction, sutured grain boundaries and development of individual subgrains with well-defined boundaries (Fig. 4.3b).

While many accessory minerals are common in both groups (Fe–Ti oxides, apatite, zircon, monazite, xenotime, allanite, sulfides and fluorite), titanite (Fig. 4.3f) is distinctly more abundant in Group II granites whereas garnet and abundant tantalo-niobates are characteristic of Group I granites. Zircon usually occurs as inclusions in biotite surrounded by pleochroic haloes and, more rarely, as isolated grains in the groundmass interstitial to K-feldspar and plagioclase.

The MME (Fig. 4.3h–k) are mainly hosted by the porphyritic coarse-grained granitic facies, varying from monzogranite to granodiorite in Group I granites to quartz monzodiorite in Group II. They range from a few millimeters up to <1 m in size. In the field, they commonly have sharp contacts with their host, are irregular to oval blobs and locally occur as dike-like trails. Textures

vary from slightly porphyritic to equigranular fine-grained. Compared with the host granite, MME generally contain the same mineral assemblage but with higher contents of biotite (in some cases highly chloritized; Fig. 4.3k) and plagioclase, and lower contents of quartz and K-feldspar.

The dacite dykes are slightly porphyritic with euhedral to subhedral tabular plagioclase (<0.5 cm) and prismatic hornblende (<0.1 cm) phenocrysts within an aphanitic matrix composed of K-feldspar and microcrystalline quartz and minor Fe–Ti oxides, zircon and apatite (Fig. 4.3l). Alteration of feldspars produces pervasive sericite.

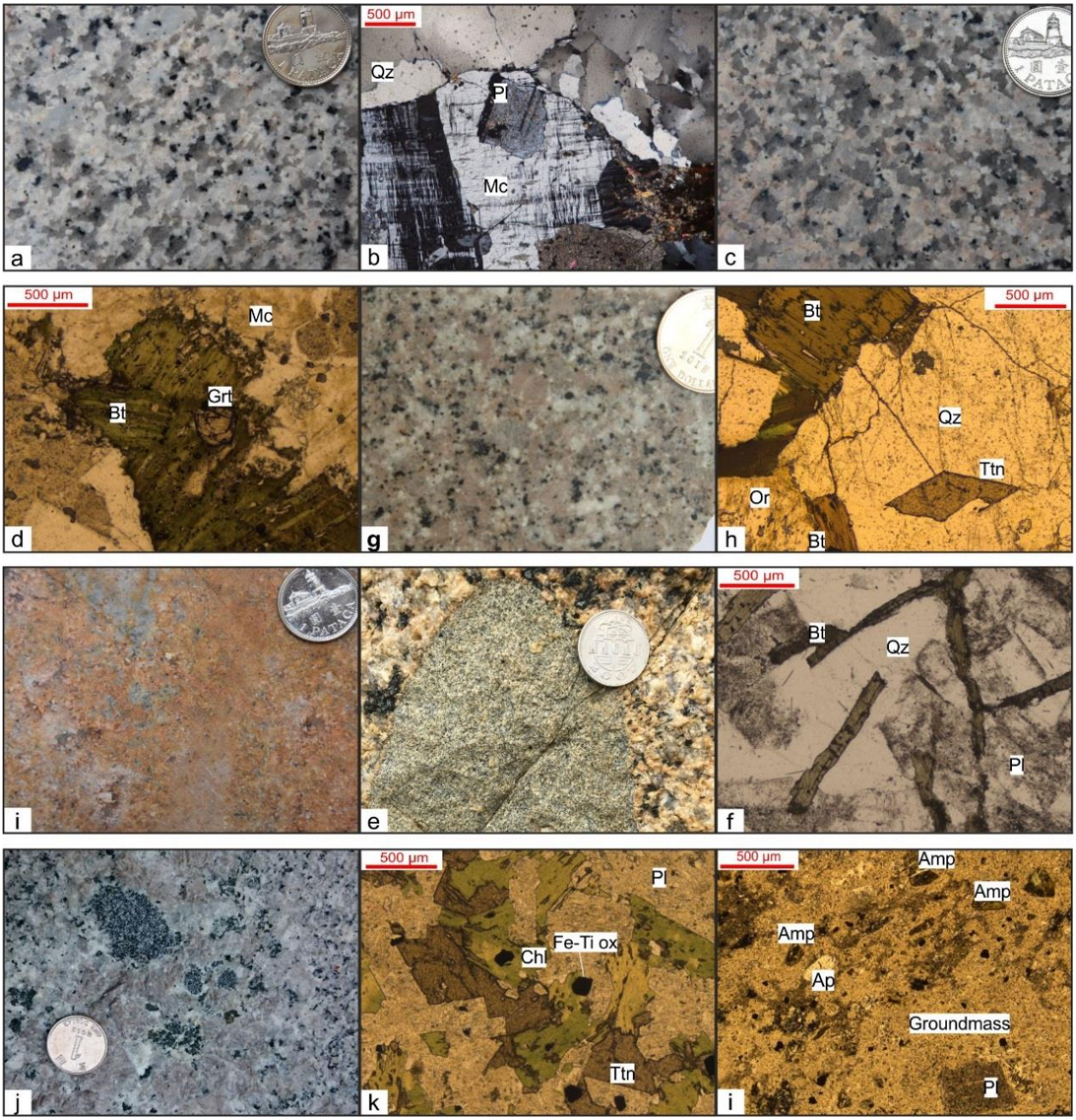

Fig. 4.3. Hand specimens and thin sections representative of the different lithofacies observed in Macao: (a) Group I coarse-grained porphyritic biotite-microcline granite; (b) poikilitic perthitic microcline megacrysts enclosing smaller plagioclase crystals in Group I; (c) Group I coarse-grained non-porphyritic garnet-bearing biotite-microcline granite; (d) accessory garnet growing at expense of biotite, common in highly fractionated granites from Group I; (e) Group II coarse-grained porphyritic biotite-orthoclase granite; (f) a well- developed euhedral titanite crystal common in Group II weakly fractionated granites; (g) Group II fine-grained biotite-orthoclase granite; (h) MME enclosed in Group I granites; (i) Group I MME with acicular biotite; (j) MME enclosed in Group II granites; (k) Group II MME with lozenge-shaped strongly chloritized biotite and titanite; (l) dacite dyke with amphibole and plagioclase phenocrysts within a feldspathic groundmass. MME: mafic microgranular enclave; Amp: Amphibole; Ap: Apatite; FeeTi ox: FeeTi oxides; Qz: quartz; Pl: plagioclase; Or: Orthoclase; Ttn: Titanite; Bt: biotite; Chl: Chlorite; Mc: microcline; Grt: garnet.

4.4.2. Mineral and whole-rock elemental chemistry

Representative electron microprobe analyses of biotites from the studied samples are displayed in Table 4.1. According to the nomenclature of micas (Speer, 1984; Deer et al., 1992; Rieder, 1999), biotites from Macao granitic rocks show a wide range of compositions between Mg-rich annite and Fe-rich siderophyllite (Fig. 4.4a and b).

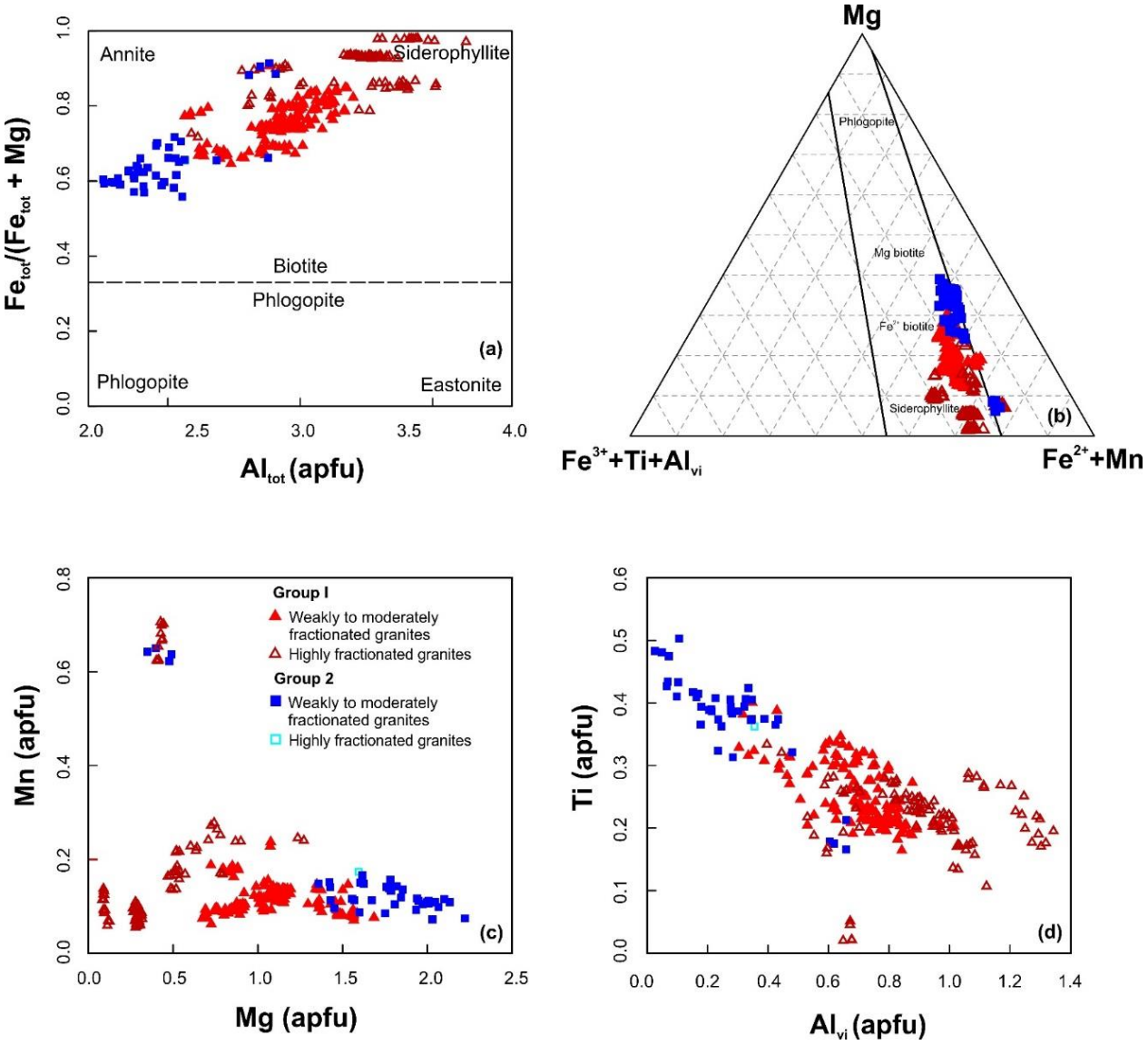

Fig. 4.4. Chemistry of biotites from the Macao granites: (a) $Fe_{tot}/(Fe_{tot} + Mg)$ *vs* Al_{tot} diagram, also known as the annite (Ann) – siderophyllite (Sdp) – phlogopite (Phl) – eastonite (Eas) quadrilateral diagram; Fe_{tot}: total iron, i.e., $Fe^{2+} + Fe^{3+}$; (b) Octahedral cations in the classification diagram of Foster (1960); (c) Mn *vs* Mg variation diagram; (d) Ti *vs* Al^{vi} variation diagram.

Representative whole-rock major and trace element analyses of Macao granites are shown in Table 4.2. They have variable SiO_2 contents (66.77–76.92 wt%), moderate total alkali ($K_2O + Na_2O$ = 7.04–8.54 wt%) and K_2O/Na_2O = 1.24–1.62, being classifiable as high-K calc-alkaline rocks. According to their molar $Al_2O_3/(CaO + Na_2O + K_2O)$ ratios, these rocks are metaluminous to weakly peraluminous (A/CNK = 0.96–1.13). REE compositions are highly variable with $(La/Yb)_N$ ratios ranging from 0.12 to 10.76 (Fig. 4.5) and negative Eu anomalies (Eu/Eu*) from 0.02 to 0.54 (Table 4.2). They are also characterized by a wide range of Zr/Hf ratios (12.24–37.60). Since Zr/Hf ratios tend to decrease with increasing evolution of high-silica melts (e.g. Irber, 1999), some authors have suggested this ratio as a granite fractionation index (e.g. Bea et al., 2006; Zaraisky et al., 2009). Therefore, in this study, we consider weakly to moderately fractionated granites those having Zr/Hf > 25, while highly fractionated granites are marked by comparatively lower Zr/Hf ratios ($\leq$ 25).

The dacite dykes have lower SiO_2 contents (63.61–65.27 wt%) and total alkali contents ($K_2O + Na_2O$ = 5.05–6.18) than the granites. They are enriched in large ion lithophile elements (LILE) relatively to high field strength elements (HSFE) with high $(Rb/La)_N$ ratios of 3.8–8.5, have high $(La/Yb)_N$ ratios of 11.45–13.86 and positive Eu anomalies (Eu/Eu* = 1.06–1.13; Table 4.2).

Table 4.1. Representative chemical compositions of biotites from Macao granites.

Sample	c51b_fb_bt6	c58_b2_bt2	c60_b1_bt6	c71_b4_bt5	m16_b2_bt1	t17_b4_bt2	m29b_b5_bt1	m6_b5_bt2	m11_b5_bt2	m6_b3_bt1	m29b_b5_bt2	m20_b1_bt3
Group	**GI**	**GI**	**GI**	**GI**	**GI**	**GI**	**GII**	**GII**	**GII**	**GII**	**GII**	**GII**
Frac. degree	**WMF**	**WMF**	**WMF**	**HF**	**HF**	**HF**	**WMF**	**WMF**	**WMF**	**WMF**	**WMF**	**HF**
Oxides (wt%)												
SiO_2	36.94	36.72	36.37	35.54	36.83	37.16	36.71	36.19	37.12	37.33	35.35	37.36
TiO_2	2.03	1.77	1.64	2.08	2.69	2.43	3.17	3.25	2.70	3.16	2.70	3.11
Al_2O_3	15.45	16.05	16.22	17.19	14.00	17.39	14.54	13.67	14.04	13.48	15.41	14.04
FeO	22.38	24.19	24.15	28.00	23.03	21.73	21.84	24.18	20.31	22.72	22.83	22.27
Fe_2O_3	2.66	2.70	2.72	2.98	2.78	0.95	3.08	3.52	3.29	3.90	4.16	2.38
MnO	0.63	0.86	0.93	0.54	1.79	1.28	0.66	1.05	0.57	0.72	0.84	1.32
MgO	6.43	4.41	4.88	1.20	5.39	3.32	6.85	6.05	9.66	6.18	7.08	6.90
CaO	0.05	0.03	0.03	0.01	0.02	0.00	0.06	0.05	0.36	0.61	0.04	0.01
Na_2O	0.07	0.05	0.03	0.09	0.21	0.08	0.25	0.09	0.07	0.08	0.11	0.10
K_2O	10.13	10.11	10.11	9.93	9.93	10.22	9.13	9.02	9.00	8.16	7.18	10.00
BaO	0.01	0.05	0.09	0.01	0.07	0.00	0.34	0.38	0.06	0.04	0.30	0.50
F*	1.26	0.58	0.87	0.02	2.13	1.93	0.71	0.49	0.69	0.57	0.71	0.69
Cl*	0.05	0.04	0.03	0.09	0.20	0.12	0.12	0.15	0.07	0.13	0.08	0.09
Cr_2O_3	0.10	0.07	0.07	0.09	0.04	0.07	0.09	0.07	0.09	0.10	0.05	0.09
Total	97.65	97.36	97.75	97.73	98.16	95.84	97.24	97.90	97.71	96.89	96.52	98.57
Cations per 22 oxygens												
Si	5.77	5.78	5.72	5.67	5.83	5.84	5.75	5.73	5.73	5.88	5.60	5.79
Al^{iv}	2.23	2.22	2.28	2.33	2.17	2.16	2.25	2.27	2.27	2.12	2.40	2.21
Al^{vi}	0.62	0.76	0.73	0.90	0.44	1.06	0.43	0.28	0.28	0.39	0.48	0.35
Ti	0.24	0.21	0.19	0.25	0.32	0.29	0.37	0.39	0.31	0.37	0.32	0.36
Cr	0.01	0.01	0.01	0.01	0.00	0.01	0.01	0.01	0.01	0.01	0.01	0.01
Fe^{2+}	2.92	3.19	3.18	3.74	3.05	2.86	2.86	3.20	2.62	3.00	3.03	2.89
Fe^{3+}	0.16	0.16	0.16	0.18	0.17	0.06	0.18	0.21	0.19	0.23	0.25	0.14
Mn	0.08	0.11	0.12	0.07	0.24	0.17	0.09	0.14	0.07	0.10	0.11	0.17
Mg	1.50	1.03	1.14	0.28	1.27	0.78	1.60	1.43	2.22	1.45	1.67	1.59
Ca	0.01	0.00	0.00	0.00	0.00	0.00	0.01	0.01	0.06	0.10	0.01	0.00
Na	0.02	0.02	0.01	0.03	0.07	0.02	0.08	0.03	0.02	0.02	0.03	0.03
K	2.02	2.03	2.03	2.02	2.01	2.05	1.82	1.82	1.77	1.64	1.45	1.98
Ba	0.00	0.00	0.01	0.00	0.00	0.00	0.02	0.02	0.00	0.00	0.02	0.03
F	0.62	0.29	0.43	0.01	1.07	0.96	0.35	0.24	0.34	0.29	0.35	0.34
Cl	0.01	0.01	0.01	0.02	0.05	0.03	0.03	0.04	0.02	0.03	0.02	0.02
Total	16.22	15.83	16.03	15.52	16.70	16.28	15.86	15.81	15.93	15.64	15.75	15.93

Abbreviations: Frac. - Fractionation; GI - Group I granites; GII - Group II granites; WMF - Weakly to moderately fractionated (Zr/Hf > 25); HF - highly fractionated. (Zr/Hf < 25).

Table 4.2. Representative whole-rock major and trace element compositions of the Macao granites and dacites.

Sample	C 66	T 33	M18	T44	M 19	M 25	M 31	M 30	C40
Group	GI	GI	GI	GI	GII	GII	GII	GII	Dacite
Frac. degree	WMF	WMF	HF	HF	WMF	WMF	HF	HF	WMF
Major elements (wt%)									
SiO_2	73.45	72.46	75.44	75.72	68.19	74.89	76.51	75.23	63.61
Al_2O_3	13.73	13.43	12.42	12.68	14.80	12.96	12.82	12.98	16.61
$Fe_2O_3^T$	2.34	2.70	1.42	1.34	3.30	1.65	1.35	1.46	4.17
MnO	0.06	0.09	0.05	0.04	0.08	0.03	0.03	0.02	0.10
MgO	0.22	0.34	0.08	0.02	0.53	0.14	0.08	0.07	1.62
CaO	1.26	1.19	0.76	0.50	1.97	0.88	0.63	0.53	4.01
Na_2O	3.17	3.25	3.70	3.96	2.89	3.18	3.40	3.42	3.62
K_2O	5.06	4.82	4.54	5.00	5.36	4.74	4.91	4.68	2.56
TiO_2	0.16	0.20	0.06	0.02	0.39	0.14	0.08	0.09	0.47
P_2O_5	0.04	0.08	0.01	0.00	0.13	0.04	0.02	0.00	0.28
LOI	0.79	0.80	0.32	0.09	1.43	0.90	0.67	0.75	2.70
Total	100.30	99.36	98.80	99.37	99.07	99.53	100.50	99.24	99.73
Trace elements (ppm)									
Ba	230.00	393.00	91.00	15.00	625.00	103.00	23.00	35.00	1179.00
Be	6.00	6.00	7.00	13.00	9.00	6.00	7.00	8.00	2.00
Bi	0.30	0.80	0.10	0.30	0.50	0.80	0.30	0.00	0.10
Co	4.00	7.00	1.70	0.00	7.40	4.00	0.80	2.70	6.80
Cr	121.00	165.00	103.00	50.00	71.70	82.10	75.10	108.00	81.00
Cs	14.70	12.00	8.70	10.60	9.60	7.50	7.80	6.10	10.70
Cu	10.00	16.00	6.00	5.00	56.00	17.00	22.00	12.00	2.00
Ga	17.00	19.00	18.00	21.00	18.00	16.00	16.00	16.00	19.00
Ge	2.00	1.70	2.10	3.30	1.70	2.00	2.00	1.90	1.50
Hf	4.30	5.00	3.80	5.60	5.30	3.60	3.50	1.90	3.90
Nb	16.40	16.00	20.20	27.80	13.50	11.50	14.60	11.00	6.80
Ni	57.00	77.00	39.00	29.00	28.00	41.00	37.00	35.00	42.00
Pb	42.00	42.00	44.00	53.00	31.00	39.00	51.00	42.00	9.00
Rb	356.00	373.00	384.00	416.00	371.00	414.00	455.00	388.00	143.00
Sb	0.40	0.50	0.00	0.30	0.10	0.30	0.30	0.20	0.30
Sc	4.80	5.10	3.78	2.27	6.60	2.80	2.90	2.00	7.19
Sn	11.00	70.00	7.00	6.00	628.00	141.00	86.00	5.00	1.00
Sr	84.00	121.00	38.00	9.00	210.00	57.00	25.00	36.00	1104.00
Ta	3.25	3.00	7.26	9.82	2.31	2.43	2.40	2.12	0.51
Th	36.80	37.60	24.80	19.60	30.10	33.20	33.70	27.40	5.01
U	21.30	11.30	16.80	31.00	12.10	16.00	18.90	21.00	0.99
V	12.00	16.00	5.00	5.00	32.00	11.00	0.00	6.00	59.00
W	0.00	14.00	3.00	0.00	51.00	6.00	1.00	0.00	0.00
Y	58.00	38.00	88.00	94.00	32.00	39.00	24.00	31.00	16.00
Zn	39.00	41.00	24.00	9.00	44.00	25.00	18.00	10.00	45.00
Zr	127.00	170.00	77.00	70.00	191.00	97.00	79.00	31.00	157.00
La	32.40	49.50	14.20	8.34	43.10	30.50	13.50	24.00	35.70
Ce	69.50	100.00	32.40	21.60	91.20	44.10	28.30	25.30	68.80
Pr	7.98	10.80	4.29	3.34	10.20	6.82	3.03	5.08	7.95
Nd	28.90	37.30	17.60	14.50	36.10	23.30	9.81	16.50	29.70

Table 4.2 (continued)

Sample	C 66	T 33	M18	T44	M 19	M 25	M 31	M 30	C40
Group	GI	GI	GI	GI	GII	GII	GII	GII	Dacite
Frac. degree	WMF	WMF	HF	HF	WMF	WMF	HF	HF	WMF
Sm	7.87	7.61	7.28	7.64	7.27	5.27	2.26	3.84	5.15
Eu	0.65	0.75	0.29	0.09	1.20	0.58	0.18	0.40	1.56
Gd	7.89	7.41	9.62	8.93	6.29	5.15	2.60	3.77	3.91
Tb	1.42	1.17	2.00	2.01	0.95	0.88	0.48	0.66	0.52
Dy	9.47	7.14	13.70	13.90	5.79	5.78	3.13	4.39	2.97
Ho	1.94	1.39	2.79	2.97	1.17	1.22	0.74	0.98	0.57
Er	6.04	4.06	8.79	10.00	3.64	4.04	2.78	3.20	1.74
Tm	0.93	0.62	1.50	1.86	0.59	0.68	0.50	0.58	0.27
Yb	6.43	4.31	10.40	14.20	4.29	5.37	4.48	5.01	1.75
Lu	0.96	0.67	1.64	2.28	0.71	0.91	0.86	0.87	0.28
Tl	1.71	1.68	1.85	1.77	1.85	1.84	1.79	1.68	1.09
Eu/Eu* [a]	0.25	0.30	0.11	0.03	0.54	0.34	0.23	0.32	1.06
Ti/Ti* [b]	0.04	0.05	0.02	0.01	0.08	0.04	0.06	0.04	0.12
$TE_{1,3}$ [c]	1.04	1.03	1.07	1.13	1.03	0.97	0.90	1.07	-

Abbreviations: Fractionation GI - Group I granites; GII - Group II granites; WMF - Weakly to moderately fractionated (Zr/Hf > 25); HF - highly fractionated. (Zr/Hf < 25).

a The Eu anomaly is the ratio between measured Eua nd the value expected for Eu on a smooth chondrite-normalized plot (Eu*), where $Eu^* = \sqrt{(Sm_N \times Gd_N)}$. If this ratio is > 1 the anomaly is positive, if the ratio is <1 the anomaly is negative.

b The Ti anomaly is the ratio between measured Ti and the value expected for Ti on a smooth chondrite-normalized plot (Ti*), where $Ti^* = \sqrt{(Eu_N \times Dy_N)}$. If this ratio is > 1 the anomaly is positive, if the ratio is <1 the anomaly is negative.

c The term 'tetrad effect' refers to the subdivision of the fifteen lanthanide elements into four groups called tetrads: (1) La–Nd, (2) Pm–Gd, (3) Gd–Ho, and (4) Er–Lu, each tetrad forming a smooth convex (M-type) or concave (W-type) pattern. Degree of the tetrad effect = $TE_{1,3} = (t1 \times t3)^{0.5}$, where $t1 = (Ce/Ce^t \times Pr/Pr^t)^{0.5}$ and $t3 = (Tb/Tb^t \times Dy/Dy^t)^{0.5}$, with $Pr/Pr^t = Pr_N/(La_N^{1/3} \times Nd_N^{2/3})$, $Tb/Tb^t = Tb_N/(Gd_N^{2/3} \times Ho_N^{1/3})$ and $Dy/Dy^t = Dy_N/(Gd_N^{1/3} \times Ho_N^{2/3})$.

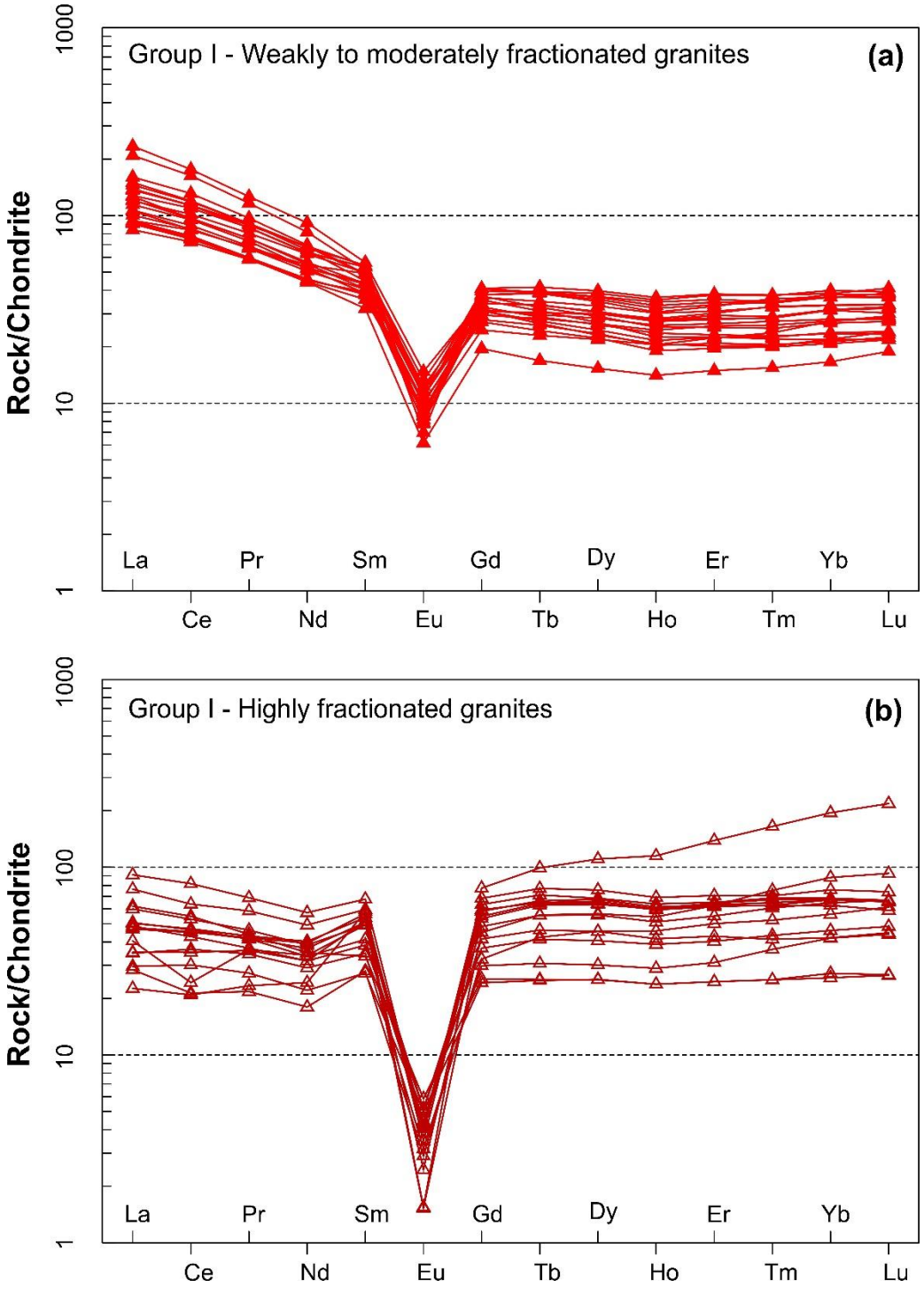
Group I - Weakly to moderately fractionated granites
(a)
Rock/Chondrite
1000
100
10
1
La
Ce
Pr
Nd
Sm
Eu
Gd
Tb
Dy
Ho
Er
Tm
Yb
Lu
Group I - Highly fractionated granites
(b)
Rock/Chondrite
1000
100
10
1
La
Ce
Pr
Nd
Sm
Eu
Gd
Tb
Dy
Ho
Er
Tm
Yb
Lu

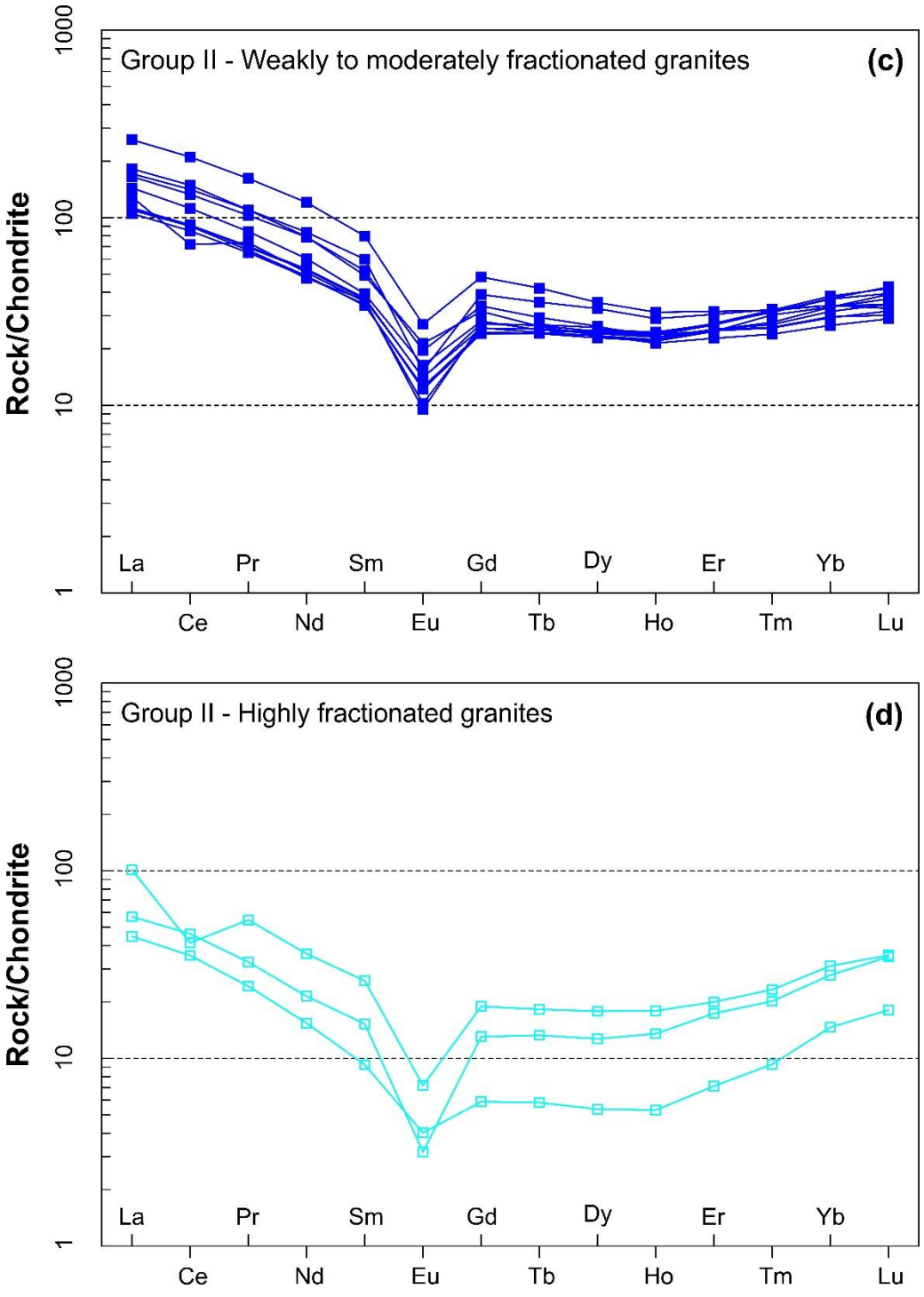

Fig. 4.5. (a) Chondrite normalized Rare Earth Elements (REE) patterns for: (a) weakly to moderately fractionated Group I granites; (b) highly fractionated Group I granites; (c) weakly to moderately fractionated Group II granites; (d) highly fractionated Group II granites. The chondrite values are from McDonough and Sun (1995).

4.4.3. ID-TIMS geochronology

Six samples were analysed for U–Pb zircon geochronology using ID-TIMS (Tables 4.3 and 4.4, Fig. 4.6 and Fig. 4.7; see also Supplementary File 2 for details on the location and general characteristics of the analysed samples). Detailed descriptions of zircons from each sample and BSE and CL images are provided in Supplementary File 3. Mass spectrometer data were reduced using in-house software (UTILAge program written by D.W. Davis). Concordia data are plotted using the Isoplot program of Ludwig (1998, 2012). Individual analyses in the data table (Table 4.3) and concordia plots are presented as 2σ absolute error and uncertainties in averages ages are quoted at the 95% level (2σ). Ages are based on $^{206}Pb/^{238}U$ ratios, which are least susceptible to analytical bias and should give robust age estimates within the quoted errors. Data may in some cases scatter slightly to the left of the concordia curve due to residual interferences affecting the small ^{204}Pb peak, which causes an overcorrection for common Pb but does not significantly affect the $^{206}Pb/^{238}U$ age. Significant scatter to the right is probably due to Precambrian inheritance.

Zircon separates from many of the granitic rocks are bimodal with a population of fresh grains and another of strongly altered and cracked crystals (see Supplementary File 3). In some instances, altered/cracked zircons may overgrow the population of fresh euhedral grains. Only fresh grains were dated even when the zircon population was dominated by the altered type.

Samples M18, T17 (Group I granites) generally produced overlapping $^{206}Pb/^{238}U$ ages for individual grains, although T17 also yielded a grain with an age that is 2 Ma younger than the main cluster (Fig. 4.7c) and another Group I sample (C58, Fig. 4.7a) produced data that scatter outside of error, at least in part due to Mesozoic and Archean inheritance. Ten out of fifteen grains from Group I define an age of 163.5 ± 0.2 Ma although with a large MSWD of 4.5. Group II granite samples T36 and M34 (Fig. 4.7d and e, respectively) mostly scatter only slightly outside of error. Nine out of eleven grains from Group II define an age of 156.6 ± 0.1 Ma with an MSWD of 1.7. A single older 164.5 Ma grain (Table 4.3) may represent an antecryst acquired from Group I. Zircon in the dacite dyke (sample C40) appears to be almost entirely inherited with a span of younger near-concordant ages from 120 Ma to 153 Ma.

Though zircon grains were chosen based on chemical and morphological criteria for determination of crystallization ages of the magmatic rocks, inheritance could not be avoided in some cases. The analysis with the oldest concordant $^{206}Pb/^{238}U$ age indicates an inherited

Phanerozoic source that is at least 205 Ma old (Fig. 4.7a). The oldest discordant analysis (from sample C58) suggests an inherited Mesoarchean age (ca. 3.5 Ga; Fig. 4.7a).

Table 4.3. ID-TIMS U–Pb isotopic data on zircon from the Macao magmatic rocks.

Spot No.	Fraction analysed	Weight (mg)	U (ppm)	Th/U
C58 - Coarse-grained porphyritic biotite-microcline granite, Group I				
dwd6193	1 CA zr, ET535, Hf collected	0.0028	344	0.76
dwd6183	1 CA zr, sl etched prism, ET535, Hf collected	0.0026	526	0.66
dwd6195	1 CA zr, ET535	0.0026	825	0.52
dwd6182	1 CA zr, etched spr, ET535, Hf collected	0.0027	948	0.39
dwd6181	1 Ca zr, etched frag, ET535, Hf collected	0.0041	172	0.64
dwd6194	1 CA zr, ET535	0.0025	366	0.86
M18 - Fine- to medium-grained non-porphyritic garnet-bearing biotite-microcline granite, Group I				
dwd6202	1 CA zr, stubby unetched, Hf saved, ET535 spike	0.0017	657	0.59
dwd6204	1 CA zr, stubby, crk, etched, ET535	0.0016	868	0.49
dwd6205	1 CA zr, stubby, well etched, ET535	0.0015	870	0.62
T17 - Coarse-grained non-porphyritic garnet-bearing biotite-microcline granite, Group I				
dwd6184	1 CA zr, etched stubby, ET535, Hf collected	0.0019	954	0.45
dwd6198	1 CA zr, ET535	0.0008	813	0.57
dwd6197	1 CA zr, ET535	0.0008	1032	0.58
dwd6185	1 CA zr, etched tip, ET535, Hf collected	0.0012	651	0.63
dwd6196	1 CA zr, ET535, Hf collected	0.0012	448	0.54
dwd6186	1 CA zr	0.0019	403	0.82
M34 - Coarse-grained porphyritic biotite-orthoclase granite, Group II				
dwd6178	1 CA zr, tip, ET535, Hf collected	0.0061	548	0.44
dwd6191	1 CA zr, ET535	0.0034	1313	0.50
dwd6190	1 CA zr, ET535, Hf saved	0.0042	967	0.52
dwd6180	1 CA zr, spr, ET535, Hf collected	0.0026	652	0.67
dwd6179	1 CA zr, tip, ET535, Hf collected	0.0039	428	0.60
T36 - Coarse-grained porphyritic biotite-orthoclase granite, Group II				
dwd6211	1 CA zr, stubby, melt incls, sl. etched, ET535 spike	0.0014	1590	0.61
dwd6208	1 CA zr, stubby, melt incls, sl. etched, ET535 spike	0.0038	921	0.61
dwd6207	1 CA zr, stubby, melt incls, sl. etched, ET535 spike	0.005	420	0.64
dwd6209	1 CA zr, stubby, melt incls, sl. etched, ET535	0.0031	757	0.65
dwd6206	1 CA zr, stubby, melt incls, sl. etched, ET535 spike	0.005	771	0.65
dwd6210	1 CA zr, stubby, melt incls, sl. etched, ET535	0.0014	893	0.25
C40 - Dacite dyke				
dwd6201	1 CA zr, ET535	0.0018	426	0.63
dwd6187	1 CA zr, etched, incls, spr	0.0024	355	0.80
dwd6200	1 CA zr, ET535	0.0022	230	0.83
dwd6189	1 CA zr, stubby, incls, unetched, ET535, Hf collected	0.0016	423	0.45
dwd6188	1 CA zr, etched, incls, spr	0.0023	794	0.40
dwd6199	1 CA zr, ET535, Hf collected	0.0023	370	0.65

Table 4.3 (continued)

$^{206}Pb/^{204}Pb$[a]	$^{206}Pb/^{238}U$[b] Age (Ma)	2σ abs	$^{207}Pb/^{235}U$[b] Age (Ma)	2σ abs	$^{207}Pb/^{206}Pb$[b] Age (Ma)	2σ abs	Rho Concordia
1832.57	164.19	0.19	165.06	0.51	177.54	5.74	0.818
2766.73	163.12	0.23	164.91	0.45	190.69	4.43	0.844
4475.07	163.29	0.17	163.89	0.67	172.55	9.33	0.504
3780.12	163.64	0.20	165.08	0.39	185.80	3.61	0.898
18323.30	166.39	0.47	182.61	1.78	398.04	21.23	0.511
1893.82	204.24	0.28	205.76	0.72	223.15	7.06	0.703
1076.81	163.51	0.27	161.76	0.82	136.26	11.03	0.568
4015.59	163.61	0.19	164.01	0.52	169.80	6.44	0.714
4535.69	163.63	0.19	164.81	0.52	181.74	6.30	0.714
2329.98	161.50	0.21	161.44	0.63	160.57	8.10	0.670
1628.92	163.51	0.22	165.89	1.07	199.92	15.16	0.415
2225.12	163.56	0.18	165.27	0.81	189.74	11.00	0.603
606.54	163.68	0.26	162.91	2.41	151.69	34.74	0.725
773.42	163.97	0.22	168.21	0.75	228.27	9.02	0.737
46.87	172.64	3.63	192.53	56.08	443.83	786.55	0.028
6221.87	156.48	0.18	157.34	0.46	170.46	5.92	0.685
7584.71	156.50	0.16	157.13	0.83	166.74	12.58	0.363
4261.53	156.55	0.18	156.98	0.57	163.38	7.81	0.589
2931.87	156.64	0.20	157.06	0.73	163.36	10.18	0.609
3841.56	156.85	0.24	158.11	0.62	177.05	8.20	0.609
5863.14	156.33	0.19	156.78	0.37	163.53	3.63	0.885
8392.12	156.52	0.19	156.73	0.34	159.80	2.93	0.936
5354.31	156.60	0.18	156.92	0.50	161.79	6.50	0.690
3491.92	156.61	0.17	156.86	0.44	160.64	5.44	0.765
10778.09	156.76	0.17	157.14	0.39	162.95	4.58	0.787
2118.53	164.53	0.22	164.57	0.80	165.05	10.76	0.580
910.77	119.68	0.14	117.81	0.50	80.18	8.61	0.786
542.44	123.71	0.20	125.28	0.83	155.14	14.54	0.620
1075.67	128.06	0.19	131.86	1.11	200.99	18.84	0.612
1122.23	137.33	0.19	139.02	1.05	167.95	17.35	0.543
3983.46	137.57	0.20	138.90	0.60	161.77	9.25	0.590
1965.71	153.34	0.21	154.19	0.83	167.33	11.85	0.596

Notes: analyses are ordered from youngest to oldest $^{206}Pb/^{238}U$ age. Weights are based on estimates from microphotographs. Number of grains analysed is at beginning of the "Fraction analysed" column. Abbreviations: CA - chemically abraded, ZR - zircon, INCLS - inclusions, EQ - equant, SPR - short prismatic, LPR - long prismatic, CRK - cracked, FRAG - fragmented, SL – slightly.
Th/U: calculated from radiogenic $^{208}Pb/^{206}Pb$ ratio and $^{206}Pb/^{238}U$ age assuming concordance. PbC: common Pb assuming the isotopic composition of lab blank: $^{206}Pb/^{204}Pb$ - 18.221; $^{207}Pb/^{204}Pb$ - 15.612; $^{208}Pb/^{204}Pb$ - 39.360 (2% error). Uranium decay constants: L238 = 1.55125 * 10^{-4}/Ma, L235 = 938485 * 10^{-4}/Ma (Jaffey et al., 1971). Concordia coordinates: Y = $^{206}Pb/^{238}U$ = EXP(L238 * (206-238 Age)) - 1; X = $^{207}Pb/^{235}U$ = EXP(L235 * (207-235 Age)) - 1. $^{207}Pb/^{206}Pb$ = X/(137.88 * Y); Rho: Error correlation coefficient for concordia coordinates.
a $^{206}Pb/^{204}Pb$ are measured values corrected for fractionation and spike.
b $^{206}Pb/^{238}U$ age, $^{207}Pb/^{235}U$ age and $^{207}Pb/^{206}Pb$ age are corrected for common Pb assuming laboratory blank composition and ^{230}Th disequilibrium assuming a magmatic Th/U of 4.2.

Table 4.4. Summary of LA-MC-ICPMS and ID-TIMS dating.

LA-MC-ICPMS dating				
Group I samples	**Avg Age (Ma)**	**95% conf**	**MSWD**	**N**
T22	162.91	0.73	0.8	12
C64	163.34	0.50	1.7	28
T33	163.79	0.53	1.5	19
C05old	163.60	0.64	0.3	15
C33	164.23	0.90	2.6	15
C66	163.87	0.70	1.6	20
T43	164.28	0.86	2.1	12
C68	164.47	0.61	1.9	20
Avg:	**163.75**	**0.42**	**2.4**	**8**
Group II samples				
C05yng	155.48	0.82	1.6	13
M35	155.86	0.56	1.5	22
M19	156.34	0.33	0.8	35
M29	156.44	0.61	0.6	15
T36	156.05	0.52	1.5	19
Avg:	**156.16**	**0.38**	**1.5**	**5**
Dacite Dyke				
T49	150.64	0.55	1.15	10

ID-TIMS dating				
Group I samples	**Avg Age (Ma)**	**2σ**	**MSWD**	**N**
M18	163.60	0.12	0.3	3
T17	163.67	0.32	3.5	4
C58	163.36	0.61	6.2	3
Avg:	**163.54**	**0.16**	**4.5**	**10**
Group II samples				
M34	156.53	0.16	0.1	4
T36	156.57	0.19	2.9	5
Avg:	**156.56**	**0.10**	**1.7**	**9**
Dacite Dyke				
C40	<119.68	0.14	-	1

Notes: abbreviations: avg - average; old - older zircon population; yng - younger zircon population; conf - confidence; MSWD - Mean square weighted deviation.

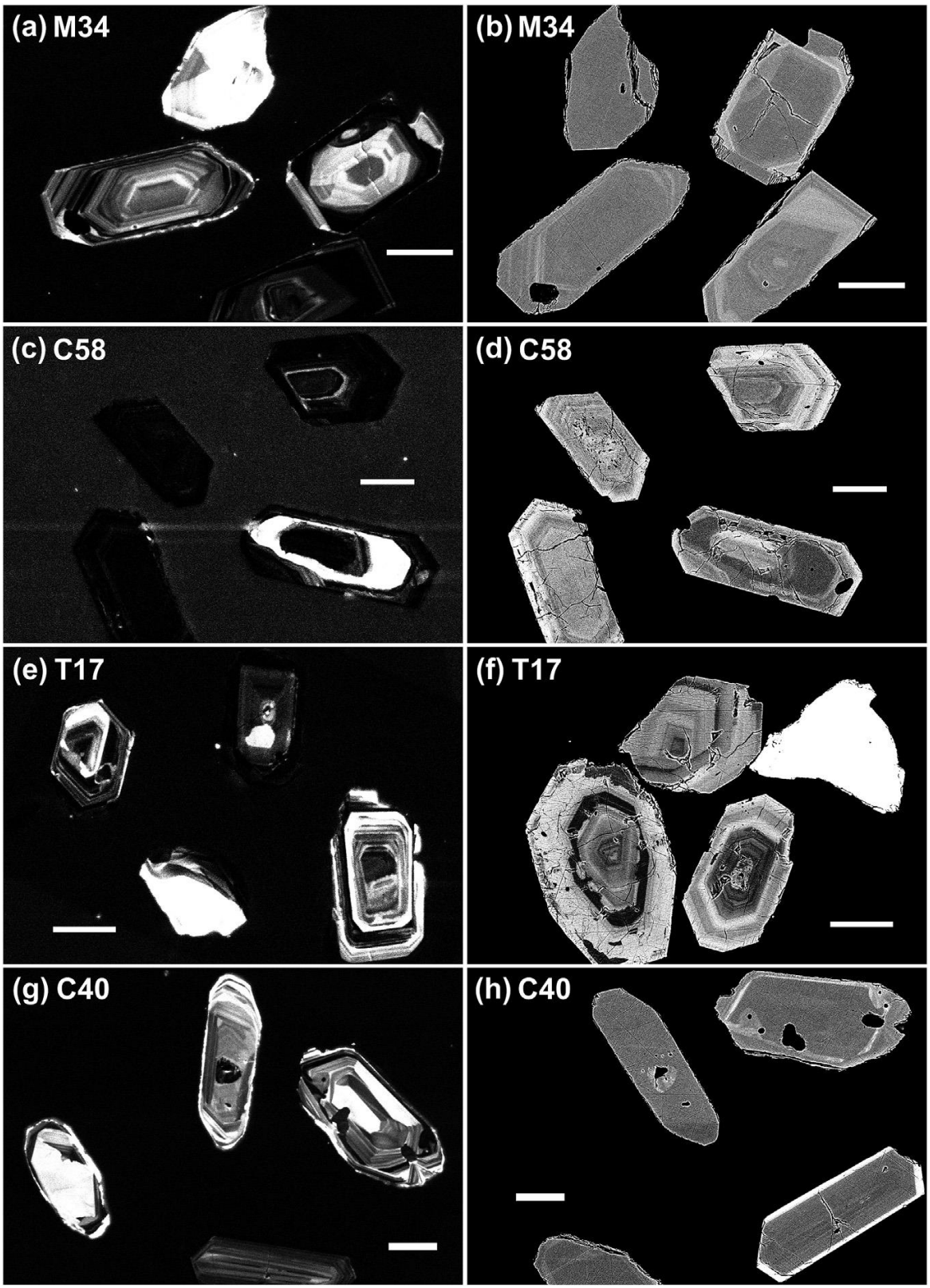

Fig. 4.6. Backscattered Electron (BSE) and cathodoluminescence (CL) images of representative zircons from Macao samples analysed by ID-TIMS. The scale bar represents 50 μm.

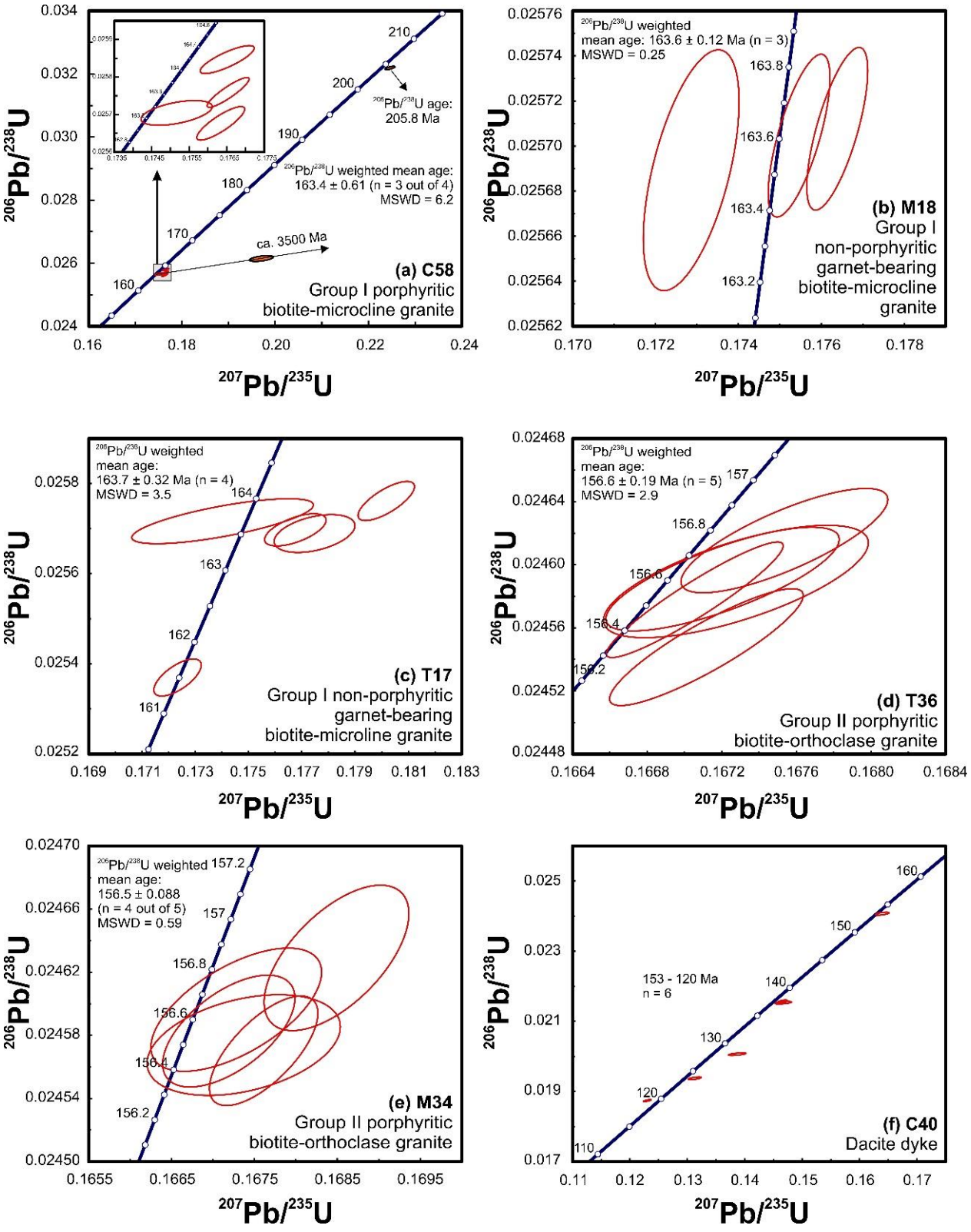

Fig. 4.7. Zircon U–Pb concordia diagrams for Macao samples dated by ID-TIMS: (a–e) granites and (f) dacite dyke.

4.4.4. LA-MC-ICPMS geochronology

Thirteen samples were analysed for U–Pb zircon geochronology using the LA-MC-ICPMS method (Table 4.4 and Supplementary File 4, Fig. 4.8 and Fig. 4.9; see also Supplementary File 2 for details on the location and general characteristics of the analysed samples). Off- line data reduction was performed by the software ICPMSDataCal. Version 8.0 (Liu et al., 2009). No common Pb has been corrected. All reported ages were calculated using the Isoplot program (Ludwig, 1998; Ludwig, 2012). Individual analyses in the data table (Supplementary File 4) and concordia plots are presented as 1σ absolute error and uncertainties in average ages are given at the 95% level (2σ). As was done for ID-TIMS results, $^{206}Pb/^{238}U$ ages were calculated and used in the following discussion.

The zircons chosen for these analyses are subhedral to euhedral with pyramidal and prismatic shape, 80–200 mm long, with length- to-width ratios of 2:1 to 5:1. Representative zircon BSE images (Figs. 4.6 and 4.8) show that most grains are internally homogeneous or have oscillatory zoning, which is indicative of a magmatic origin (Rubatto and Gebauer, 2000), with a minority of grains exhibiting inherited cores and magmatic rims.

The zircons of the less fractionated granites (Zr/Hf > 25) are usually transparent, euhedral, colourless to pale yellow in colour. Some appear brownish due to radiation damage from high U content, with the number of this type of grains tending to increase with increasing degree of evolution (e.g. Zr/Hf ratio). These metamict zircons generally have a lower refractive index compared with non-damaged zircons. Some of the most fractionated samples (Zr/Hf ≤ 25) still preserve a small population of fresh zircons that could provide crystallization age results, while others could not be dated as the whole population of zircon grains was altered and therefore subject to significant Pb loss. Many zircons from these highly fractionated samples have mineral inclusions, such as REE phosphate phases and calcite (see Supplementary File 3 for more details), which were avoided to prevent inaccurate age results.

The zircon U–Pb ages obtained by LA-MC-ICPMS for the granitic rocks are presented in detail in Supplementary File 4 and summarized in Table 4.4. Except for obvious inheritance, they form two groups with average ages of 163.8 ± 0.4 Ma and 156.2 ± 0.4 Ma. Sample C05 (Fig. 4.9a) seems to contain two populations of zircons representative of each of those two periods. The Taipa

dacite dyke yields a relatively young age of ~150 Ma, although still older than the Coloane dacite dyke dated by ID-TIMS (<119.68 ± 0.14 Ma, Fig. 4.7f).

Although most of the zircon grains crystallized from granitic magmas, some of the grains revealed inheritance (see Fig. 4.9). The oldest concordant inherited age obtained was 2407 Ma (Paleo-Proterozoic), although several more recent Proterozoic and Paleozoic concordant ages were also obtained.

To verify the agreement between ID-TIMS and LA-MC-ICPMS data, sample T36 was dated by both methods yielding similar ages within error (156.05 ± 0.52 Ma for LA-MC-ICPMS and 156.6 ± 0.19 Ma for ID-TIMS).

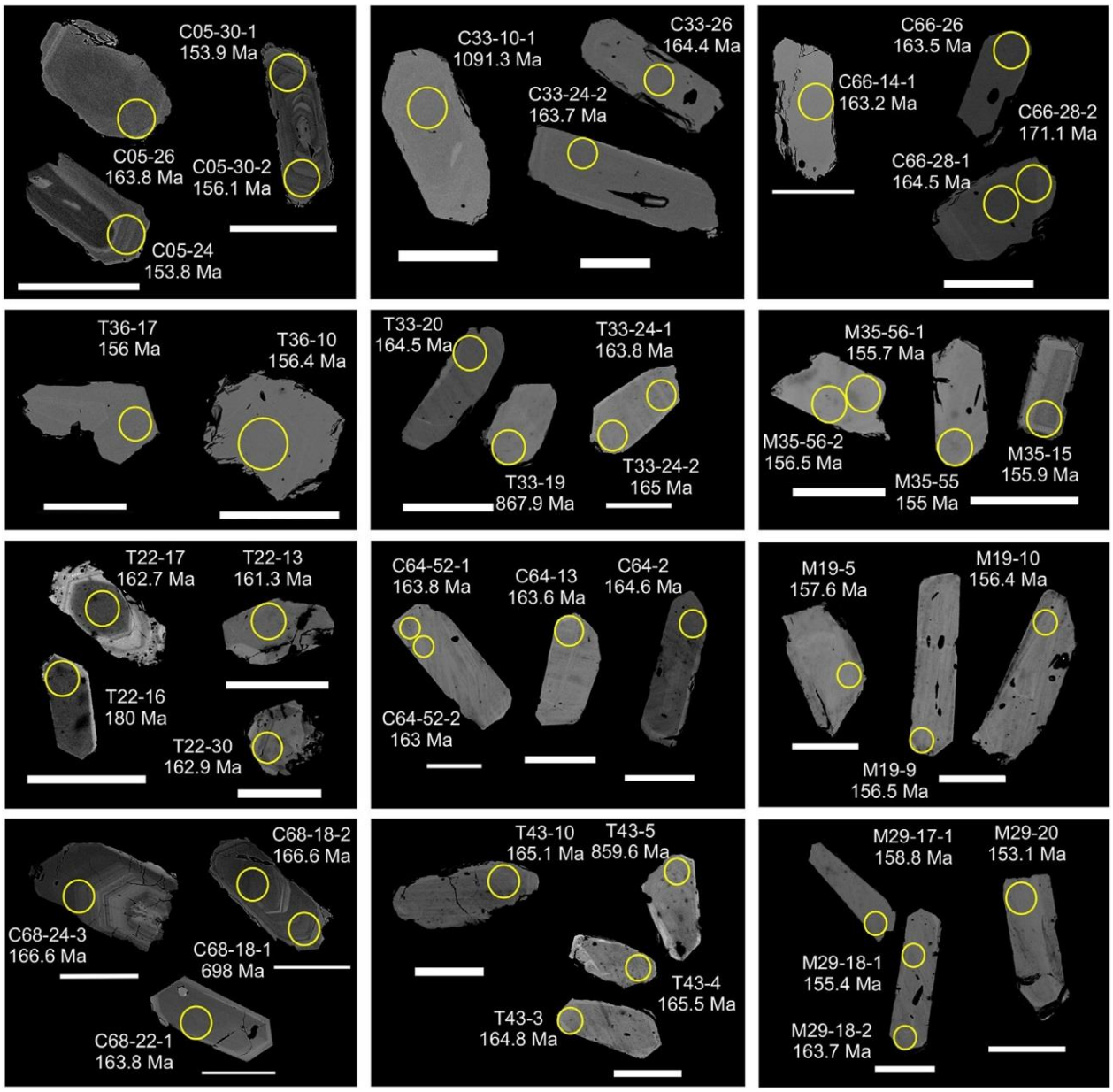

Fig. 4.8. Backscattered Electron (BSE) images of representative zircons from Macao samples analysed with LA-MC-ICPMS. The yellow circles represent the laser spot, the corresponding age also being shown. The scale bar represents 100 µm.

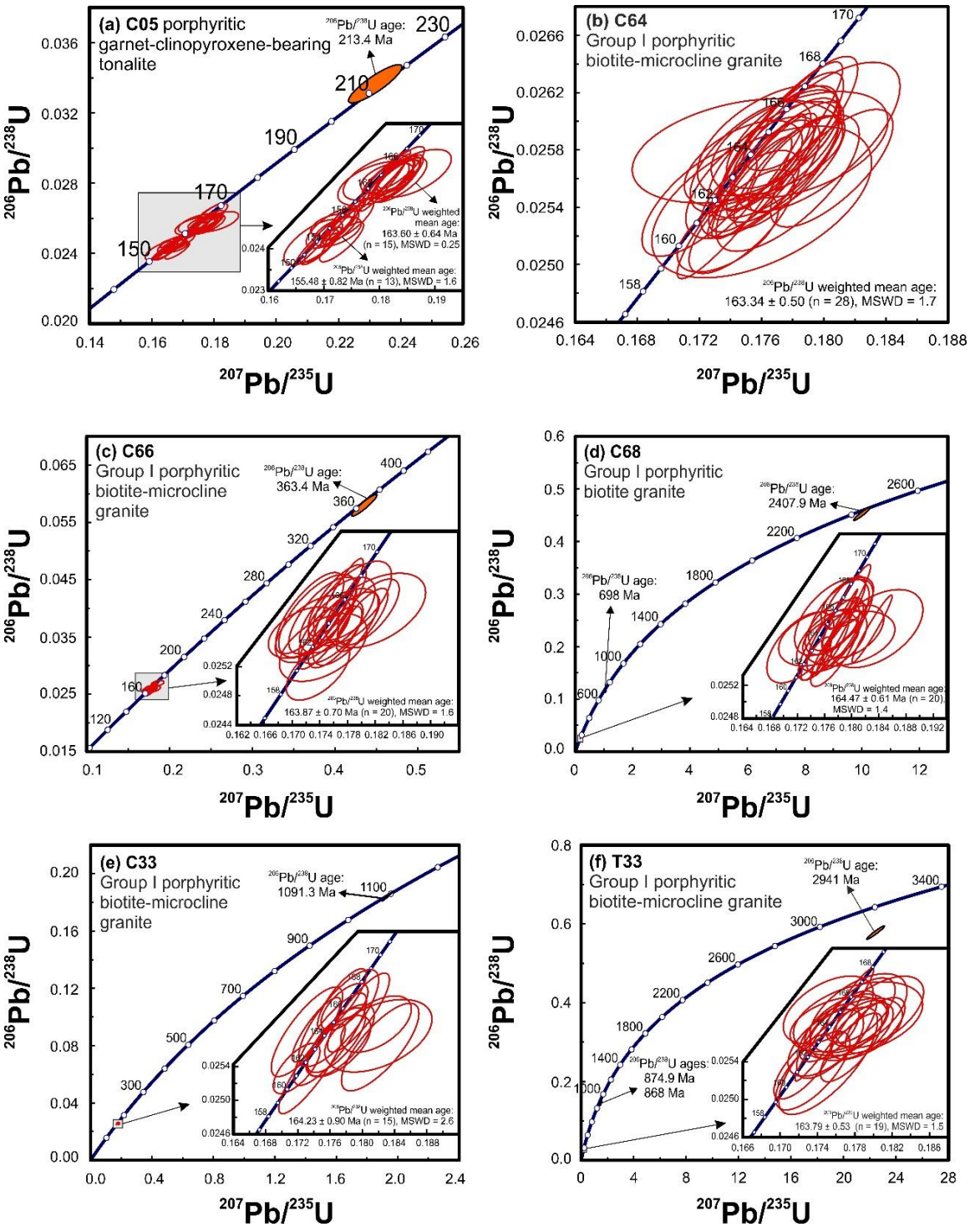
(a) C05 porphyritic garnet-clinopyroxene-bearing tonalite
(b) C64 Group I porphyritic biotite-microcline granite
(c) C66 Group I porphyritic biotite-microcline granite
(d) C68 Group I porphyritic biotite granite
(e) C33 Group I porphyritic biotite-microcline granite
(f) T33 Group I porphyritic biotite-microcline granite
$^{206}Pb/^{238}U$
$^{207}Pb/^{235}U$
$^{206}Pb/^{238}U$ weighted mean age: 163.34 ± 0.50 (n = 28), MSWD = 1.7
$^{206}Pb/^{238}U$ weighted mean age: 163.60 ± 0.64 Ma (n = 15), MSWD = 0.25
$^{207}Pb/^{235}U$ weighted mean age: 155.48 ± 0.82 Ma (n = 13), MSWD = 1.6
$^{206}Pb/^{238}U$ weighted mean age: 163.87 ± 0.70 Ma (n = 20), MSWD = 1.6
$^{207}Pb/^{235}U$ weighted mean age: 164.47 ± 0.61 Ma (n = 20), MSWD = 1.4
$^{207}Pb/^{235}U$ weighted mean age: 164.23 ± 0.90 Ma (n = 15), MSWD = 2.6
$^{207}Pb/^{235}U$ weighted mean age: 163.79 ± 0.53 (n = 19), MSWD = 1.5

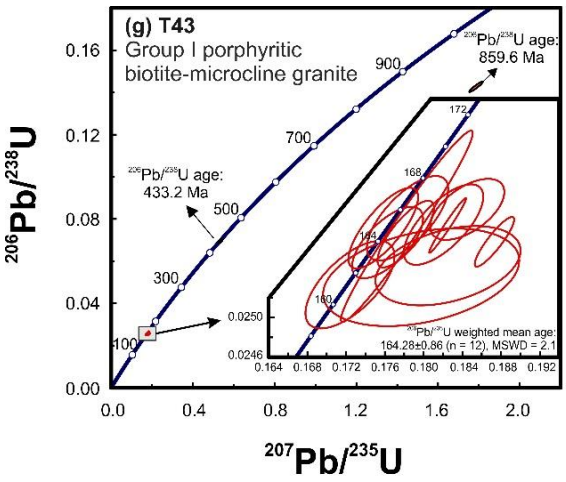
(g) T43
Group I porphyritic
biotite-microcline granite
206Pb/238U age:
859.6 Ma
206Pb/238U age:
433.2 Ma
207Pb/235U weighted mean age:
164.28±0.86 (n = 12), MSWD = 2.1
206Pb/238U
207Pb/235U

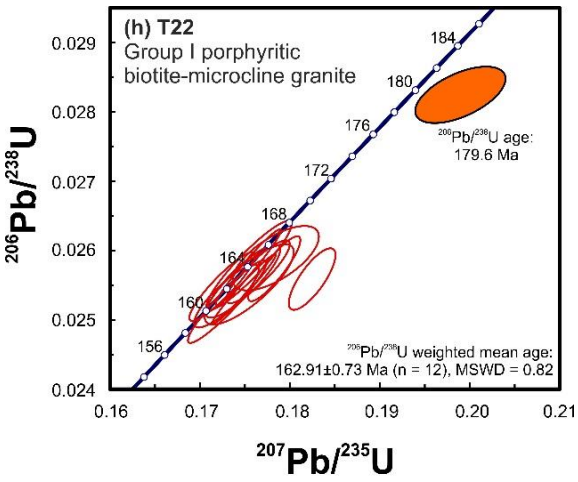
(h) T22
Group I porphyritic
biotite-microcline granite
206Pb/238U age:
179.6 Ma
206Pb/238U weighted mean age:
162.91±0.73 Ma (n = 12), MSWD = 0.82
206Pb/238U
207Pb/235U

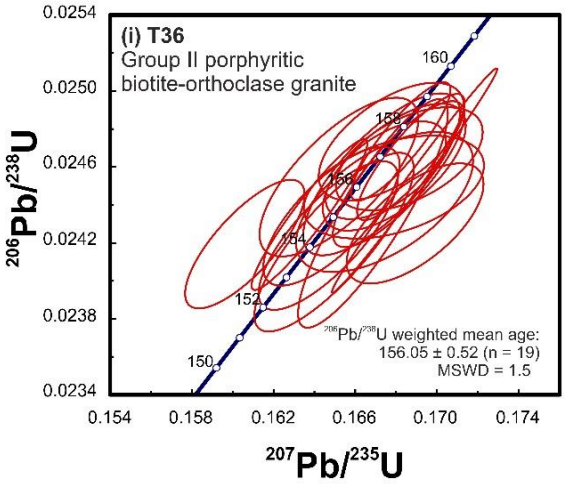
(i) T36
Group II porphyritic
biotite-orthoclase granite
206Pb/238U weighted mean age:
156.05 ± 0.52 (n = 19)
MSWD = 1.5
206Pb/238U
207Pb/235U

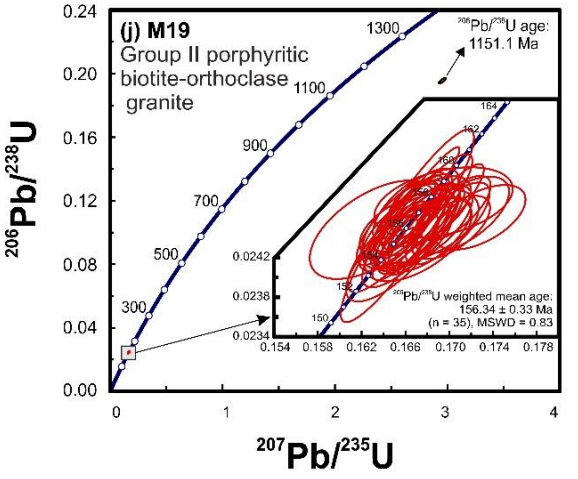
(j) M19
Group II porphyritic
biotite-orthoclase granite
206Pb/238U age:
1151.1 Ma
206Pb/238U weighted mean age:
156.34 ± 0.33 Ma
(n = 35), MSWD = 0.83
206Pb/238U
207Pb/235U

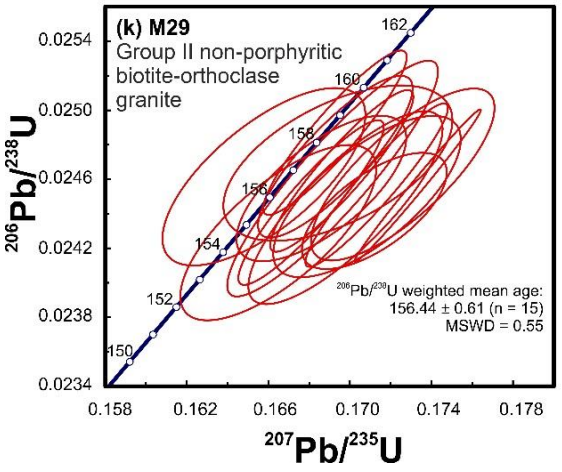
(k) M29
Group II non-porphyritic
biotite-orthoclase granite
206Pb/238U weighted mean age:
156.44 ± 0.61 (n = 15)
MSWD = 0.55
206Pb/238U
207Pb/235U

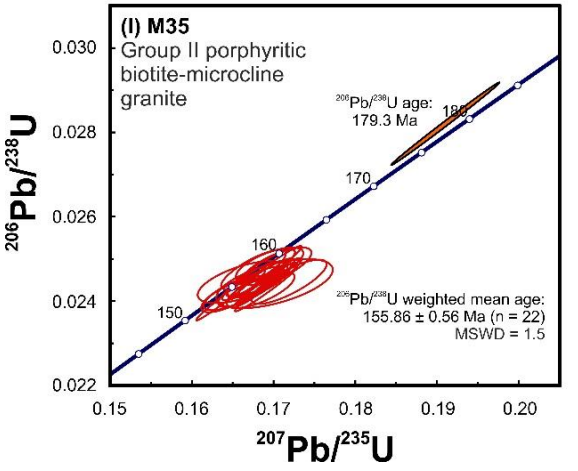
(l) M35
Group II porphyritic
biotite-microcline granite
206Pb/238U age:
179.3 Ma
206Pb/238U weighted mean age:
155.86 ± 0.56 Ma (n = 22)
MSWD = 1.5
206Pb/238U
207Pb/235U

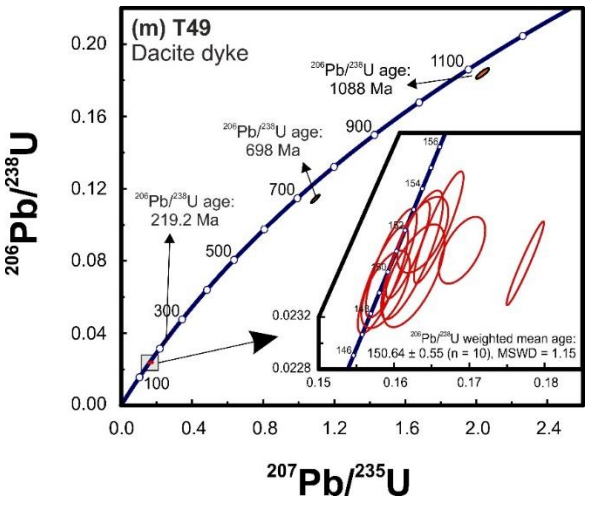

Fig. 4.9. Zircon U–Pb concordia diagrams for Macao samples dated by LA-MC-ICPMS: (a–l) granites and (m) dacite dyke.

4.5. Discussion

4.5.1. Multistage emplacement of Macao granites

The analysed samples provide a robust dataset for geochronological characterization of this region of SE Asia, adding significantly to existing data.

In previous works on the geology of Macao (Ribeiro et al., 1992, 2010), K–Ar Jurassic ages of 154 ± 5 Ma to 168 ± 4 Ma were reported, which are, within error, similar to the ages obtained in this study (see Tables 4.3 and 4.4 and Supplementary File 4). An age of 94 ± 2 Ma was also reported by those authors for one granite from Coloane, which led them to suggest the existence of Upper Cretaceous granites in Macao. Despite the large number of age determinations performed in this study, no age similar to that was obtained.

Although Late Cretaceous magmatism is known to have affected SE China during the second period of the Yanshanian Orogeny (e.g. C.-H. Chen et al., 2008a; Xu et al., 2015; Zhao et al., 2015; Zhao et al., 2016; Q. H. Yan et al., 2017; Zheng et al., 2017), no studies have been found mentioning ~90 Ma granitic rocks outcropping in areas adjacent to Macao. In Hong Kong, the more recent pulse occurred around 140.8 ± 0.6 Ma (Sewell et al., 2012). Moreover, considering that the sample dated by Ribeiro et al. (1992) is a non-porphyritic fine-grained garnet-bearing biotite-microcline granite, with the same petrographic and geochemical characteristics as the highly

fractionated samples of the ca. 163.5 Ma Group I granites from this study, we assume that the 94 ± 2 Ma age results from loss of Ar. In fact, this sample was collected near an important fault zone in the easternmost area of Coloane; such setting may have allowed hydrothermal fluid circulation to damage the biotite from adjacent granites. This age may thus hypothetically indicate the time of an important movement of that fault during the Late Cretaceous. Similar isotope resetting situations have been observed in SE Asia, where granites of now known Jurassic age were previously considered to be Cretaceous using the K/Ar method (Bignell and Snelling, 1977; Beckinsale, 1979; Cobbing, 2000). Taking all these into account, the existence of Cretaceous granites will not be considered in the next discussion, which will be based on U–Pb zircon geochronological analyses.

The U–Pb geochronological data presented in this study allow us to assign distinct ages to the two granite groups (I and II), as initially anticipated on the basis of petrographic characteristics (see section 4.4.1; see also below).

LA-MC-ICPMS average ages of 163.8 ± 0.4 Ma and 156.2 ± 0.4 Ma overlap with the respective ages for groups I and II determined by ID-TIMS: 163.5 ± 0.2 Ma and 156.6 ± 0.1 Ma (see Table 4.4). The individual analyses from LA-MC-ICPMS generally scatter within error of the average. This is not the case for the more precise ID-TIMS data, which shows significant scatter, especially for the Group I zircons. This may be due to the ID-TIMS errors being smaller than the time span for crystallization of zircon within the granitic complexes. Crystallization is unlikely to occur within a magma chamber, but rather within a fluctuating zone of partial melt that may retain small proportions of magma for several million years (Bachmann and Bergantz, 2008; Frazer et al., 2014). A single zircon grain may thus display a range of ages, or zircon that crystallized during an early phase of partial melting may become incorporated into a later phase. Sample C05 contains populations of zircon from Group I and Group II events and was therefore apparently subject to crystallization during both. The earliest Group I magmatism appears to have been more susceptible to picking up inheritance than the later Group II magmas.

The exceptionally tightly constrained record of Mesozoic plutonic activity in Macao provided by this study suggests a multistage granite emplacement in this relatively small area. Indeed the results obtained for sixteen samples point to the existence of two periods of granitic emplacement: Group I – 164.5 ± 0.6 Ma to 162.9 ± 0.7 Ma; Group II – 156.6 ± 0.2 Ma to 155.5 ± 0.8 Ma. The average age of eight dated samples from Group I is 163.75 ± 0.42 Ma (MSWD = 2.4) while that of

the four dated samples from Group II is 156.16 ± 0.38 Ma (MSWD = 1.5). The scatter of individual ages suggests that both groups may have been emplaced over a noticeable, although barely resolvable, age range. Probability density plots (Ludwig, 2012) for both groups are shown in Fig. 4.10. These are based on the summation of average ages, not individual U–Pb analyses, so that each sample age has equal slightly older component in Group I and a slightly younger one in Group II. Applying the unmixing algorithm of Sambridge and Compston (1994) using Isoplot, and assuming only two components, yields ages that differ by about 0.9 ± 0.6 Ma for Group I and about 0.35 ± 0.8 Ma for Group II (Fig. 4.10). The estimate for Group II is within error and that for Group I barely outside of error. However, a two-age approximation is likely to give a minimum estimate. Given that each of the pluton ages represents the average of a significant number of measurements, it should be valid to take the difference between the oldest and youngest average age, which is 1.6 ± 0.9 Ma for Group I and 1.1 ± 0.8 Ma for Group II. As these are 2σ errors, the differences are non-zero outside of error. The Group I and II magmatic periods were separated by a much longer, ca. 6 Ma, period of quiescence. Considering that the crystallization of zircons may span 10^4 to 10^6 years in magmatic systems (Charlier et al., 2005; Matzel et al., 2006; Bachman et al., 2007; Memeti et al., 2010; Schoene et al., 2012; Barboni et al., 2013; Keller et al., 2018), it is important to evaluate if the two clusters of dates identified correspond to two geochemically distinct groups of granites. With this purpose, a comparison of some characteristics of rocks of each of those groups is made below.

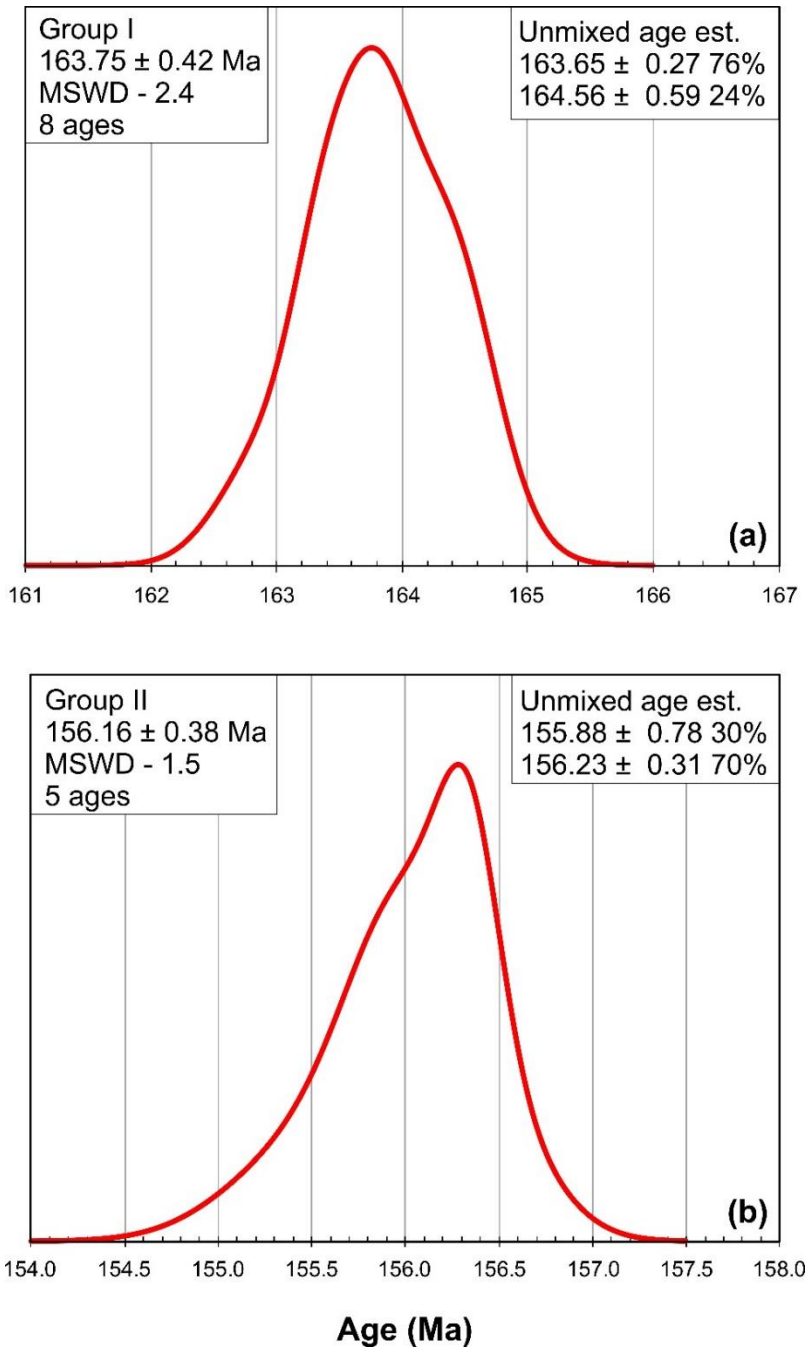

Fig. 4.10. Probability density distributions for: (a) eight zircon ages measured from Group I populations and (b) five ages measured on Group II zircon populations. Also shown are best estimates for unmixing of two ages from each curve as discussed in the text.

The structure of K-feldspar crystals of each group is different. Group I is marked by the presence of microcline (Fig. 4.3a and c) while Group II contains orthoclase (Fig. 4.3e), easily distinguishable in hand specimen by the grey whitish colour of the first as opposed to the pinkish

colour of orthoclase and also, under microscope, by different types of twinning (albite/pericline *vs* Carlsbad, respectively; Fig. 4.3b). While orthoclase is monoclinic and stable at weight. Both populations are somewhat asymmetrical suggesting a temperatures between 500 ºC and 900 ºC, microcline is a triclinic low-temperature K-feldspar stable at temperatures below than 500 ºC (Smith and Brown, 1974; Deer et al., 1992). It is generally accepted that microcline rarely crystallizes directly from magma, and is formed typically by inversion of an earlier monoclinic K-feldspar phase or, in some cases, by ion exchange and recrystallization of sodic plagioclase to microcline ± muscovite (Smith and Brown, 1974; Blasi et al., 1984; Collins, 2000). Since no evidence for pervasive K-metasomatic processes in the studied samples of Group I granites was found, the last hypothesis is unlikely. The ordering of K-feldspars can be linked to the cooling rates of magmas (e.g. Horvat, 2011), which could suggest a slower cooling rate for Group I relatively to the later Group II magmas thus providing temporal conditions for the inversion of monoclinic K-feldspar (orthoclase) to triclinic K-feldspar (microcline). However, considering that both groups occur in a small area (30 km^2) at similar altitude, it is probable that they were emplaced at identical depths. This and the fact that Group I granites are only ca. 6 Ma older than Group II granites, makes difficult that magmas from Group II could have cooled much faster than those of Group I. As reported above (see section 4.4.1), Group I granites are clearly more deformed than Group II granites, suggesting that, in Macao, deformation acted as an external mechanism in the monoclinic-triclinic transition, as proposed, for example, by Bell and Johnson (1989) and Vernon and Paterson (2002) for microcline occurrences elsewhere. Subtle differences can also be identified in the accessory phases. Titanite is an abundant accessory phase in Group II granites, occurring as well-developed euhedral lozenge-shaped crystals (Fig. 4.3f), but tends to be rare and poorly developed in Group I. With increasing degree of differentiation, the porphyritic character tends to become less prominent in both groups until it is totally unrecognizable in the most fractionated rocks (fine-grained granites and microgranite and aplite dykes). However, the highly fractionated granites of Group I are marked by the presence of spessartine-rich garnet as accessory mineral (Fig. 4.3d), which is absent in Group II granites.

The MME of the two groups also differ in texture and mineralogy. MME in Group I granites (Fig.4.3h and i) usually have bigger dimensions (up to 1 m in diameter), granodiorite composition, acicular biotite and no accessory titanite. MME in Group II granites (Fig. 4.3j and k) on the other

hand, have smaller dimensions (centimetre to decimetre-wide), quartz monzodioritic compositions, lozenge-shaped biotite, abundant titanite and in some cases hornblende.

Biotite is the dominant ferromagnesian mineral in Macao granitic rocks. Although the chemical compositions of biotites from both groups overlap for most elements, differences can be observed for specific elements such as Mg (Fig. 4.4c), Ti (Fig. 4.4d) and Al (Fig. 4.4a and d). Apart from some Mn-rich biotite flakes (Fig. 4.4c), the biotites from Group I granites have Mg = 0.08–1.69 apfu, Ti = 0.11–0.40 apfu and Al^{vi} = 0.30–1.34 apfu, whereas those from Group II granites are characterized by comparatively higher Mg = 1.36–2.22 apfu, higher Ti = 0.31–0.5 apfu and lower Al^{vi} < 0.48 apfu. The higher Ti contents of biotites from Group II granites (Fig. 4.4d) are consistent with more abundant and well-developed titanite in these rocks. Considering the biotite tendency to reflect magmatic physico-chemical conditions (e.g. Wones and Eugster, 1965; Nachit et al., 1985; Abdel-Rahman, 1994; Nachit et al., 2005; Bónová et al., 2010; Esmaeily et al., 2013), the chemistry of biotites from the studied samples reinforces the existence of two chemically distinct groups.

REE whole-rock compositions of different lithofacies from the two groups follow different evolutionary trends with increasing differentiation, suggesting distinct fractional crystallization paths. Though the less fractionated types of both groups display moderately fractionated REE patterns [$(La/Yb)_N$ = 2.41–10.76] and Eu negative anomalies (Fig. 4.5a and c), the REE patterns of the highly fractionated types clearly differ. In Group I (Fig. 4.5b) the REE patterns are flat to slightly upward [$(La/Yb)_N$ = 0.12–1.2] and have well-pronounced Eu anomalies (Eu/Eu* = 0.02–0.19), with some samples showing evidence for the M-type tetrad effect ($TE_{1,3}$ up to 1.13) as defined by Irber (1999) (see also footnotes of Table 4.2). The flat shape of Group I REE patterns suggests fractionation of light REE-bearing phases such as allanite and monazite. On the other hand, Group II (Fig. 4.5d) REE patterns are concave upwards with comparatively smaller Eu anomalies (Eu/Eu* = 0.23–0.54) and are characterized by the absence of the tetrad effect. The concave upwards shape of Group II REE patterns could be achieved through higher fractionation percentages of middle REE-compatible minerals such as apatite and/or titanite. The two groups also show distinguishable evolutionary trends on diagrams involving ratios between REE (Fig. 4.11).

In conclusion, the mineralogical and whole-rock geochemical characteristics support the existence of two chemically distinct groups of granites in Macao, which, judging by the ages presented in this study, were emplaced in two pulses during the Upper Jurassic.

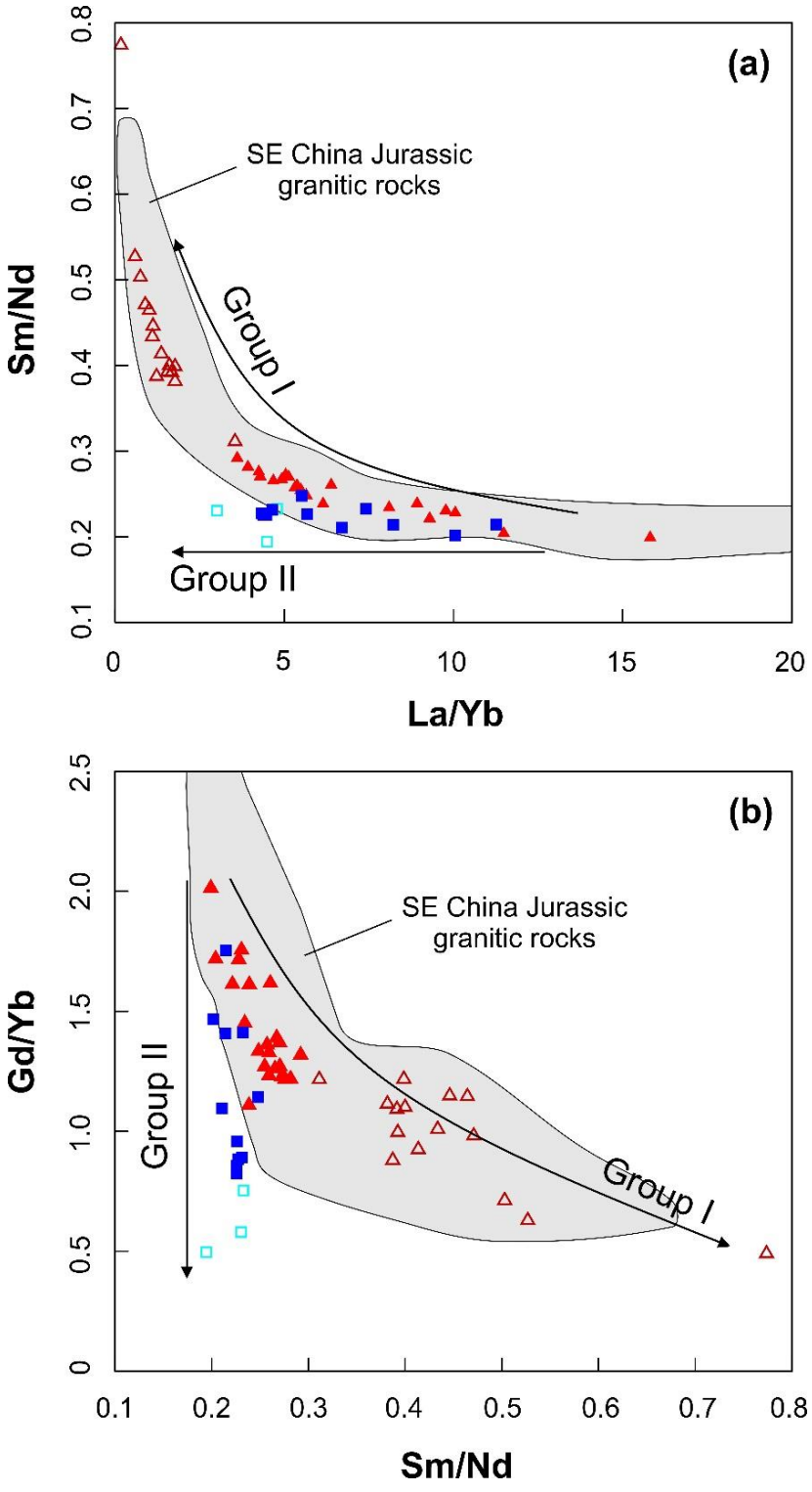
(a)
SE China Jurassic
granitic rocks
Group I
Group II
Sm/Nd
La/Yb
0.1
0.2
0.3
0.4
0.5
0.6
0.7
0.8
0
5
10
15
20
(b)
SE China Jurassic
granitic rocks
Group II
Group I
Gd/Yb
Sm/Nd
0
0.5
1.0
1.5
2.0
2.5
0.1
0.2
0.3
0.4
0.5
0.6
0.7
0.8

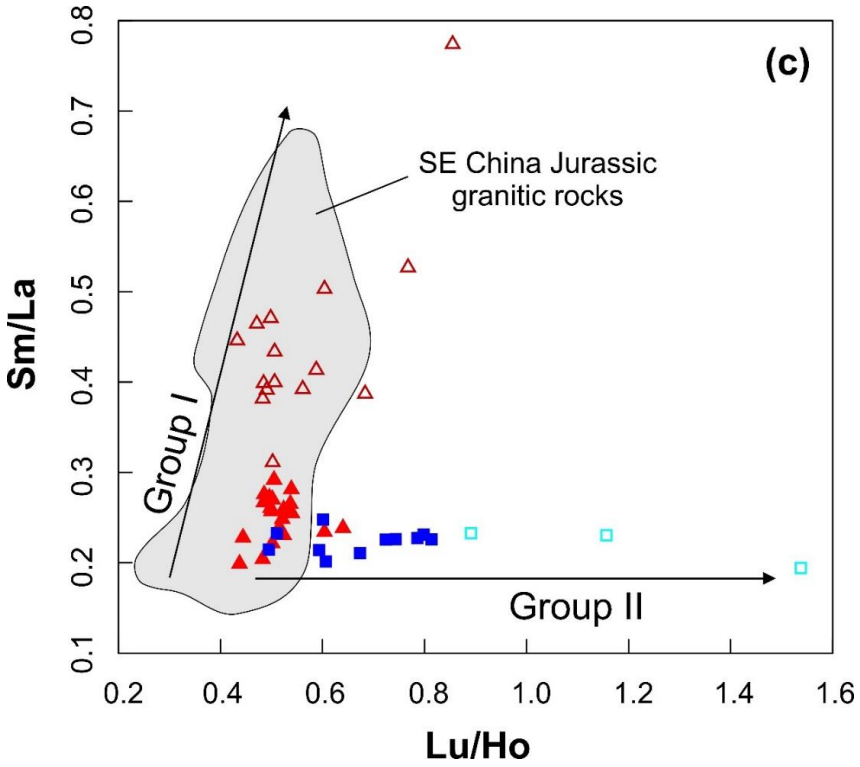

Fig. 4.11. REE ratios variation diagrams for the Macao granites. (a) Sm/Nd *vs* La/Yb; (b) Gd/Yb *vs* Sm/Nd; (c) Sm/La *vs* Lu/Ho. Arrows represent the distinct evolutionary trends followed by the two groups. The gray area contains data from Jurassic (160e150 Ma) granitic rocks from SE China (Li et al., 2007; Huang et al., 2012; Huang et al., 2015; Y. Zhang et al., 2015; Qiu et al., 2016; Jiang and Zhu, 2017; Zhang et al., 2017; Jiang et al., 2018).

4.5.2. Inheritance ages

The age spectra for inherited zircons from granites can be a useful tool to obtain insights on the age of potential protoliths (Keay et al., 1999). However, the number of analyses of inherited zircon grains in the present study was not sufficient to identify significant inherited age populations. This is in part due to the fact that most of the Macao granites are metaluminous to weakly peraluminous (A/CNK = 0.96–1.13), which are typically inheritance-poor, in contrast with what has been usually observed for highly peraluminous granites (Miller et al., 2003; Miller et al., 2007; see also Watson and Harrison, 1983). Moreover, many of the zircon grains were strongly altered (see sections 4.3.2.2 and 4.3.2.3) and consequently the achievement of accurate results was not possible in these cases.

Most of analysed inherited zircon grains or cores were extracted from Group I granites, while samples from Group II contain little or no inheritance making it impossible to draw conclusions on

the differences of the involved magmatic sources in both periods. Zircon inheritance ages obtained from both methodologies suggest a wide range of Phanerozoic and Precambrian sources (Fig. 4.12). Since long-lived felsic magmatic systems may be highly complex, made up of several inputs of magma, not all such zircon crystals in a particular rock need have crystallized from the same pulse or increment of melt (Miller et al., 2007). Thus, the occurrence of antecrysts, that were crystallized from an earlier magmatic pulse and were later incorporated in a subsequent pulse(s), is common in these magmatic systems. This is probably the case for the range of inherited ages between 165–180Ma (see Supplementary File 4 and Fig. 4.12). Many of the older inherited grains (>180 Ma) are probably xenocrystic in origin, belonging to wall rock assimilated during ascent and emplacement of the granitic magmas, or representing residual zircons inherited from the magma source. The oldest concordant inherited age found in this study is a $^{206}Pb/^{238}U$ age of 2407 Ma, suggesting that the source of the Macao granites might be as old as Paleo-Proterozoic. However, a less concordant (91%) $^{206}Pb/^{238}U$ age of 2941 Ma obtained for sample T33 means that an Archean component cannot be ruled out. This is in agreement with studies on crustal xenoliths and zircon xenocrysts entrained in Mesozoic and Cenozoic volcanic rocks from neighbouring areas, suggesting the existence of a highly evolved Archean to Paleoproterozoic basement beneath the western Cathaysia Block (Zheng et al., 2011; Li et al., 2018).

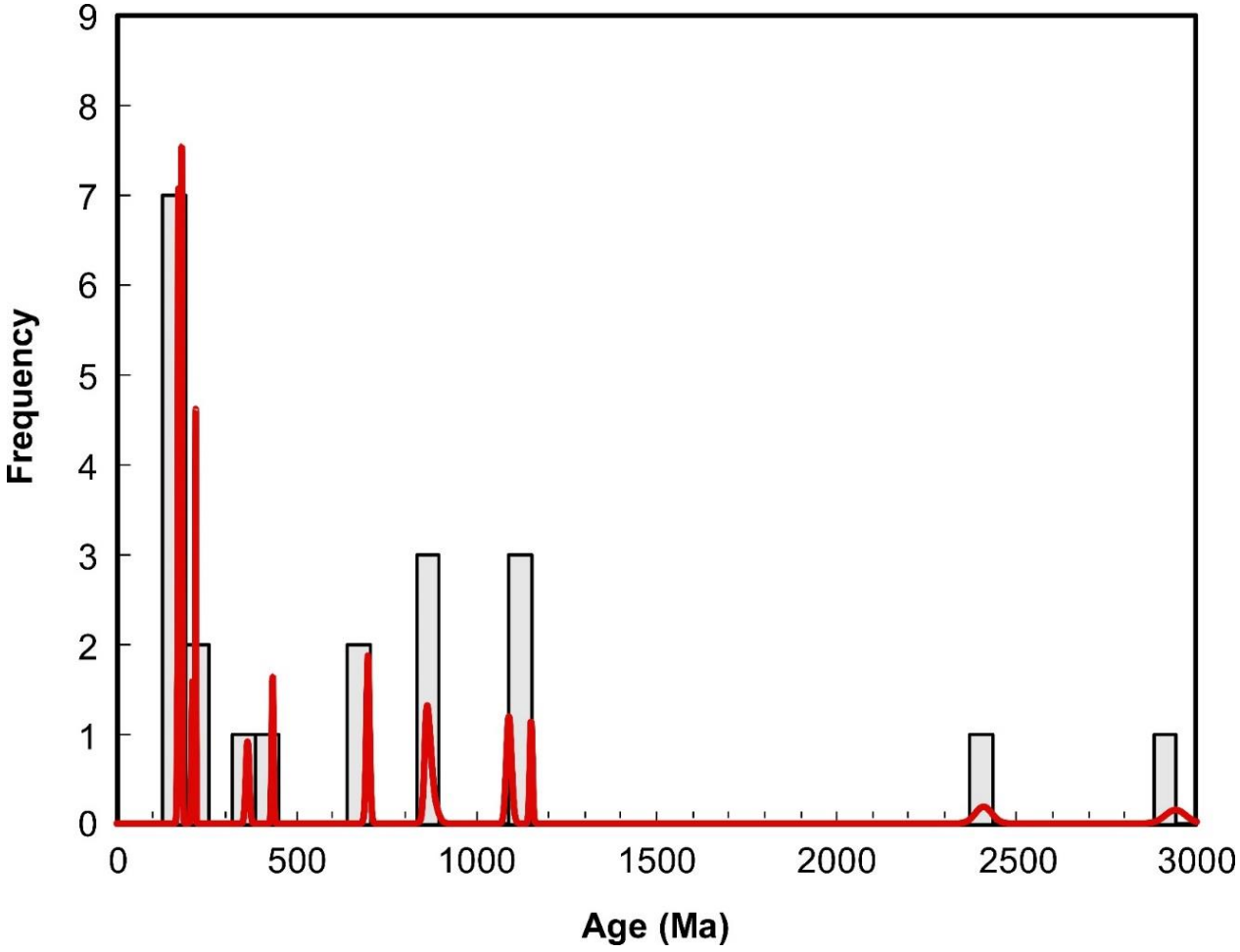

Fig. 4.12. Frequency plot of inherited ages of zircons from the Macao magmatic rocks.

4.5.3. Macao granitic magmatism in the SE China context

It is well known that a major magmatic event took place in a vast area of SE China between 165 and 140 Ma (e.g. Sewell et al., 1992; Zhou and Li, 2000; Li et al., 2004; Li et al., 2007; Guo et al., 2012; Huang et al., 2012; Y. Zhang et al., 2015; Chen et al., 2017). Among the igneous rocks formed during this time span, strongly metaluminous to weakly-peraluminous biotite monzogranites are predominant (e.g. Sewell et al., 1992; Li et al., 2007; Huang et al., 2012; Y. Zhang et al., 2015), associated with minor gabbros, basalts, syenites, peraluminous granites and A-type granites (e.g. X.-H. Li et al., 2003; Li et al., 2004; Li et al., 2007; Xu et al., 2007a; Y. Wang et al., 2008; He et al., 2010; Meng et al., 2012; Zhang et al., 2017). On the other hand, high precision U–Pb zircon ages published for the neighbouring region of Hong Kong (Sewell et al., 2012; see

also Sewell et al., 1992) enabled the identification of four main magmatic pulses: (1) 165–160 Ma (Lamma Suite); (2) 148–146 Ma (Kwai Chung Suite); (3) 143 Ma (Cheung Chau Suite) and; (4) 141 Ma (Lion Rock Suite). Based on inherited zircon ages from subsequent Hong Kong pulses and a date from a rhyolite dyke, Sewell et al. (2012) suggested the existence of a more localized magmatic event in Hong Kong region ca. 152 Ma ago.

This study demonstrates that granitic magmatism in the Macao territory, some 50 km from Hong Kong,was emplaced as two pulses occurring between 164.5 ± 0.6 Ma and 162.9 ± 0.7 Ma (Group I) and between 156.6 ± 0.2 Ma and 155.5 ± 0.8 Ma (Group II). These two periods of granitic magmatism in Macao can be integrated into the major magmatic event recorded in SE China (see above), the Group I granites being coeval with the Lamma Suite of Hong Kong, whereas no counterparts of the Group II have been identified (see Fig. 4.13). Our data for the Macao Group II granites indicate the occurrence in the Pearl River Delta region (southern coast of Guangdong province) of another granitic pulse in addition to those proposed by Swell et al. (2012) based on the study of the Hong Kong region.

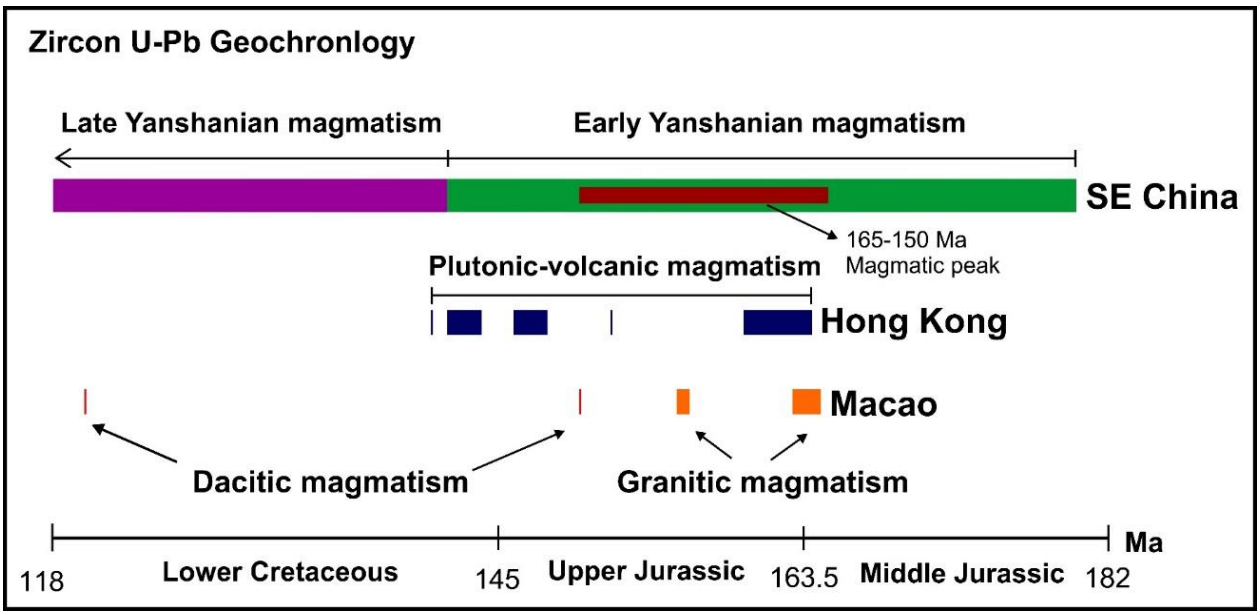

Fig. 4.13. Scheme showing the timing of magmatic pulses in Macao (this study) and Hong Kong (Sewell et al., 2012) territories, plus the Early and Late Yanshanian periods (Zhou et al., 2006) and the 160–150 Ma magmatic peak in SE China (Li et al., 2007; Huang et al., 2012; Huang et al., 2015; Y. Zhang et al., 2015; Qiu et al., 2016; Jiang and Zhu, 2017; Zhang et al., 2017; Jiang et al., 2018).

Considering the existence in Macao of two distinct but proximal granitic pulses spanning about 9 Ma, we suggest that the Macao granitic suite was incrementally assembled, as proposed by Coleman et al. (2004) for a Californian intrusive suite (see also Glazner et al., 2004; Annen, 2011; Menand et al., 2015). Such incremental growth of granitic plutonism in the region is also shown time for approximately 24 Ma.

It is noteworthy that the Macao Jurassic granites are mostly biotite monzogranites as in other areas of SE China. In this study, key differences in petrography, mineralogy and geochemistry have been shown to exist between the two pulses. This suggests that the same type of temporal-related mineralogical and chemical variations may exist in other granitic regions of SE China. The knowledge of such variations could help correlate different areas and constrain the spatial-temporal distribution of individual magma pulses on a regional scale. The understanding of the petrogenetic causes of such differences might yield important clues to better explain the still controversial Jurassic–Cretaceous granitic magmatism in the Cathaysia Block (SE China).

However, we emphasize that most of the studies have regarded these rocks as the result of a single magmatic event rather than discrete pulses with distinct compositional characteristics (e.g. Li et al., 2007; Huang et al., 2012; Huang et al., 2015; Y. Zhang et al., 2015; Qiu et al., 2016; Jiang and Zhu, 2017; Zhang et al., 2017; Jiang et al., 2018). Indeed, a peak of magmatic activity in SE China took place around 165–150 Ma during the Early Yanshanian Orogeny (Fig. 4.13; Zhou et al., 2006; Li et al., 2007). When comparing REE data of the Macao granites with Jurassic granites (165–150 Ma) from nearby areas in SE China, it is clear that the Macao Group I granites and the SE China granites follow a similar evolutionary trend (Fig. 4.11). In contrast, the Macao Group II granites follow a distinct evolutionary path marked by relatively constant Sm/Nd ratios and increasing Lu/Ho ratios (Fig. 4.11c). Therefore, either the latter group has not been identified in other areas of SE China or it may represent a more localized magmatic pulse, which outcrops only in Macao and possibly in its close surroundings. However, regarding ages, both groups fall within the Jurassic magmatic peak (Fig. 4.13), and therefore are likely to have been formed in the same tectonic setting. We thus propose that, rather than a significant change in tectonic setting, the observed petrographic and compositional differences between Group I and Group II granites were caused by different magmatic evolution processes.

The ages obtained for dacite dykes (Taipa: 150.64 ± 0.55 Ma; Coloane: <120 Ma) clearly differ from those obtained for the granitic rocks. The Coloane dacite is distinctly younger than the youngest ages obtained in Hong Kong, which date back to around 140 Ma (Davis et al., 1997; Campbell et al., 2007; Sewell et al., 2012a). Despite the fact that most of the magmatic activity in Macao happened during the Early Yanshanian period, the age of the younger dacite dyke indicates that the territory was also affected, though to a lesser extent, by Late Yanshanian magmatism.

It is not a central objective of this paper to discuss the origin of the studied rocks. However, we note that the change in the type of magmatism in Macao from granitic to dacitic is likely to correspond to a change in the regional tectonic regime inducing a significant change on the magma genesis processes. The origin of Jurassic granites in SE China has been associated to an extensional regime coeval with foundering of the subducting Paleo-Pacific plate, leading to asthenosphere upwelling and high crustal geothermal gradients required for granite genesis (e.g. Li et al., 2007; Li and Li, 2007; Huang et al., 2012; Huang et al., 2015; Sewell et al., 2016). On the other hand, the Macao dacite dykes are characterized by high LILE/HFSE ratios [e.g. $(Rb/La)_N$ = 3.8–8.5)] and negative anomalies of Nb, Ta and Ti (Ti/Ti* up to 1.12). Though the dacites may have suffered some degree of crustal contamination as indicated by the presence of inherited zircons, these elemental characteristics are also identical to those characterizing arc-like subduction-related magmas (e.g. Kelemen et al., 2003; Hürlimann et al., 2016). The Macao dacites could thus be evolved products of arc-like magmatism, suggesting reestablishment of a normal subduction system in this area, as it has been proposed for the Early to Late Cretaceous tectonic setting in SE China (e.g. He and Xu, 2012; Meng et al., 2012; Zhu et al., 2014).

4.6. Concluding remarks

(1) Zircon LA-MC-ICPMS and ID-TIMS U–Pb dating results obtained in this study indicate that the Macao region was the locus of multistage magmatism during the Yanshanian Orogeny. Granitic magmatism occurred within approximately 155 and 165 Ma, concentrated between 164.5 ± 0.6 Ma and 162.9 ± 0.7 Ma (Group I) and 156.6 ± 0.2 Ma and 155.5 ± 0.8 Ma (Group II). In addition, dacite dykes cutting granites were dated at 150.6 ± 0.6 Ma and <120 Ma.

(2) Differences in the type of K-feldspar, accessory phases, biotite and whole-rock chemistry and in the mineralogy and textures of the associated MME, suggest that the two age groups

correspond to two distinct pulses of granitic magmatism rather than a continuum of comagmatic activity.

(3) Trace element compositions show that magmas of the two groups evolved in different ways, producing distinct REE evolutionary paths. While Group I magmas seem to have evolved by progressive enrichment in heavy REE relatively to light REE, magmas from Group II are marked by depletion of middle REE leading to progressively concave REE patterns.

(4) Inheritance patterns in the zircon U–Pb data suggest the presence of a population of antecrysts (165–180 Ma) crystallized from earlier magmatic pulses and a population of inherited zircons and/or xenocrysts from Precambrian to Phanerozoic sources incorporated into the magmas during melting and/or ascent/emplacement at crustal levels. The oldest inherited ages (2.4 Ga and possibly 2.9 Ga) suggest contribution of Proterozoic and possibly of late Archaean crustal sources for the Macao magmatism.

(5) The Macao Group II granites clearly indicate the occurrence on the Pearl River Delta region of a magmatic pulse between those at the origin of Lamma Suite (165–160 Ma) and the Kwai Chung Suite (148–146 Ma) in the neighbouring Hong Kong region. In addition, REE ratios suggest that this pulse may only occur in Macao area, while Macao Group I granites show evolving trends of REE ratios similar to those of Jurassic granites outcropping in vast areas of the Cathaysia Block (SE China).

(6) Considering the existence in Macao of two proximal but distinct granitic pulses spanning for a time of ca. 9 Ma and separated by ca. 6 Ma, we suggest that the Macao granitic suite was incrementally assembled, a hypothesis also extendable to the neighbouring Hong Kong region. Given the relatively short time span between the two pulses and the chemical similarity of the less evolved rocks, the observed differences in the evolutionary trends are probably the result of a change in magma evolution processes rather than in tectonic setting, which was dominantly extensional related to the foundering of the subducting Paleo-Pacific plate under the Eurasian plate during the Middle to Upper Jurassic.

(7) Despite Early Yanshanian magmatism being predominant in Macao, the younger ages obtained for the dacite dykes indicate that the territory was affected, to a lesser degree, by Late Yashanian magmatism. The change in the type of magmatism in Macao from granitic to dacitic is likely to correspond to a change in the regional tectonic regime inducing a

significant change in the magma genesis processes. The dacite dykes may testify the reestablishment of a normal subduction system in this area of SE China.

Acknowledgments

This research was supported by the Macao Science and Technology Development Fund (FDCT 043/2014/A1). We also acknowledge the support of FCT (Portugal) through UID/GEO/50019/2013 to Instituto Dom Luiz, Universidade de Lisboa. We are very grateful to Varon Lou (Lou U. Tat) and Ricardo Borges for their important help during the field and lab work and to Pedro Rodrigues for skilled assistance during electron microprobe analyses. We thank the two anonymous reviewers for their thoughtful reviews and constructive comments that greatly improved the manuscript.

Electronic Appendices

Supplementary data to this article can be found online at https://doi.org/10.1016/j.gsf.2019.04.011, Appendix A:

Supplementary File 1. Standards and detection limits of analytical methods.

Supplementary File 2. Location and general characteristics of analysed samples.

Supplementary File 3. Detailed sample description of Macao magmatic rocks dated by ID-TIMS.

Supplementary File 4. LA-MC-ICPMS U–Pb isotopic data on zircon from Macao magmatic rocks.

Chapter 5. Evidence for mixed contribution of mantle, lower and upper crust to the genesis of Jurassic I-type granites from Macao, SE China

---

Submitted as:

Quelhas, P., Dias, Á A., Mata, J. (2019) Evidence for mixed contribution of mantle, lower and upper crust to the genesis of Jurassic I-type granites from Macao, SE China. Lithos. Submitted.

Abstract

The Southeast China Magmatic Belt is characterized by widespread Jurassic to Cretaceous magmatic rocks, consisting mainly of granites and rhyolites and subordinate mafic rocks. However, much controversy has sprung in the past few decades regarding the nature of the source, the involved petrogenetic processes and the tectonic regime(s) of the Jurassic magmatism in this region. This study aims to contribute to the discussion with mineral chemistry, whole-rock elemental and Sr–Nd–Hf–Pb isotopic geochemical data of Jurassic granitic rocks and microgranular mafic enclaves (MME) from Macao, Southeast (SE) China. The granitic rocks of Macao consist of two groups of biotite granites with distinct ages (MGI and MGII), which are high-K calc-alkaline metaluminous to weakly peraluminous I-type granites with variable degrees of fractionation. Fractional crystallization played an important role in the evolution of the Macao granites, though the fractionation paths differ for the highly fractionated facies of both groups mainly due to distinct accessory fractionating phases. In addition, MGI highly fractionated granites are marked by distinct elemental signatures suggesting late-stage melt/fluid interaction involving F-rich fluids. Moreover, significant differences in isotopic composition were observed, with the MGII being characterized by a much narrow range of initial $^{87}Sr/^{86}Sr$ ratios and $\varepsilon_{Nd}(t)$ and $\varepsilon_{Hf}(t)$ values than MGI. Based on these differences, the MGII granites are considered a comagmatic suite having evolved in closed system, contrasting with what can be inferred for MGI. The increase in initial $^{87}Sr/^{86}Sr$ ratios with degree of evolution, presence of metasedimentary enclaves and high percentage of inherited zircon with Paleozoic ages in MGI suggest the occurrence of an assimilation fractionation crystallization (AFC) process. The observed decoupling of Sr and Nd and Hf isotope systems might have resulted from magma mixing, which caused the homogenization of Sr isotope ratios but not of the Nd and Hf isotopes. Isotope and major element compositions together with model ages strongly suggest that Macao granitic magmas were generated by partial melting of infracrustal medium-to-high K basaltic Paleo-Proterozoic to Mesoproterozoic protoliths heated by, and mixed to some degrees with, the contemporaneous underplating and/or intrusion of hot, mantle-derived magmas. The Jurassic Macao and SE China granites are interpreted as being generated in an intraplate extensional setting related to the foundering of a previous flat-slab (Paleo-Pacific plate) beneath SE China.

Keywords: I-type granites; Jurassic; Yanshanian Orogeny; Macao (South China); Cathaysia Block; Crustal assimilation

5.1. Introduction

Granitic rocks are considered the building blocks of the continental crust. In the last decades, much research on granites has focused on their applicability to unravel source regions, petrogenetic processes and crustal evolution (e.g. Kemp and Hawkesworth, 2003). Some authors suggest that most of the chemical variation within granitic bodies is a primary or near-source feature, reflecting the constraints imposed to magmas by source composition, incongruent melting and peritetic minerals (e.g. Clemens et al., 2011). The importance of the source composition is also emphasized by the genetic classification of Chappell and White (1992), which considers two broad categories: I-type granites, derived from igneous or infracrustal protoliths, and S-type granites, originated by anatexis of sedimentary or supracrustal protoliths.

However, magma evolution processes such as mingling/mixing between crustal and mantle-derived magmas, crustal assimilation and late-stage fluid/melt interaction can significantly alter the elemental and isotopic composition of the magmas. In addition, highly evolved granitic magmas tend to converge towards near minimum-temperature melt compositions (King et al., 1997), no longer reflecting the mineralogical and chemical features of their primary magmas. Because of these, the assignment of granites to one of the S-I-A-M genetic groups (Chappell and White, 1992) can be ambiguous and the extent to which the compositional features of granitic rocks reflect those of the source rocks remains a matter of intense debate.

Macao is located along the coast of Southeast (SE) China, being part of the Cathaysia Block (Fig. 5.1). Most of the rocks outcropping in Macao are granites of Jurassic age formed during the Yanshanian Orogeny (Quelhas et al., 2019). Despite being generally consensual that the Yanshanian Orogeny took place in response to the northwestern-ward subduction of the Paleo-Pacific plate under the Eurasian plate (e.g. Zhou et al., 2006), the details are still intensely debated leading to the proposition of different tectonic models (e.g. Lapierre et al., 1997; Zhou and Li, 2000; Li and Li, 2007; Jiang et al., 2009). Morevover, the widespread occurrence of different types of granites (I-, S- and A-types) and associated intermediate to mafic rocks and their spatial-temporal distribution across SE China, has aroused controversy regarding the nature and variability of the source rocks. Some studies have proposed the contribution of mantle-derived magmas for the genesis of Yanshanian granites (Liu et al., 2013; Y. Zhang et al., 2015), though it is not always clear at which extent they contributed to the geochemical variability of these rocks. The same yields

true for other magmatic evolution processes such as crustal assimilation and late-stage fluid/melt and/or fluid/rock interactions.

Most studies of Yanshanian granitic rocks in SE China have been carried out on large batholith areas, often lacking detailed small-scale variation of the plutonic bodies. A recent study demonstrated the existence at Macao of two Jurassic granitic pulses characterized by distinct mineralogical and geochemical characteristics. Additionally, younger dacite dykes also occur with ages up to Lower Cretaceous (Quelhas et al., 2019), pointing to the occurrence of a less important Late Yanshanian magmatic activity in the territory. All these confer to the study of Macao magmatism the potential to contribute to a better understanding of the magmatic activity in SE China during the Yanshanian Orogeny.

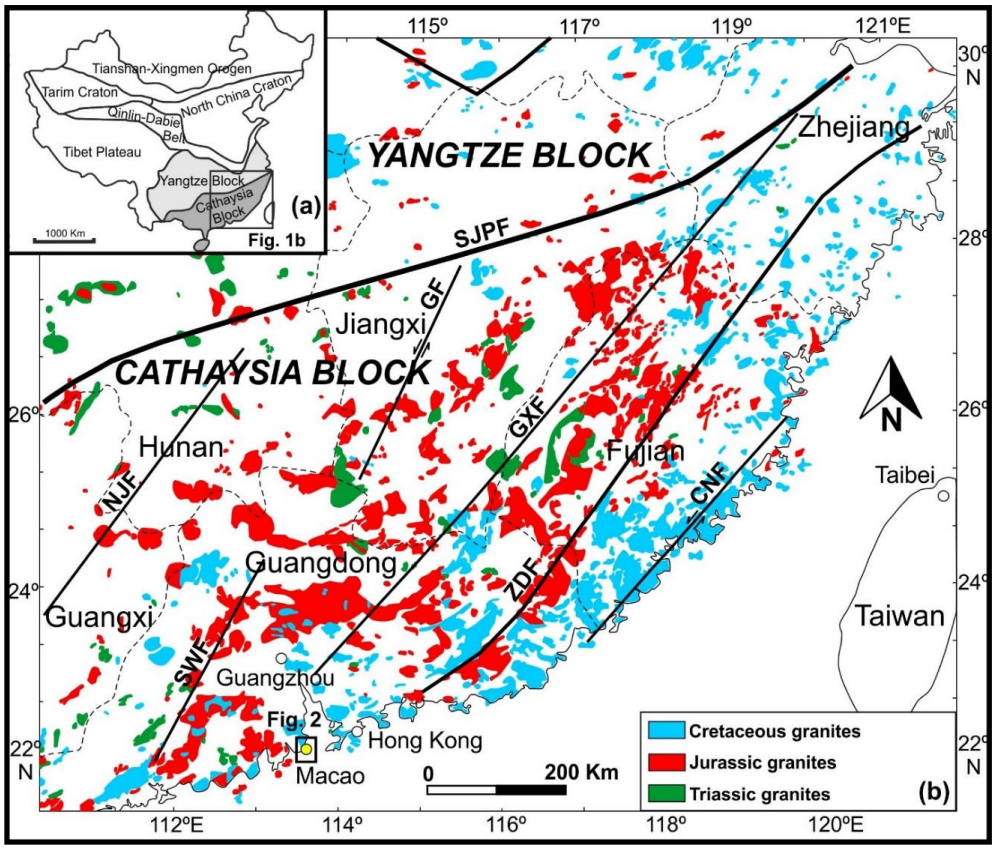

Fig. 5.1. (a) Simplified tectonic sketch showing the main crustal blocks of China; (b) Geological map of SE China showing the distribution of Mesozoic granitic rocks and the main tectonic features (modified after Zhou et al., 2006; Yang et al., 2018). SJPF: Shaoxing-Jiangshan-Pingxiang Fault Zone; CNF: Changle-Nan'ao Fault Zone; ZDF: Zhenghe-Dapu Fault Zone; GXF: Guangchang-Xunwu Fault Zone; GF: Ganjiang Fault Zone; SWF: Sihui-Wuchuan Fault Zone; NJF: Ningyuan-Jianghua Fault Zone.

The aims of the present study were: (1) to characterize geochemically the Macao granites, contributing to a better knowledge of the different granite types in the Cathasyia Block; (2) to assess whether the two pulses of granitic magmatism have distinct sources; (3) to characterize magma evolution processes operating in each pulse; (4) to better constrain the mantle to crust heat and mass transfer processes during the Yanshanian Orogeny; (5) to unravel the prevailing tectonic setting at the time of granitoid generation and emplacement, providing additional contributions to the understanding of Yanshanian orogenic evolution.

To achieve these objectives, an integrated study involving mineral chemistry, whole-rock elemental and Sr–Nd–Hf–Pb isotopic geochemistry is presented in this paper, allowing to demonstrate the role of the mantle and of the lower and upper crust in the genesis of the studied I-type granites, as well as the occurrence of closed- and open-system magmatic evolution processes.

5.2. Geological background

Macao is located in the SE part of the Cathaysia Block, which is part of the South China Block (SCB; Fig. 5.1a). The SCB was formed by amalgamation of the Yangtze and the Cathaysia blocks along a Neoproterozoic (~900 Ma) ophiolitic suture (e.g. Li et al., 2009a), nowadays materialized by the Shaoxing-Jiangshan-Pingxiang Fault Zone (SJPF; Fig. 5.1b). The Cathaysia Block is further divided into the western Cathaysia (inland areas) and eastern Cathaysia (coastal areas) blocks, along the Zhenghe-Dapu Fault (ZDF; Fig. 5.1b), which have been regarded as having different crustal evolution histories (e.g. Chen and Jahn, 1998; Xu et al., 2007b). Overall, the Cathaysia Block is commonly assumed to consist of a Paleo-Proterozoic to Mesoproterozoic metamorphic basement, with minor Archean rocks, overlain by Protorezoic metasediments and a Ediacaran to Mesozoic sedimentary and volcanic cover (e.g. Chen and Jahn, 1998; Sewell et al., 2000b; Xu et al., 2007b; Zheng et al., 2011). The Precambrian basement rocks mainly crop out under Mesozoic volcanic rocks in the southern Zhejiang and northwestem Fujian provinces (Chen and Jahn, 1998).

The Mesozoic geology of the Cathaysia Block is characterized by widespread granitic magmatism associated with rhyolites and minor mafic intrusive and volcanic rocks, occupying a total outcrop area of more than 200,000 km^2 (Fig. 5.1; Zhou and Li, 2000; Zhou et al., 2006; Li et al., 2007). The Triassic granites were formed during the Indosinian Orogeny as a result of the continental collision between the Indochina Block and the SCB. The extensive Late Mesozoic magmatic activity during the Yanshanian Orogeny resulted in a NE-trending belt of volcanic–

intrusive complexes (~ 3500 km long and ~ 800 km wide) that runs parallel to the present coastline. These Late Mesozoic magmatic rocks fall into two main age groups, Jurassic (Early Yanshanian) and Cretaceous (Late Yanshanian; Zhou et al., 2006). Despite the observable younging trend of these Late Mesozoic magmatic rocks at a regional scale (Fig. 5.1), with the Jurassic magmatic rocks inland and the Cretaceous magmatic rocks along the coastal areas, some studies have also shown the occurrence of Jurassic magmatic rocks along coastal areas (Sewell et al., 1992; Huang et al., 2012; Sewell et al., 2012a; Y. Zhang et al., 2015). The Macao granitic suite is one of these examples of Middle to Upper Jurassic granitic rocks outcropping in the coastal area of SE China (Quelhas et al., 2019).

In Macao, biotite granites, ranging in age from 164.88 ± 0.59 to 155.86 ± 0.56 Ma, are the dominant lithology and were emplaced as two discrete magmatic pulses with distinct crystallization ages and different petrographic, mineralogical and geochemical features (Fig. 5.2; Quelhas et al., 2019). They intrude metasedimentary rocks of Devonian age, whose remnants are found as sparse metasedimentary enclaves within the granites. In addition, microgranular mafic enclaves (MME) with variable shape, size and composition, are common within the granites. The granites are intruded by a swarm of quasi-coeval granitic dykes (microgranite, aplite and pegmatite) and by Upper Jurassic to Lower Cretaceous dacite dykes (150–120 Ma; Quelhas et al., 2019).

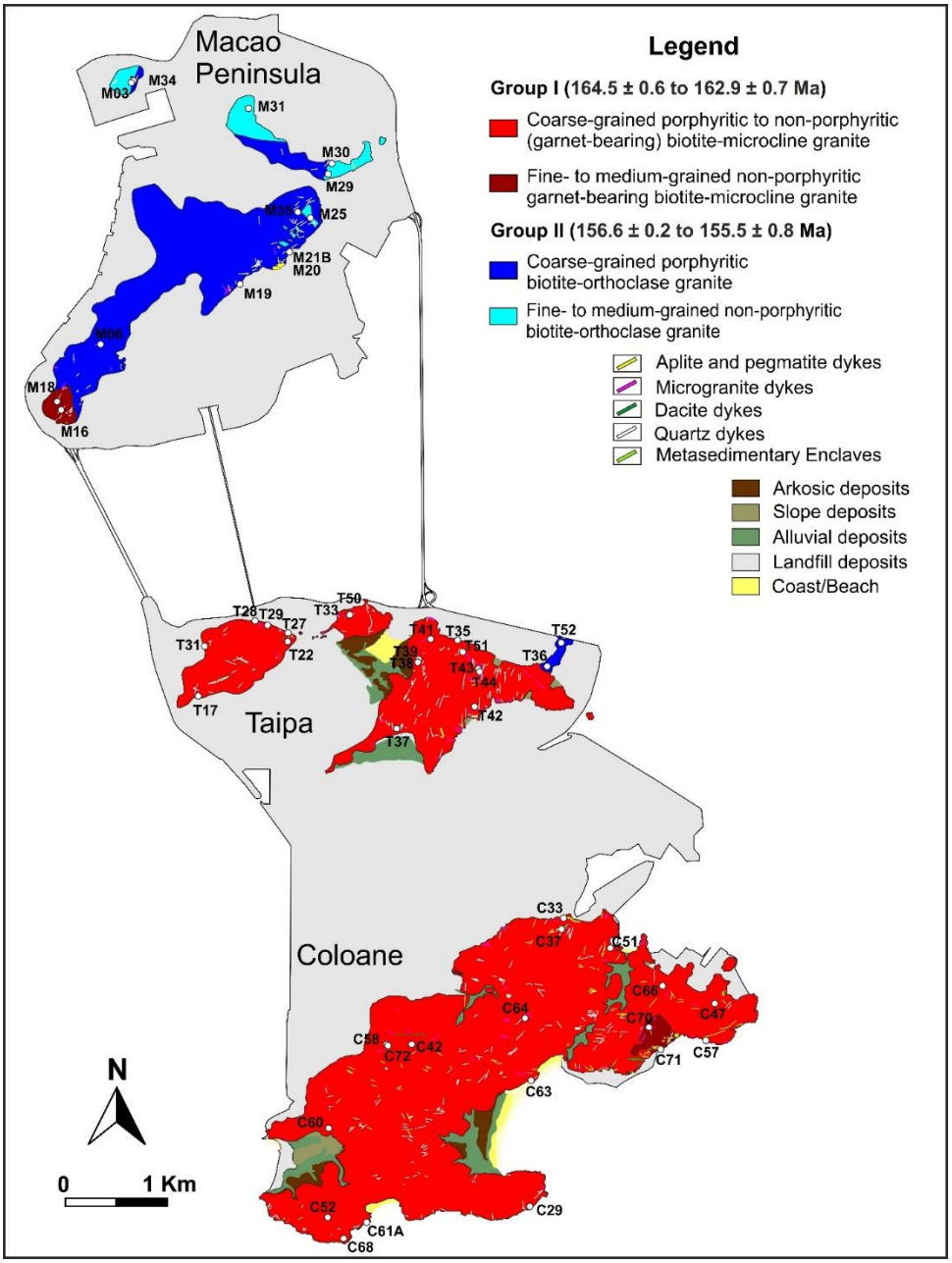

Fig. 5.2. Simplified geological map of Macao showing the distribution of the two groups of granites in the territory and the location of samples chosen for geochemical analysis.

5.3. Sampling and analytical procedures

Representative samples of granitic facies defined by Quelhas et al. (2019) and MME have been collected from fresh surface exposures and drill cores. Details on sample locations are given in Table B.1 (Appendix B). After careful thin section examinations under an optic microscope, the

least-altered samples were selected for whole-rock elemental (forty-nine samples plus four duplicates) and isotopic analyses (twenty samples plus three duplicates) and grounded to 200-mesh using a jaw crusher and an agate mill. Thirty-two samples were selected for mineral chemistry analysis.

5.3.1. Mineral chemistry

Mineral analyses were performed on carbon-coated polished thin sections using a JEOL SUPERPROBE™, model JXA-8200, in wavelength dispersive mode at the Departamento de Geologia da Faculdade de Ciências da Universidade de Lisboa (Portugal). Minerals were analysed with an acceleration voltage of 15 kV and a current of 25 nA, using a 5 μm wide beam. The analyses were calibrated using the composition of in-house standard materials, with reproducibility errors being lower than 2% and ordinarily around 1%. Matrix effects were corrected using the ZAF software provided by JEOL. Information about standards and detection limits are given in Tables C.1 and C.2 (Appendix C).

5.3.2. Whole-rock elemental geochemistry

Whole-rock major and trace element concentrations were obtained at Activation Laboratories, Ltd. (Ancaster, Ontario, Canada) using the geochemical analytical package 4E - Research. Major oxide content was analysed using Inductively Coupled Plasma-Optical Emission Spectrometry (ICP-OES) using a Thermo Jarrell-Ash ENVIRO II ICP and/or Spectro Cirros ICP. Trace elements, including Rare Earth Elements (REE), were obtained using Inductively Coupled Plasma Mass-Spectrometry (ICP-MS) on a Perkin Elmer SCIEX ELAN 6000, 6100 or 9000 ICP/MS and by Instrumental Neutron Activation Analysis (INAA). In-house standards and several certified reference materials of granitic to dioritic compositions (s.l.) from USGS (United States Geological Survey), GSJ (Geological Survey of Japan) and CCRMP (Canadian Certificate Reference Material Project) were used. Errors associated with the accuracy are $\leq$ 4% for major elements and better than 9% for the REE and the most widely used incompatible elements. Duplicate measurements of samples indicate that errors associated with reproducibility were generally lower than 5% for both major and trace elements. Information about detection limits is given in Table D.1 (Appendix D). For detailed information regarding analytical and control procedures consult the Actlabs website (www.actlabs.com).

5.3.3. Whole-rock Sr–Nd–Hf–Pb isotope geochemistry

Isotopic analyses of Pb, Nd, Sr and Hf were performed at the Laboratoire G-Time of the Université Libre de Bruxelles (ULB, Belgium) on a Nu Plasma I Multi-Collector Inductively Coupled Plasma Mass Spectrometer (MC-ICP-MS; @ Nu instruments).

Sr analyses were performed in wet mode. In routine, the raw data was normalized to $^{86}Sr/^{88}Sr = 0.1194$, and corrected for mass bias by standard sample bracketing using the lab's in-house Sr standard solution. The in-house shelf Sr standard was calibrated and normalized to the certified value of NBS 987 Sr standard (0.710248) reported by Weis et al.(2006). During our analytical sessions, in-house standard solution was run every two samples and gave an average value of 0.710287 ± 50 (2σ) for raw $^{87}Sr/^{86}Sr$ data (21 runs).

Nd and Hf were run in dry mode with an Aridus II Desolvating Nebulizer System. To monitor the instrumental mass bias during the analysis sessions, the standard sample bracketing method was also applied. Standards were systematically run between every two samples, giving an average value in $^{143}Nd/^{144}Nd$ of 0.511921 ± 41 (2σ, 8 runs) for the Rennes Nd standard, and $^{176}Hf/^{177}Hf$ = 0.282172 ± 30 (2σ, 10 runs) for the JMC 475 Hf standard. The Nd and Hf isotopic measurements were internally normalized to $^{146}Nd/^{144}Nd = 0.7219$ and $^{179}Hf/^{177}Hf = 0.7325$, respectively. All Hf and Nd isotopic data were normalized to the reference values of 0.282160 and 0.511961, respectively, as published by Chauvel and Blichert-Toft (2001) and Chauvel et al. (2011).

For the Pb isotope analyses, a Tl dopant solution was added for every sample and standard, within a Pb-Tl concentration ratio of ±5:1 (for a minimum signal of 100 mV in the axial collector - ^{204}Pb). ^{202}Hg is routinely monitored to correct for the potential isobaric interference of ^{204}Hg on ^{204}Pb. Mass discrimination was monitored using ln – ln plots and corrected by the external normalization and the standard sample bracketing technique using the recommended values of Galer and Abouchami (1998), i.e. $^{206}Pb/^{204}Pb = 16.9405 \pm 15$; $^{207}Pb/^{204}Pb = 15.4963 \pm 16$; $^{208}Pb/^{204}Pb = 36.7219 \pm 44$. The repeated measurements of the NBS981 gave the following values: $^{206}Pb/^{204}Pb = 16.9403 \pm 8$, $^{207}Pb/^{204}Pb = 15.4961 \pm 10$, $^{208}Pb/^{204}Pb = 36.7217 \pm 31$ (2σ) for the NBS981 Pb standard (5 runs).

5.4. Results

5.4.1. Petrography and mineralogy

The Macao granites consist of two main groups with distinct crystallization ages as well as different petrographic and mineralogical characteristics. They will be here referred as Macao Group I (MGI) and Macao Group II (MGII) for which 164.88 ± 0.59 to 162.91 ± 0.73 Ma (MGI; Fig. 5.3a) and 156.57 ± 0.19 to 155.86 ± 0.56 Ma (MGII; Fig. 5.3g) were assigned based on zircon U–Pb ages, respectively (Quelhas et al.,2019). The main petrographic and mineralogical characteristics of each group are summarized in Table 5.1 and in Fig. 5.3. Mineral compositions of biotites and feldspars and are given in Tables C.3 and C.4 (Appendix C), respectively, and graphically depicted in Fig. 5.4. In both groups textures vary from medium- to coarse-grained porphyritic (monzogranite) to fine-grained non-porphyritic moderately equigranular (syenogranite to alkali feldspar granite; Fig. 5.5a).

Table 5.1. Summary of the mineralogical composition and textural features of the Macao granites.

Group	Facies	Systematics	Rock-forming minerals	Mineral Chemistry	Accessory minerals	MME
MGI	Coarse-grained porphyritic biotite-microcline granite	Monzogranite	Qz (30–35 vol%), Mc (35–40 vol%), Pl (20–25 vol%), Bt (5–10 vol%)	Plagioclase: andesine (An < 35 %) to oligoclase Biotite: ferri-biotite and siderophyllite.	Grt; Ilm; Mag; Rt; Ap; Xtm; Mnz; Ep; Fl; Zrn; Aln; tantalo-niobates; sulphides; Ttn; Thr	Irregular to oval blobs (<1 meter), granodiorite composition, acicular biotite; no accessory Ttn.
	Coarse-grained non-porphyritic garnet-bearing biotite-microcline granite	Syenogranite to alkali feldspar granite	Qz (30–35 vol%), Mc (35–40 vol%), Pl (20 vol%) Bt (5 vol%), Grt (2%)			
	Fine- to medium-grained non-porphyritic garnet-bearing biotite-microcline granite	Syenogranite to alkali feldspar granite	Qz (30–35 vol%), Mc (35–40 vol%), Pl (20 vol%), Bt (<5 vol%), Grt (2–5 vol%)			
MGII	Coarse-grained porphyritic biotite-orthoclase granite	Monzogranite	Qz (30–35 vol%), Or (35–40 vol%), Pl (20–25 vol%) and Bt (5–10 vol%)	Plagioclase: andesine (An < 37%) to oligoclase; Biotite: close to the Annite end-member.	Ilm; Mag; Rt; Ap; Xtm; Mnz; Ep; Fl; Zrn; Aln; tantalo-niobates; sulphides; Ttn; Thr	Round-shaped (centimetre to decimetre-wide), quartz monzodioritic composition, abundant lozenge-shaped Bt; abundant Ttn; acessory Hbl.
	Fine- to medium-grained non-porphyritic biotite-orthoclase granite	Syenogranite	Qz (30–35 vol%), Or (35–40 vol%), Pl (20 vol%), Bt (<5 vol%)			

Abbreviations: MGI - Macao Group I granites; MGII - Macao Group II granites; An - anorthite; Qz - quartz; Mc - microcline; Or - orthoclase; Pl - plagioclase; Bt - Biotite; Grt - garnet; Ilm - ilmenite; Mag - magnetite; Rt - rutile; Ap - apatite; Xtm - xenotime; Mnz - monazite; Ep - epidote; Fl - fluorite; Zrn - zircon; Aln - allanite; Ttn - titanite; Thr – thorite. Granite systematics is according to the Q'-ANOR normative classification for Macao granites (Fig. 5.5a; Streckeisen and Le Maitre, 1979), with normative compositions calculated through the Improved Granite Mesornorm of Mielke and Winkler (1979).

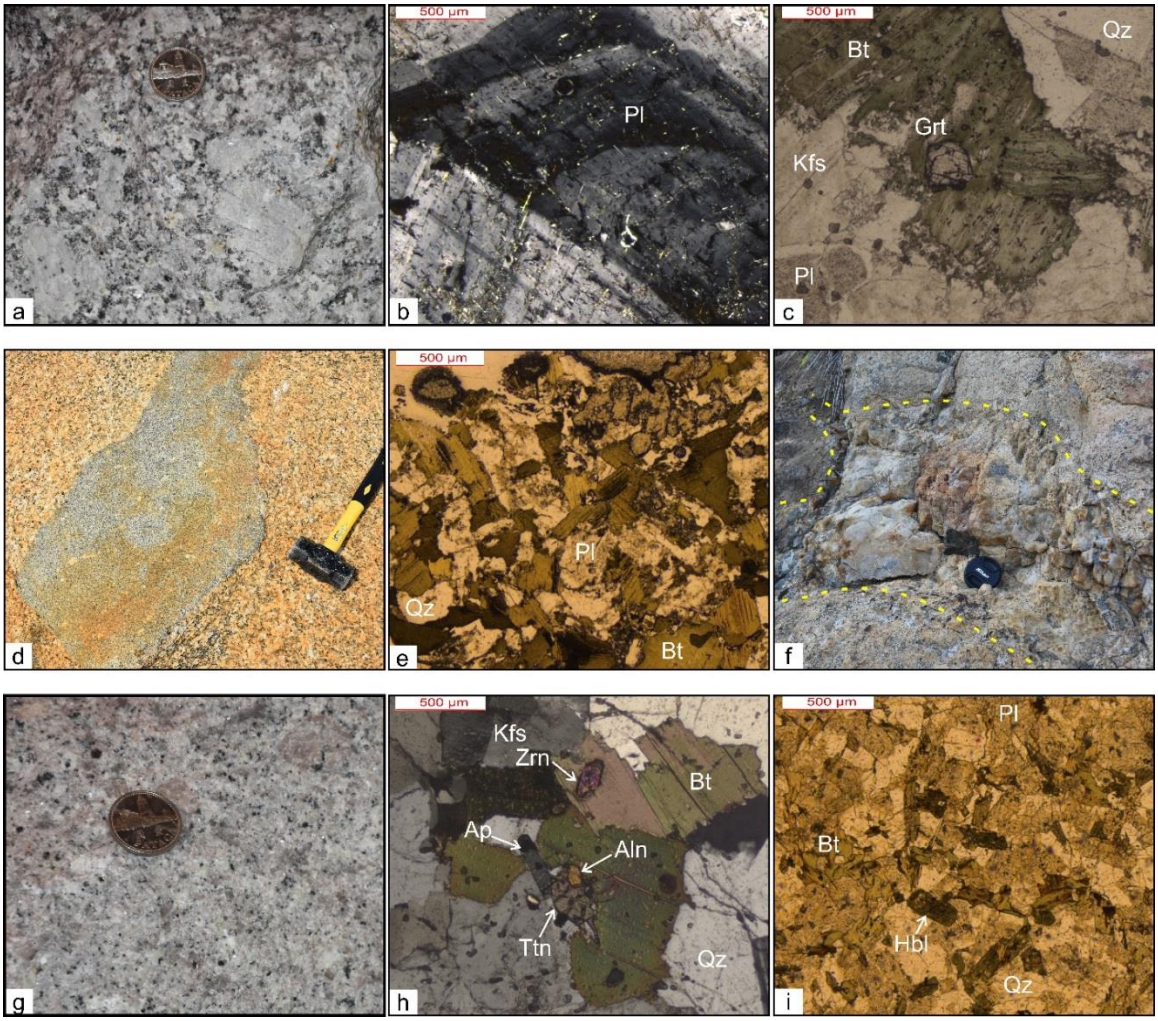

Fig. 5.3. Hand specimens and thin sections representative of the different lithofacies observed in Macao: (a) MGI coarse-grained porphyritic biotite-microcline granite; (b) Plagioclase with oscillatory zoning in MGI coarse-grained porphyritic biotite-microcline granite; (c) Garnet crystal growing at the expense of biotite in a MGI coarse-grained non-porphyritic garnet-bearing biotite-microcline granite; (d) Granodiorite MME enclosed in MGI granite; (e) Microtexture of granodiorite MME enclosed in MGI, mainly composed of biotite, plagioclase and minor quartz; (f) Pod-shaped pegmatite associated with MGI non-porphyritic garnet-bearing biotite-microcline granite; (g) MGII coarse-grained porphyritic biotite-orthoclase granite; (h) Biotite aggregation with concentrarion of accessory minerals in MGII granite; (i) Microtexture of the quartz monzodiorite MME enclosed in MGII granites, characterized by accessory hornblende. MME – mafic microgranular enclave; Qz– quartz; Pl – plagioclase; Kfs – K-feldspar; Ttn – titanite; Bt – biotite; Grt – garnet ; Hbl – hornblende; Zrn – zircon; Aln – allanite; Ap – apatite.

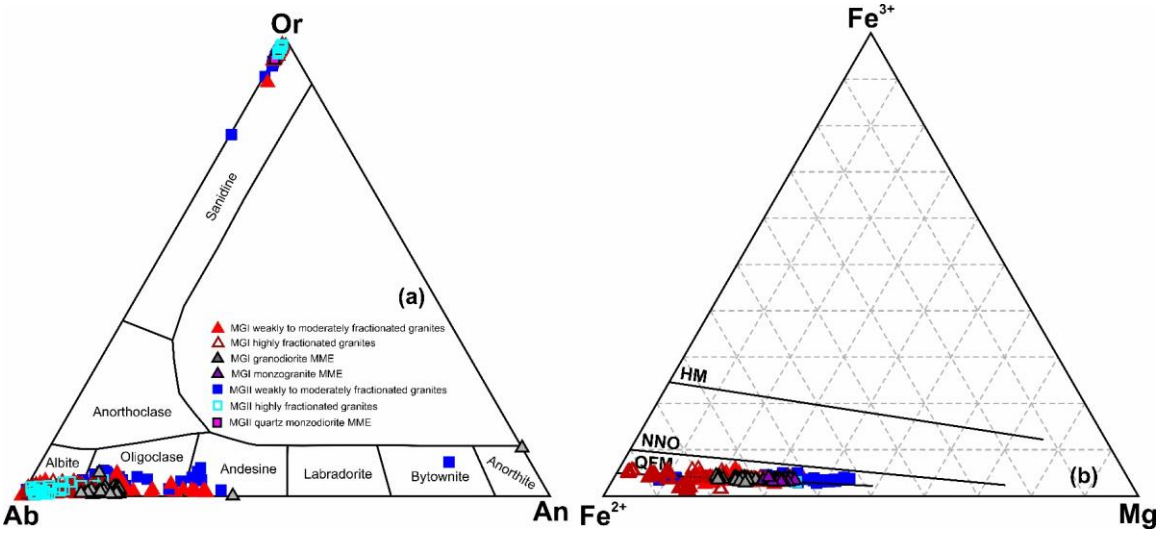

Fig. 5.4. Mineral chemistry of the major mineral phases of the Macao granites (see also Quelhas et al., 2019): (a) Classification diagram for feldspars; (b) Composition of biotite plotted in the Fe^{2+}–Fe^{3+}–Mg ternary diagram (Wones and Eugster, 1965), along with the three common oxygen fugacity buffers: quartz–fayalite –magnetite (QFM), nickel–nickel oxide (NNO) and hematite–magnetite (HM).

5.4.2. Whole-rock major and trace element geochemistry

Macao granites range from metaluminous to weakly peraluminous (A/CNK = 0.96 to 1.13; Fig. 5.5b) plotting in the field of high-K calc-alkaline rocks (K_2O up to 5.36 wt%; K_2O/Na_2O up to 1.85; see Fig. 5.5c). The MGII granites are characterized by a wider range in silica (SiO_2 = 66.77–76.51 wt%), iron oxide ($Fe_2O_3^T$ = 0.97–5.11%) and CaO (0.53–2.56 wt%) than the ones reported for MGI (SiO_2 = 71.2–76.9 wt%; $Fe_2O_3^T$ = 1.20–2.83 wt%; CaO = 0.32 to 1.41 wt%; see Fig. 5.6). However, both groups are characterized by similar variations in Al_2O_3 (MGI: 12.58–14.80 wt%; MGII: 11.82–13.88 wt%) and K_2O (MGI: 4.52–5.36 wt%; MGII: 3.92–5.09 wt%).

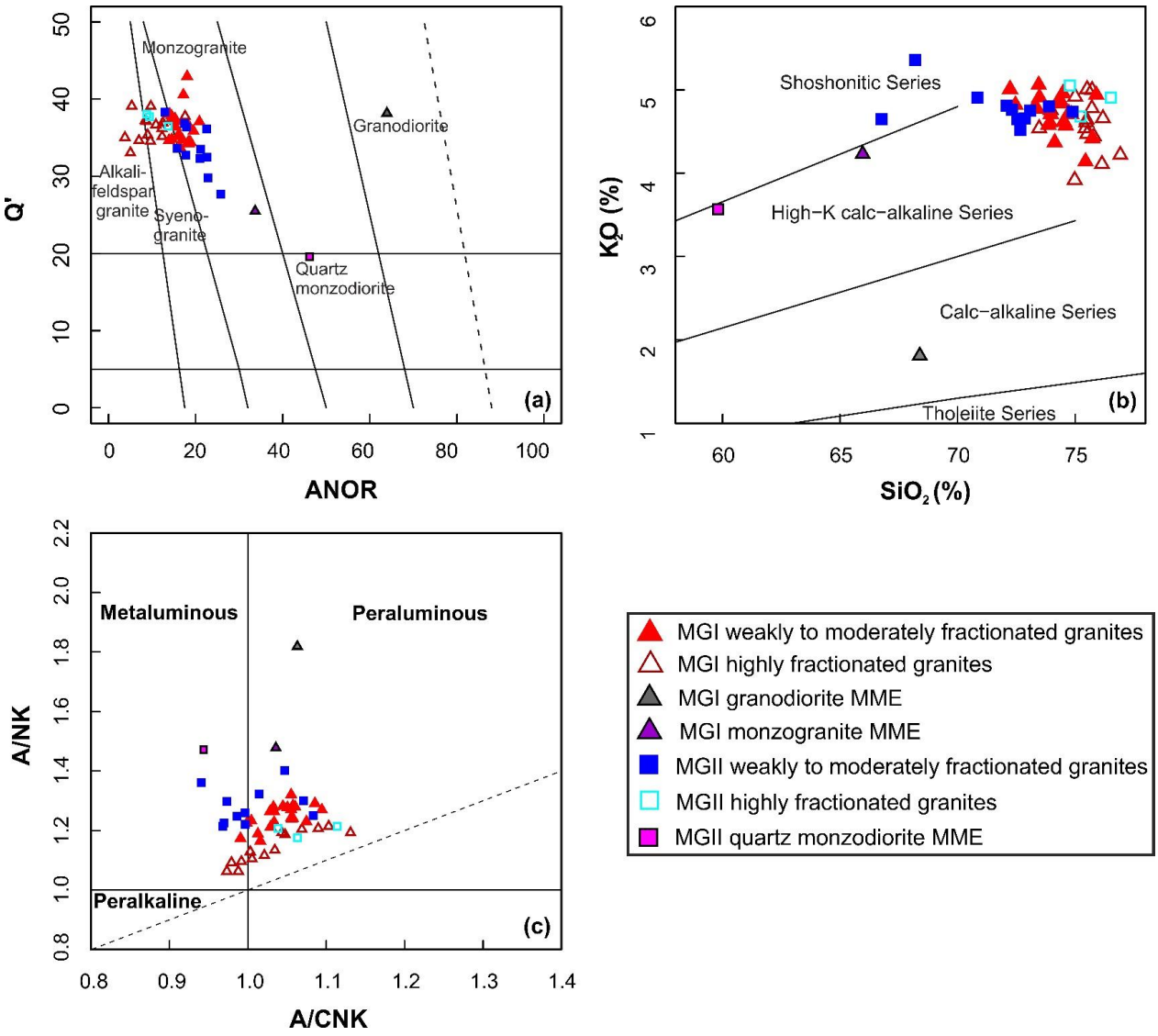

Fig. 5.5. Classification diagrams for the Macao granites and MME: (a) Q'-ANOR normative composition diagram (Streckeisen and Le Maitre, 1979), where Q' = Q/(Q+Or+Ab+An)×100; ANOR = An/(Or+An)×100; (b) A/NK [molar ratio $Al_2O_3/(Na_2O + K_2O)$] *vs* A/CNK [molar ratio $Al_2O_3/(CaO + Na_2O + K_2O)$]; (c) K_2O *vs* SiO_2.

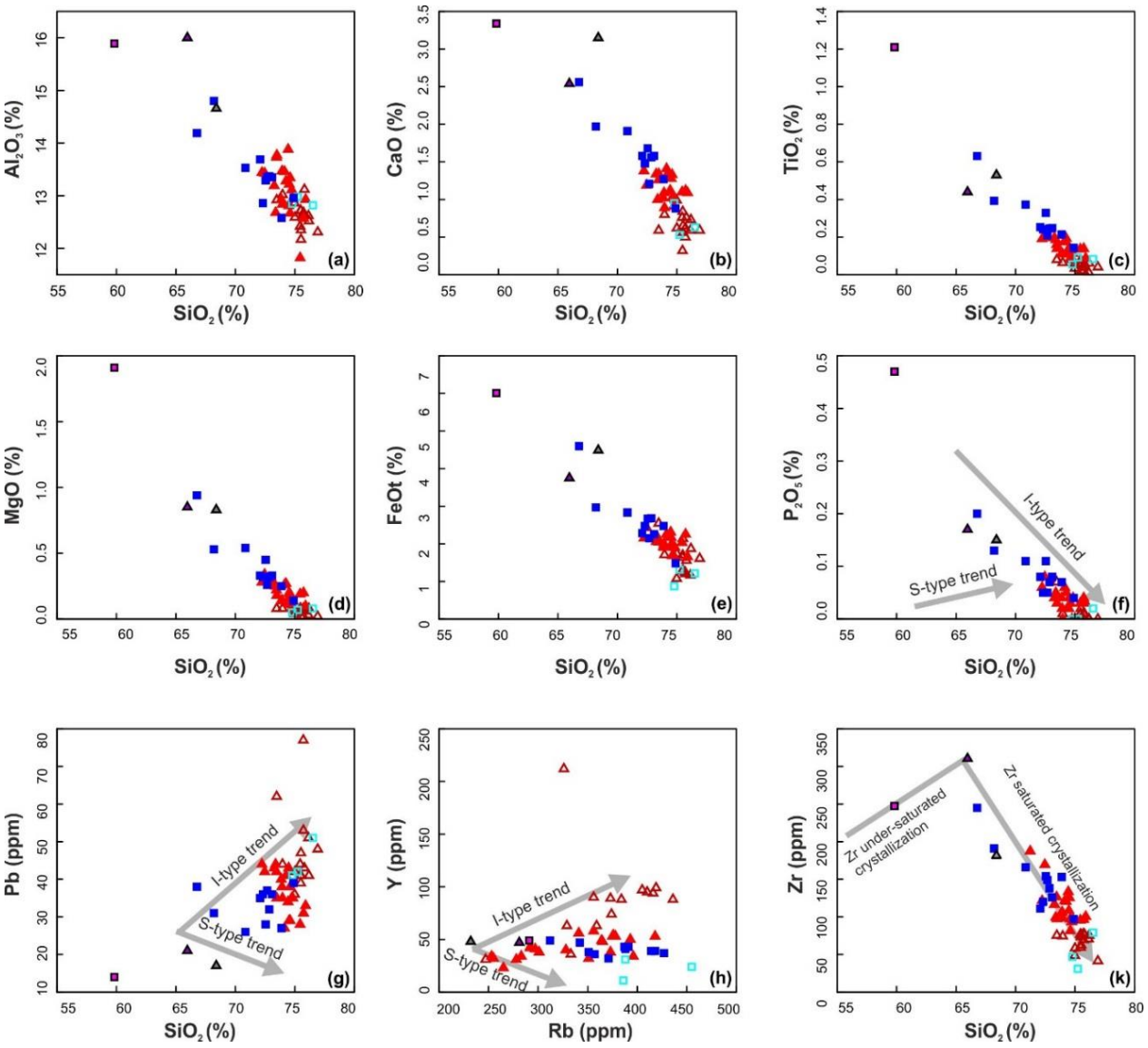

Fig. 5.6. Chemical variation diagrams for the Macao granites and MME. Symbols are as in Fig. 5.5.

Overall, there is a wide range of Zr/Hf ratios (12.24–37.60). Since Zr/Hf tend to decrease with increasing evolution of high-silica melts (e.g. Irber, 1999), in this study we use this ratio as a granite fractionation index. We consider weakly to moderately fractionated granites those having Zr/Hf > 25, while highly fractionated granites are marked by comparatively lower Zr/Hf ratios (≤ 25).

As a common characteristic, all the Macao granites show enrichment in large ion lithophile elements (LILE; e.g. Rb, K, Pb) relative to high field strength elements (HFSE; eg. Nb, Ta, and

REE), but depicting very pronounced negative Ba, Sr, P, and Ti anomalies (Fig. 5.7), which are enhanced with increasing SiO_2 and decreasing Zr/Hf.

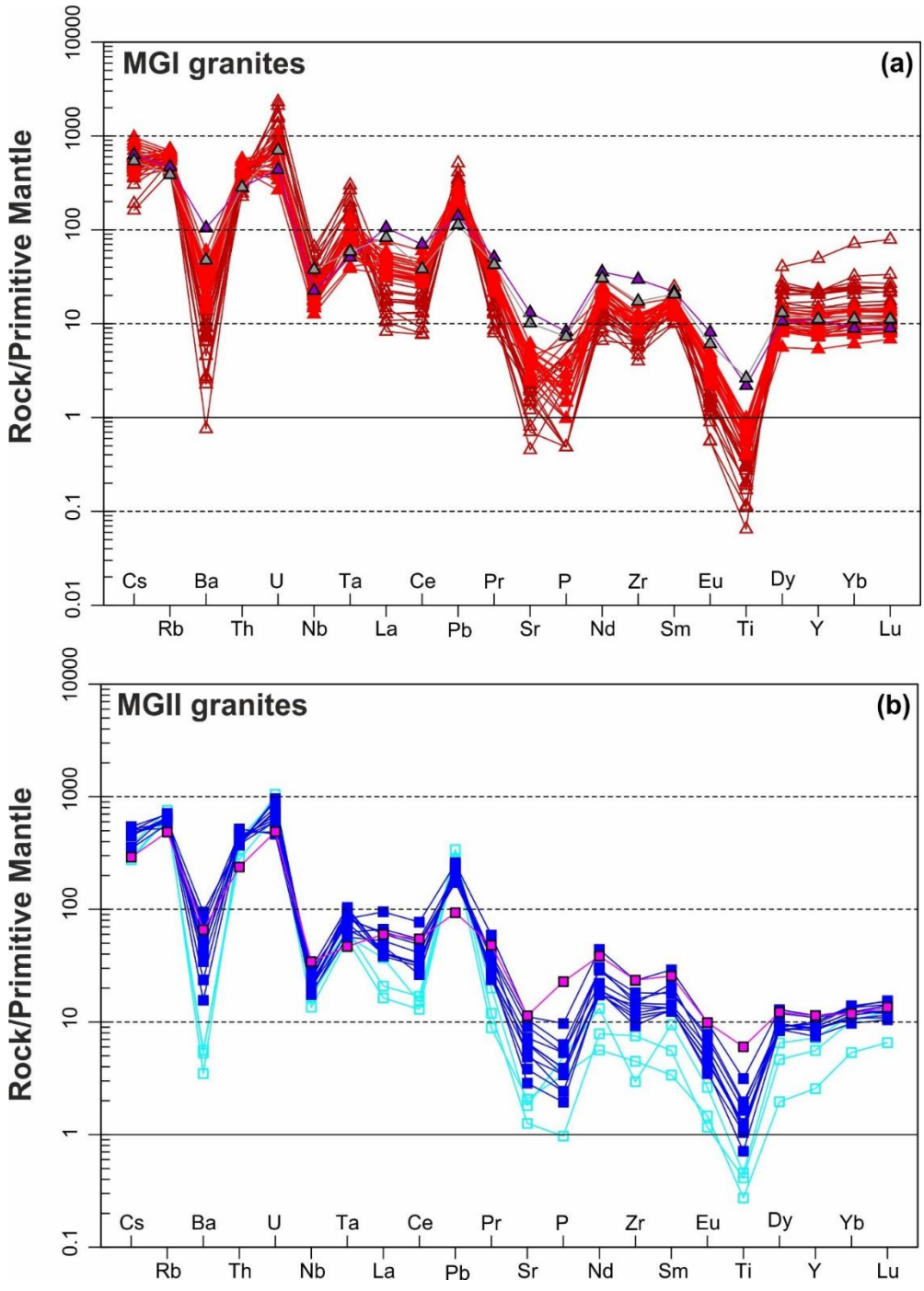

Fig. 5.7. Primitive mantle (PM) normalized trace element spidergrams for: (a) MGI granites and MME; (b) MGII granites and MME. The Primitive Mantle values are from Sun and McDonough (1989). Symbols are as in Fig. 5.5.

While the weakly to moderately fractionated granites of both groups are similar showing light REE (LREE) enrichment relative to heavy REE [HREE; $(La/Yb)_N$ = 2.41–10.76] and Eu negative anomalies (Fig. 5.8), the REE patterns of the highly fractionated granites of the two groups are distinct. Those pertaining to MGI (Fig. 5.8a) commonly have flat to slightly upwards fractionated patterns [$(La/Yb)_N$ = 0.12–1.2], well-pronounced Eu anomalies (Eu/Eu* = 0.02–0.19) and show evidence for the tetrad effect ($TE_{1,3}$ = 1–1.13; see footnotes of Table D.2, Appendix B). With increasing SiO_2 contents, the HREE contents increase and the Eu anomalies become more negative. The MGII highly fractionated granites (Fig. 5.8b) are characterized by concave upwards REE patterns, by the absence of the tetrad effect and by their comparatively smaller Eu negative anomalies (Eu/Eu* = 0.23–0.54).

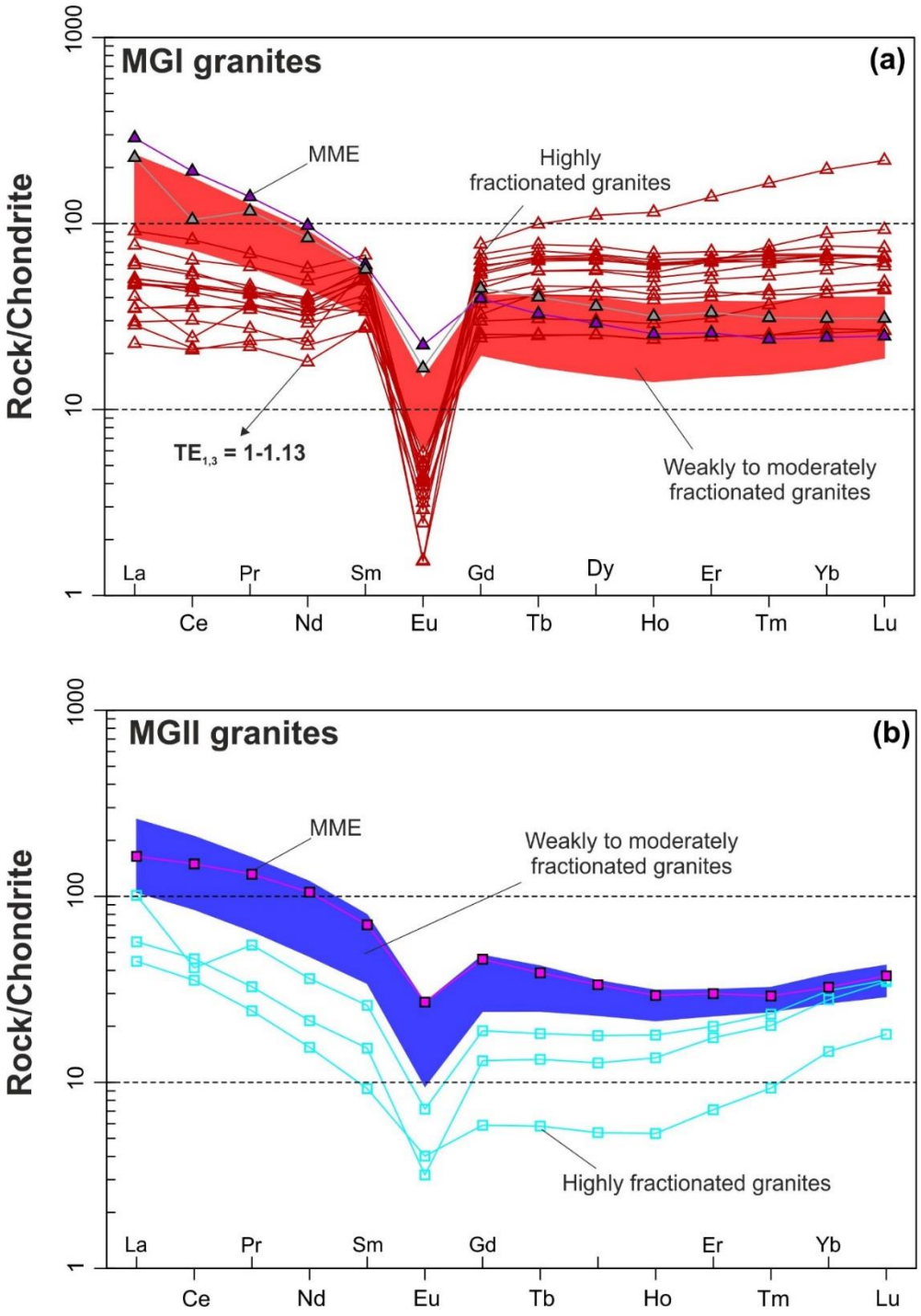

Fig. 5.8. Chondrite normalized Rare Earth Elements (REE) patterns for: (a) MGI granites and MME; (b) MGII granites and MME (see also Quelhas et al., 2019). The chondrite values are from Sun and McDonough (1989). Symbols are as in Fig. 5.5.

The MME of both groups have similar, though more primitive, major and trace element compositions when compared with their host granites. The MGI MME are intermediate to acid in

composition and plot in the monzogranite and granodiorite fields (Fig. 5.5a; Table D.2, Appendix D). All MME have high HFSE/LILE ratios and negative anomalies of Ba, Nb, Ta and Ti, which are similar to those of the host rocks (Fig. 5.7). However, at odds with the observed for the host rocks, MME do not display pronounced negative Sr and P anomalies. REE patterns for the MME are similar and sub-parallel to those of the less evolved granites, but with smaller negative Eu anomalies (Eu/Eu* = 0.33–0.48; Fig. 5.8).

5.4.3. Whole-rock Sr–Nd–Hf–Pb isotope geochemistry

The isotopic compositions of twenty samples (seventeen granite samples and three MME), plus three duplicates, are listed in Table E.1 (Appendix E). Four different whole-rock isotope systems were analysed: Sr (Figs. 5.9a and 5.9b), Nd (Figs. 5.9b, 5.9c and 5.10), Hf (Fig. 5.9c) and Pb (Fig. 5.11). All Sr–Nd–Hf–Pb isotopic ratios were calculated back to 160 Ma, which, given the small difference in the crystallization ages of both groups of granites (ca. 6 Ma; Quelhas et al., 2019) and the low values of decay constants, does not have a significant effect in the calculated initial isotopic ratios.

In the $\varepsilon_{Nd}(t)$ *vs* initial $^{87}Sr/^{86}Sr$ diagram (Fig. 5.9b), all the granite samples plot in the fourth quadrant indicating time-integrated Rb/Sr and Nd/Sm higher than the Bulk Silicate Earth (BSE) and the CHondritic Uniform Reservoir (CHUR), respectively.

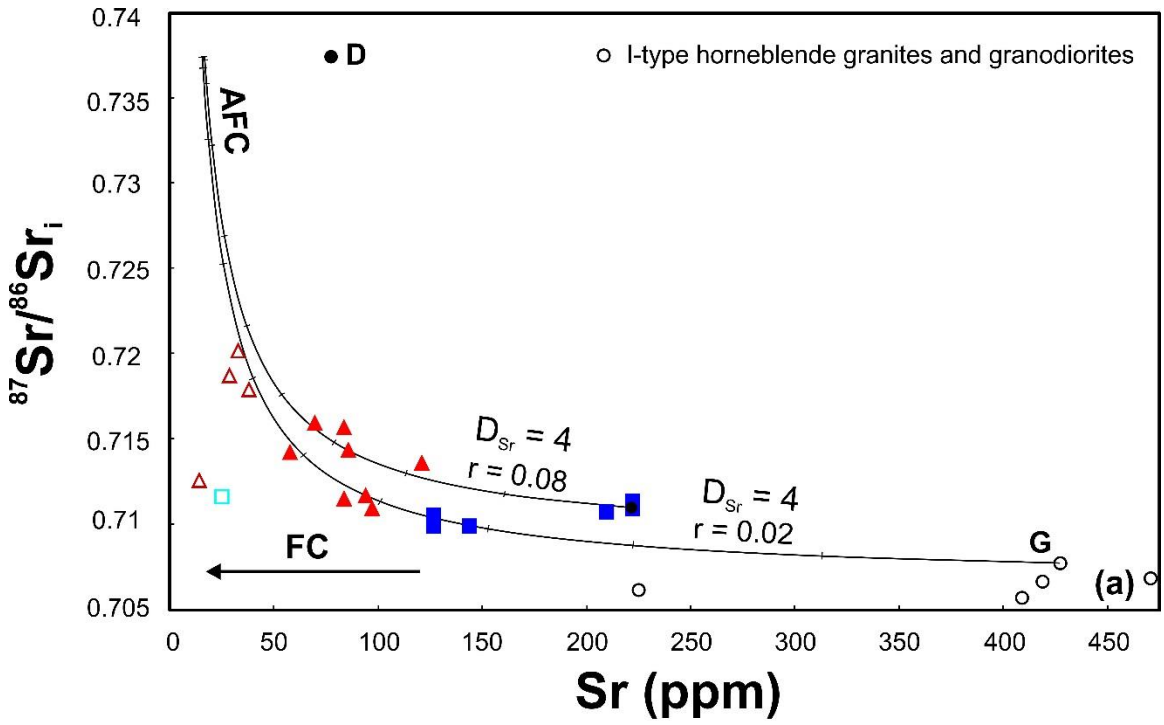
D
I-type horneblende granites and granodiorites
AFC
FC
D_{Sr} = 4
r = 0.08
D_{Sr} = 4
r = 0.02
G
(a)
$^{87}Sr/^{86}Sr_i$
Sr (ppm)

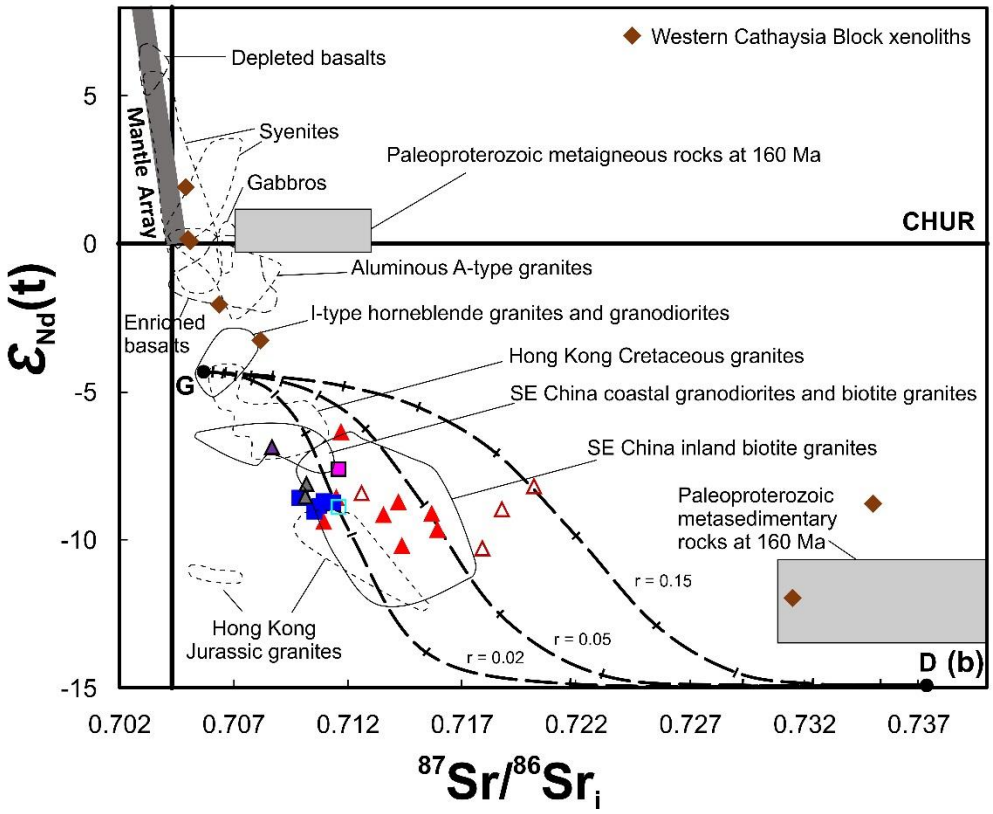
Western Cathaysia Block xenoliths
Depleted basalts
Mantle Array
Syenites
Gabbros
Paleoproterozoic metaigneous rocks at 160 Ma
CHUR
Aluminous A-type granites
I-type horneblende granites and granodiorites
Enriched basalts
G
Hong Kong Cretaceous granites
SE China coastal granodiorites and biotite granites
SE China inland biotite granites
Paleoproterozoic metasedimentary rocks at 160 Ma
r = 0.15
r = 0.05
r = 0.02
Hong Kong Jurassic granites
D (b)
$\varepsilon_{Nd}(t)$
$^{87}Sr/^{86}Sr_i$

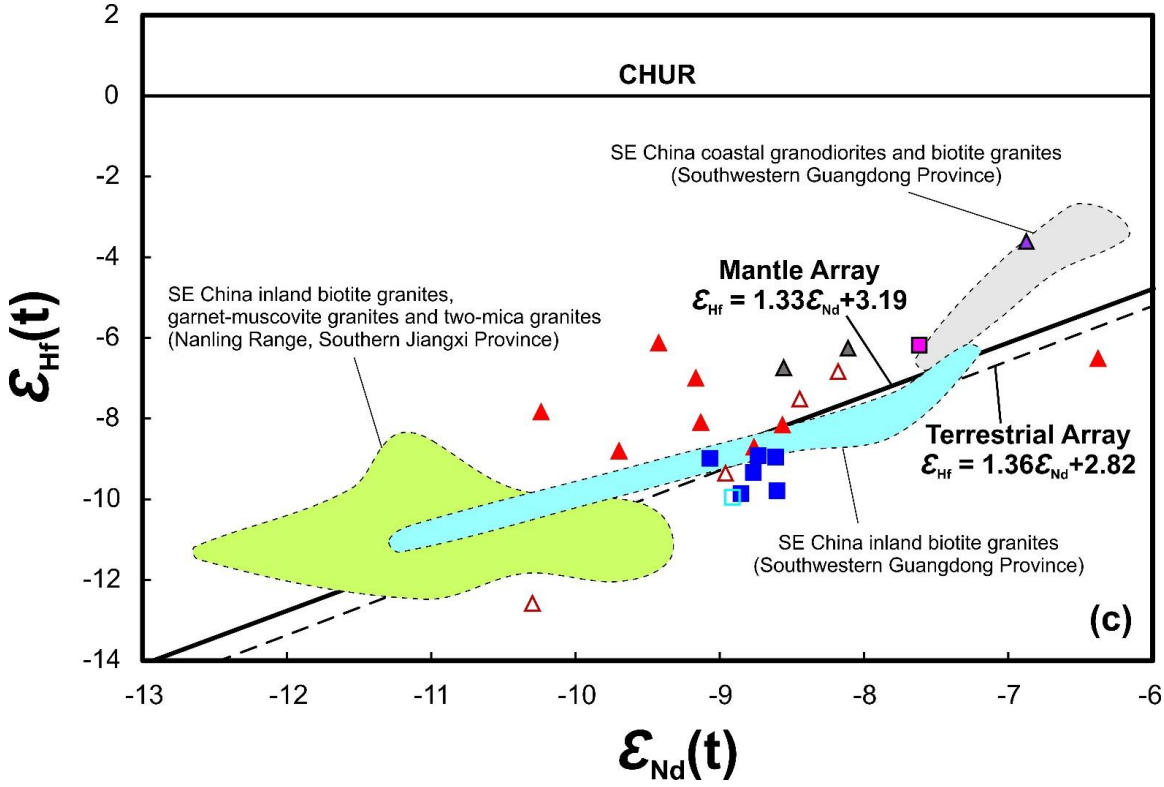

Fig. 5.9. Whole-rock isotopic diagrams for the Macao granitic rocks and MME: (a) Initial $^{87}Sr/^{86}Sr$ *vs* Sr (ppm); AFC curves calculated for $D_{Sr} = 4$, with tick marks representing 10% increments; contaminant: SE China upper continental crust represented by the Darongshan peraluminous granite at 160 Ma (point D, Sr = 78 ppm, Nd = 38 ppm, initial $^{87}Sr/^{86}Sr = 0.7374$ and $\varepsilon_{Nd}(t) = -14.9$; Hsieh et al., 2008); parental magma: SW Guangdong hornblende-bearing I-type granite at 160 Ma (point G, Sr = 427 ppm, Nd = 24 ppm, $^{87}Sr/^{86}Sr_i = 0.7077$, and $\varepsilon_{Nd}(t) = -3.27$; Huang et al., 2012); for details on the calculation of the AFC model see Appendix A, section 1.3.2.3. Abbreviations: AFC – Assimilation Fractional Crystallization; FC – Fractional Crystallization. (b) $\varepsilon_{Nd}(t)$ *vs* initial $^{87}Sr/^{86}Sr$. AFC curves (dashed lines) calculated assuming $D_{Sr} = 2$ and $D_{Nd} = 6$ and using as parental magma a SW Guangdong hornblende-bearing I-type granite at 160 Ma (point G, Sr = 409 ppm, Nd = 21.9 ppm, $^{87}Sr/^{86}Sr_i = 0.7057$, and $\varepsilon_{Nd}(t) = -4.33$; Huang et al., 2012) and the same contaminant composition as referred for Fig. 5.9a, with tick marks representing 10% increments; The metaigneous and metasedimentary basement rocks are taken from Yuan et al., (1991); Western Cathaysia Block xenoliths from Li et al. (2018); SE China Jurassic rocks: basalts (Y. Wang et al., 2008); Chebbu gabbro and Southern Jiangxi syenite (X.-H. Li et al., 2003); Eastern Guangxi syenite (Li et al., 2004); Nankunshan aluminous A-type granite (Li et al., 2007); SW Guangdong hornblende granites and granodiorites (Huang et al., 2012); SE China coastal Guangdong I-type granodiorites and biotite monzogranites (Y. Zhang et al., 2015); SE China inland I-type granites (Li et al., 2007; Y. Zhang et al., 2015; Zhang et al., 2017); Hong Kong granites (Darbyshire and Sewell, 1997). (c) $\varepsilon_{Nd}(t)$ *vs* $\varepsilon_{Hf}(t)$; SE China Jurassic granites: Guangdong Province inland and coastal granites from Y. Zhang et al. (2015b); Nanling Range granites from Zhang et al. (2017). Mantle and terrestrial array after Vervoort et al. (1999). Symbols are as in Fig. 5.5.

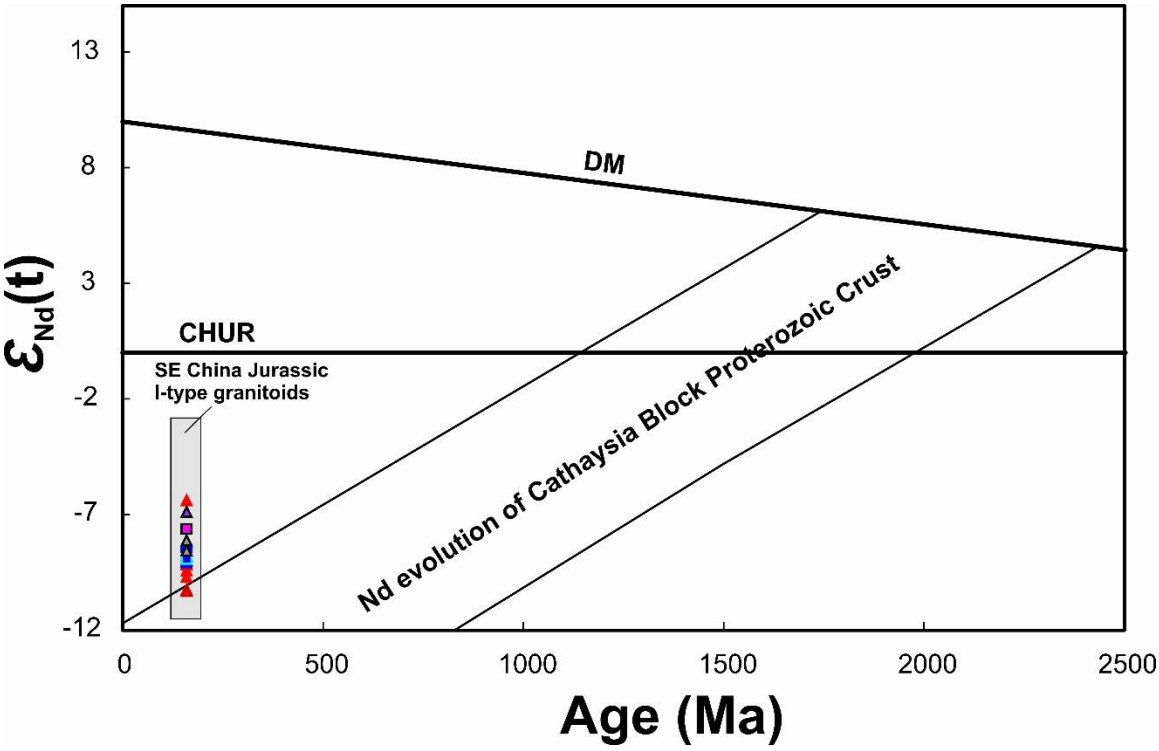

Fig. 5.10. $\varepsilon_{Nd}(t)$ *vs* t (crystallization age); SE China Jurassic granitic rocks (Darbyshire and Sewell, 1997; Li et al., 2007; Huang et al., 2012; Y. Zhang et al., 2015; Zhang et al., 2017); Cathaysia Block Proterozoic crust (Hu and Zhang, 1998; Shen et al., 2003). Symbols are as in Fig. 5.5.

While the Sr isotope data from granitic rocks and MME define a well-correlated isochron ($r = 0.998$; $n = 23$; $p < 0.001$), with initial $^{87}Sr/^{86}Sr = 0.7121$ and $t = 161.8$ Ma, the Sm-Nd ($r = 0.714$; $n = 23$; $p < 0.001$) and Lu-Hf ($r = 0.332$; $n = 23$; $p < 0.122$) diagrams show a scattered set of data (see Appendix F). This aspect, at first sight unexpected, since Rb and Sr are more mobile than Sm, Nd, Lu and Hf during alteration processes, will be discussed in section 5.5.2.2.2. Some Nd–Hf isotopic decoupling is suggested by the dispersion in the $\varepsilon_{Nd}(t)$ *vs* $\varepsilon_{Hf}(t)$ diagram (Fig. 5.9c), where some samples deviate significantly from the mantle and terrestrial arrays as defined by Vervoort et al. (1999).

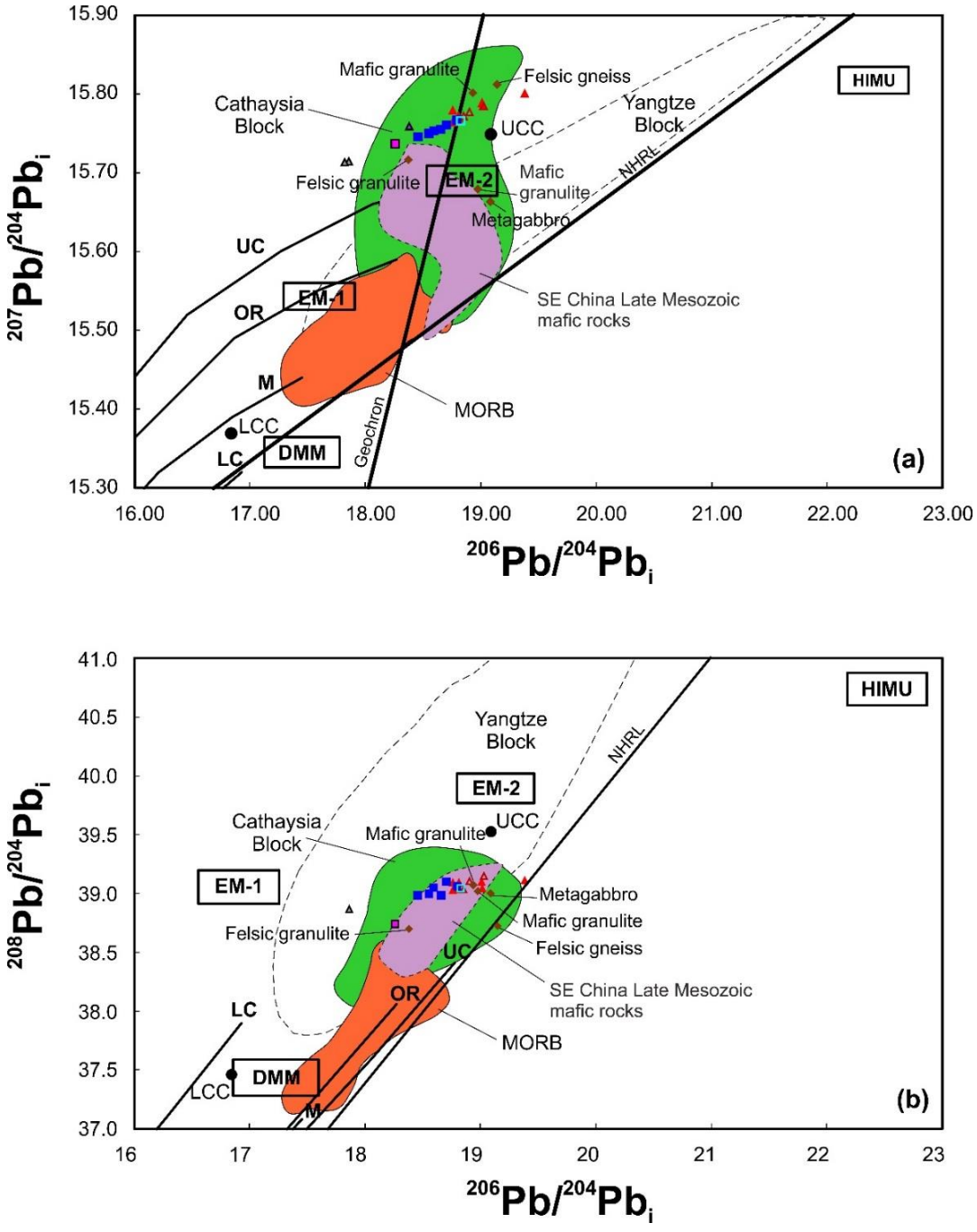

Fig. 5.11. (a) $^{207}Pb/^{204}Pb_i$ *vs* $^{206}Pb/^{204}Pb_i$ and (b) $^{208}Pb/^{204}Pb_i$ *vs* $^{206}Pb/^{204}Pb_i$ diagrams for Macao granitic rocks and MME. $^{206}Pb/^{204}Pb_i$, $^{207}Pb/^{204}Pb_i$ and $^{208}Pb/^{204}Pb_i$ are the initial Pb isotopic ratios at t = 160 Ma. Western Cathaysia Block xenoliths from Li et al. (2018); Late Mesozoic mafic rocks from Y. Wang et al. (2008); Yangtze and Cathaysia blocks Pb isotopic compositions from Zhang (1995); MORB from DMM (Depleted MORB Mantle), EM-1 (Enriched Mantle 1), EM-2 (Enriched Mantle 2) and HIMU ("High-μ"; μ = $^{238}U/^{204}Pb$) mantle domains from Hofmann (2003). Evolutionary Pb curves for different terrestrial reservoirs from the Plumbtectonics model (Zartman and Doe, 1981): UC – Upper Crust; OR – Orogene; M – Mantle; LC – Lower Crust. LCC – Lower Continental Crust (Rudnick and Goldstein, 1990; Paul et al., 2003), UCC – Upper Continental Crust (Asmerom and Jacobsen, 1993). Symbols are as in Fig. 5.5.

The MGI granites have a wide range of isotopic values (Figs. 5.9 to 5.11), with initial $^{87}Sr/^{86}Sr$ ratios of 0.7109–0.7201, $\varepsilon_{Nd}(t)$ = -10.3 to -6.4, $\varepsilon_{Hf}(t)$ = -12.56 to -6.13, and two-stage depleted mantle model ages of 1.42–1.72 Ga (Nd T_{DM2}) and 1.60–2.00 Ga (Hf T_{DM2}). The initial Pb isotopic ratios are $^{206}Pb/^{204}Pb$ = 18.7552–19.3800, $^{207}Pb/^{204}Pb$ = 15.7641–15.8001 and $^{208}Pb/^{204}Pb$ = 39.0281–39.1518.

The MGII granites, on the other hand, show a much more limited range of values, with initial $^{87}Sr/^{86}Sr$ ratios of 0.7099–0.7116, $\varepsilon_{Nd}(t)$ = -9.1 to -8.6, $\varepsilon_{Hf}(t)$ = -10.0 to -6.8, Nd T_{DM2} of 1.59–1.63 Ga and Hf T_{DM2} of 1.64–1.76 Ga. The initial Pb isotopic ratios are: $^{206}Pb/^{204}Pb$ = 18.4575–18.7964, $^{207}Pb/^{204}Pb$ = 15.7446–15.7662 and $^{208}Pb/^{204}Pb$ = 38.9839–39.1022. They are slightly less radiogenic than those reported for MGI (Fig. 5.11).

The studied samples define an array above the Northern Hemisphere Reference Line (NHRL; Hart, 1984) in the $^{207}Pb/^{204}Pb$ *vs* $^{206}Pb/^{204}Pb$ (Fig. 5.11a) and $^{208}Pb/^{204}Pb$ *vs* $^{206}Pb/^{204}Pb$ (Fig. 5.11b) diagrams, but closer to the NHRL in the latter. In general, Pb isotopic signatures plot progressively away from the NHRL, towards more radiogenic compositions (Fig. 5.11). Macao Granites plot close to the upper continental crust composition (Asmerom & Jacobsen, 1993), but above the upper continental crust evolution curve of Zartman and Doe (1981).

Overall the isotopic compositions of the MME are identical to those of the granites, plotting above the NHRL and presenting negative $\varepsilon_{Nd}(t)$ and $\varepsilon_{Hf}(t)$ values as well as Sr isotopic signatures more radiogenic than the BSE. Most of the MME and host rocks plot above the evolutionary trend of the Cathaysia Block Proterozoic basement (Fig. 5.10). However, it should be noticed that the isotopic similarity between MME and host granites is variable, being more evident for Sr isotopic ratios than for other systems (see Table E.1 and Appendix F).

5.5. Discussion

5.5.1. Petrogenetic type: I-, S- or A-type granites?

Most of granitic rocks in Macao are strongly evolved (SiO_2 up to 76.92 wt%), making a difficult task to determine their genetic type. Indeed, highly fractionated granites tend to have converging major-element compositions and similar mineral compositions (King et al., 1997). The best approach in these cases is through the study of distinctive granite associations where the

granite type can be identified using the chemical and mineralogical composition of the least evolved members (Chappell and White, 1992).

The mineralogy of the Macao granites is characterized by absence of primary Al-rich minerals such as muscovite, cordierite and andalusite, typical of S-type granites, as well as of symptomatic minerals of peralkalinity (e.g. alkali pyroxene and riebeckite) characteristic of A-types. Al-deficient minerals like hornblende and biotite are common in I-types, but only the latter occurs in the studied samples and this mineral can also occur in the other genetic types (e.g. Chappell and White, 1992; King et al., 1997). MGI highly fractionated granites contain garnet, which is most common in S-type granites. However, this accessory phase has also been found in some I- and A-type granites (e.g. Wu et al., 2004; Zhang et al., 2017) and therefore its use as a diagnostic mineral may be misleading. The Macao granites have relatively low Zr + Nb + Ce + Y contents (< 350 ppm) and, except for the MGI highly fractionated granites, 10^4 x Ga/Al values are lower than 2.6 and Y < 80 ppm (Fig. 5.12a and 5.12b), distinct from the typical A-type granites (Whalen et al., 1987). Those MGI highly fractionated granites have Y (31–212 ppm; Fig. 5.12b) and Nb (9.7–43.3 ppm) contents transitional between A-type and I-type (Whalen et al., 1987). However, as shown in section 5.5.2.1.2, these higher Nb and Y contents are probably the result of late-stage magmatic processes. Even though low Zr contents could be due to fractionation of zircon, the less fractionated granites in Macao still have lower Zr contents (Zr = 82–245 ppm) than those characteristic of A-types (>250 ppm; Whalen et al., 1987). In addition, the samples that plot into the A-type field have very low temperatures of formation (T_{Zr} = 679–750 ºC; see also footnotes of Table D.2, Appendix D) compared with the relatively high temperatures commonly reported for A-type granites (T_{Zr} > 830 ºC; Clemens et al., 1986).

The studied granites are metaluminous to weakly peraluminous (A/CNK < 1.13; Fig. 5.5b) and have high Na_2O (2.89–4.26), in contrast to highly fractionated S-type granites which are strongly peraluminous with A/CNK >> 1.1 and have lower Na_2O contents (~2.51 wt%; Chappell and White, 1992). Plus, the Macao granites have decreasing P_2O_5 with increasing SiO_2 (down to less than 0.01 wt%; Fig. 5.6f) contrasting with the observed for S-types (Chappell and White, 1992). This is because apatite usually reaches saturation in metaluminous and mildly peraluminous melts (A/CNK < 1.1), but is highly soluble in strongly peraluminous melts (Wolf and London, 1994). The positive correlations between Pb and SiO_2 (Fig. 5.6g) and between Rb and Y (Fig. 5.6h)

are also consistent with I-type evolutionary trends (Chappell and White, 1992). The Macao granites also show strong negative Ba, Sr and Eu anomalies, more common in I-type granites (Fig. 5.7).

Thus, despite the inherent difficulties in assigning genetic type when studying fractionated granites, it is possible to conclude that the granitic rocks from Macao most likely belong to the I-type.

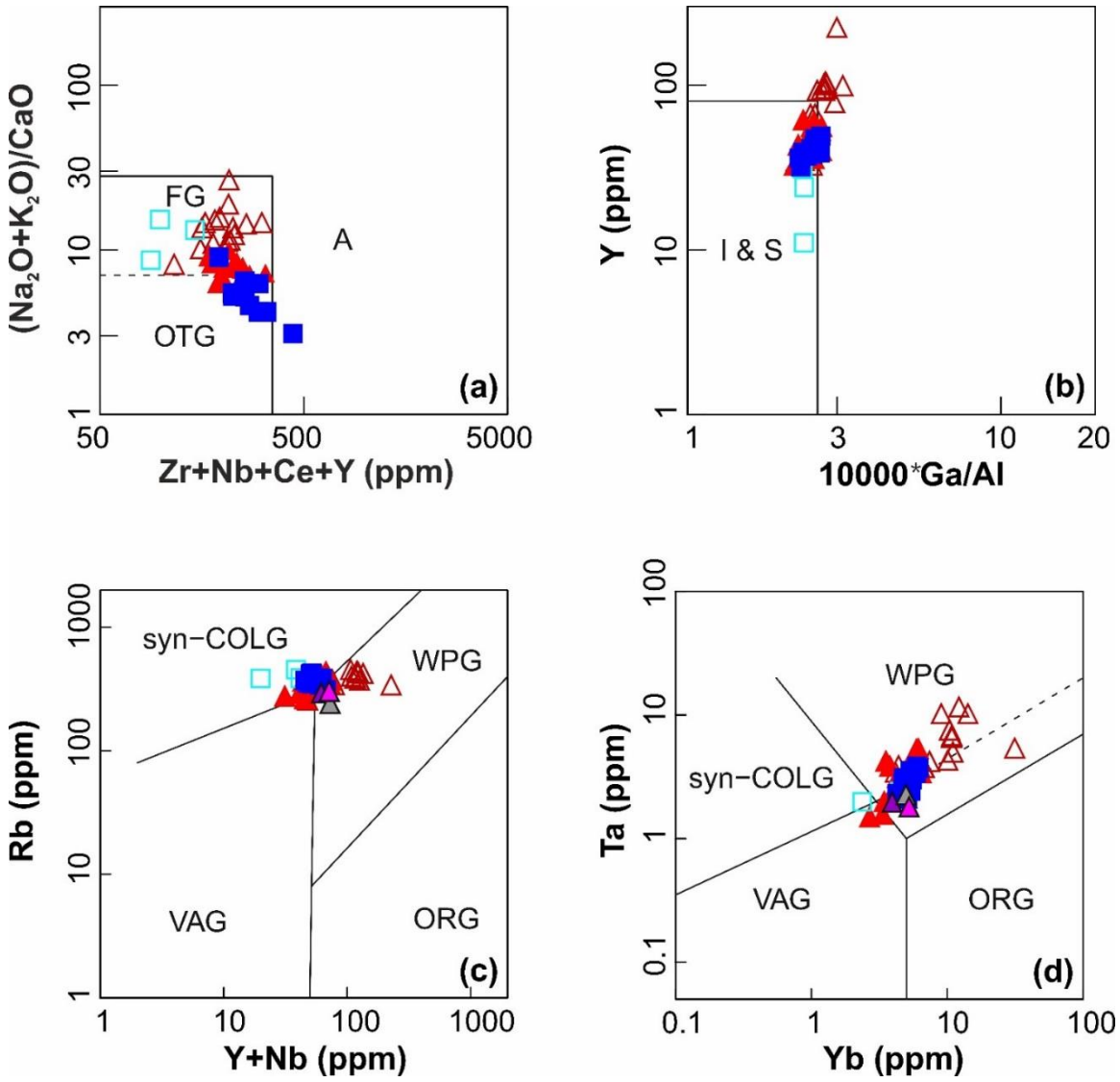

Fig. 5.12. Geotectonic discrimiant diagrams for the Macao granites: (a) $(Na_2O+K_2O)/CaO$ *vs* Zr+Nb+Ce+Y (ppm) and (b) Y *vs* 10,000*Ga/Al from Whalen et al. (1987); (c) Rb (ppm) *vs* Y+Nb (ppm) and (d) Ta (ppm) *vs* Yb (ppm) from Pearce et al. (1984). FG: Fractionated felsic granites; OGT: unfractionated M-, I- and S-type granites; Syn-COLG: syn-collision granites; WPG: within-plate granites; VAG: volcanic arc granites; ORG: ocean ridge granites. Symbols are as in Fig. 5.5.

5.5.2. Causes of the chemical variability

MGI and MGII granites are mainly biotite granites (see section 5.4.1), each having a wide range of textures, mineral assemblages and geochemical compositions. The coarse-grained porphyritic varieties of each group have lower SiO_2 and higher FeO^T, TiO_2, MgO, Sr, Ba and Eu concentrations as well as higher Zr/Hf ratios than the non-porphyritic medium- to fine-grained varieties, suggesting that magma evolution processes explain at least part of the chemical variability.

The MGII granites have relatively constant initial isotopic compositions with a range (Δ) of initial $^{87}Sr/^{86}Sr$ ratios of 0.017, indicating that elemental variation reflects fractional crystallization. On the other hand, the MGI granites show a wider variation of initial isotopic ratios (e.g. Δ of initial $^{87}Sr/^{86}Sr = 0.075$) and $^{87}Sr/^{86}Sr$ up to 0.7201, suggesting open-system behaviour during magmatic evolution.

5.5.2.1. Closed-system magmatic evolution processes

5.5.2.1.1 Fractional crystallization

Considering the isotope characteristics described above, the discussion of the fractional crystallization will be mainly focused on MGII and on the less evolved rocks (weakly to moderately fractionated granites) of MGI. The MGI highly fractionated granites have chemical characteristics that are better explained by the process explained in section 5.5.2.1.2. Overall, the two groups show similar fractionation trends for major and trace elements.

The role of plagioclase fractionation is well evidenced by the Al_2O_3 (Fig. 5.6a), CaO (Fig. 5.6b) and Sr (Figs. 5.7, 5.13a and 5.13b) decrease with increasing SiO_2 contents and by more marked Eu negative anomalies in the more evolved rocks (Figs. 5.8 and 5.13c). These Eu anomalies are in line with the estimated conditions of oxygen fugacity, using biotite compositions, which are below that characterizing the nickel-nickel oxide (NNO) buffer (Fig. 5.4b). In fact, such conditions allowed significant amount of Eu to be present in the divalent state, which is highly compatible with plagioclase (e.g. Bindeman and Davis, 2000). During fractionation there was a gradual change of plagioclase chemistry from andesine to albite (Fig. 5.4a).

The role of K-feldspar on the magma evolution is best seen on the Sr *vs* Ba diagram (Fig. 5.13b) by a steep decrease of Ba contents with decreasing Sr. Separation of biotite contributed to decreasing MgO and FeO^T contents with increasing SiO_2 (Figs. 5.6d and 5.6e) and is also evidenced by the clear decrease of V (55–0 ppm) and Sc (11.6–1.4 ppm) contents, given the very high compatibility of these elements with biotite (e.g. $D_V^{Biotite/melt} = 79.5$ and $D_{Sc}^{Biotite/melt} = 42.4$; Bea et al., 1994).

Negative correlations between SiO_2 and TiO_2 (Fig. 5.6c) suggest fractionation of Ti-bearing minerals such as titanite and Fe-Ti oxides, the latter also influencing the FeO^T decrease (Fig. 5.6e). Fractionation of titanite was probably more important in MGII where this mineral is particularly abundant. Negative Nb, Ta and Ti depletions (Fig. 5.7) are also related to the fractionation of Ti-bearing phases. The decrease in Zr contents with increasing SiO_2 is indicative of zircon fractionation (Fig. 5.6i). Despite zircon's relatively high partition coefficients for HREE, modelling suggests that its fractionation did not exert much control on the REE variation (Figs. 5.13d–f). In addition, MGI and MGII granites have increasing U contents with evolution indicating that the global partition coefficient for U is <1. Since the partition coefficient of U in zircon is relatively high ($D_U^{Zircon/melt} = 354$; Bea et al., 1994), this also supports that zircon was not a major fractionating phase.

The fractionation of phosphate minerals such us apatite and monazite promoted decrease in P_2O_5 contents with increasing SiO_2 (Fig. 5.6f). Accessory phases such as allanite and monazite that have extremely high partition coefficients for LREE ($D_{La}^{Allanite/melt} = 2594.5$; $D_{La}^{Monzite/melt} = 3200$; see Appendix G for references) seem to have partially controlled the REE variation of Macao granites, as it can be seen on the $(La/Yb)_N$ *vs* La (Fig. 5.13d) and Th/La *vs* Sm/La (Fig. 5.13e) vector diagrams.

The concave upwards shape of the MGII REE patterns (Fig. 5.8b) could be achieved through higher fractionation of MREE-compatible minerals such as apatite and/or titanite, corroborating the fractionation vectors in the Sm/Nd *vs* Lu/Gd diagram (Fig. 5.13f). During the evolution of MGII, the LREE were more compatible than the HREE (Fig. 5.8b). Indeed, the depletion of La was almost 14 times greater than that of Lu. However, in agreement with Quelhas et al. (2019), the most evolved rocks of both groups probably underwent different fractional crystallization paths producing distinct REE patterns (cf. Fig. 5.8a and Fig. 5.8b). Indeed, the Sm/La *vs* Th/La diagram

(Fig. 5.13e) shows that a slight increase of these ratios in the MGI granites reflects a stronger influence of allanite fractionation, whereas the increase of Th/La ratios (with nearly constant Sm/La ratios) in the MGII granites seems to be consistent with a stronger effect of monazite fractionation. The role of allanite fractionation in MGI, and eventually of monazite and xenotime, is further supported by progressive depletion of LREE and enrichment of HREE (Fig. 5.8a).

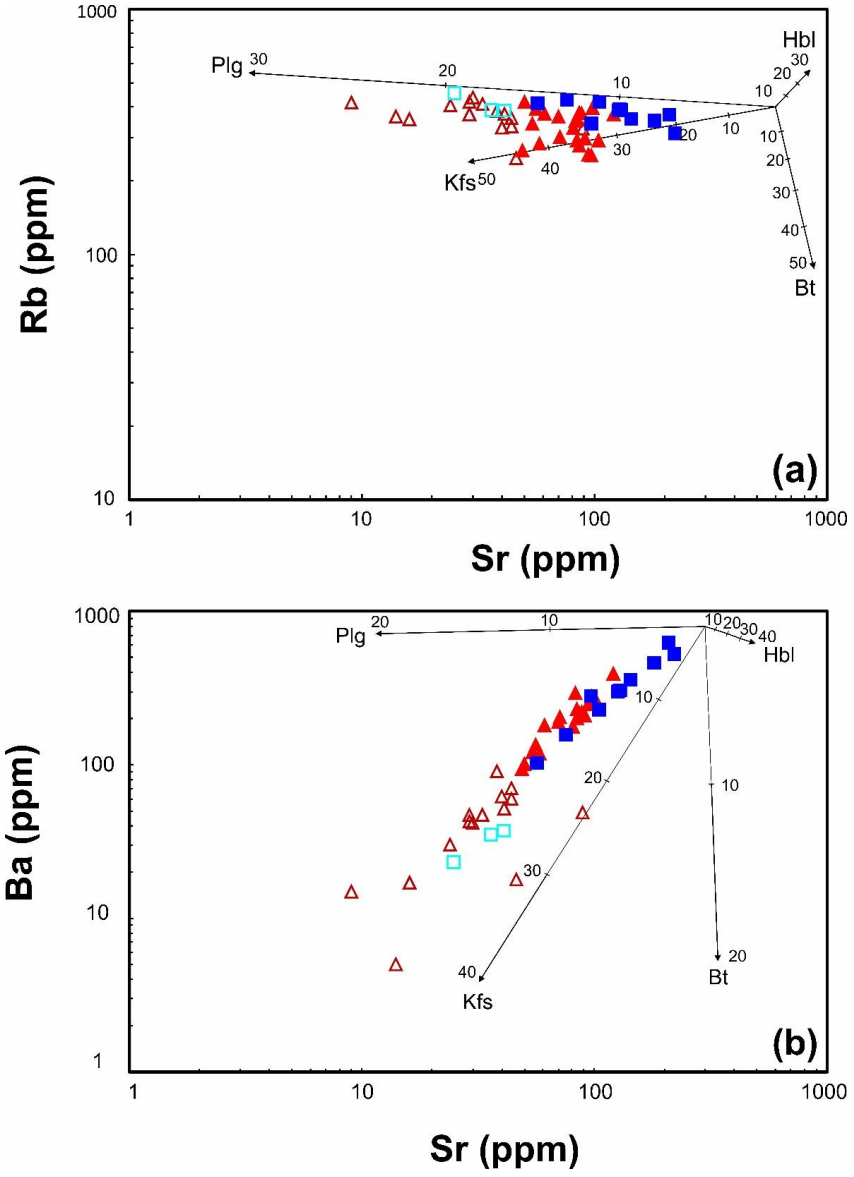

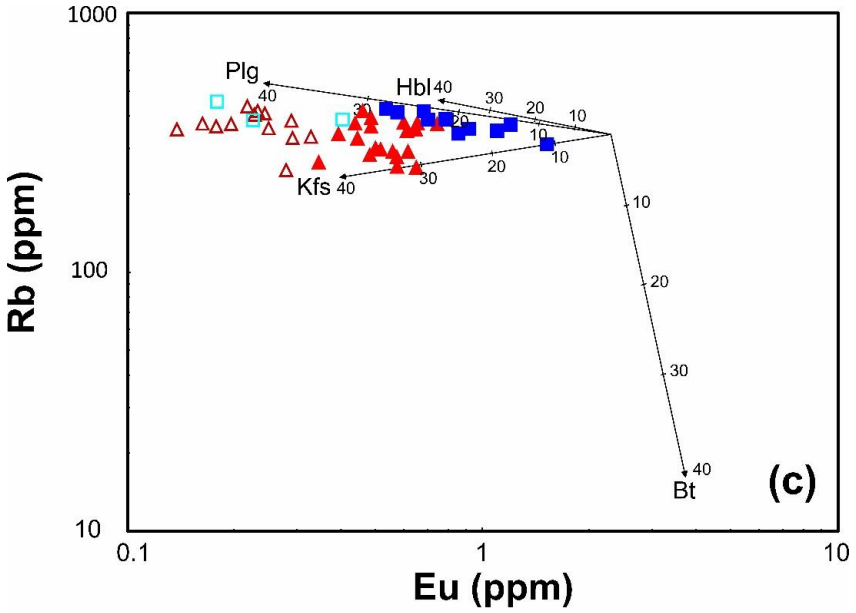
Rb (ppm)
Eu (ppm)
Plg
Hbl
Kfs
Bt
(c)

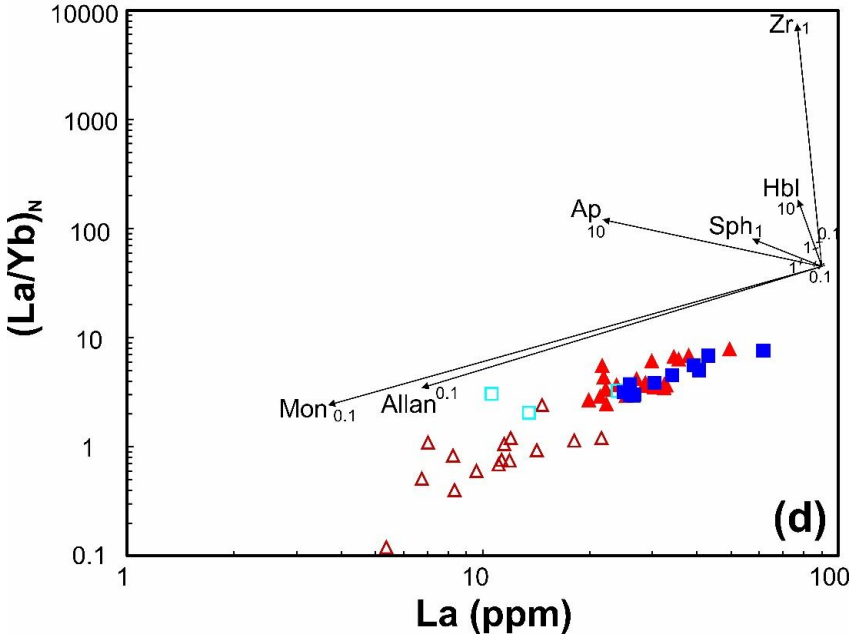
(La/Yb)N
La (ppm)
Zr
Hbl
Ap
Sph
Mon
Allan
(d)

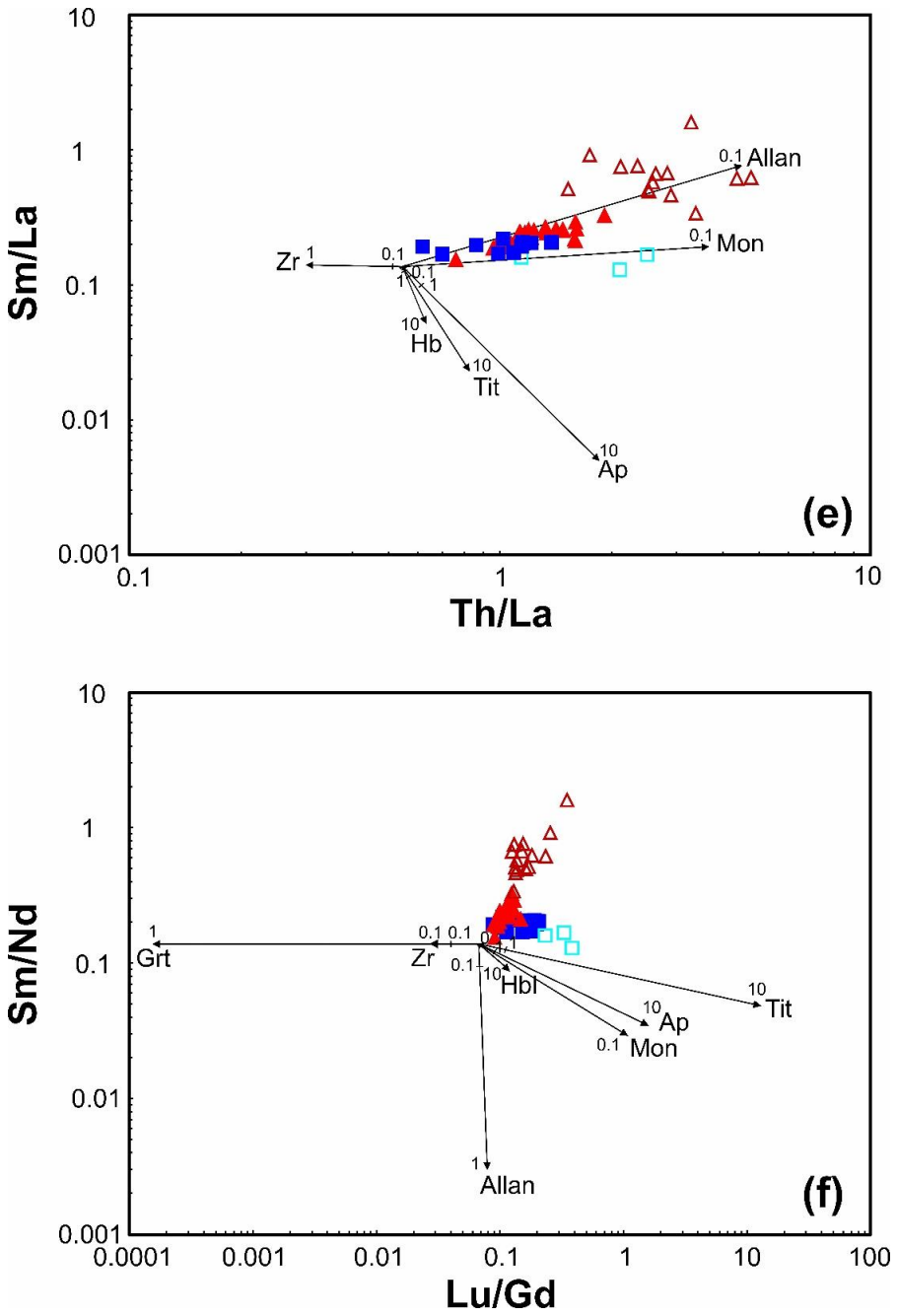

Fig. 5.13. Trace element fractionation vector diagrams for the Macao granites: (a) Rb (ppm) *vs* Sr (ppm); (b) Ba (ppm) *vs* Sr (ppm); (c) Rb (ppm) *vs* Eu (ppm); (d) $(La/Yb)_N$ *vs* La (ppm); (e) Sm/La *vs* Th/La; (f) Sm/Nd *vs* Lu/Gd. Vectors represent the fractionation effect of accessory minerals calculated using the Rayleigh fractional crystallization equation (see Appendix A, section 1.3.2.2) and the partition coefficients from the literature (see Appendix G for the values and respective references); tick marks indicate the percentage of mineral phase removed. Abbreviations: Kfs – Alkali feldspar; Pl – plagioclase; Bt – biotite; Hbl – hornblende; Zrn – zircon; Ap – apatite; Ttn – titanite; Grt – garnet; Mnz – monazite; Aln – allanite. Symbols are as in Fig. 5.5.

In summary, the weakly to moderately fractionated granites of both groups are characterized by similar liquid lines of descent, while these differ for the highly fractionated facies mainly due to distinct accessory fractionating phases. The fact that I-type granites from Macao do not contain hornblende (characteristic of I-type granites), indicates that they probably represent evolved stages of a fractionating magma from which this mineral had already been completely removed. In adjacent areas, less evolved hornblende-bearing I-type granodiorites and monzogranites are spatially associated with Jurassic I-type biotite monzogranites similar to those of Macao and in the field a gradual change in lithotypes is observed (Sewell et al., 1992; Huang et al., 2012; Y. Zhang et al., 2015). Those rocks are coeval with Macao biotite granites and, therefore, it can be assumed that the latter represent relatively evolved lithotypes of a granitic suite having as less fractionated members hornblende-bearing I-type granodiorites and monzogranites.

5.5.2.1.2 Late-stage melt/fluid interactions in the MGI granites

Apparently no mineral vector explains the steep increase in Sm/Nd ratios of the MGI granites (Fig. 5.13f), suggesting that other process must have been involved. The MGI highly fractionated granites show evidence for the REE tetrad effect ($TE_{1,3}$ = 1–1.13), which can lead to an increase in Sm/Nd ratios (Irber, 1999). Other peculiarities of this facies are the enrichment in Y, HREE and high field strength elements (HFSE) such as Nb, Ta, U and Pb, which were accommodated in accessory phases such as spessartine-rich garnet, thorite and tantalo-niobates. They also have non-chondritic ratios of Zr/Hf (12.24–25), K/Ba (498.9–9560), K/Rb (101.83–158.7), La/Nb (0.15–2.18) and La/Ta (0.69–11.32), and their non-CHARAC (CHArge-and-RAdius-Controlled; Bau, 1996) trace element behaviour is shown on the Y/Ho *vs* Zr/Hf diagram (Fig. 5.14a).

Different processes have been proposed for the formation of the REE tetrad effect: (1) fractionation of accessory minerals (e.g. Yurimoto et al., 1990); (2) post-magmatic water-rock interactions (e.g. Takahashi et al., 2002), and (3) late-stage melt/fluid interactions (e.g. Bau, 1996; Irber, 1999; Jahn et al., 2001; Tao et al., 2013), in particular with F-rich fluids (e.g. Veksler et al., 2005).

It has been shown that the tetrad effect cannot be adequately modelled with currently known REE mineral/melt partition coefficients (e.g. Bau, 1996; Irber, 1999), which are smooth functions of ionic radii. Furthermore, accessory minerals that display tetrad effects similar to those of the host rocks have been reported (Irber, 1999), indicating that the accessory mineral tetrad effect was

inherited from a melt tetrad effect rather than through a process of mineral fractionation. This argument also makes the second process unlikely. Moreover, no REE tetrad effects have been observed in hydrothermally altered rocks that are not highly evolved.

The third hypothesis invokes the interaction of highly volatile-enriched late magmatic fluids with evolved granitic melts as the cause for the tetrad effect (Irber, 1999; Jahn et al., 2001), a process frequently interpreted as involving fluorine-rich fluids (e.g. Zhang et al., 2017; Jiang et al., 2018). This model seems to be applicable to the MGI granites. Indeed, some of the biotites from the highly fractionated MGI granites with the tetrad effect have relatively high F (up to 2.13 wt%), and large crystals of purple fluorite have also been found associated with quartz veins, suggesting circulation of F-rich fluids. Additionally, the MGI highly fractionated granites and the more evolved coeval granites from surrounding areas, characterized by non-chondritic Y/Ho and Zr/Hf ratios and pronounced REE tetrad effects (Tao et al., 2013; Huang et al., 2015; Jiang and Zhu, 2017; Zhang et al., 2017), show a progressive decrease and increase in Zr/Hf and Y/Ho ratios, respectively, towards the hydrothermal fluorite veins field (Fig. 5.14a). Therefore, we propose that the stage of evolution represented by the MGI highly fractionated granites corresponds to the onset of fluid/melt interaction in a highly evolved granitic system, which may have led to enhanced hydrothermal activity in more evolved stages as those represented in neighbouring areas.

The behaviour of Nb and Ta also seems to support this process. The MGI highly fractionated granites are characterized by significantly higher contents of Nb and Ta than the less evolved facies (Fig. 5.14b). Experimentally determined partition coefficients of Ta and Nb between hydrothermal fluid and magma are low (e.g. $D_{Nb}^{Fluid/melt} < 0.1$; Zajacz et al., 2008), meaning that these elements are more compatible with the granitic magma than with the fluid.

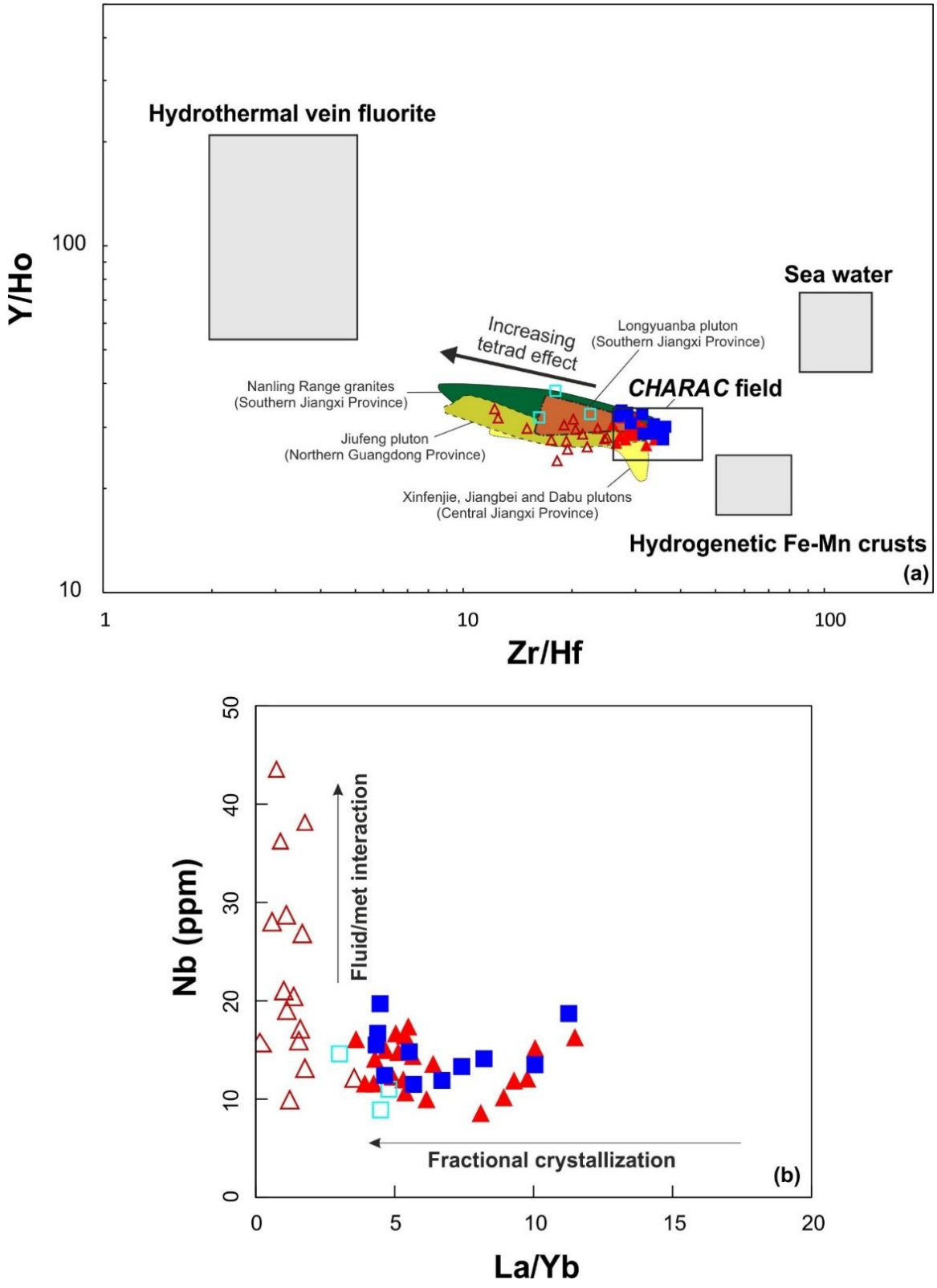

Fig. 5.14. Y/Ho *vs* Zr/Hf diagram (after Bau, 1996). SE China granitic rocks: Nanling Range (Zhang et al., 2017); Longyuanba pluton (Tao et al., 2013); Jiufeng pluton (Huang et al., 2015); Xingfengjie, Jiangbei and Dabu plutons (Jiang and Zhu, 2017). (b) Nb *vs* La/Yb diagram. Symbols are as in Fig. 5.5.

In conclusion, some of the geochemical elemental peculiarities of the MGI highly fractionated facies are the result of late-stage melt/fluid interactions. Considering that this late-stage fluid is considered to be exsolved from the magma, it should have the same initial isotopic ratios as the magma. Plus, one of the samples with the REE tetrad effect (C71, $TE_{1,3}$ = 1.10; see Table D.2, Appendix D), has a similar initial $^{87}Sr/^{86}Sr$ ratio as the less evolved samples of MGI and MGII (see Fig. 5.9a and Table E.1, Appendix E). Therefore, it is most unlikely that isotopic signatures of the granitic rocks significantly reflect such process.

5.5.2.2. Open-system magmatic processes

5.5.2.2.1 Origin of high radiogenic Sr isotope compositions

A significant difference in Sr and Nd isotopic compositions between MGI and MGII granites is observed (Fig. 5.9b). While the MGII clusters at about $\varepsilon_{Nd}(t)$ = -9 and initial $^{87}Sr/^{86}Sr \approx 0.7108$, the MGI granites are characterized by $\varepsilon_{Nd}(t)$ ranging from -10.3 to -6.4 and initial $^{87}Sr/^{86}Sr$ varying between 0.7109 and 0.7201. Based on these differences, the MGII granites can be considered a comagmatic suite having evolved in closed system, at odds with what can be inferred for MGI.

In Macao, metasedimentary enclaves of Devonian age are enclosed within the MGI granites suggesting that Jurassic granitic magmas were emplaced at shallow crustal levels, a percept reinforced by the fact that in the neighbouring area of Hong Kong granite plutons, of similar age, intrude basement rocks consisting of deformed Devonian, Carboniferous, Permian and Lower Jurassic metasedimentary rocks (see Sewell et al., 1992). The zircon population of the MGI granites is characterized by a significant percentage of inherited grains (xenocrysts) with identical ages to the Paleozoic strata (Quelhas et al., 2019). Additionally, the MGI highly fractionated granites contain spessartine-rich garnet, whose origin, in highly fractionated granites from other areas of SE China, has been linked to assimilation of Mn-rich metasedimentary materials (e.g. Zhang et al., 2017). All these indicate that MGI granitic magmas assimilated metasedimentary crustal materials when in route to shallow crustal levels.

In the $^{87}Sr/^{86}Sr_i$ *vs* Sr diagram (Fig. 5.9a), the MGI granites show a progressive increase of Sr isotopes with increasing Sr (used as a proxy for the degree of evolution), suggesting that the increase in isotope ratios is likely to reflect an AFC (Assimilation Fractional Crystallization) process.

To evaluate the feasibility of such process (Fig. 5.9b), the Darongshan peraluminous granite at 160 Ma (point D, Sr = 78 ppm, Nd = 38 ppm, initial $^{87}Sr/^{86}Sr$ = 0.7374, and $\varepsilon_{Nd}(t)$ = -14.9; Hsieh et al., 2008) was chosen as a representative of the SE China upper crust, while the melt derived from lower crust metaigneous rocks is represented by the ca. 160 Ma hornblende-bearing I-type granodiorite in an adjacent area of Macao (point G, Sr = 409 ppm, Nd = 21.9 ppm, $^{87}Sr/^{86}Sr_i$ = 0.7057, and $\varepsilon_{Nd}(t)$ = -4.33; Huang et al., 2012), here considered a proxy for the parental magma of the MGI granites. The resulting AFC curves , for different degrees of assimilation, pass through the range of MGI Sr–Nd isotopic data (Fig. 5.9b), endorsing the hypothesis of assimilation of upper crustal materials by the ascending I-type granitic magmas as a cause for the more radiogenic initial $^{87}Sr/^{86}Sr$ ratios of the MGI granites.

The Macao granites display a linear trend on the $^{206}Pb/^{204}Pb$ *vs* $^{207}Pb/^{204}Pb$ diagram (Fig. 5.11a), which can be interpreted either as a secondary isochron or, given that the used ratios have the same denominator, as mixing lines. Interestingly, the MGI granites are generally more radiogenic plotting to the right of the Geochron, with the more radiogenic samples being the most fractionated, and contaminated (see above), facies. In contrast, the MGII granites, for which no evident signs of contamination were found, plot to the left of the Geochron, being in general less radiogenic. Considering these facts and the similar initial $^{87}Sr/^{86}Sr$ and $^{143}Nd/^{144}Nd$ ratios of the less evolved rocks of both groups, we interpret the linear trend as a mixing line between a granitic magma and a more radiogenic crustal component, supporting a model involving AFC as the cause of the relatively radiogenic Sr isotope ratios of the MGI.

5.5.2.2.2 Isotopic decoupling – evidence for magma mixing

Notwithstanding the clear influence of AFC processes on the isotopic composition of the MGI granites, it does not completely explain part of the of $\varepsilon_{Nd}(t)$ and $\varepsilon_{Hf}(t)$ variation not dependent of the degree of evolution of the samples.

The Macao granites from both groups contain abundant MME with magmatic textures and SiO_2 contents down to 59.8 wt%. They are intermingled and variably hybridized with the host granites, with some K-feldspars megacrysts straddling the boundaries between enclaves and host rocks. These observations indicate mixing between granitic and mafic magmas (e.g. Vernon, 1990).

Magma mixing is here considered to be the cause for somewhat distinct behaviour of the several isotopic systems. This is emphasized by the fact that the Sr isotope signatures from the

Macao granitic rocks and MME define a good correlation with $^{87}Rb/^{86}Sr$ ratios, in contrast with the observed for the Nd and Hf isotope data, which scatter significantly in the same type of diagram (see section 5.3.3 and Appendix F).

Pankhurst et al. (2011) studied the variation of trace elements across the boundary between MME and the host granite. While Sr shows a sigmoidal pattern of distribution indicating chemical diffusion, REE elements such as Ce and Nd show concentration peaks at the MME-granite boundary, suggesting accumulation of REE-bearing phases. It is possible that these accessory phases acted as barriers that prevented subsequent diffusion processes and Nd isotopic homogenization. On the other hand, Hf is extremely compatible with zircon [$D_{Hf}^{Zircon/melt} = 3193.5$; Mahood and Hildreth (1983)] and, because zircon is a highly resistant and refractory mineral, it has the ability to lock distinct Hf isotopic ratios from different magmas, thus preventing an efficient chemical homogenization.

Sr is strongly partitioned into plagioclase ($D_{Sr}^{Plag/melt} = 15.63$; see Appendix G for reference). In the Macao granitic rocks, many large plagioclase crystals show oscillatory zoning with variable An% contents (see Table C.4, Appendix C). This can be attributed to several cycles of magma chambers recharge promoting magma mixing. The homogenization of the Sr isotope signatures may have been achieved by effective release and re-incorporation of Sr during repeated cycles of magma mixing, a process facilitated by the relatively high diffusion coefficient of Sr in plagioclase ($1*10^{-12}$ to $1*10^{-15}$ m^2s^{-1}; Magaritz and Hofmann, 1978). These values are significantly higher in comparison to those of Nd in titanite ($1.10*10^{-22}$ to $2.23*10^{-18}$ m^2s^{-1}, Cherniak, 1995), Sm in xenotime ($6.01*10^{-22}$ to $2.78*10^{-18}$ m^2s^{-1}; Cherniak, 2010) and Hf in zircon ($8.02*10^{-23}$ to $3.77*10^{-20}$ m^2s^{-1}; Cherniak et al., 1997). In addition, the rate of exchange of Nd isotopes is two times lower than the rate of exchange of Sr isotopes ($5.1*10^{-8}$ cm^2s^{-2} in a mafic material with 50% SiO_2 to $1.9*10^{-7}$ cm^2s^{-2} in a felsic material with 70% SiO_2, at 1255ºC and 10 kbar; Lesher, 1990).

Thus, decoupling of Sr and Nd and Hf isotope systems in Macao granites might have resulted from magma mixing. This process was able to cause the homogenization of Sr isotope ratios but not of the Nd and Hf isotopes, which have not participated in this interaction to the degree of Sr because they were strongly partitioned into REE-bearing refractory phases characterized by very low diffusion rates. We note that, given the greater degree of isotopic decoupling and higher abundance and bigger dimensions of MME in the MGI granites, magma mixing probably played a

more important role in the evolution of MGI magmas than in those of the MGII, where its influence was probably vestigial.

5.5.3. Magma sources

It has been proposed that the SE China Jurassic biotite granites, with features transitional between I-type and S-type granites, were formed in a source region characterized by physical juxtaposition between infracrustal metaluminous and supracrustal peraluminous rocks (Huang et al., 2012). However, as pointed out by Clemens et al. (2011), melting of biotite + sillimanite assemblages in evolved metapelitic sources will occur significantly earlier during a crustal heating cycle than will that of the hornblende + biotite assemblages characteristic of I-type sources. Consequently, even where interlayered sources exist, S- and I- type magmas are most likely produced as temporally separate batches. Considering this and the fact that I-S transitional characteristics are more evident in the MGI highly evolved facies, such features in Jurassic biotite granites from Macao, and possibly other areas of SE China, most likely result from AFC processes affecting I-type granitic magmas, as described in section 5.5.2.2.1.

I-type granites are considered to be formed mainly by partial melting of mafic to intermediate metaigneous crustal sources (e.g. Chappell, 2004; Clemens et al., 2011). For the Macao I-type granites, such origin is supported by the their positioning in the $^{208}Pb/^{204}Pb$ *vs* $^{206}Pb/^{204}Pb$ diagram (Fig. 5.11b) overlapping the isotopic signatures of metagabbro and mafic granulite xenoliths enclosed in Mesozoic basalts in the neighbouring southern Hunan Province, SE China (Li et al., 2018).

Experimental studies show that ~ 20 – 40% melting between 1050 and 1100°C of low-K tholeiitic amphibolites can produce silicic to intermediate composition liquids (high-Al_2O_3 trondhjemitic—tonalitic, granodioritic, quartz dioritic, dioritic) leaving a granulite (plagioclase + clinopyroxene ± orthopyroxene ± olivine) residue at 8 kbar and garnet granulite to eclogite (garnet + clinopyroxene) residues at 12 – 32 kbar (Rapp and Watson, 1995). However, the resultant melts are usually low in K_2O and have $Na_2O/K_2O > 1$, in contrast with Macao granites which are high in K_2O (3.92-5.36 %) and have $Na_2O/K_2O < 1$. Thus, tholeiitic amphibolite sources are unlikely the source of the Macao granites. Plus, high pressure melting, in which garnet is present as a residual mineral, can also be precluded, since REE patterns do not show significant Y or HREE depletion. Indeed, the weakly to moderately fractionated Macao granites have Sr/Y (0.94–6.56) and La/Yb

(3.61–11.49) significantly lower than those of the experimental melts obtained by Rapp and Watson (1995) from melting of garnet amphibolite and eclogite (Sr/Y and La/Yb up to 680 and 71, respectively).

Compositions similar to those of the Macao granites were obtained experimentally by Sisson et al. (2005). These authors obtained granitic–rhyolitic liquids with $Na_2O/K_2O < 1$ at $SiO_2 > 65\%$ from moderately hydrous (1.7–2.3 wt% H_2O) medium-to-high K basaltic compositions (plagioclase-rich with no garnet) at 700 MPa and fO_2 ranging from ~1.3 to 4 unites above the Ni-NiO buffer. Thus, the less evolved Macao granitic magmas were likely generated by partial melting of infracrustal medium-to-high K basaltic protoliths, probably after some degree of AFC of the coeval hornblende I-type granodiorites and monzogranites (high K_2O, $Na_2O/K_2O < 1$ and SiO_2 = 65–70%) outcropping in neighbouring areas (Huang et al., 2012; Y. Zhang et al., 2015).

As shown above, the MGII granites have a restricted range of isotopic compositions (initial $^{87}Sr/^{86}Sr$ = 0.7099 to 0.7116; $\varepsilon_{Nd}(t)$ = -9.1 to -8.6; $\varepsilon_{Hf}(t)$ = -10.0 to -6.8) suggesting that these rocks were derived from a relatively homogenous source and evolved in a closed-system. In contrast, the wider range of isotopic signatures of MGI granites reflects the occurrence of open-system processes, yet the less evolved rocks have isotope characteristics similar to those of the MGII. This suggests that, despite the ca. 6 Ma time lag between the emplacement of these two groups of granites (see Quelhas et al., 2019), both originated from a similar source.

Model ages of the MGII granites should thus provide a more accurate estimate of the age of the protolith, which, according to the whole-rock Nd and Hf T_{DM2}, might be as old as late Paleo-Proterozoic (1.6–1.7 Ga and 1.6–1.8 Ga, respectively). Late Paleo-Proterozoic was indeed an important timing of crustal growth as inferred from the 1888–1855 Ma gneisses and gneissic granites of southern Zhejiang Province, SE China (Yu et al., 2009). On the $\varepsilon_{Nd}(t)$ *vs* t diagram (Fig. 5.10) most of the Macao and SE China granitic rocks plot above the field defined by the metasedimentary Paleo-Proterozoic Cathaysia basement, indirectly suggesting derivation from metaigneous basement rocks. A juvenile mantle contribution through magma mixing cannot be completely precluded, but it was probably minimal for the MGII granites, in view of the predominant negative $\varepsilon_{Nd}(t)$ and $\varepsilon_{Hf}(t)$ values and the narrow range of their isotopic values (see section 5.5.2.2.2).

Inherited zircon grains with Archean ages have been identified in Macao (Quelhas et al., 2019) and Hong Kong (Sewell et al., 2000b) granitic rocks. Despite no outcrops of Archean rocks have been found in SE China (e.g. Li et al., 2007), studies on crustal xenoliths and zircon xenocrysts entrained in Mesozoic and Cenozoic volcanic rocks from neighbouring areas suggest the existence of a highly evolved Archean- to Paleo-Proterozoic basement beneath the western Cathaysia Block (Zheng et al., 2011; Li et al., 2018). Given these, the contribution of an Archean component to Macao granites cannot be completely ruled out.

5.5.4. Geodynamic setting

The Macao granites date from Jurassic (164.47 ± 0.61 to 155.86 ± 0.56 Ma; Quelhas et al., 2019), being part of a major magmatic event that took place in SE China between 165 and 150 Ma (e.g. Sewell et al., 1992; Zhou and Li, 2000; Li et al., 2004; Li et al., 2007; Huang et al., 2012; Y. Zhang et al., 2015; Zhang et al., 2017). Among the igneous rocks formed during this time interval, strongly metaluminous to weakly-peraluminous biotite monzogranites are predominant (e.g. Sewell et al., 1992; Li et al., 2007; Huang et al., 2012; Y. Zhang et al., 2015), associated with minor gabbros, basalts, syenites, peraluminous granites and A-type granites (e.g. X.-H. Li et al., 2003; Li et al., 2004; Li et al., 2007; Y. Wang et al., 2008; Meng et al., 2012; Zhang et al., 2017).

The tectonic regime prevalent at the time of genesis of these rocks has long been debated and remains controversial. There is a general consensus that this event was related to the northwestward subduction of the Paleo-Pacific plate under the Eurasian plate during the late Mesozoic (e.g. Lapierre et al., 1997; Zhou and Li, 2000; Zhou et al., 2006). Nevertheless, field relationships, petrographic and geochemical data strongly suggest a dominant intraplate extensional regime during the above-mentioned period in Guangdong Province region (e.g. Li et al., 2007; Li and Li, 2007), rather than an active continental margin (e.g. Lapierre et al., 1997; Zhou and Li, 2000; Zhou et al., 2006).

The temporal and spatial association of the Macao and SE China Jurassic I-type granites with basaltic/gabbroic rocks displaying typical intraplate chemical features (Fig. 5.9c; C.-H. Chen et al., 2008b; Y. Wang et al., 2008; Meng et al., 2012), as well as with aluminous A-type granites (e.g. Nankunshan Pluton; Li et al., 2007) and syenites (Fig. 5.9b; X.-H. Li et al., 2003; Li et al., 2004), indeed suggests an extensional regime rather than an active margin. It also points to an important role of mantle-derived magmas in the production of SE China Jurassic granites. Adiabatic

decompression partial melting of asthenospheric mantle produced mafic magmas, which underplated at the Moho, subsequently triggering partial melting of the lower crust to generate intermediate to felsic magmas. This explains the within plate characteristics of the Macao I-type granites inferred from their elemental signatures (Fig. 5.12c and).

It is worthy to mention that seismic profiling (e.g. Xia and Zhao, 2014) confirms the existence of a massive basaltic intrusion in the lower parts of the SE China crust in this region, which probably acted as a major heat source for the partial melting of the lower crust and consequent formation of large volumes of granitic magmas. The contribution of mantle-derived magmas may have also played a role to the composition of Macao and SE China granitic magmas through magma mixing processes as described in section 5.5.2.2.2.

Considering the existence in the region of a subducting slab plunging beneath SE China during the Early Mesozoic (e.g. Zhou and Li, 2000; Zhou et al., 2006; Li et al., 2007; Li and Li, 2007) and, also, the absence of subduction-related fingerprints in the Jurassic mafic magmas, the Jurassic granitic magmatism may have resulted from the slab break-up and foundering (Fig. 5.15a and b) as proposed by Li and Li (2007). In addition, younger dacite dykes intruding Macao granites, with geochemical features similar to arc-like magmas, suggest the return to a normal subduction system during the Cretaceous in this area of SE China (Fig. 5.15c; Quelhas et al., 2019).

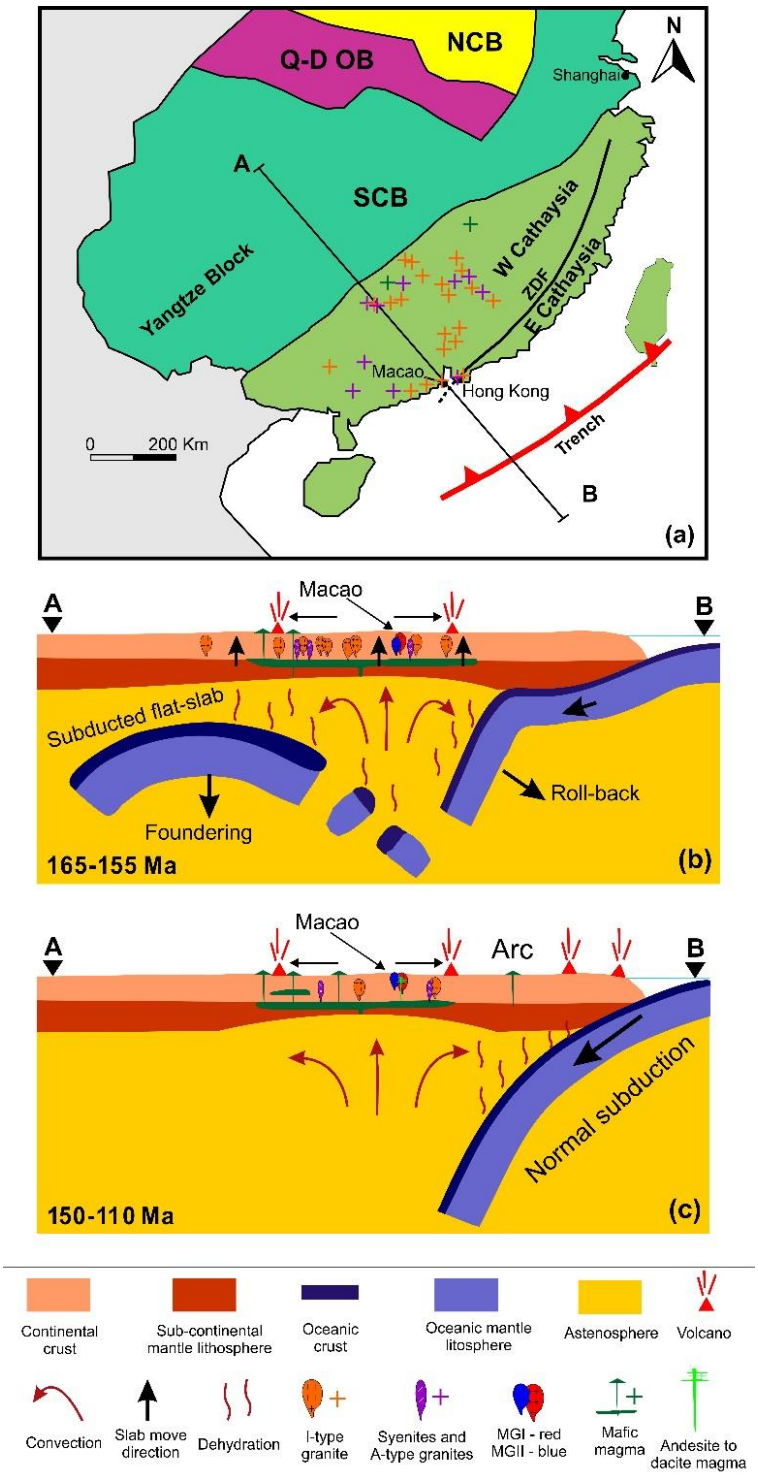

Fig. 5.15. Schematic diagram showing the proposed two-stage tectono-magmatic evolution of Macao and SE China during the Jurassic to Cretaceous period (modified after Li and Li, 2007; Meng et al., 2012; Sewell et al., 2016): (a) Distribution of granitic rocks and related intrusions following collision and rollback of subduction zone between 165–155 Ma; (b) Schematic cross section along the line A–B showing the main magmatic event between 165–155 Ma in response to foundering of a flat-slab; (c) Schematic cross section along the line A–B showing the return to a normal subduction system between 150–110 Ma. SCB – South China Block; NCB – North China Block; Q-D OB – Qingling–Dabie Orogenic Belt.

The boundary between east and west Cathaysia (Fig. 5.1b and Fig. 5.15a) is roughly along the Zhenghe-Dapu Fault (ZDF) which intersects the SE China coast near the Hong Kong region (Chen and Jahn,1998). It has been suggested that this large-scale structure corresponds to a basement terrane boundary (e.g. Darbyshire and Sewell, 1997; Xu et al., 2007b). In Hong Kong, it was proposed the existence of a NE-trending deep crustal discontinuity (within the ZDF zone), which controls the distribution of isotopically distinct granitic rocks in the territory. The Hong Kong Jurassic granitic rocks are located to the northwest of the referred discontinuity and show very similar isotopic signatures to those of Macao granites (see Fig. 5.9b), unlike the Early Cretaceous granitic rocks located along and to the southeast of this discontinuity which depict less radiogenic initial $^{87}Sr/^{86}Sr$ and higher $\varepsilon_{Nd}(t)$ and are not represented in Macao. The Macao granites also show similar $\varepsilon_{Nd}(t)$ and $\varepsilon_{Hf}(t)$ compositions to Jurassic granites occurring within the western Cathaysia Block in surrounding regions (Fig. 5.9c; Y. Zhang et al., 2015; Zhang et al., 2017) and similar Pb isotopic compositions to those of the western Cathaysia Block xenoliths (Fig. 5.11). Even though previous authors have not traced the ZDF further to the SW of Hong Kong region, we propose that this major structure is likely to pass south of Macao in view of the isotopic characteristics of its granitic rocks. It also reinforces the role of the ZDF zone (Fig. 5.15a) as a present day testimony of the Mesozoic suture between the western and eastern Cathaysia blocks.

The age distribution of granitic rocks in SE China has been described as a function of its location in coastal areas or more inland (e.g. Chen and Jahn, 1998; Zhou and Li, 2000; Zhou et al., 2006). The above mentioned data suggest that the distribution of different types of granites in SE China should instead be considered in the light of the nature of crustal blocks in which they occur.

5.6. Concluding remarks

The major findings of this study are summarized as follows:

(1) The two groups (MGI and MGII) of granitic rocks in Macao consist of Jurassic biotite granites hosting minor MME. Petrographic, mineralogical and geochemical observations allow to classify them as high-K calc-alkaline metaluminous to weakly peraluminous I-type granites, with variable degrees of fractionation (monzogranite to alkali feldspar granite).

(2) Fractional crystallization played an important role in the evolution of Macao granites as evidenced by variable major and trace element compositions. The weakly to moderately

fractionated granites of both groups are characterized by similar liquid lines of descent, while these differ for the highly fractionated facies mainly due to distinct accessory fractionating phases resulting from additional processes mainly constraining the evolution of MGI.

(3) MGI highly fractionated granites show evidence for the REE tetrad effect and are characterized by non-CHARAC behaviour of trace elements suggesting late-stage melt/fluid interaction involving F-rich fluids. The stage of evolution represented by the MGI highly fractionated granites corresponds to the onset of fluid/melt interaction in a highly evolved granitic system, which may have led to enhanced hydrothermal activity in more evolved stages as those represented in neighbouring areas in SE China.

(4) Variations in isotopic compositions of MGI and MGII suggest different magma evolution processes. While MGII granites can be considered a comagmatic suite having evolved in closed system, the isotopic variability of MGI granites is consistent with occurrence of open-system magmatic processes. The increase in initial $^{87}Sr/^{86}Sr$ ratios with degree of evolution, occurrence of metasedimentary enclaves and high percentage of inherited zircon with Paleozoic ages in MGI suggests the occurrence of AFC processes.

(5) Decoupling of Sr and Nd and Hf isotope systems in Macao granitic rocks might have resulted from magma mixing. This process was able to cause the homogenization of Sr isotope ratios but not of the Nd and Hf isotopes, which have not participated in this interaction to the degree of Sr because they were strongly partitioned into REE-bearing refractory phases characterized by very low diffusion rates.

(6) Isotope and major element compositions together with model ages and mixing modelling strongly suggest that Macao granitic magmas were generated by partial melting of infracrustal medium-to-high K basaltic Paleo-Proterozoic to Mesoproterozoic protoliths heated by, and mixed to some degrees with, the contemporaneous underplating and/or intrusion of hot, mantle-derived magmas.

(7) The Jurassic Macao granites are interpreted as being produced in an intraplate extensional setting related to the foundering of a previously flat-slab (Paleo-Pacific plate) beneath SE China continent.

(8) Given the stronger isotopic affinities of Macao granites with the western Cathaysia Block, the Zhenghe-Dapu Fault is likely to pass south of Macao.

Acknowledgements

This research was supported by the Macao Science and Technology Development Fund (FDCT 043/2014/A1). We also acknowledge the support of FCT (Portugal) through UID/GEO/50019/2013 to Instituto Dom Luiz. We are very grateful to Varon Lou (Lou U. Tat) and Ricardo Borges for their important help during the field and lab work and to Pedro Rodrigues for skilled assistance during electron microprobe analyses. We also extend our gratitude to Dr. Rod Sewell for his useful advice and support throughout this research.

Chapter 6. A short note on the geochemistry of the dacite dykes

---

6.1. Introduction

Most of the present dissertation is dedicated to the granites of Macao, the dominant lithotype in the territory. As referred above, these granites are cross-cut by dacitic dykes. Despite the small number of samples analysed, due to the scarcity of outcrops of this minor lithology in Macao, an attempt was made to interpret the geochemical data of the dacite dykes from a petrogenetic point of view. The resulting interpretation is the focus of this chapter.

The petrography and geochronology of the dacite dykes was addressed in chapter 3 and 4, respectively. In summary, one dacite from Taipa was dated at 150.64 ± 0.55 Ma (Upper Jurassic), while the dacite from Coloane was dated at <119.68 ± 0.14 Ma (Lower Cretaceous).

Cretaceous volcanic/hypabyssal rocks have not been reported in adjacent areas of Macao, except in Hong Kong where volcanic rocks are dated between about 165–140 Ma (e.g. Sewell et al., 2012a). However, no 150 Ma and 120 Ma rocks have been identified in Hong Kong, making it difficult to compare the dacite dykes from this study with similar rocks from nearby areas.

In this chapter, five dacitic samples were used: E26C, L_C22 and L_C2 were taken during geological surveys carried out in the 90s' and reported in Ribeiro et al. (1992) and C40 and T49 were collected along this study (see Table 6.1). For the first three samples, only whole-rock major elements and a few trace elements were available, while for the samples collected in this study whole-rock major and trace elements and Sr–Nd–Hf–Pb isotopes were analysed (according to the methodologies described in chapter 5).

6.2. Results

6.2.1. Whole-rock elemental geochemistry

The dacite dykes have a quite distinct elemental composition than that characterizing the granitic rocks that they intrude. They have a relatively short range of major element compositions: SiO_2 with 62.68–65.27 wt%, Al_2O_3 with 15.36–17.74 wt%, MgO with 0.67–1.62 wt%, $Fe_2O_3^T$ with 4.17–4.51 wt%, CaO with 2.28–4.53wt%, and TiO_2 with 0.39–0.823 wt% (Table 6.1). However, the Taipa dacite is clearly more depleted in MgO, P_2O_5, CaO and Na_2O and enriched in K_2O, TiO_2 and MnO when compared with the Coloane dacites (Table 6.1).

Table 6.1. Whole-rock major and trace element compositions of the Macao dacite dykes.

Sample	E26C	L_C22	L_C2	T 49	C40
Group	Coloane dacite	Coloane dacite	Coloane dacite	Taipa dacite	Coloane dacite
Major elements (wt%)					
SiO_2	63.68	62.68	63.64	65.27	63.61
Al_2O_3	16.36	17.74	17.10	16.54	16.61
FeOt	4.02	3.80	3.94	4.06	3.75
MnO	0.07	0.07	0.07	0.11	0.10
MgO	1.54	1.44	1.47	0.67	1.62
CaO	4.53	4.46	3.41	2.28	4.01
Na_2O	3.92	3.81	3.81	0.17	3.62
K_2O	1.99	2.59	2.23	4.88	2.56
TiO_2	0.39	0.53	0.47	0.82	0.47
P_2O_5	0.28	0.31	0.26	0.22	0.28
LOI				4.58	2.70
Total	99.53	99.90	98.99	100.10	99.73
Trace elements (ppm)					
As				2.00	0.00
Ba	419.00	1487.00	546.00	685.00	1179.00
Be				6.00	2.00
Bi				0.10	0.10
Co				5.90	6.80
Cr				26.20	81.00
Cs				16.10	10.70
Cu				5.00	2.00
Ga				20.00	19.00
Ge				1.70	1.50
Hf				7.00	3.90
Nb	13.00	11.00	13.00	11.60	6.80
Ni				15.00	42.00
Pb				17.00	9.00
Rb	61.00	110.00	119.00	395.00	143.00
S				0.03	0.05
Sb				0.70	0.30
Sc				12.30	7.19
Sn				18.00	1.00
Sr	1030.00	1091.00	662.00	121.00	1104.00
Ta		0.50	0.40	0.73	0.51
Th		4.60	4.50	9.90	5.01
U		0.90	5.70	12.20	0.99
V				23.00	59.00
W				4.00	0.00
Y	17.00	18.00	22.00	31.00	16.00

Table 6.1. (continued)

Sample	E26C	L_C22	L_C2	T 49	C40
Group	Coloane dacite	Coloane dacite	Coloane dacite	Taipa dacite	Coloane dacite
Zn				69.00	45.00
Zr	166.00	177.00	180.00	346.00	157.00
La		30.70	33.90	50.40	35.70
Ce		62.00	64.00	97.00	68.80
Pr				10.90	7.95
Nd		28.00	28.00	41.40	29.70
Sm		4.10	4.60	7.93	5.15
Eu		1.20	1.34	2.71	1.56
Gd				6.75	3.91
Tb		0.50	0.60	0.99	0.52
Dy				5.94	2.97
Ho				1.14	0.57
Er				3.24	1.74
Tm				0.47	0.27
Yb		1.49	1.54	2.99	1.75
Lu		0.23	0.22	0.48	0.28
Eu/Eu* [a]				1.13	1.06

a The Eu anomaly is the ratio between measured Eu and the value expected for Eu on a smooth chondrite-normalized plot (Eu*).

There is a significant range of compositions for some trace elements (e.g. Ba = 419–1487 ppm; Rb = 61–395; Sr = 121–1104). Taipa and Coloane dacites are also distinct: the Taipa dacite has low contents of Ba and Sr (Fig. 6.1a and c) and has much higher contents of Rb and Zr (Fig. 6.1b and d) compared with the Coloane dacites. The Coloane dacites have also variable Ba and Sr contents.

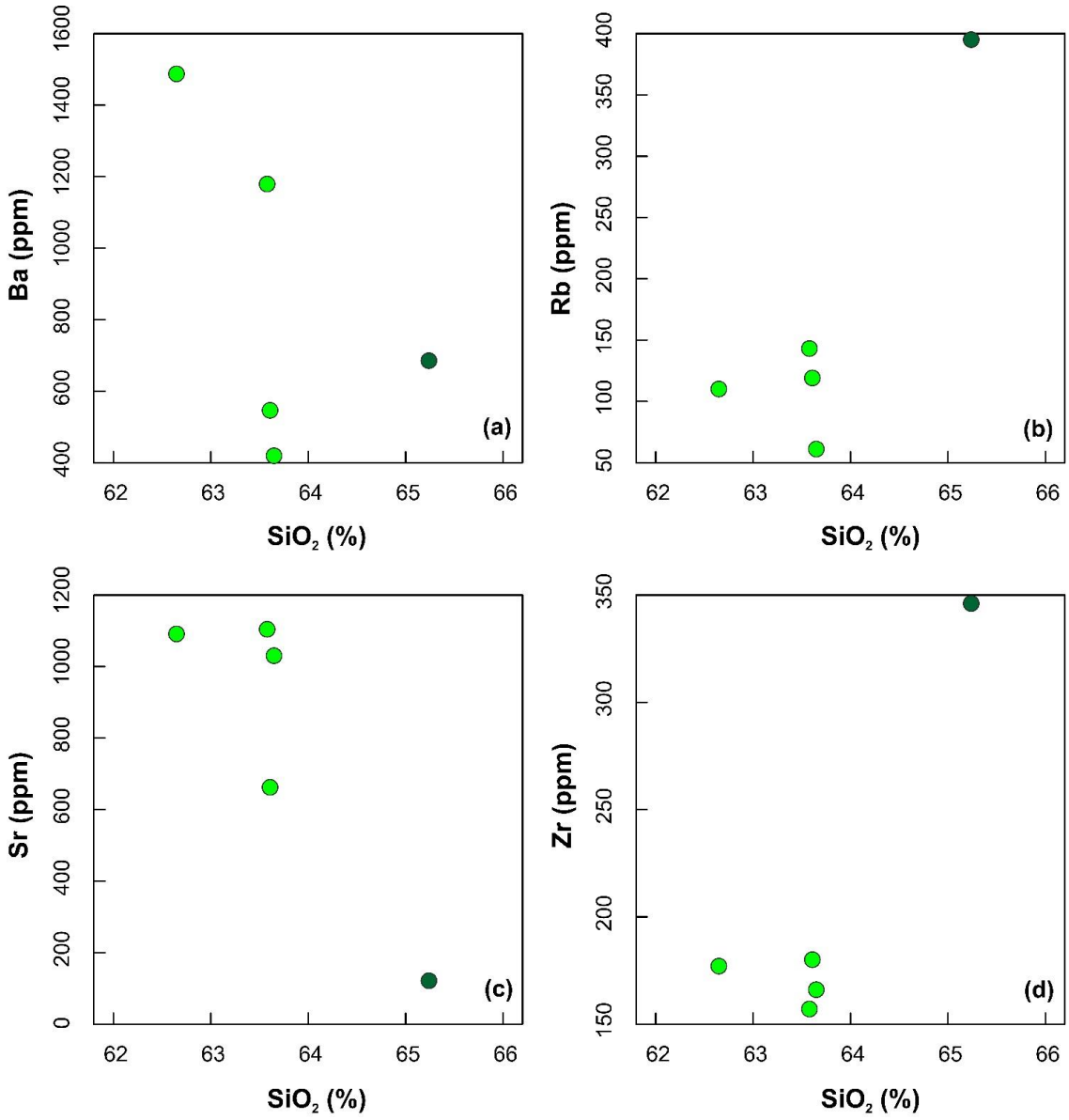

Fig. 6.1. Trace elements *vs* SiO_2. The light green symbols are the Coloane dacites and the dark green symbol the Taipa dacite.

Regarding their classification, all of the samples fall in the dacite field in the total alkali-silica (TAS) diagram, except for one Coloane sample falling inside the andesite field (but still close to the boundary with the dacite field; Fig. 6.2a). Since the alkali metals Na and K (used in the TAS classification) are amongst the most mobile elements during post-magmatic alteration (e.g. Gill, 2010), the studied samples were also plotted in the Zr/TiO_2 *vs* Nb/Y diagram (Fig. 6.2b; Winchester and Floyd, 1976) with most of them falling in the rhyodacite/dacite field and one sample falling in

the trachy-andesite field. The Taipa dacite has higher K_2O, plotting in the shoshonite field in the K_2O *vs* SiO_2 diagram (Fig. 6.2c), whereas the Coloane dacites plot in the transition of the calc-alkaline series to the high-K calc-alkaline series in the same diagram. The Taipa dacite has a more peraluminous character (A/CNK = 1.75) than the Coloane dacites (Fig. 6.2d), which are essentially metaluminous to weakly peraluminous (A/CNK = 0.99–1.17).

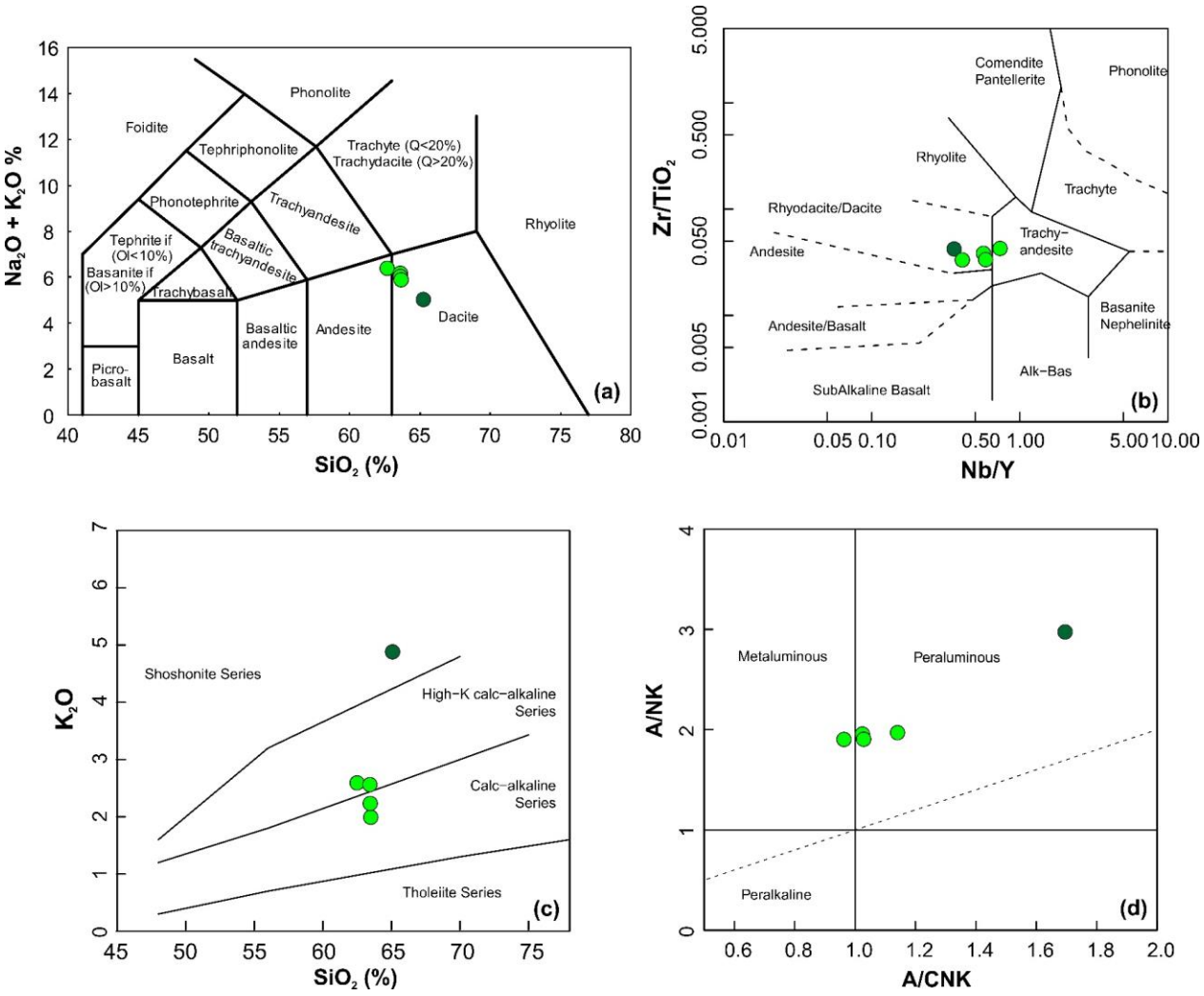

Fig. 6.2. Classification diagrams for the Macao dacites: (a) TAS diagram (after Le Maitre et al., 2002); (b) Zr/TiO_2 *vs* Nb/Y (Floyd and Winchester, 1978); (c) K_2O *vs* SiO_2 (Peccerillo and Taylor, 1976); (d) A/NK [molar ratio $Al_2O_3/(Na_2O + K_2O)$] *vs* A/CNK [molar ratio $Al_2O_3/(CaO + Na_2O + K_2O)$; Shand, 1943]. The light green symbols are the Coloane dacites and the dark green symbol the Taipa dacite.

Despite Taipa and Coloane dacites having clearly distinct K_2O contents, leading to plotting in distinct compositional fields in Fig. 6.2c, they form a cluster in the Ta/Yb *vs* Ce/Yb and Ta/Yb *vs*

Th/Yb classification diagrams plotting in the shoshonite field (Fig. 6.3a and b). Notwithstanding the evolved characteristics of these rocks requiring some precaution when using discriminant diagrams, Fig. 6.3a and b suggests a supra-subduction tectonic setting (e.g. Morrison, 1980), a percept reinforced by their positioning in the Ba/Nb *vs* La/Nb and Th-Nb-Zr diagrams (Fig. 6.3c and d).

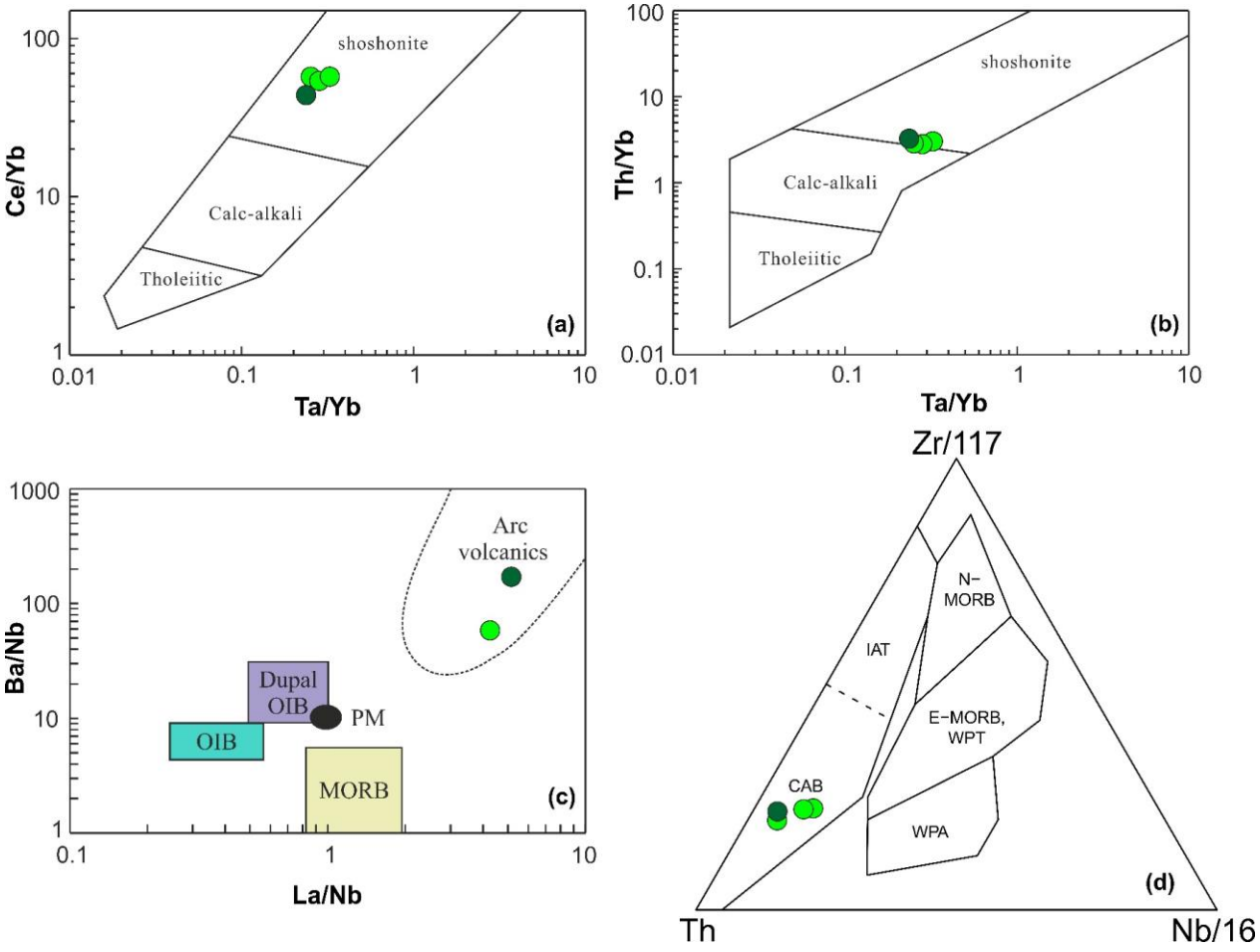

Fig. 6.3. Discrimination diagrams for the Macao dacites: (a) Ce/Yb *vs* Ta/Yb and (b) Th/Yb *vs* Ta (Adams et al., 2005); (c) Ba/Nb *vs* La/Nb (Wilson, 1989); (d) Th-Nb-Zr (Wood, 1980). The light green symbols are the Coloane dacites and the dark green symbol the Taipa dacite.

The dacite rocks are enriched in LILE (e.g. Cs, Ba and Rb) relative to HSFE, with high Rb/La ratios of 3.5–7.8 (Fig. 6.4a). They also show pronounced negative anomalies in HFSE such as Nb, Ta and Ti, which are similar to those of arc-type magmatic rocks (Rudnick, 1995; Taylor and Mclennan, 1995). Moreover, most of the samples have relatively low contents of compatible trace elements such as Cr (26.2–81 ppm), Ni (15–42 ppm) and Co (5.9–6.8 ppm), showing that they are

representatives of significantly evolved magmas. The chondrite-normalized REE patterns of the dacite rocks invariably show LREE enrichments relative to HREE (see Fig. 6.4b) with high $(La/Yb)_N$ ratios of 11.45–13.86 and positive Eu anomalies (Eu/Eu* = 1.06–1.13; Table 6.1).

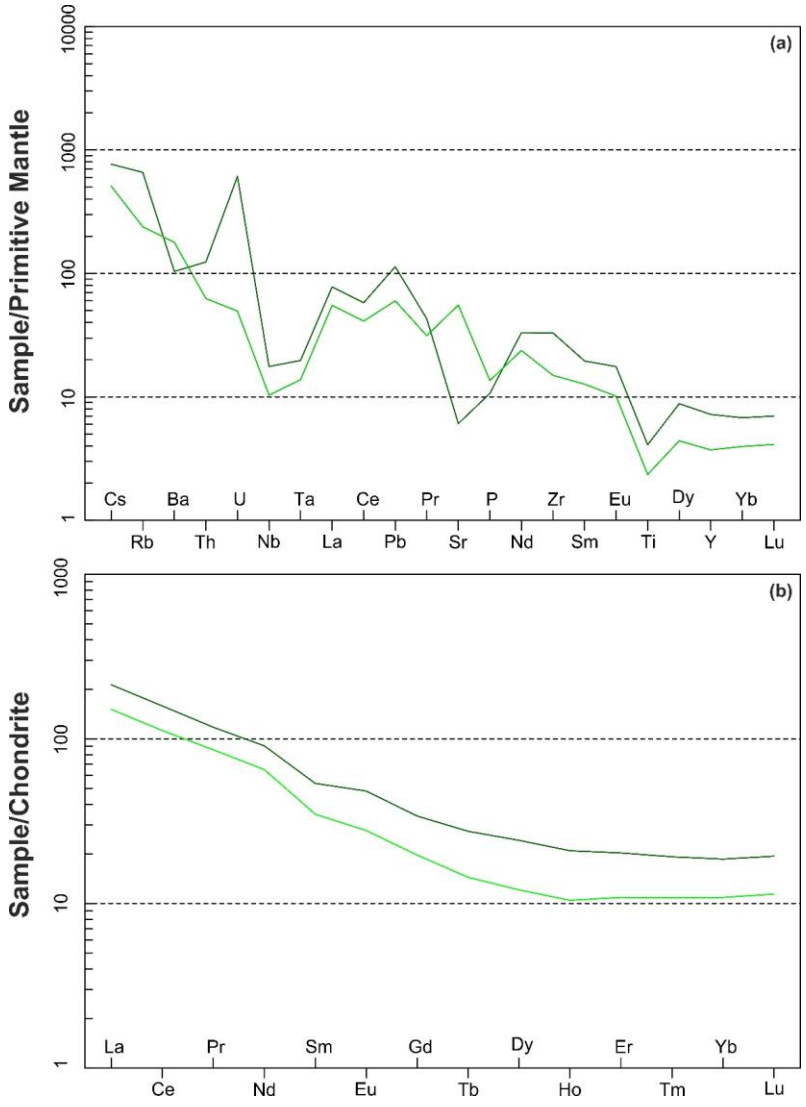

Fig. 6.4. (a) Primitive Mantle (PM)-normalized trace element spidergram and (b) Chondrite-normalized Rare Earth Elements (REE) for Macao dacites. The Primitive Mantle and Chondrite values are from Sun and McDonough (1989). The light green line is the Coloane dacite and the dark green line is the Taipa dacite.

6.2.2. Whole-rock Sr–Nd–Hf–Pb isotope geochemistry

Since the two dacite dykes analysed have distinct crystallization ages, the initial isotopic ratios of the Taipa dacite were calculated back to 150 Ma, whereas those of the Coloane dacite were calculated back to 120 Ma.

Table 6.2. Whole-rock Sr–Nd–Hf–Pb isotopic compositions of the Macao dacite dykes.

Sample	T49	C40
Group	Jurassic dacite	Cretaceous dacite
Rb (ppm)	395	143
Sr (ppm)	121	1104
$^{87}Rb/^{86}Sr$	9.4468	0.3748
$^{87}Sr/^{86}Sr$	0.7333	0.7090
2σ	0.000011	0.000011
$(^{87}Sr/^{86}Sr)_i$	0.7132	0.7083
Sm (ppm)	7.93	5.15
Nd (ppm)	41.40	29.70
$^{147}Sm/^{144}Nd$	0.1253	0.1134
$^{143}Nd/^{144}Nd$	0.5122	0.5121
2σ	0.000010	0.000009
$\varepsilon_{Nd}(t)$	-7.31	-9.18
T_{DM2} (Ga)	1.52	1.67
Lu (ppm)	0.48	0.28
Hf (ppm)	7.00	3.90
$^{176}Lu/^{177}Hf$	0.0097	0.0102
$^{176}Hf/^{177}Hf$	0.2825	0.2826
2σ	0.000009	0.000008
$\varepsilon_{Hf}(t)$	-8.89	-3.98
T_{DM2} (Ga)	1.74	1.40
Th (ppm)	9.90	5.01
U (ppm)	12.20	0.99
Pb (ppm)	17.00	9.00
$^{206}Pb/^{204}Pb$	19.1115	18.8035
2σ	0.000918	0.000900
$^{207}Pb/^{204}Pb$	15.7779	15.7375
2σ	0.000840	0.000718
$^{208}Pb/^{204}Pb$	39.4708	39.1828
2σ	0.002320	0.002000
$(^{206}Pb/^{204}Pb)_i$	18.0687	18.6759
$(^{207}Pb/^{204}Pb)_i$	15.7268	15.7313
$(^{208}Pb/^{204}Pb)_i$	39.1941	38.9713

The Taipa dacite has an initial $^{87}Sr/^{86}Sr$ ratio of 0.7132, $\varepsilon_{Nd}(t)$ = -7.3, $\varepsilon_{Hf}(t)$ = -8.9, Nd T_{DM2} = 1.5 Ga and Hf T_{DM2} = 1.7 Ga, whereas . The Coloane dacite dyke has an initial $^{87}Sr/^{86}Sr$ ratio of 0.7083, $\varepsilon_{Nd}(t)$ = -9.2, $\varepsilon_{Hf}(t)$ = -4.0, Nd T_{DM2} = 1.7 Ga and Hf T_{DM2} = 1.4 Ga (Fig. 6.5 and Table 6.2). Taking also into account the data obtained for granites (see Table E.1, Appendix E), the Coloane dacite yields the youngest Hf model age in the territory.

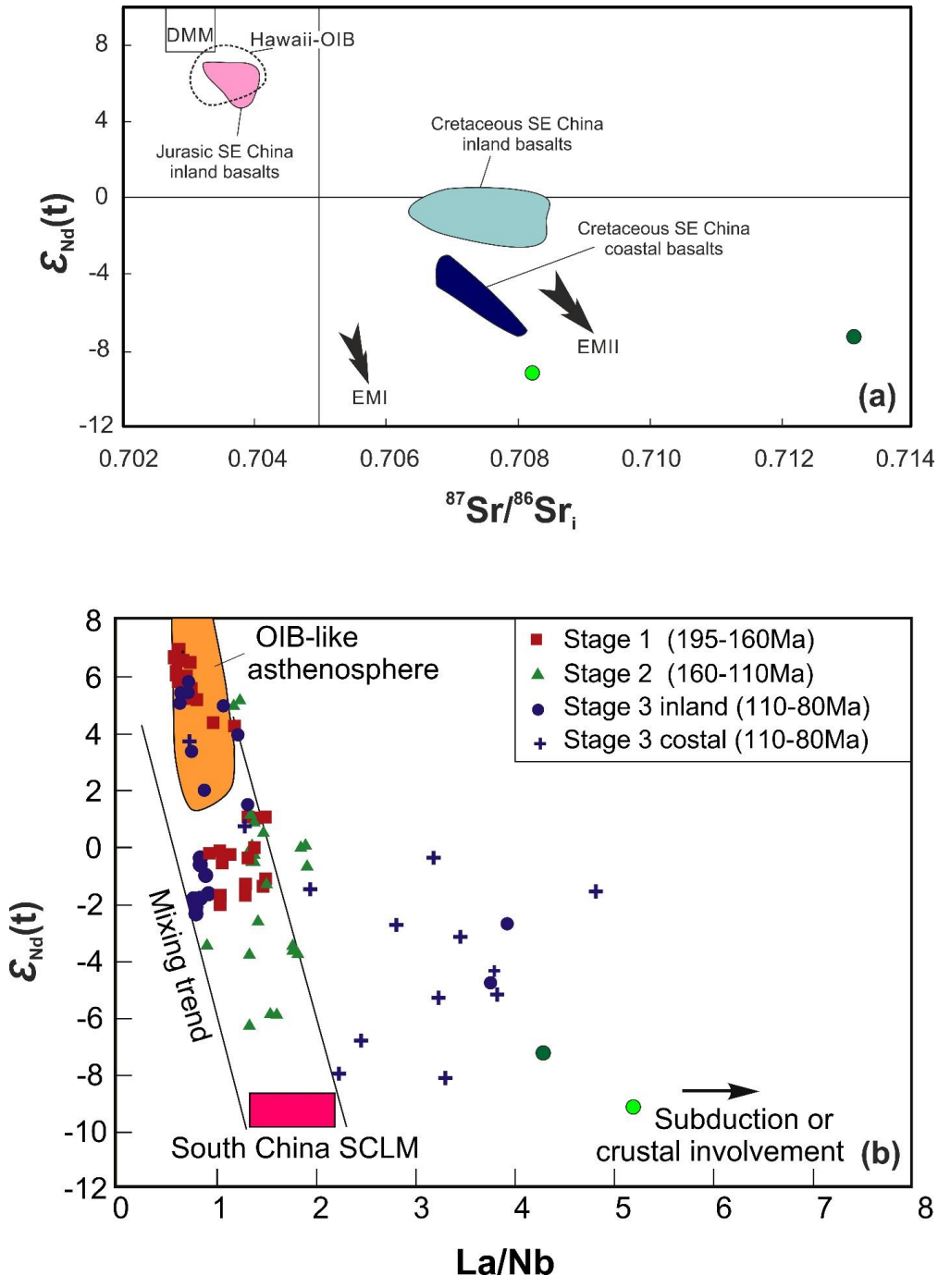

Fig. 6.5. Whole-rock isotopic diagrams for Macao dacites: (a) $\varepsilon_{Nd}(t)$ *vs* initial $^{87}Sr/^{86}Sr$; basaltic rocks are from Meng et al. (2012); the DMM, Hawaii-OIB, EMI and EMII values are from Zindler and Hart, (1986); (b) $\varepsilon_{Nd}(t)$ *vs* La/Nb of the Mesozoic basalts from inland and coastal areas of SE China (data from Meng et al., 2012). The OIB-asthenosphere and South China SCLM (subcontinental lithosphere mantle) components are after C.-H. Chen et al. (2008b). The light green symbol is the Coloane dacite and the dark green symbol the Taipa dacite.

The initial Pb isotopic ratios of the Coloane dacite are $^{206}Pb/^{204}Pb$ = 18.6759, $^{207}Pb/^{204}Pb$ = 15.7313 and $^{208}Pb/^{204}Pb$ = 38.9713, while the Taipa dacite has $^{206}Pb/^{204}Pb$ = 18.0687, $^{207}Pb/^{204}Pb$ = 15.7268 and $^{208}Pb/^{204}Pb$ = 39.1941 (Fig. 6.6 and Table 6.2).

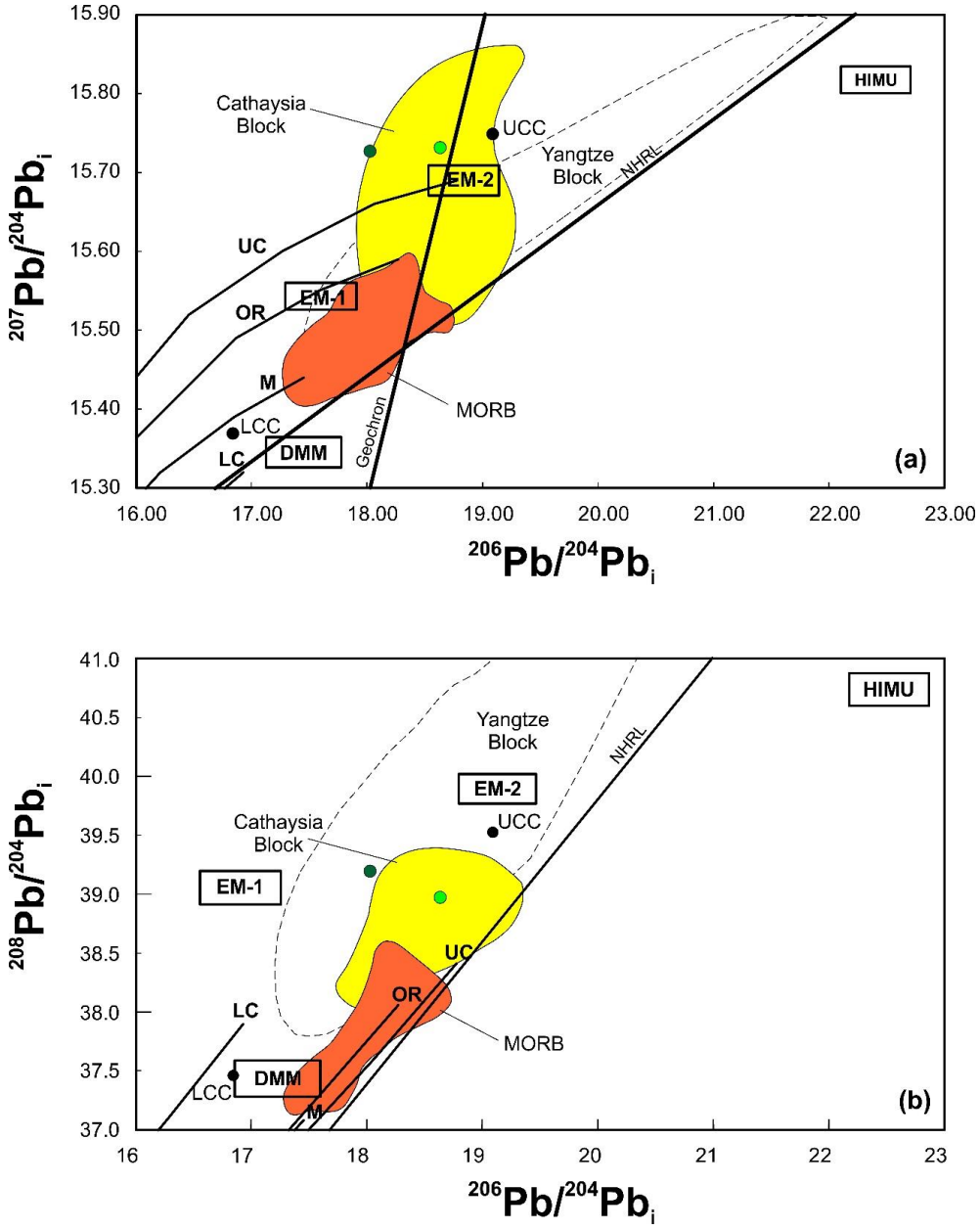

Fig. 6.6. (a) $^{207}Pb/^{204}Pb_i$ *vs* $^{206}Pb/^{204}Pb_i$ and (b) $^{208}Pb/^{204}Pb_i$ *vs* $^{206}Pb/^{204}Pb_i$ diagrams for Macao dacites. $^{206}Pb/^{204}Pb_i$, $^{207}Pb/^{204}Pb_i$ and $^{208}Pb/^{204}Pb_i$ are the initial Pb isotopic ratios. NHRL (Northern Hemisphere Reference Line) from Hart, (1984); Western Cathaysia Block xenoliths from Li et al. (2018); Yangtze and Cathaysia blocks Pb isotopic compositions from Zhang (1995); MORB from Gertisser and Keller (2003); DMM (Depleted MORB Mantle), EM-1 (Enriched Mantle 1), EM-2 (Enriched Mantle 2) and HIMU ("High-μ"; μ = $^{238}U/^{204}Pb$) mantle domains from Hofmann (2003). Evolutionary Pb curves for different terrestrial reservoirs from the Plumbtectonics model (Zartman and Doe, 1981): UC (Upper Crust), OR (Orogene), M (Mantle) and LC (Lower Crust). LCC (Lower Continental Crust; Rudnick and Goldstein, 1990; Paul et al., 2003) and UCC (Upper Continental Crust; Asmerom and Jacobsen, 1993). The light green symbol is the Coloane dacite and the dark green symbol the Taipa dacite.

6.3. Discussion/conclusions

6.3.1. Controls on the geochemical composition of the Macao dacite dykes

The main geochemical characteristics of the Macao dacite rocks are the high values of LILE/HFSE ratios and also the normalized values of ratios like Ba/Nb (4.29 to 17.68), Ba/La (1.34 to 4.76) and Rb/La (3.80 to 8.48), accompanied by negative anomalies of some HFSE (e.g., Nb ,Ta and Ti; Fig. 6.4a). In addition, the dacites have high radiogenic Sr and Pb isotope compositions (Figs. 6.5a and Fig. 6.6, respectively) and negative $\varepsilon_{Nd}(t)$ and $\varepsilon_{Hf}(t)$ values (Fig. 6.5; see also Table 6.2). These characteristics are compatible with a supra-subduction origin of the primary magmas, but also with crustal contamination.

Indeed, the presence of some zircon xenocrysts in both dykes (see chapter 4) indicates that some degree of crustal contamination took place during magma ascent/emplacement and differentiation (e.g. Ni = 15–42 ppm) in the continental crust. It is of interest to determine if the above-mentioned characteristics are mainly a consequence of such process.

Incompatible trace element ratios such as Nb/U, Ba/Nb and Ba/La are sensitive indicators of crustal contamination (e.g. Hofmann et al., 1986; Hofmann, 1997; Jahn et al., 1999). In general, the Taipa dacite has lower Nb/U (0.95), Ba/Nb (59.06) and Ba/La (13.59) than the Coloane dacites (Nb/U = 2.28–12.22; Ba/Nb = 32.23–173.38; Ba/La = 16.10–48.44). When compared with the values for the bulk continental crust (Nb/U = 6.15; Ba/La = 22.8; Ba/Nb = 57; Rudnick and Gao, 2003), some samples have lower Nb/U, Ba/La and Ba/Nb higher ratios than those characterizing the bulk continental crust, probably reflecting a crustal input through contamination. However, other samples have lower Nb/U, Ba/La and Ba/Nb ratios suggesting that these features are most likely inherited from their sources.

Post-Archean arc magmatism mainly results from the interaction between hydrous fluids stemming from the subducting plate and the overlying mantle wedge (Defant and Drummond, 1990; Martin et al., 2005; Castro et al., 2013). Such process can efficiently introduce crustal-signatures into the mantle, this mixing mechanism being the main responsible for oceanic and continental arc magmatism characteristics (e.g. Tatsumi, 2006; Zheng, 2019), namely the high LILE/HFSE ratios and the negative anomalies of Nb, Ta and Ti, in agreement with those characterizing the Macao dacites.

As dacites are relatively evolved rocks, fractional crystallization processes are likely to occur during magmatic differentiation. For example, the Taipa dacite has a pronounced Sr negative anomaly and the four samples of Coloane show a wide range of Sr (662–1104 ppm) and Ba (419–1487 ppm) contents, possibly suggesting fractionation of feldspars.

In summary, the geochemical features of the Macao dacite dykes mostly reflect their sources, with additional contribution from crustal contamination in some samples.

6.3.2. Regional implications

Meng et al. (2012) showed that arc-like features in the late Mesozoic basaltic rocks become more prominent from the Early Jurassic to the mid- and Late Jurassic, but diminished from then in the inland region of the SCB, whereas Late Cretaceous basalts in the coastal region show much stronger arc affinities (see Fig. 6.5a and b). They interpreted such compositional changes in the late Mesozoic basaltic rocks using the delamination of a previously flat-subducted slab between the Jurassic and the Early Cretaceous (as initially proposed by Li and Li, 2007), and the return to normal subduction during the Late Cretaceous. Dacite dykes in Macao (150 – <120 Ma) indicate that supra-subduction magmatic activity went on with a more localized expression in the territory over an interval of at least ~30 Ma and in the form of intermediate to acid volcanism.

The change in the type of magmatism, from granitic to andesitic/dacitic, is likely to correspond to a change in the regional tectonic regime. As explained in the chapter 4 and 5, the Macao I-type granites were probably generated during an extensional period coincident with a slab breakoff of the subducting Paleo-Pacific plate under the Eurasian plate. On the other hand, dacite dykes can be considered the evolved products of arc-like basaltic magmatism similar in characteristics to the type that took place during the Late Cretaceous along the SE China coastal regions (see Fig. 6.5a and b). We interpret this as indicating the reestablishment of a normal subduction system as first proposed by some authors for other areas of SE China (e.g. He and Xu, 2012; Meng et al., 2012; Zhu et al., 2014).

Chapter 7. Key findings and future research

7.1. Key findings

The research developed in this thesis required multi-disciplinary approaches to investigate the magma genesis and evolution history of the igneous rocks from Macao. The results of this study give new perspectives on the petrogenetic processes involved in the formation of plutons and its implications for the larger tectono-magmatic context related to the formation of granite belts in general, and in particular of the SCMB. This study showed that granitic intrusions within a pluton can be composed by a wide range of granite varieties, even in relatively small areas such as Macao. Such variability is expressed in the Macao territory by the occurrence of different facies in the field, reflecting distinct magmatic episodes and different magma evolution stages within each of these episodes. Thus, Macao can be considered as a microcosm of what happened at a larger scale during the Yanshanian Orogeny, in particular during the time of genesis and emplacement of the Macao granites (Jurassic).

The findings arising from this thesis were only possible by the application of an integrated range of methodologies including: (a) field studies to establish the spatial-temporal relationships of the different facies outcropping in the territory; (b) petrography analysis to characterized texturally and mineralogically the different types of granites and other minor magmatic rocks (e.g. MME and dacite dykes); (c) zircon U–Pb geochronology using in-situ LA-MC-ICPMS and high-precision ID-TIMS techniques to identify the different magmatic episodes, as well as, through the study of inherited zircons, to constrain the age of potential sources for the granitic magmas; (d) an integrated mineral-chemistry, whole-rock elemental and isotopic geochemical study, of the magmatic rocks which provided important insights into the sources, petrogenetic processes and related tectonic setting by the time of granite genesis.

Though the main conclusions of this study are mentioned separately in each of the two chapters composing the discussion of this thesis (chapters 4 and 5), the main aim of this chapter is to provide a more integrated, ordered and coherent overview of those major findings as listed below.

7.1.1. Geology and petrography

(1) The geology of Macao is dominated by plutonic rocks mainly consisting of biotite granites with variable petrographic, mineralogical and geochemical features, which

often contain MME. The granites are cut by a swarm of granitic (microgranite, aplite and pegmatite) and dacite dykes.

(2) Macao biotite granites are mainly composed of quartz (30–35 vol%), K-feldspar (35–40 vol%), plagioclase (20–25 vol%) and biotite (5–10 vol%). According to the type of K-feldspar, they can be divided into microcline granites (Macao Group I granites or MGI) and orthoclase granites (Macao Group II granites or MGII), which are also distinct in age. In both groups, textures vary from medium- to coarse-grained porphyritic to fine-grained non-porphyritic moderately equigranular.

(3) While many accessory minerals are common in both groups, titanite is distinctly more abundant in MGII granites whereas garnet and abundant tantalo-niobates are characteristic of MGI granites.

(4) MME of the two groups differ in texture and mineralogy. MME in MGI granites usually have bigger dimensions (up to 1 meter in diameter), granodiorite composition, acicular biotite and no accessory titanite. MME of MGII granites on the other hand, have smaller dimensions (centimetre to decimetre-wide), quartz monzodioritic compositions, lozenge-shaped biotite, abundant titanite and in some cases hornblende.

(5) In contrast with the observed for MGII granites, quartz grains from MGI show evidence for significant deformation such as pervasive undulatory extinction, sutured grain boundaries and development of individual subgrains with well-defined boundaries. Such features suggest that, in Macao, deformation acted as an external forcing mechanism in the monoclinic-triclinic transition from orthoclase to microcline in MGI granites.

7.1.2. Geochronology

(1) Macao region was the locus of multistage magmatism during the Yanshanian Orogeny. This conclusion was supported by an integrated approach using petrography, mineral chemistry, trace elements and zircon U–Pb geochronology showing the existence of two temporally and chemically distinct groups of granitic rocks in Macao. Overall, the granitic magmatism occurred within approximately 155 and 165 Ma (Jurassic), concentrated between 164.5 ± 0.6 and 162.9 ± 0.7 Ma (MGI) and 156.6 ± 0.2 and 155.5

± 0.8 Ma (MGII). Therefore, rather than a continuum of comagmatic activity, the two groups of granite were the result of different magmatic episodes with distinct geochemical features. In addition to these granitic pulses, two dacite dykes cutting granites were dated at 150.6 ± 0.6 Ma (Upper Jurassic) and < 120 Ma (Lower Cretaceous).

(2) The previously obtained Cretaceous age (94 ± 2 Ma) by Ribeiro et al. (1992) for a granite sample from Coloane, is most likely the result of loss of Ar. This sample was collected near an important fault zone in the easternmost area of Coloane; such setting may have allowed hydrothermal fluid circulation to damage the biotite from adjacent granites. This age may thus hypothetically indicate the time of an important movement of that fault during the Late Cretaceous.

(3) Considering the existence in Macao of two proximal but distinct granitic pulses spanning for a time of about 9 Ma and separated by ca. 6 Ma, the Macao granitic suite was most likely incrementally assembled. This hypothesis is also extendable to the neighbouring Hong Kong region, where the magmatic activity occurred in four major pulses spanning for about 24 Ma. However, the MGII granites indicate the occurrence on the Pearl River Delta region of a magmatic pulse between those at the origin of Lamma Suite (165–160 Ma) and the Kwai Chung Suite (148–146 Ma) in Hong Kong. REE compositions of the Macao granites suggest that the MGII granites may only occur in Macao area, while the MGI granites show evolving trends of REE ratios similar to those of Jurassic granites outcropping in vast areas of the Cathaysia Block (SE China).

(4) Given the relatively short time span between the two pulses and the chemical similarity of the less evolved rocks, the observed differences in the two groups were probably the result of distinct magma evolution processes rather than in tectonic setting.

(5) Additionally to the crystallization ages of the granites, inheritance patterns in the zircon U–Pb data suggest the presence of a population of antecrysts (165–180 Ma) crystallized from earlier magmatic pulses and a population of inherited zircons and/or xenocrysts from Precambrian to Phanerozoic sources incorporated into the magmas during melting and/or ascent/emplacement at crustal levels. The oldest inherited ages (2.4 Ga

and possibly 2.9 Ga) suggest contribution of Proterozoic and possibly of late Archaean crustal sources for the Macao magmatism.

7.1.3. Petrogenesis

(1) Petrogaphic, mineralogical and geochemical features allowed classifying Macao granites as high-K calc-alkaline metaluminous to weakly peraluminous I-type granites, with variable degrees of fractionation (monzogranite to alkali feldspar granite).

(2) Though fractional crystallization played a significant role in the evolution of the Macao granites, as evidenced by variable major and trace element compositions, the evolutionary paths were not the same. While the weakly to moderately fractionated granites of both groups are characterized by similar liquid lines of descent, these differ for the highly fractionated facies, mainly due to distinct accessory fractionating phases. Such difference is evident by distinct REE evolution trends: the MGI magmas seem to have evolved by progressive enrichment in heavy REE relatively to light REE, whereas magmas from MGII are marked by depletion of middle REE leading to progressively concave REE patterns.

(3) While most of the geochemical variation of the MGII granites can be explained by fractional crystallization, the same is not true for the MGI granites. The MGI highly fractionated granites show evidence for the REE tetrad effect and are characterized by non-CHARAC behaviour of trace elements suggesting late-stage melt/fluid interactions involving F-rich fluids. The stage of evolution represented by the MGI highly fractionated granites corresponds to the onset of fluid/melt interaction in a highly evolved granitic system, which may have led to enhanced hydrothermal activity in more evolved stages as those represented in neighbouring areas in SE China.

(4) Variations in isotopic compositions of MGI and MGII suggest different magma evolution processes. While the MGII granites can be considered a comagmatic suite having evolved in closed system, the isotopic variability of the MGI granites is consistent with the occurrence of open-system magmatic processes. The increase in initial $^{87}Sr/^{86}Sr$ ratios with degree of evolution, occurrence of metasedimentary enclaves and high percentage of inherited zircon with Paleozoic ages in MGI suggests the occurrence of AFC processes. The AFC processes were most likely the cause for

the I-S transitional characteristics of the MGI highly fractionate granites and other similar Jurassic biotite granites in SE China.

(5) Decoupling of Sr, Nd and Hf isotope systems in Macao granitic rocks might have resulted from magma mixing. This process was able to cause the homogenization of Sr isotope ratios but not of the Nd and Hf isotopes, which have not participated in this interaction to the degree of Sr because they were strongly partitioned into REE-bearing refractory phases characterized by very low diffusion rates.

(6) Isotope and major element compositions together with model ages strongly suggest that Macao granitic magmas were generated by partial melting of infracrustal medium-to-high K basaltic Paleo-Proterozoic to Mesoproterozoic protoliths heated by, and mixed to some degrees with, the contemporaneous underplating and/or intrusion of hot, mantle-derived magmas.

(7) The temporal and spatial association of the Macao and SE China Jurassic I-type granites with basaltic/gabbroic rocks, syenites and A-type granites displaying typical intraplate chemical features, suggests an extensional regime rather than an active margin for the origin of these rocks. It also points to an important role of mantle-derived magmas in the production of SE China Jurassic granites. Adiabatic decompression partial melting of asthenospheric mantle produced mafic magmas, which underplated at the Moho, subsequently triggering partial melting of the lower crust to generate the granitic magmas. The Jurassic Macao granites are interpreted as being produced in an intraplate extensional setting related to the foundering of a previously flat-slab (Paleo-Pacific plate) beneath the SE China continent.

(8) The boundary between east and west Cathaysia blocks is roughly along the Zhenghe-Dapu Fault, which intersects the SE China coast near the Hong Kong region and has not been traced farther from this region. Given the stronger isotopic affinities of Macao granites with the western Cathaysia Block, the Zhenghe-Dapu Fault is likely to pass south of Macao.

(9) Though the age distribution of granitic rocks in SE China has been described as a function of its location in coastal or more inland areas, the data in this thesis suggest

that the distribution of different types of granites in SE China should be instead considered in the light of the nature of crustal blocks in which they occur.

(10) Despite Early Yanshanian magmatism being predominant in Macao, the younger ages obtained for the dacite dykes indicate that the territory was affected, to a lesser degree, by Late Yashanian magmatism. The change in the type of magmatism in Macao from granitic to dacitic with shoshonitic affinities is likely to correspond to a change in the regional tectonic regime inducing a significant change in the magma genesis processes. In contrast with the intraplate features of Macao and SE China Jurassic granites and coeval mafic rocks, the geochemical features of the Macao dacite dykes (e.g. high LILE/HFSE ratios and negative anomalies of Nb, Ta and Ti) are quite distinct. While the dacites may have suffered some degree of crustal contamination, as indicated by the presence of zircon xenocrysts, these elemental characteristics are identical to those characterizing arc-like subduction-related magmas. These dacites are most likely evolved products of arc-like magmatism and may testify the reestablishment of a normal subduction system in this area of SE China.

7.2. Suggestions for future research

In the course of this study, some future research opportunities have been identified:

(1) The aim of this thesis was to study the magmatic rocks from Macao and frame their petrogenesis in the larger geodynamic context of SE China. However, most studies on the petrogenesis of SE China Late Mesozoic igneous rocks dealt with large batholith areas where sampling cannot adequately represent the small-scale compositional variation within individual plutons. Therefore, in some areas of SE China detailed geochemical and age variation information can have been missed, potentially leading to an incomplete understanding of the regional magmatic evolution during the Yanshanian Orogeny. More detailed studies should thus be conducted in areas adjacent to Macao and Hong Kong, aiming to construct a more integrated and detailed petrogenetic model for the Mesozoic magmatism in this region of SE China.

(2) Determination of in-situ combined isotopic analyses of U–Pb, O and Hf for zircons for the Macao granites could better constrain the nature of protoliths. In addition, it would be possible to determine in a more reliable way the relative contribution of recycled

and/or pre-existed crustal material and juvenile/mantle derived component to the magmas that originated the granites.

(3) This study showed that crustal assimilation and magma mixing processes were involved in the petrogenesis of the Macao granites. To better constrain these processes, sampling and geochemical elemental and isotopic analyses of the metasedimentary enclaves and MME in the territory could be conducted in the future. This would allow to better constrain the nature of the assimilant and the mantle-derived magmas involved in the petrogenesis of the Macao granites and the proportions of upper crust and mantle involved in the genesis and evolution of the Macao granitic magmas.

(4) Fission-track thermochronology for zircon and apatite could be carried out in the future to determine the low-temperature ($\leq$ 250 ºC) thermal history of the granitic rocks, constraining temporally the burial and exhumation of the Mesozoic plutons in Macao.

(5) Due to the small number of samples of dacite dykes obtained in this thesis, it was not possible to study their petrogenesis with the same detail as it was done for the granitic rocks. The dacite dykes in Macao represent products of the Late Yanshanian Orogeny, which took place during the Cretaceous period. Most of the Cretaceous magmatic rocks in SE China concentrate in the eastern coastal areas of the Cathaysia Block. In contrast, this magmatic event is poorly constrained in the western parts where Macao is located. Therefore, a more robust and representative sampling of the Late Yanshanian magmatic rocks in Macao and surrounding areas should be carried out to improve the knowledge on the petrogenesis and tectonic setting operating during the Early to Late Cretaceous in the western areas of the Cathaysia Block.

References

Abdel-Rahman A. F. M. (1994) Nature of biotites from alkaline, calc-alkaline, and peraluminous magmas. *J. Petrol.* **35**, 525–541.

Adams M. G., Lentz D. R., Shaw C. S., Williams P. F., Archibald D. A. and Cousens B. (2005) Eocene shoshonitic mafic dykes intruding the Monashee Complex, British Columbia: a petrogenetic relationship with the Kamloops Group volcanic sequence? *Can. J. Earth Sci.* **42**, 11–24.

Annen C. (2011) Implications of incremental emplacement of magma bodies for magma differentiation, thermal aureole dimensions and plutonism-volcanism relationships. *Tectonophysics* **500**, 3–10.

Arndt N. T. (2013) Formation and Evolution of the Continental Crust. *Geochemical Perspect.* **2**, 405–533.

Asmerom Y. and Jacobsen S. B. (1993) The Pb isotopic evolution of the Earth: inferences from river water suspended loads. *Earth Planet. Sci. Lett.* **115**, 245–256.

Bachman O., Charlier B. L. A. and Lowenstern J. B. (2007) Zircon crytallization and recycling in the magma chamber of the rhyolitic Kos Plateau Tuff (Aegean arc). *Geology* **35**, 73–76.

Bachmann O. and Bergantz G. W. (2008) Rhyolites and their source mushes across tectonic settings. *J. Petrol.* **49**, 2277–2285.

Barboni M., Schoene B., Ovtcharova M., Bussy F., Schaltegger U. and Gerdes A. (2013) Timing of incremental pluton construction and magmatic activity in a back-arc setting revealed by ID-TIMS U/Pb and Hf isotopes on complex zircon grains. *Chem. Geol.* **342**, 76–93.

Bau M. (1996) Controls on the fractionation of isovalent trace elements in magmatic and aqueous systems: evidence from Y/Ho, Zr/Hf, and lanthanide tetrad effect - a discussion of the article by M. Bau (1996). *Contrib. to Mineral. Petrol.* **128**, 405–408.

Bea F., Montero P. and Ortega M. (2006) A LA-ICP-MS evaluation of Zr reservoirs in common crustal rocks: Implications for Zr and Hf geochemistry, and zircon-forming processes. *Can. Mineral.* **44**, 693–714.

Bea F., Pereira M. D. and Stroh A. (1994) Mineral/leucosome trace-element partitioning in a peraluminous migmatite (a laser ablation-ICP-MS study). *Chem. Geol.* **117**, 291–312.

Beckinsale R. D. (1979) Granite magmatism in the tin belt of Southeast Asia. In *Origin of Granite Batholiths Geochemical Evidence* (eds. J. Tarney and M. P. Atherton). Shiva Publishing Limited, Orpington. pp. 34–44.

Bell T. H. and Johnson S. E. (1989) The role of deformation partitioning in the deformation and recrystallization of plagioclase and K-feldspar in the Woodroffe Thrust mylonite zone, central Australia. *J. Metamorph. Geol.* **7**, 151–168.

Bignell J. D. and Snelling N. J. (1977) The geochronology of Malayan granites. In *Overseas Geology and Mineral Resources* H.M. Stationery Office Books, London. pp. 1–72.

Bindeman I. N. and Davis A. M. (2000) Trace element partitioning between plagioclase and melt: Investigation of dopant influence on partition behavior. *Geochim. Cosmochim. Acta* **64**, 2863–2878.

Blasi A., Brajkovic A. and de Pol Blasi C. (1984) Dry-heating conversion of low microcline to high sanidine via a one-step disordering process. *Bull Minéral* **107**, 423–435.

Bónová K., Broska I. and Petrík I. (2010) Biotite from Čierna hora Mountains granitoids (Western Carpathians , Slovakia) and estimation of water contents in granitoid melts. *Geol. Carpathica* **61**, 3–17.

Cai D., Tang Y., Zhang H., Lv Z. and Liu Y. (2017) Petrogenesis and tectonic setting of the Devonian Xiqin A-type granite in the northeastern Cathaysia Block, SE China. *J. Asian Earth Sci.* **141**, 43–58.

Cai H.-T., Kuo-Cheng H., Jin X., Wang C.-Y., Huang B.-S. and Yen H.-Y. (2015) A three-dimensional Vp, Vs, and Vp/Vs crustal structure in Fujian, Southeast China, from active- and passive-source experiments. *J. Asian Earth Sci.* **111**, 517–527.

Cai J. and Zhang K. (2009) Tectonophysics A new model for the Indochina and South China collision during the Late Permian to the Middle Triassic. *Tectonophysics* **467**, 35–43.

Cai Y., Lu J., Ma D., Huang H., Zhang H. and Zhang R. (2015) The Late Triassic Dengfuxian A-type granite, Hunan Province: age, petrogenesis, and implications for understanding the late Indosinian tectonic transition in South China. *Int. Geol. Rev.* **57**, 428–445.

Campbell S. D. G. and Sewell R. J. (1997) Structural control and tectonic setting of Mesozoic volcanism in Hong Kong. *J. Geol. Soc. London.* **154**, 1039–1052.

Campbell S. D. G., Sewell R. J., Davis D. W. and So A. C. T. (2007) New U-Pb age and geochemical constraints on the stratigraphy and distribution of the Lantau Volcanic Group, Hong Kong. *J. Asian Earth Sci.* **31**, 139–152.

Cao J., Yang X., Du J., Wu Q., Kong H., Li H., Wan Q., Xi X., Gong Y. and Zhao H. (2018) Formation and geodynamic implication of the Early Yanshanian granites associated with W–Sn mineralization in the Nanling range, South China: an overview. *Int. Geol. Rev.* **60**, 1744–1771.

Carrington da Costa J. and Lemos M. S. (1964) Fisiografia e Geologia da Província de Macau: Centro de Informação e Turismo.

Carter A., Roques D., Bristow C., Kinny P. and Carter A. (2001) Understanding Mesozoic accretion in Southeast Asia: Significance of Triassic thermotectonism (Indosinian orogeny) in Vietnam. *Geology* **29**, 211–214.

Castro A., Vogt K. and Gerya T. (2013) Generation of new continental crust by sublithospheric silicic-magma relamination in arcs: A test of Taylor's andesite model. *Gondwana Res.* **23**, 1554–1566.

Cawood P. A., Wang Y., Xu Y. and Zhao G. (2013) Locating South China in Rodinia and Gondwana: A fragment of greater India lithosphere? *Geology* **41**, 903–906.

Chappell B. W. (2004) Towards a unified model for granite genesis. *Trans. R. Soc. Edinburgh-Earth Sci.* **95**, 1–10.

Chappell B. W. and White A. J. R. (1992) I- and S-type granites in the Lachlan Fold Belt. *Trans. R. Soc. Edinb. Earth Sci.* **83**, 1–26.

Charlier B. L. A., Wilson C. J. N., Lowenstern J. B., Blake S., Van Calsteren P. W. and Davidson J. P. (2005) Magma generation at a large, hyperactive silicic volcano (Taupo, New Zealand) revealed by U-Th and U-Pb systematics in zircons. *J. Petrol.* **46**, 3–32.

Charvet J. (2013) The Neoproterozoic-Early Paleozoic tectonic evolution of the South China Block: An overview. *J. Asian Earth Sci.* **74**, 198–209.

Charvet J. and Faure M. (1996) The building of south China: collision of Yangzi and Cathaysia blocks, problems and tentative answers. *J. Southeast Asian Earth Sci.* **13**, 223–235.

Charvet J., Lapierre H. and Yu Y. (1994) Geodynamic significance of the Mesozoic volcanism of southeastern China. *J. Asian Earth Sci.* **9**, 387–396.

Charvet J., Shu L., Faure M., Choulet F., Wang B. and Lu H. (2010) Structural development of the Lower Paleozoic belt of South China: Genesis of an intracontinental orogen. *J. Asian Earth Sci.* **39**, 309–330.

Chauvel C. and Blichert-Toft J. (2001) A hafnium isotope and trace element perspective on melting of the depleted mantle. *Earth Planet. Sci. Lett.* **190**, 137–151.

Chauvel C., Bureau S. and Poggi C. (2011) Comprehensive Chemical and Isotopic Analyses of Basalt and Sediment Reference Materials. *Geostand. Geoanalytical Res.* **35**, 125–143.

Chen C.-H., Lee C.-Y., Lu H.-Y. and Hsieh P.-S. (2008a) Generation of Late Cretaceous silicic rocks in SE China: Age, major element and numerical simulation constraints. *J. Asian Earth Sci.* **31**, 479–498.

Chen C.-H., Lee C.-Y. and Shinjo R. (2016) The epilog of the western paleo-Pacific subduction: Inferred from spatial and temporal variations and geochemistry of the Late Cretaceous to Early Cenozoic silicic magmatism in coastal South China. *J. Asian Earth Sci.* **115**, 520–546.

Chen C.-H., Lee C.-Y. and Shinjo R. (2008b) Was there Jurassic paleo-Pacific subduction in South China?: Constraints from $^{40}Ar/^{39}Ar$ dating, elemental and Sr-Nd-Pb isotopic geochemistry of the Mesozoic basalts. *Lithos* **106**, 83–92.

Chen C.-H., Lin W., Lu H.-Y., Lee C.-Y., Tien J.-L. and Lai Y.-H. (2000) Cretaceous fractionated I-type granitoids and metaluminous A-type granites in SE China: the Late Yanshanian post-orogenic magmatism. *Earth Environ. Sci. Trans. R. Soc. Edinburgh* **91**, 195–205.

Chen J.-Y., Yang J.-H. and Ji W.-Q. (2017) Ages and petrogenesis of Jurassic and Cretaceous intrusive rocks in the Matsu Islands: Implications for lower crust modification beneath southeastern China. *J. Asian Earth Sci.* **150**, 14–24.

Chen J., Foland K. A., Xing F., Xu X. and Zhou T. (1991) Magmatism along the southeast margin of the Yangtze block: Precambrian collision of the Yangtze and Cathysia blocks of China. *Geology* **19**, 815–818.

Chen J. and Jahn B. M. (1998) Crustal evolution of southeastern China: Nd and Sr isotopic evidence. *Tectonophysics* **284**, 101–133.

Chen T. G. (1987) Basic features of the Lianhuashan Fault Zone in the Hong Kong and Shenzhen areas. *J. Guangdong Geol.* **2**, 57–68.

Chen W., Chen P., Huang H., Ding X. and Sun T. (2007) Chronological and geochemical studies of granite and enclave in Baimashan pluton, Hunan, South China. *Sci. China Earth Sci.* **50**, 1606–1627.

Chen X., Rong J. Y., Rowley D. B., Zhang J., Zhang Y. Y. and Zhang R. B. (1995) Is the Early Paleozoic Banxi ocean in south China necessary? *Geol. Rev.* **41**, 389–400.

Chen X., Zhang Y., Fan J., Tang L. and Sun H. (2012) Onset of the Kwangsian Orogeny as evidenced by biofacies and lithofacies. *Sci. China Earth Sci.* **55**, 1592–1600.

Chen Y., Courtillot V., Cogné J.-P., Besse J., Yang Z. and Enkin R. (1993) The configuration of Asia prior to the collision of India: Cretaceous paleomagnetic constraints. *J. Geophys. Res.* **98**, 21927.

Chen Y. W., Bi X. W., Hu R. Z. and Dong S. H. (2012) Element geochemistry, mineralogy, geochronology and zircon Hf isotope of the Luxi and Xiazhuang granites in Guangdong province, China: Implications for U mineralization. *Lithos* **150**, 119–134.

Cheng H. (1993) Geochemistry of Proterozoic island-arc volcanic rocks in northwest Zhejiang. *Geochim.* **22**, 18–27 (in Chinese with English abstract).

Cherniak D. J. (2010) Diffusion in Accessory Minerals: Zircon, Titanite, Apatite, Monazite and Xenotime. *Rev. Mineral. Geochemistry* **72**, 827–869.

Cherniak D. J. (1995) Sr and Nd diffusion in titanite. *Chem. Geol.* **125**, 219–232.

Cherniak D. J., Hanchar J. M. and Watson E. B. (1997a) Diffusion of tetravalent cations in zircon. *Contrib. to Mineral. Petrol.* **127**, 383–390.

Cherniak D. J., Hanchar J. M. and Watson E. B. (1997b) Rare-earth diffusion in zircon. *Chem. Geol.* **134**, 289–301.

Clemens J. D., Holloway J. R. and White A. J. R. (1986) Origin of an A-type granite: experimental constraints. *Am. Mineral.* **71**, 317–324.

Clemens J. D., Stevens G. and Farina F. (2011) The enigmatic sources of I-type granites: The peritectic connexion. *Lithos* **126**, 174–181.

Cobbing J. (2000) *Lecture Notes Earth Sciences*. eds. S. Bhattacharji, G. M. Friedman, H. J. Neugebauer, and A. Seilacher, Springer, New York.

Cocks L. R. M. and Torsvik T. H. (2013) The dynamic evolution of the Palaeozoic geography of eastern Asia. *Earth-Science Rev.* **117**, 40–79.

Coleman D. S., Gray W. and Glazner A. F. (2004) Rethinking the emplacement and evolution of zoned plutons: Geochronologic evidence for incremental assembly of the Tuolumne Intrusive Suite, California. *Geology* **32**, 433–436.

Collins L. G. (2000) Overlooked experimental evidence for K-replacements of plagioclase and origin of microcline in granite plutons. *Myrmekite Electron. J.* **37**, 1–9.

Costa J. C. D. A. (1944) Geologia da Província de Macau. *Bol. da Soc. Geológica Port.* **3**, 181–222.

Dai B.-Z., Jiang S.-Y., Jiang Y.-H., Zhao K.-D. and Liu D.-Y. (2008) Geochronology, geochemistry and Hf-Sr-Nd isotopic compositions of Huziyan mafic xenoliths, southern Hunan Province, South China: Petrogenesis and implications for lower crust evolution. *Lithos* **102**, 65–87.

Darbyshire D. P. F. and Sewell R. J. (1997) Nd and Sr isotope geochemistry of plutonic rocks from Hong Kong: implications for granite petrogenesis, regional structure and crustal evolution. *Chem. Geol.* **143**, 81–93.

Davis D. W., Sewell R. J. and Campbell S. D. G. (1997) U-Pb dating of Mesozoic igneous rocks from Hong Kong. *J. Geol. Soc. London.* **154**, 1067–1076.

Davis D. W., Williams I. S. and Krogh T. E. (2003) Historical Development of Zircon Geochronology. *Rev. Mineral. Geochemistry* **53**, 145–181.

Deer W. A., Howie R. A. and Zussman J. (1992) *An Introduction to the Rock-Forming Minerals*. 2nd ed., Prentice Hall, Harlow.

Defant M. J. and Drummond M. S. (1990) Derivation of some modern arc magmas by melting of young subducted litosphere. *Nature* **37**, 662–665.

Ding Y. Z. and Lai K. W. (1997) Neotectonic fault activity in Hong Kong: evidence from seismic events and thermoluminescence dating of fault gouge. *J. Geol. Soc. London.* **154**, 1001–1007.

Duan L., Meng Q.-R., Zhang C.-L. and Liu X.-M. (2011) Tracing the position of the South China block in Gondwana: U-Pb ages and Hf isotopes of Devonian detrital zircons. *Gondwana Res.* **19**, 141–149.

Esmaeily D., Maghdour-Mashhour R., Shabani T. and Ali A. (2013) Chemical characteristics of biotite from Boroujerd Granitoid complex (Middle Jurassic), Western Iran. *Geopersia* **3**, 69–78.

Faure M., Lepvrier C., Vuong N. Van, Tich V. Van, Lin W. and Chen Z. (2014) The South China block-Indochina collision: Where, when, and how? *J. Asian Earth Sci.* **79**, 260–274.

Faure M., Shu L. S., Wang B., Charvet J., Choulet F. and Monie P. (2009) Intracontinental subduction: a possible mechanism for the Early Palaeozoic Orogen of SE China. *Terra Nov.* **21**, 360–368.

Feng S.-J., Zhao K.-D., Ling H.-F., Chen P.-R., Chen W.-F., Sun T., Jiang S.-Y. and Pu W. (2014) Geochronology, elemental and Nd-Hf isotopic geochemistry of Devonian A-type granites in central Jiangxi, South China: Constraints on petrogenesis and post-collisional extension of the Wuyi-Yunkai orogeny. *Lithos* **206**–**207**, 1–18.

Floyd P. A. and Winchester J. A. (1978) Identification and discrimination of altered and metamorphosed volcanic rocks using immobile elements. *Chem. Geol.* **21**, 291–306.

Foster M. D. (1960) Interpretation of the composition of trictahedral micas. *U.S. Geol. Surv. Prof. Pap.* **354**-**B**, 11–49.

Frazer R. E., Coleman D. S. and Mills R. D. (2014) Zircon U-Pb geochronology of the Mount Givens Granodiorite: Implications for the genesis of large volumes of eruptible magma. *J. Geophys. Res. Earth* **119**, 2907–2924.

Galer S. J. G. and Abouchami W. (1998) Practical application of lead triple spiking for correction of instrumental mass discrimination. *Mineral. Mag.* **62A**, 491–492.

Gao J., Klemd R., Long L., Xiong X. and Qian Q. (2009) Adakitic signature formed by fractional crystallization: An interpretation for the Neo-Proterozoic meta-plagiogranites of the NE Jiangxi ophiolitic mélange belt, South China. *Lithos* **110**, 277–293.

Gao P., Zheng Y. and Zhao Z. (2017) Triassic granites in South China: A geochemical perspective on their characteristics, petrogenesis, and tectonic significance. *Earth-Science Rev.* **173**, 266–294.

Gao S., Yang J. I. E., Zhou L., Li M., Hu Z., Guo J., Yuan H., Gong H., Xiao G. and Wei J. (2011) Age and growth of the Archean Kongling terrain, South China, with emphasis on 3.3 Ga granitoid gneisses. *Am. J. Sci.* **311**, 153–182.

Geng H. and Xu X. (2006) Geochemistry of cretaceous volcanic-intrusive magmatism in western Guangdong and its geological significance. *Sci. China Ser. D Earth Sci.* **49**, 696–713.

Gertisser R. and Keller J. (2003) Trace element and Sr, Nd, Pb and O isotope variations in medium-K and high-K volcanic rocks from Merapi Volcano, Central Java, Indonesia: evidence for the involvement of subducted sediments in Sunda Arc magma genesis. *J. Petrol.* **44**, 457–489.

Gilder S. A., Keller G. R., Luo M. and Goode P. C. (1991) Eastern Asia and the Westem Pacific Timing and spatial distribution of rifting in China. *Tectonophysics* **197**, 225–243.

Gill R. (2010) *Igneous Rocks and Processes: a pratical guide*., Wiley-Blackwell, West Sussex, UK.

Gillot P. Y., Hildenbrand A., Lefèvre J. C. and Albore Livadie C. (2006) The K/Ar dating method: principle, analytical techniques, and application to holocene volcanic eruptions in Southern Italy. *Acta Vulcanol.* **18**, 55–66.

Glazner A. F., Bartley J. M., Coleman D. S., Walt G. and Ryan Z. T. (2004) Are plutons assembled over millions of years by amalgamation from small magma chambers? *Gsa Today* **14**, 4–10.

Grabau A. W. (1924) *Stratigraphy of China, part I, Paleozoic and older*., Geol. Surv. of Agric. and Commer., Peking.

Greentree M. R., Li Z.-X., Li X.-H. and Wu H. (2006) Late Mesoproterozoic to earliest Neoproterozoic basin record of the Sibao orogenesis in western South China and relationship to the assembly of Rodinia. *Precambrian Res.* **151**, 79–100.

Grimmer J. C., Ratschbacher L., Mcwilliams M., Franz L., Gaitzsch I., Tichomirowa M., Hacker B. R. and Zhang Y. (2003) When did the ultrahigh-pressure rocks reach the surface? A $^{207}Pb/^{206}Pb$ zircon, $^{40}Ar/^{39}Ar$ white mica, Si-in-white mica, single-grain provenance study of Dabie Shan synorogenic foreland sediments. *Chem. Geol.* **197**, 87–110.

Guo C., Chen Y., Zeng Z. and Lou F. (2012) Petrogenesis of the Xihuashan granites in southeastern China: Constraints from geochemistry and in-situ analyses of zircon U-Pb-Hf-O isotopes. *Lithos* **148**, 209–227.

Guo F., Fan W. M., Lin G. and Wu Y. L. (1997) Petrological characteristics and dating on gneiss xenoliths in Mesozoic basalts in Huziyan, Daoxian Region, Hunan Province. *J. Chang. Univ. Earth Sci.* **27**, 25–30 (in Chinese with English abstract).

Guo L., Shi Y., Lu H., Ma R., Dong H. and Yang S. (1989) The pre-Devonian tectonic patterns and evolution of South China. *J. Asian Earth Sci.* **3**, 87–93.

Hanchat J. M. and Miller C. F. (1993) Zircon zonation patterns as revealed by cathodoluminescence and backscattered electron images: Implications for interpretation of complex crustal histories. *Chem. Geol.* **110**, 1–13.

Harley S. L. and Kelly N. M. (2007) Zircon - Tiny but timely. *Elements* **3**, 13–18.

Hart S. R. (1984) A large-scale isotope anomaly in the Southern Hemisphere mantle. *Nature* **309**, 753–757.

He Z.-Y. and Xu X.-S. (2012) Petrogenesis of the Late Yanshanian mantle-derived intrusions in southeastern China: Response to the geodynamics of paleo-Pacific plate subduction. *Chem. Geol.* **328**, 208–221.

He Z.-Y., Xu X.-S. and Niu Y. (2010) Petrogenesis and tectonic significance of a Mesozoic granite-syenite-gabbro association from inland South China. *Lithos* **119**, 621–641.

Hofmann A. W. (1997) Mantle geochemistry the message from ocean volcanism. *Nature* **385**, 219–229.

Hofmann A. W. (2003) Sampling Mantle Heterogeneity through Oceanic Basalts: Isotopes and Trace Elements. In *Treatise on Geochemistry* pp. 61–101.

Hofmann A. W., Jochum K. P., Seufert M. and White W. M. (1986) Nb and Pb in oceanic basalts: new constraints on mantle evolution. *Earth Planet. Sci. Lett.* **79**, 33–45.

Horvat M. (2011) X-ray study of potassium feldspars from different granitoid types and gneisses of Papuk Mt. (Slavonia , Croatia). *Geol. Croat.* **64**, 153–162.

Hsieh P.-S., Chen C.-H., Yang H.-J. and Lee C.-Y. (2008) Petrogenesis of the Nanling Mountains granites from South China: Constraints from systematic apatite geochemistry and whole-rock geochemical and Sr-Nd isotope compositions. *J. Asian Earth Sci.* **33**, 428–451.

Hsu K. J., Li J., Chen H., Wang Q., Shu S. and Şengör A. M. C. (1990) Tectonics of South China: Key to understanding West Pacific geology. *Tectonics* **183**, 9–39.

Hu G. and Zhang B. (1998) Neodymium Isotope composition and souce materials of the meta-basement in Central Jiangxi Province. *Acta Pet. Miner.* **17**, 36–40.

Huang C.-C. (1978) An outline of the tectonic characteristics of China. *Eclogae Geol. Helv.* **71**, 611–635.

Huang H.-Q., Li X.-H., Li Z.-X. and Li W.-X. (2015) Formation of the Jurassic South China Large Granitic Province: Insights from the genesis of the Jiufeng pluton. *Chem. Geol.* **401**, 43–58.

Huang H.-Q., Li X.-H., Li Z.-X. and Li W.-X. (2012) Intraplate crustal remelting as the genesis of Jurassic high-K granites in the coastal region of the Guangdong Province, SE China. *J. Asian Earth Sci.* **74**, 280–302.

Huang J. Q., Ren J. S., Jiang C. F., Zhang Z. K. and Qin D. Y. (1987) *Geotectonic Evolution of China.*, Springer-Verlag, Berlin.

Huang K. and Opdyke N. D. (2016) Paleomagnetism of the Upper Triassic rocks from south of the Ailaoshan Suture and the timing of the amalgamation between the South China and the Indochina blocks. *J. Asian Earth Sci.* **119**, 118–127.

Huang Y. K. and Zhang K. 1990 (1990) Some characteristics of Neotectonic movements in the Lianhuashan Fault Zone, Guangdong. *J. South Chinese Seismol.* **10**, 25–34.

Hürlimann N., Müntener O., Ulmer P., Nandedkar R., Chiaradia M. and Ovtcharova M. (2016) Primary magmas in continental arcs and their differentiated products: Petrology of a post-plutonic dyke suite in the Tertiary Adamello Batholith (Alps). *J. Petrol.* **57**, 495–534.

Irber W. (1999) The lanthanide tetrad effect and its correlation with K/Rb, Eu/Eu*, Sr/Eu, Y/Ho, and Zr/Hf of evolving peraluminous granite suites. *Geochim. Cosmochim. Acta* **63**, 489–508.

Jackson S. E., Pearson N. J., Griffin W. L. and Belousova E. A. (2004) The application of laser ablation-inductively coupled plasma-mass spectrometry to in situ U-Pb zircon geochronology. *Chem. Geol.* **211**, 47–69.

Jahn B. M. (1974) Mesozoic thermal events in Southeast China. *Nature* **248**, 480–483.

Jahn B. M., Wu F., Capdevila R., Martineau F., Zhao Z. and Wang Y. (2001) Highly evolved juvenile granites with tetrad REE patterns: The Woduhe and Baerzhe granites from the Great Xing'an Mountains in NE China. *Lithos* **59**, 171–198.

Jahn B. M., Wu F., Lo C. H. and Tsai C. H. (1999) Crust-mantle interaction induced by deep subduction of the continental crust: Geochemical and Sr-Nd isotopic evidence from post-collisional mafic-ultramafic intrusions of the northern Dabie complex, central China. *Chem. Geol.* **157**, 119–146.

Jahn B. M., Zhoub X. H. and Li J. L. (1990) Formation and tectonic evolution of Southeastern China and Taiwan: Isotopic and geochemical constraints. *Tectonophysics* **183**, 145–160.

Jiang H., Jiang S. Y., Li W. Q., Zhao K. D. and Peng N. J. (2018) Highly fractionated Jurassic I-type granites and related tungsten mineralization in the Shirenzhang deposit, northern Guangdong, South China: Evidence from cassiterite and zircon U-Pb ages, geochemistry and Sr-Nd-Pb-Hf isotopes. *Lithos* **312**–**313**, 186–203.

Jiang Y.-H., Jiang S.-Y., Dai B.-Z., Liao S.-Y., Zhao K.-D. and Ling H.-F. (2009) Middle to late Jurassic felsic and mafic magmatism in southern Hunan province, southeast China: Implications for a continental arc to rifting. *Lithos* **107**, 185–204.

Jiang Y.-H., Wang G.-C., Liu Z., Ni C.-Y., Qing L. and Zhang Q. (2015) Repeated slab advance–retreat of the Palaeo-Pacific plate underneath SE China. *Int. Geol. Rev.* **57**, 472–491.

Jiang Y.-H., Zhao P., Zhou Q., Liao S.-Y. and Jin G.-D. (2011) Petrogenesis and tectonic implications of Early Cretaceous S- and A-type granites in the northwest of the Gan-Hang rift, SE China. *Lithos* **121**, 55–73.

Jiang Y.-H. and Zhu S. (2017) Petrogenesis of the Late Jurassic peraluminous biotite granites and muscovite-bearing granites in SE China: geochronological, elemental and Sr–Nd–O–Hf isotopic constraints. *Contrib. to Mineral. Petrol.* **172**, 101.

Keay S., Steele D. and Compston W. (1999) Identifying granite sources by SHRIMP U-Pb zircon geochronology: An application to the Lachlan foldbelt. *Contrib. to Mineral. Petrol.* **137**, 323–341.

Kelemen P. B., Hanghøj K. and Greene A. R. (2003) One view of the Geochemistry of Subduction-related Magmatic Arcs, with an Emphasis on Primitive Andesite and Lower Crust. In *Treatise on Geochemistry* pp. 593–659.

Keller C. B., Schoene B. and Samperton K. M. (2018) A stochastic sampling approach to zircon eruption age interpretation. *Geochemical Perspect. Lett.* **8**, 31–35.

Kemp A. I. S. and Hawkesworth C. J. (2003) Granitic Perspectives on the Generation and Secular Evolution of the Continental Crust. In *Treatise on Geochemistry* pp. 350–410.

King P. L., White A. J. R., Chappell B. W. and Allen C. M. (1997) Characterization and Origin of Aluminous A-type Granites from the Lachlan Fold Belt, Southeastern Australia. *J. Petrol.* **38**, 371–391.

Krogh T. E. (1973) A low-contamination method for hydrothermal decomposition of zircon and extraction of U and Pb for isotopic age determinations. *Geochim. Cosmochim. Acta* **37**, 485–494.

Lan C.-Y., Jahn B. M., Mertzmant S. A. and Wu T.-W. (1996) Subduction-related granitic rocks of Taiwan. *J. Southeast Asian Earth Sci.* **14**, 11–28.

Lapierre H., Jahn B. M., Charvet J. and Yu Y. W. (1997) Mesozoic felsic arc magmatism and continental olivine tholeiites in Zhejiang Province and their relationship with the tectonic activity in southeastern China. *Tectonophysics* **274**, 321–338.

Lee J. K. W. (2014) Ar–Ar and K–Ar Dating. In *Encyclopedia of Scientific Dating Methods* pp. 1–27.

Lee J. K. W., Williams I. S. and Ellis D. J. (1997) Pb, U and Th diffusion in natural zircon. *Nature* **390**, 159–162.

Lemos M. S. (1963) Esboço Geológico da Província Ultramarina de Macau, Escala 1/25000: Centro de Informação e Turismo.

Lepvrier C., Maluski H., Van Tich V., Leyreloup A., Truong Thi P. and Van Vuong N. (2004) The Early Triassic Indosinian orogeny in Vietnam (Truong Son Belt and Kontum Massif); implications for the geodynamic evolution of Indochina. *Tectonophysics* **393**, 87–118.

Lesher C. E. (1990) Decoupling of Chemical and Isotopic Exchange during Magma Mixing. *Nature* **344**, 235–237.

Li B., Jiang S.-Y. Y., Zhang Q., Zhao H.-X. X. and Zhao K.-D. D. (2015) Cretaceous crust-mantle interaction and tectonic evolution of Cathaysia Block in South China: Evidence from pulsed mafic rocks and related magmatism. *Tectonophysics* **661**, 136–155.

Li W.-X., Li X.-H. and Li Z.-X. (2005) Neoproterozoic bimodal magmatism in the Cathaysia Block of South China and its tectonic significance. *Precambrian Res.* **136**, 51–66.

Li W.-X., Li X.-H., Li Z.-X. and Lou F.-S. (2008) Obduction-type granites within the NE Jiangxi Ophiolite: Implications for the final amalgamation between the Yangtze and Cathaysia Blocks. *Gondwana Res.* **13**, 288–301.

Li X.-H. (2000) Cretaceous magmatism and lithospheric extension in Southeast China. *J. Asian Earth Sci.* **18**, 293–305.

Li X.-H. (1997) Timing of the Chathaysia Block formation: Constraints from SHRIMP U-Pb zircon geochronology. *Episodes* **20**, 188–192.

Li X.-H. (1999) U–Pb zircon ages of granites from the southern margin of the Yangtze Block: timing of Neoproterozoic Jinning: Orogeny in SE China and implications for Rodinia Assembly. *Precambrian Res.* **97**, 43–57.

Li X.-H., Chen Z., Liu D. and Li W.-X. (2003) Jurassic Gabbro-Granite-Syenite Suites from Southern Jiangxi Province, SE China: Age, Origin, and Tectonic Significance. *Int. Geol. Rev.* **45**, 898–921.

Li X.-H., Chung S.-L., Zhou H., Lo C.-H., Liu Y. and Chen C.-H. (2004) Jurassic intraplate magmatism in southern Hunan-eastern Guangxi: $^{40}Ar/^{39}Ar$ dating, geochemistry, Sr-Nd isotopes and implications for the tectonic evolution of SE China. *Geol. Soc. London, Spec. Publ.* **226**, 193–215.

Li X.-H., Li W.-H., Li Z.-H., Lo C.-H., Wang J., Ye M.-F. and Yang Y.-H. (2009a) Amalgamation between the Yangtze and Cathaysia Blocks in South China: Constraints from SHRIMP U–Pb zircon ages, geochemistry and Nd–Hf isotopes of the Shuangxiwu volcanic rocks. *Precambrian Res.* **174**, 117–128.

Li X.-H., Li W.-H., Wang X.-C., Li Q.-L., Liu Y. and Tang G.-Q. (2009b) Role of mantle-derived magma in genesis of early Yanshanian granites in the Nanling range, South China: In situ zircon Hf-O isotopic constraints. *Sci. China, Ser. D Earth Sci.* **52**, 1262–1278.

Li X.-H., Li Z.-H., He B., Li W.-X., Li Q.-L., Gao Y. and Wang X.-C. (2012) The Early Permian active continental margin and crustal growth of the Cathaysia Block: In situ U – Pb , Lu – Hf and O isotope analyses of detrital zircons. *Chem. Geol.* **328**, 195–207.

Li X.-H., Li Z.-H. and Li W.-H. (2014) Detrital zircon U–Pb age and Hf isotope constrains on the generation and reworking of Precambrian continental crust in the Cathaysia Block, South China: A synthesis. *Gondwana Res.* **25**, 1202–1215.

Li X.-H., Li Z.-H., Li W.-H. and Wang Y. (2006) Initiation of the Indosinian Orogeny in South China: Evidence for a Permian Magmatic Arc on Hainan Island. *J. Geol.* **114**, 341–353.

Li X.-H., Li Z.-X., Li W.-X., Liu Y., Yuan C., Wei G. and Qi C. (2007) U–Pb zircon, geochemical and Sr–Nd–Hf isotopic constraints on age and origin of Jurassic I- and A-type granites from central Guangdong, SE China: A major igneous event in response to foundering of a subducted flat-slab? *Lithos* **96**, 186–204.

Li X.-H., Sun M., Wei G.-J., Liu Y., Lee C.-Y. and Malpas J. (2000a) Geochemical and Sm-Nd isotopic study of amphibolites in the Cathaysia Block, southeastern China: Evidence for an extremely depleted mantle in the Paleoproterozoic. *Precambrian Res.* **102**, 251–262.

Li X.-H., Zhou G., Zhao J.-X., Fanning C. M. and Compston W. (1994) SHRIMP Ion Microprobe Zircon U-Pb Age and Sm-Nd Isotopic Characteristics of the NE Jiangxi Ophiolite and Its Tectonic Implications. *Chinese J. Geochemistry* **13**, 318–325.

Li X.-H., Zhou H.-W., Liu Y., Lee C.-Y., Chen Z.-H., Yu J.-S. and Gui X.-T. (2000b) Mesozoic shoshonitic intrusives in the Yangchun Basin, western Guangdong, and their tectonic significance. I. Petrology and isotope geochronology. *Geochemica* **29**, 513–520 (in Chinese with English abstract).

Li X.-Y., Zheng J.-P., Xiong Q., Zhou X. and Xiang L. (2018) Triassic rejuvenation of unexposed Archean-Paleoproterozoic deep crust beneath the western Cathaysia block, South China. *Tectonophysics* **724–725**.

Li X. H., Zhou H., Liu Y., Lee C.-Y., Sun M. and Chen C.-H. (2000) Shoshonitic intrusive suite in SE Guangxi: Petrology and geochemistry. *Chinese Sci. Bull.* **45**, 653–659.

Li Z.-H. and Li X.-H. (2007) Formation of the 1300-km-wide intracontinental orogen and postorogenic magmatic province in Mesozoic South China: A flat-slab subduction model. *Geology* **35**, 179–182.

Li Z.-H., Li X.-H., Wartho J.-A., Clark C., Li W.-X., Zhang C.-L. and Bao C. (2010) Magmatic and metamorphic events during the early Paleozoic Wuyi-Yunkai orogeny, southeastern South China: New age constraints and pressure-temperature conditions. *Bull. Geol. Soc. Am.* **122**, 772–793.

Li Z.-H., Li X.-H., Zhou H. and Kinny P. D. (2002) Grenvillian continental collision in south China: New SHRIMP U-Pb zircon results and implications for the configuration of Rodinia. *Geology* **30**, 163–166.

Li Z.-X. (1998) Tectonic History of the Major East Asian Lithospheric Since the Mid-Proterozoic - A Synthesis. In *Mantle Dynamics and Plate Interactions in East Asia* American Geophysical Union. pp. 221–243.

Li Z.-X., Li X.-H., Kinny P. D., Wang J., Zhang S. and Zhou H. (2003) Geochronology of Neoproterozoic syn-rift magmatism in the Yangtze Craton, South China and correlations with other continents: evidence for a mantle superplume that broke up Rodinia. *Precambrian Res.* **122**, 85–109.

Liu B. G., Zheng G. C., Chen S. M. and Tang H. F. (1995) The breakup of the Songmuwu group in western Zhejiang: evidence from isotope dating. *Geol. Rev.* **41**, 457–462 (in Chinese with English abstract).

Liu L., Qiu J.-S. and Li Z. (2013) Origin of mafic microgranular enclaves (MMEs) and their host quartz monzonites from the Muchen pluton in Zhejiang Province, Southeast China: Implications for magma mixing and crust–mantle interaction. *Lithos* **160**–**161**, 145–163.

Liu Q., Yu J.-H., O'Reilly S. Y., Zhou M.-F., Griffin W. L., Wang L. and Cui X. (2014) Origin and geological significance of Paleoproterozoic granites in the northeastern Cathaysia Block, South China. *Precambrian Res.* **248**, 72–95.

Liu R., Zhou H., Zhang L., Zhong Z.-Q., Zeng W., Xiang H., Jin S., Lu X. and Li C.-Z. (2009) Paleoproterozoic reworking of ancient crust in the Cathaysia Block, South China: Evidence from zircon trace elements, U-Pb and Lu-Hf isotopes. *Chinese Sci. Bull.* **54**, 1543–1554.

Liu Y., Gao S., Hu Z., Gao C., Zong K. and Wang D. (2009) Continental and oceanic crust recycling-induced melt-peridotite interactions in the Trans-North China Orogen: U-Pb dating, Hf isotopes and trace elements in zircons from mantle xenoliths. *J. Petrol.* **51**, 537–571.

London D., Hervig R. L. and Morgan G. B. (1988) Melt-vapor solubilities and elemental partitioning in peraluminous granite- pegmatite systems: experimental results with Macusani glass at 200 MPa. *Contrib. to Mineral. Petrol.* **99**, 360–373.

Ludwig K. R. (1998) On the treatment of concordant uranium-lead ages. *Geochim. Cosmochim. Acta* **62**, 665–676.

Ludwig K. R. (2012) User's Manual for Isoplot 3.75, a geochronological toolkit for Microsoft Excel. *Berkeley Geochronol. Cent. Spec. Publ.* **5**, 1–72.

Ma X. and Wu Z. (1981) Early tectonic evolution of china. *Precambrian Res.* **14**, 185–202.

Magaritz M. and Hofmann A. W. (1978) Diffusion of Sr, Ba and Na in obsidian. *Geochim. Cosmochim. Acta* **42**, 595–605.

Mahood G. and Hildreth W. (1983) Large partition coefficients for trace elements in high-silica rhyolites. *Geochim. Cosmochim. Acta* **47**, 11–30.

Le Maitre R. W., Streckeisen A., Zanettin B., Le Bas M. J., Bonin B., Bateman P., Bellieni G., Dudek A., Efremova S., Keller J., Lameyre J., Sabine P. A., Schmid R., Sorensen H. and Woolley A. R. (2002) *Igneous Rocks A Classification and Glossary of Terms*. 2nd ed. ed. R. W. Le Maitre, Cambridge University Press, New York.

Mao Jingwen, Cheng Y., Chen M. and Franco P. (2013) Major types and time-space distribution of Mesozoic ore deposits in South China and their geodynamic settings. *Miner. Depos.* **48**, 267–294.

Mao J., Li Z. and Ye H. (2014) Mesozoic tectono-magmatic activities in South China: Retrospect and prospect. *Sci. China Earth Sci.* **57**, 2853–2877.

Mao J., Takahashi Y., Kee W. S., Li Z., Ye H., Zhao X., Liu K. and Zhou J. (2011) Characteristics and geodynamic evolution of Indosinian magmatism in South China: A case study of the Guikeng pluton. *Lithos* **127**, 535–551.

Mao Jianren, Ye H., Liu K., Li Z., Takahashi Y., Zhao X. and Kee W. (2013) The Indosinian collision–extension event between the South China Block and the Palaeo-Pacific plate: Evidence from Indosinian alkaline granitic rocks in Dashuang, eastern Zhejiang, South China. *Lithos* **172**–**173**, 81–97.

Marques F. M. S. F. (1988) Contribuição para o conhecimento geológico e geotécnico do Território de Macau. Faculdade de Ciências da Universidade de Lisboa.

Marques F. M. S. F. and Silva M. O. (1990a) Geotechnical properties and provenance of the Pleistocene alluvium of Macau. In *VIth Intern. Congr. Intern. Assoc. of Engineering Geology, Amsterdam* (ed. A. A.). Balkema, Rotterdam. pp. 2899–2905.

Marques F. M. S. F. and Silva M. O. (1990b) Geotechnical properties of the Holocene muds of Macau. *Geologis* **4**, 177–191.

Martin H., Smithies R. H., Rapp R., Moyen J. F. and Champion D. (2005) An overview of adakite, tonalite-trondhjemiten-granodiorite (TTG), and sanukitoid: relationships and some implications for crustal evolution. *Lithos* **79**, 1–24.

Mattinson J. M. (2005) Zircon U-Pb chemical abrasion ("CA-TIMS") method: Combined annealing and multi-step partial dissolution analysis for improved precision and accuracy of zircon ages. *Chem. Geol.* **220**, 47–66.

Matzel J. E. P., Bowring S. A. and Miller R. B. (2006) Time scales of pluton construction at differing crustal levels: Examples from the Mount Stuart and Tenpeak intrusions, North Cascades, Washington. *Bull. Geol. Soc. Am.* **118**, 1412–1430.

McDonough W. F. and Sun S. -s. (1995) The composition of the Earth. *Chem. Geol.* **120**, 223–253.

Memeti V., Paterson S., Matzel J., Mundil R. and Okaya D. (2010) Magmatic lobes as "snapshots" of magma chamber growth and evolution in large, composite batholiths: An example from the Tuolumne intrusion, Sierra Nevada, California. *Bull. Geol. Soc. Am.* **122**, 1912–1931.

Menand T., Annen C. and Blanquat M. de Saint (2015) Rates of magma transfer in the crust: Insights into magma reservoir recharge and pluton growth. *Geology* **43**, 199–202.

Meng L., Li Z.-X., Chen H., Li X.-H. and Wang X.-C. (2012) Geochronological and geochemical results from Mesozoic basalts in southern South China Block support the flat-slab subduction model. *Lithos* **132–133**, 127–140.

Mielke P. and Winkler H. G. F. (1979) Eine bessere Berechnung der Mesonorm für granitische Gesteine. *Neu. Jb. Miner. Mh.*, 471—480.

Miller C. F., McDowell S. M. and Mapes R. W. (2003) Hot and cold granites: Implications of zircon saturation temperatures and preservation of inheritance. *Geology* **31**, 529–532.

Miller J. S., Matzel J. E. P., Miller C. F., Burgess S. D. and Miller R. B. (2007) Zircon growth and recycling during the assembly of large, composite arc plutons. *J. Volcanol. Geotherm. Res.* **167**, 282–299.

Morrison G. W. (1980) Characteristics and tectonic setting of the shoshonite rock association. *Lithos* **13**, 97–80.

Nachit H., Ibhi A., Abia E. H. and Ben Ohoud M. (2005) Discrimination between primary magmatic biotites, reequilibrated biotites and neoformed biotites. *Comptes Rendus Geosci.* **337**, 1415–1420.

Nachit H., Razafimahefa N., Stussi J. M. and Carron J. P. (1985) Composition chimique des biotites et typologie magmatique des granites. *C.R. Acad. Sci. Paris* **Sér. II**, 813-818.

Neiva J. M. C. (1944) Rochas eruptivas da Península de Macau e das ilhas de Taipa e Coloane. *Bol. da Soc. Geológica Port.* **3**, 145–180.

Pankhurst M. J., Vernon R. H., Turner S. P., Schaefer B. F. and Foden J. D. (2011) Contrasting Sr and Nd isotopic behaviour during magma mingling; new insights from the Mannum A-type granite. *Lithos* **126**, 135–146.

Paul D., White W. M. and Turcotte D. L. (2003) Constraints on the $^{232}Th/^{238}U$ ratio (κ) of the continental crust. *Geochemistry, Geophys. Geosystems* **4**, 1–17.

Pearce J. A., Harris N. B. W. and Tindle A. G. (1984) Trace element discrimination diagrams for the tectonic interpretation of granitic rocks. *J. Petrol.* **25**, 956–983.

Peccerillo A. and Taylor S. R. (1976) Geochemistry of eocene calc-alkaline volcanic rocks from the Kastamonu area, Northern Turkey. *Contrib. to Mineral. Petrol.* **58**, 63–81.

Peng T., Fan W., Zhao G., Peng B., Xia X. and Mao Y. (2015) Petrogenesis of the early Paleozoic strongly peraluminous granites in the Western South China Block and its tectonic implications. *J. Asian Earth Sci.* **98**, 399–420.

Qiu Y. M., Gao S., McNaughton N. J., Groves D. I. and Ling W. (2000) First evidence of >3.2 Ga continental crust in the Yangtze craton of south China and its implications for Archean crustal evolution and Phanerozoic tectonics. *Geology* **28**, 11–14.

Qiu Z., Li S., Yan Q., Wang H., Wei X., Li P., Wang L. and Bu A. (2017) Late Jurassic Sn metallogeny in eastern Guangdong, SE China coast: Evidence from geochronology, geochemistry and Sr–Nd–Hf–S isotopes of the Dadaoshan Sn deposit. *Ore Geol. Rev.* **83**, 63–83.

Qiu Z., Yan Q., Li S., Wang H., Tong L., Zhang R., Wei X., Li P., Wang L., Bu A. and Yan L. (2016) Highly fractionated Early Cretaceous I-type granites and related Sn polymetallic mineralization in the Jinkeng deposit, eastern Guangdong, SE China: Constraints from geochronology, geochemistry, and Hf isotopes. *Ore Geol. Rev.* **88**, 718–738.

Quelhas P., Dias Á. A., Mata J., Davis D. W. and Ribeiro M. L. (2019) High-precision geochronology of Mesozoic magmatism in Macao, Southeast China: evidence for multistage granite emplacement. *Geosci. Front.*

Rapp R. P. and Watson E. B. (1995) Dehydration melting of metabasalt at 8-32 kbar: Implications for continental growth and crust-mantle recycling. *J. Petrol.* **36**, 891–931.

Ren J. S. (1964) A preliminary study on pre-Devonian geotectonic problems of southeastern China. *Acta Geol. Sin.* **44**, 418–431.

Ren J. S. (1991) On the Geotectonics of Southern China. *Acta Geol. Sin.* **4**, 111–130.

Ren J. S., Wang Z. X., Chen B. W., Jiang C. F., Niu B. G., Li J. Y., Xie G. L., He Z. J. and Liu Z. G. (1999) *The Tectonics of China from a Global View – A Guide to the Tectonic Map of China and Adjacent Regions*., Geological Publishing House, Beijing.

Ribeiro M. L., Ramos J. F., Pereira E. and Dias R. (2010) The Evolution of the Macao Geological Knowledge. *Geol. das Ex-Colónias da Ásia e Oceânia, Macau* **III**, 259–266.

Ribeiro M. L., Ramos J. M. ., Pereira E. and Dias R. P. (1992) *Notícia Explicativa da Carta Geológica de Macau na escala 1/5000.*, Lisboa.

Rieder M. (1999) Nomenclature of the Micas. *Mineral. Mag.* **63**, 267–279.

Roberts N. M. W. and Spencer C. J. (2015) The zircon archive of continent formation through time. *Geol. Soc. London, Spec. Publ.* **389**, 197–225.

Rocha A. T. and Torquato J. R. (1967) Contribuição para o conhecimento da mineralogia das areias de praia das Ilhas da Taipa e de Coloane (Província Portuguesa de Macau). *Bol. Inst. Invest. Cient. Angola* **4**, 89–104.

Rong J., Wang Y. and Zhang X. (2012) Tracking shallow marine red beds through geological time as exemplified by the lower Telychian (Silurian) in the Upper Yangtze Region, South China. **55**, 699–713.

Rubatto D. and Gebauer D. (2000) Use of Cathodoluminescence for U-Pb Zircon Dating by Ion Microprobe: Some Examples from the Western Alps Chapter. In *Cathodoluminescence in Geosciences* Springer Berlin Heidelberg. pp. 373–400.

Rudnick R. L. (1995) Making continental crust. *Nature* **38**, 571–578.

Rudnick R. L. and Gao S. (2003) Composition of the Continental Crust. In *Treatise on Geochemistry* Elsevier Ltd. pp. 1–64.

Rudnick R. L. and Goldstein S. L. (1990) The Pb isotopic compositions of lower crustal xenoliths and the evolution of lower crustal Pb. *Earth Planet. Sci. Lett.* **98**, 192–207.

Sambridge M. S. and Compston W. (1994) Mixture modeling of multi-component data sets with application to ion-probe zircon ages. *Earth Planet. Sci. Lett.* **128**, 373–390.

Scherer E. E., Whitehouse M. J. and Münker C. (2007) Zircon as a monitor of crustal growth. *Elements* **3**, 19–24.

Schoene B., Schaltegger U., Brack P., Latkoczy C., Stracke A. and Günther D. (2012) Rates of magma differentiation and emplacement in a ballooning pluton recorded by U-Pb TIMS-TEA, Adamello batholith, Italy. *Earth Planet. Sci. Lett.* **355–356**, 162–173.

Sewell R. J. and Campbell S. D. G. (1997) Geochemistry of coeval Mesozoic plutonic and volcanic suites in Hong Kong. *J. Geol. Soc. London.* **154**, 1053–1066.

Sewell R. J., Campbell S. D. G., Fletcher C. J. N., Lai K. W. and Kirk P. A. (2000a) *The pre-Quaternary geology of Hong Kong. Civil Engineering Department, Hong Kong SAR Government, Hong Kong*.

Sewell R. J., Carter A. and Rittner M. (2016) Middle Jurassic collision of an exotic microcontinental fragment: Implications for magmatism across the Southeast China continental margin. *Gondwana Res.* **38**, 304–312.

Sewell R. J., Chan L. S., Fletcher C. J. N., Brewer T. S. and Zhu J. C. (2000b) Isotope zonation in basement crustal blocks of southeastern China : Evidence for multiple terrane amalgamation. *Episodes* **23**, 257–261.

Sewell R. J., Darbyshire D. P. F., Langford R. L. and Strange P. J. (1992) Geochemistry and Rb-Sr geochronology of Mesozoic granites from Hong Kong. *Earth Environ. Sci. Trans. R. Soc. Edinburgh* **83**, 269–280.

Sewell R. J., Davis D. W. and Campbell S. D. G. (2012a) High precision U–Pb zircon ages for Mesozoic igneous rocks from Hong Kong. *J. Asian Earth Sci.* **43**, 164–175.

Sewell R. J., Tang D. L. K. and Campbell S. D. G. (2012b) Volcanic-plutonic connections in a tilted nested caldera complex in Hong Kong. *Geochemistry, Geophys. Geosystems* **13**, 1–17.

Shand S. J. (1943) *Eruptive Rocks. Their Genesis, Composition, Classification, and Their Relation to Ore-Deposits with a Chapter on Meteorite*., John Wiley & Sons, New York.

Shaw R., Tang D. L. K., Owen R. B. and Sewell R. J. (2010) The Geological History of Hong Kong. *Asian Geogr.* **1**–**2**, 2010.

Shen W., Ling H., Li W. and Wang D. (2000) Crust evolution in Southeast China: evidence from Nd model ages of granitoids. *Sci. China Ser. D Earth Sci.* **43**, 36–49.

Shen W., Yu J., Zhao L., Chen Z. and Lin H. (2003) Nd isotopic characteristics of post-Archean sediments from the Eastern Nanling Range: Evidence for crustal evolution. *Chinese Sci. Bull.* **48**, 1679–1685.

Shu L. S. and Charvet J. (1996) Kinematics and geochronology of the Proterozoic Dongxiang-Shexian ductile shear zone: with HP metamorphism and ophiolitic melange (Jiangnan Region, South China). *Tectonophysics* **267**, 291–302.

Shu L. S., Faure M., Jiang S. Y., Yang Q. and Wang Y. J. (2006) SHRIMP zircon U-Pb age, litho- and biostratigraphic analyses of the Huaiyu Domain in south China - Evidence for a Neoproterozoic orogen, not Late Paleozoic-Early Mesozoic collision. *Episodes* **29**, 244–252.

Shu L. S., Faure M., Wang B., Zhou X. and Song B. (2008a) Late Palaeozoic–Early Mesozoic geological features of South China: Response to the Indosinian collision events in Southeast Asia. *Comptes Rendus Geosci.* **340**, 151–165.

Shu L. S., Faure M., Yu J. H. and Jahn B. M. (2011) Geochronological and geochemical features of the Cathaysia block (South China): New evidence for the Neoproterozoic breakup of Rodinia. *Precambrian Res.* **187**, 263–276.

Shu L. S., Jahn B. M., Charvet J., Santosh M., Wang B., Xu X. S. and Jiang S. Y. (2014) Intraplate tectono-magmatism in the Cathaysia Block (south China): Evidence from stratigraphic, structural, geochemical and geochronological investigations. *Am. J. Sci.* **314**, 154–186.

Shu L. S., Wang B., Cawood P. A., Santosh M. and Xu Z. (2015) Early Paleozoic and Early Mesozoic intraplate tectonic and magmatic events in the Cathaysia Block, South China. *Tectonics* **34**, 1600–1621.

Shu L. S., Yu J. H., Jia D., Wang B., Shen W. Z. and Zhang Y. Q. (2008b) Early Paleozoic orogenic belt in the eastern segment of south China. *Geol. Bull. China* **27**, 1581–1593.

Shu L. S., Zhou G. Q., Shi Y. S. and Yin J. (1994) Study of the high-pressure metamorphic blueschist and its late Proterozoic age in the eastern Jiangnan belt. *Chinese Sci. Bull.* **39**, 1200–1204.

Sisson T. W., Ratajeski K., Hankins W. B. and Glazner A. F. (2005) Voluminous granitic magmas from common basaltic sources. *Contrib. to Mineral. Petrol.* **148**, 635–661.

Smith J. V. and Brown W. L. (1974) *Feldspar Minerals 1. Crystal Structures, Physical, Chemical and Microtextural Properties*., Springer, Berlin, Heidelberg.

So C. and Ribeiro M. (1997) Portugal: Macao. In *Encyclopedia of European and Asian Regional Geology* (eds. E.M. Moores and R. W. Fairbridge). Chapman & Hall, London. pp. 620–621.

Speer J. A. (1984) Micas in igneous rocks. *Rev. Mineral. Geochemistry* **13**, 299–356.

Stern R. J., Li S. and Keller G. R. (2018) Continental crust of China: A brief guide for the perplexed. *Earth-Science Rev.* **179**, 72–94.

Streckeisen A. and Le Maitre R. W. (1979) A chemical approximation to the modal QAPF classification of the igneous rocks. *Neues Jahrb. fur Mineral. Abteilung*, 169–206.

Sun S. -s. and McDonough W. F. (1989) Chemical and isotopic systematics of oceanic basalts: implications for mantle composition and processes. *Geol. Soc. London, Spec. Publ.* **42**, 313–345.

Sun T. (2005) Strongly peraluminous granites of Mesozoic in Eastern Nanling Range, southern China: Petrogenesis and implications for tectonics. *Sci. China Ser. D* **48**, 165.

Sun W. D., Yang X. Y., Fan W. M. and Wu F. Y. (2012) Mesozoic large scale magmatism and mineralization in South China: Preface. *Lithos* **150**, 1–5.

Sun Y., Ma C., Liu Y. and She Z. (2011) Geochronological and geochemical constraints on the petrogenesis of late Triassic aluminous A-type granites in southeast China. *J. Asian Earth Sci.* **42**, 1117–1131.

Takahashi Y., Yoshida H., Sato N., Hama K., Yusa Y. and Shimizu H. (2002) W- and M-type tetrad effects in REE patterns for water–rock systems in the Tono uranium deposit, central Japan. *Chem. Geol.* **184**, 311–335.

Tang D. L. K., Seward D., Wilson C. J. N., Sewell R. J., Carter A. and Paul B. T. (2014) Thermotectonic history of SE China since the Late Mesozoic: insights from detailed thermochronological studies of Hong Kong. *J. Geol. Soc. London.* **171**, 591–604.

Tang L., Chen H., Dong C., Yang S., Shen Z., Cheng X. and Fu L. (2013) Middle Triassic post-orogenic extension on Hainan Island : Chronology and geochemistry constraints of bimodal intrusive rocks. *Sci. China Earth Sci.* **56**, 783–793.

Tao J.-H., Li W.-X., Li X.-H. and Cen T. (2013) Petrogenesis of early Yanshanian highly evolved granites in the Longyuanba area, southern Jiangxi Province: Evidence from zircon U-Pb dating, Hf-O isotope and whole-rock geochemistry. *Sci. China Earth Sci.* **56**, 922–939.

Tatsumi Y. (2006) High-Mg Andesites in the Setouchi Volcanic Belt , Southwestern Japan: Analogy to Archean Magmatism and Continental Crust Formation? *Annu. Rev. Earth Planet. Sci.* **34**, 467–499.

Taylor S. R. and Mclennan S. M. (1995) The Geochemical Evolution of the Continental Crust. *Rev. Geophys.* **32**, 241–265.

Veksler I. V., Dorfman A. M., Kamenetsky M., Dulski P. and Dingwell D. B. (2005) Partitioning of lanthanides and Y between immiscible silicate and fluoride melts, fluorite and cryolite and the origin of the lanthanide tetrad effect in igneous rocks. *Geochim. Cosmochim. Acta* **69**, 2847–2860.

Vernon R. H. (1990) Crystallization and hybridism in microgranitoid enclave magmas: Microstructural evidence. *J. Geophys. Res.* **95**, 17849–17859.

Vernon R. H. and Paterson S. R. (2002) Igneous origin of K-feldspar megacrysts in deformed granite of the Papoose Flat Pluton, California, USA. *Electonic Geosci.* **7**, 31–39.

Vervoort J. D., Patchett P. J., Blichert-Toft J. and Albarède F. (1999) Relationships between Lu-Hf and Sm-Nd isotopic systems in the global sedimentary system. *Earth Planet. Sci. Lett.* **168**, 79–99.

Wan Y., Liu D., Wilde S. A., Cao J., Chen B., Dong C., Song B. and Du L. (2010) Evolution of the Yunkai Terrane, South China: Evidence from SHRIMP zircon U–Pb dating, geochemistry and Nd isotope. *J. Asian Earth Sci.* **37**, 140–153.

Wan Y., Liu D., Xu M., Zhuang J., Song B., Shi Y. and Du L. (2007) SHRIMP U–Pb zircon geochronology and geochemistry of metavolcanic and metasedimentary rocks in Northwestern Fujian, Cathaysia block, China: Tectonic implications and the need to redefine lithostratigraphic units. *Gondwana Res.* **12**, 166–183.

Wang D., Zheng J., Ma Q., Griffin W. L., Zhao H. and Wong J. (2013) Early Paleozoic crustal anatexis in the intraplate Wuyi-Yunkai orogen, South China. *Lithos* **175**–**176**, 124–145.

Wang H. Z. and Mo X. X. (1995) An outline of the tectonic evolution of China. *Episodes* **18**, 6–16.

Wang K.-X., Sun T., Chen P.-R., Ling H.-F. and Xiang T.-F. (2013) The geochronological and geochemical constraints on the petrogenesis of the Early Mesozoic A-type granite and diabase in northwestern Fujian province. *Lithos* **179**, 364–381.

Wang Q., Li J.-W., Jian P., Zhao Z.-H., Xiong X.-L., Bao Z.-W., Xu J.-F., Li C.-F. and Ma J.-L. (2005) Alkaline syenites in eastern Cathaysia (South China): link to Permian-Triassic transtension. *Earth Planet. Sci. Lett.* **230**, 339–354.

Wang X.-L., Zhao G., Zhou J.-C., Liu Y. and Hu J. (2008) Geochronology and Hf isotopes of zircon from volcanic rocks of the Shuangqiaoshan Group, South China: Implications for the Neoproterozoic tectonic evolution of the eastern Jiangnan orogen. *Gondwana Res.* **14**, 355–367.

Wang X.-L., Zhou J.-C., Griffin W. L., Wang R.-C., Qiu J.-Q., O'Reilly S. Y., Xu X., Liu X.-M. and Zhang G.-L. (2007) Detrital zircon geochronology of Precambrian basement sequences in the Jiangnan orogen: Dating the assembly of the Yangtze and Cathaysia Blocks. *Precambrian Res.* **159**, 117–131.

Wang X.-L., Zhou J.-C., Qiu J.-S., Zhang W.-L., Liu X.-M. and Zhang G.-L. (2006) LA-ICP-MS U-Pb zircon geochronology of the Neoproterozoic igneous rocks from Northern Guangxi, South China: Implications for tectonic evolution. *Precambrian Res.* **145**, 111–130.

Wang Y., Fan W., Cawood P. A. and Li S. (2008) Sr-Nd-Pb isotopic constraints on multiple mantle domains for Mesozoic mafic rocks beneath the South China Block hinterland. *Lithos* **106**, 297–308.

Wang Y., Fan W., Guo F., Peng T. and Li C. (2003) Geochemistry of Mesozoic Mafic Rocks Adjacent to the Chenzhou-Linwu fault, South China: Implications for the Lithospheric Boundary between the Yangtze and Cathaysia Blocks. *Int. Geol. Rev.* **45**, 263–286.

Wang Y., Fan W., Sun M., Liang X., Zhang Y. and Peng T. (2007a) Geochronological, geochemical and geothermal constraints on petrogenesis of the Indosinian peraluminous granites in the South China Block: A case study in the Hunan Province. *Lithos* **96**, 475–502.

Wang Y., Fan W., Zhang G. and Zhang Y. (2013) Phanerozoic tectonics of the South China Block: Key observations and controversies. *Gondwana Res.* **23**, 1273–1305.

Wang Y., Fan W., Zhao G., Ji S. and Peng T. (2007b) Zircon U–Pb geochronology of gneissic rocks in the Yunkai massif and its implications on the Caledonian event in the South China Block. *Gondwana Res.* **12**, 404–416.

Wang Y., Zhang A., Fan W., Zhao G., Zhang G. and Zhang Y. (2011) Kwangsian crustal anatexis within the eastern South China Block: Geochemical, zircon U–Pb geochronological and Hf isotopic fingerprints from the gneissoid granites of Wugong and Wuyi–Yunkai Domains. *Lithos* **127**, 239–260.

Wang Y., Zhang F., Fan W., Zhang G., Chen S., Cawood P. A. and Zhang A. (2010) Tectonic setting of the South China Block in the early Paleozoic: Resolving intracontinental and ocean closure models from detrital zircon U-Pb geochronology Yuejun. *Tectonics* **29**, 1–16.

Watson E. B. and Harrison T. M. (1983) Zircon saturation revisited: temperature and composition effects in a variety of crustal magma types. *Earth Planet. Sci. Lett.* **64**, 295–304.

Wedepohl K. H. (1995) The composition of the continental crust. *Geochim. Cosmochim. Acta* **59**, 1217–1232.

Weis D., Kieffer B., Maerschalk C., Barling J., De Jong J., Williams G. A., Hanano D., Pretorius W., Mattielli N., Scoates J. S., Goolaerts A., Friedman R. M. and Mahoney J. B. (2006) High-precision isotopic characterization of USGS reference materials by TIMS and MC-ICP-MS. *Geochemistry, Geophys. Geosystems* **7**.

Whalen J. B., Currie K. L. and Chappell B. W. (1987) A-type granites: geochemical characteristics, discrimination and petrogenesis. *Contrib. to Mineral. Petrol.* **95**, 407–419.

Wiedenbeck M., Allé P., Corfu F., Griffin W. L., Meier M., Oberli F., Quadt A. VON, Roddick J. C. and Spiegel W. (1995) Three Natural Zircon Standards for U-Th-Pb, Lu-Hf, Trace Element and Ree Analyses. *Geostand. Newsl.* **19**, 1–23.

Wilson B. M. (1989) *Igneous Petrogenesis A Global Tectonic Approach*., Chapman & Hall, London.

Wolf M. B. and London D. (1994) Apatite dissolution into peraluminous haplogranitic melts: An experimental study of solubilities and mechanisms. *Geochim. Cosmochim. Acta* **58**, 4127–4145.

Wones D. R. and Eugster H. P. (1965) Stability of biotite: Experiment, Theory, and Application. *Am. Mineral.* **50**, 1228–1272.

Wood D. A. (1980) The application of a Th-Hf-Ta diagram to problems of tectonomagmatic classification and to establishing the nature of crustal contamination of basaltic lavas of the British Tertiary volcanic province. *Earth Planet. Sci. Lett.* **50**, 11–30.

Wu F. Y., Sun D. Y., Jahn B. M. and Wilde S. (2004) A Jurassic garnet-bearing granitic pluton from NE China showing tetrad REE patterns. *J. Asian Earth Sci.* **23**, 731–744.

Xia S., Shen Y., Zhao D. and Qiu X. (2015) Lateral variation of crustal structure and composition in the Cathaysia block of South China and its geodynamic implications. *J. Asian Earth Sci.* **109**, 20–28.

Xia S. and Zhao D. (2014) Late Mesozoic magmatic plumbing system in the onshore-offshore area of Hong Kong: Insight from 3-D active-source seismic tomography. *J. Asian Earth Sci.* **96**, 46–58.

Xia X., Sun M., Geng H., Sun Y., Wang Y. and Zhao G. (2011) Quasi-simultaneous determination of U-Pb and Hf isotope compositions of zircon by excimer laser-ablation multiple-collector ICPMS. *J. Anal. At. Spectrom.* **26**, 1868–1871.

Xia Y., Xu X. and Liu L. (2016) Transition from adakitic to bimodal magmatism induced by the paleo-Pacific plate subduction and slab rollback beneath SE China: Evidence from petrogenesis and tectonic setting of the dike swarms. *Lithos* **244**, 182–204.

Xia Y., Xu X., Zou H. and Liu L. (2014) Early paleozoic crust-mantle interaction and lithosphere delamination in south china block: Evidence from geochronology, geochemistry, and Sr-Nd-Hf isotopes of granites. *Lithos* **184**–**187**, 416–435.

Xiang Y. X., Yang J. H., Chen J. Y. and Zhang Y. (2017) Petrogenesis of Lingshan highly fractionated granites in the Southeast China: Implication for Nb-Ta mineralization. *Ore Geol. Rev.* **89**, 495–525.

Xie C. F., Zhu J. C., Zhao Z. J., Ding S. J., Fu T. A., Li Z. H., Zhang Y. M. and Yu D. P. (2005) Zircon SHRIMP U-Pb age dating of garnet-acmite syenite: constraints on the Hercynian-Indosinian tectonic evolution of Hainan. *Geol. J. China Univ.* **11**, 47–57.

Xu B., Jiang S.-Y., Hofmann A. W., Wang R., Yang S.-Y. and Zhao K.-D. (2016) Geochronology and geochemical constraints on petrogenesis of Early Paleozoic granites from the Laojunshan district in Yunnan Province of South China. *Gondwana Res.* **29**, 248–263.

Xu B., Jiang S.-Y., Wang R., Ma L., Zhao K.-D. and Yan X. (2015) Late Cretaceous granites from the giant Dulong Sn-polymetallic ore district in Yunnan Province, South China: Geochronology, geochemistry, mineral chemistry and Nd-Hf isotopic compositions. *Lithos* **218**–**219**, 54–72.

Xu B. and Qiao G. S. (1989) Sm–Nd isotopic age and tectonic setting of the late Proterozoic ophiolites in northeastern Jiangxi province. *J. Nanjing Univ. Earth Sci.* **3**, 108–114 (in Chinese with English abstract).

Xu H., Ma C., Zhao J. and Zhang J. (2014) Magma mixing generated Triassic I-type granites in South China. *J. Geol.* **122**, 329–351.

Xu W. and Xu X. (2015) Early Paleozoic intracontinental felsic magmatism in the South China Block: Petrogenesis and geodynamics. *Lithos* **234**–**235**, 79–92.

Xu X. B., Zhang Y. Q., Shu L. S. and Jia D. (2011) La-ICP-MS U–Pb and $^{40}Ar/^{39}Ar$ geochronology of the sheared metamorphic rocks in the Wuyishan: Constraints on the timing of Early Paleozoic and Early Mesozoic tectono-thermal events in SE China. *Tectonophysics* **501**, 71–86.

Xu X., Lu W. and He Z. (2007a) Age and generation of Fogang granite batholith and Wushi diorite-hornblende gabbro body. *Sci. China Ser. D Earth Sci.* **50**, 209–220.

Xu X., O'Reilly S. Y., Griffin W. L., Deng P. and Pearson N. J. (2005) Relict Proterozoic basement in the Nanling Mountains (SE China) and its tectonothermal overprinting. *Tectonics* **24**, 1–16.

Xu X., O'Reilly S. Y., Griffin W. L., Wang X., Pearson N. J. and He Z. (2007b) The crust of Cathaysia: Age, assembly and reworking of two terranes. *Precambrian Res.* **158**, 51–78.

Yan C., Shu L. S., Michel F., Chen Y. and Li C. (2017) Early Paleozoic intracontinental orogeny in the Yunkai domain , South China Block: New insights from fi eld observations , zircon U–Pb geochronological and geochemical investigations. *Lithos* **268**–**271**, 320–333.

Yan Q. H., Li S. S., Qiu Z. W., Wang H., Wei X. P., Pei-Li, Dong R., Zhang X. Y., Pei-Li, Dong R. and Zhang X. Y. (2017) Geochronology, geochemistry and Sr–Nd–Hf–S–Pb isotopes of the Early Cretaceous Taoxihu Sn deposit and related granitoids, SE China. *Ore Geol. Rev.* **89**, 350–368.

Yang Z.-Y., Wang Q., Zhang C., Dan W., Zhang X.-Z., Qi Y., Xia X.-P. and Zhao Z.-H. (2018) Rare earth element tetrad effect and negative Ce anomalies ofthe granite porphyries in southern Qiangtang Terrane, central Tibet: New insights into the genesis of highly evolved granites. *Lithos* **312**–**313**, 258–273.

Ye M.-F., Li X.-H., Li W.-X., Liu Y. and Li Z.-X. (2007) SHRIMP zircon U–Pb geochronological and whole-rock geochemical evidence for an early Neoproterozoic Sibaoan magmatic arc along the southeastern margin of the Yangtze Block. *Gondwana Res.* **12**, 144–156.

Yu J.-H., O'Reilly S. Y., Wang L., Griffin W. L., Zhou M.-F., Zhang M. and Shu L. S. (2010) Components and episodic growth of Precambrian crust in the Cathaysia Block, South China: Evidence from U-Pb ages and Hf isotopes of zircons in Neoproterozoic sediments. *Precambrian Res.* **181**, 97–114.

Yu J.-H., O'Reilly S. Y., Zhao L., Griffin W. L., Zhang M., Zhou X., Jiang S.-Y., Wang L.-J. and Wang R.-C. (2007) Origin and evolution of topaz-bearing granites from the Nanling Range, South China: a geochemical and Sr–Nd–Hf isotopic study. *Mineral. Petrol.* **90**, 271–300.

Yu J.-H., O'Reilly S. Y., Zhou M.-F., Griffin W. L. and Wang L. (2012) U–Pb geochronology and Hf–Nd isotopic geochemistry of the Badu Complex , Southeastern China: Implications for the Precambrian crustal evolution and paleogeography of the Cathaysia Block. *Precambrian Res.* **222–223**, 424–449.

Yu J.-H., Wang L., O'Reilly S. Y., Griffin W. L., Zhang M., Li C.-Z. and Shu L. S. (2009) A Paleoproterozoic orogeny recorded in a long-lived cratonic remnant (Wuyishan terrane), eastern Cathaysia Block, China. *Precambrian Res.* **174**, 347–363.

Yuan Z. X., Wu L. S., Zhang Z. Q. and Ye X. J. (1991) The Sm-Nd, Rb-Sr isotopic age-dating of Mayuan Group in Northern Fujian. *Acta Pet. Miner.* **10**, 127–132.

Yurimoto H., Duke E. F., Papike J. J. and Shearer C. K. (1990) Are discontinuous chondrite-normalized REE patterns in pegmatitic granite systems the results of monazite fractionation? *Geochim. Cosmochim. Acta* **54**, 2141–2145.

Zajacz Z., Halter W. E., Pettke T. and Guillong M. (2008) Determination of fluid / melt partition coefficients by LA-ICPMS analysis of co-existing fluid and silicate melt inclusions: Controls on element partitioning. *Geochemica Cosmochim. Acta* **72**, 2169–2197.

Zaraisky G. P., Aksyuk A. M., Devyatova V. N., Udoratina O. V. and Chevychelov V. Y. (2009) The Zr/Hf ratio as a fractionation indicator of rare-metal granites. *Petrology* **17**, 25–45.

Zartman R. E. and Doe B. R. (1981) Plumbotectonics - the model. *Tectonophysics* **75**, 135–162.

Zhang F., Wang Y., Zhang A., Fan W., Zhang Y. and Zi J. (2012) Geochronological and geochemical constraints on the petrogenesis of Middle Paleozoic (Kwangsian) massive granites in the eastern South China Block. *Lithos* **150**, 188–208.

Zhang G. W., Guo A. L., Wang Y. J., Li S. Z., Dong Y. P., Liu S. F., He D. F., Cheng S. Y., Lu R. K., Yao A. P., Guowei Z., Anlin G. U. O., Yuejun W., Sanzhong L. I., Yunpeng D., Shaofeng L. I. U., Dengfa H. E. and Shunyou C. (2013) Tectonics of South China continent and its implications. *Sci. China Earth Sci.* **56**, 1804–1828.

Zhang H. N. and Wu Q. H. (1994) A comparative study of main active fault zone along the coast of South China. *Seismol. Geol.* **16**, 43–52.

Zhang L. G. (1995) *Block-geology of Eastern Asia Lithosphere – Isotope Geochemistry and Dynamics of Upper Mantle, Basement and Granite.*, Chinese Science Press, Beijing.

Zhang Q., Jiang Y.-H., Wang G.-C., Liu Z., Ni C.-Y. and Qing L. (2015) Origin of Silurian gabbros and I-type granites in central Fujian, SE China: Implications for the evolution of the early Paleozoic orogen of South China. *Lithos* **216**–**217**, 285–297.

Zhang S. B. and Zheng Y. F. (2013) Formation and evolution of Precambrian continental lithosphere in South China. *Gondwana Res.* **23**, 1241–1260.

Zhang Y., Yang J.-H., Chen J.-Y., Wang H. and Xi-ang Y.-X. (2017) Petrogenesis of Jurassic tungsten-bearing granites in the Nanling Range, South China: Evidence from whole-rock geochemistry and zircon U–Pb and Hf–O isotopes. *Lithos* **278**–**281**, 166–180.

Zhang Y., Yang J.-H., Sun J.-F., Zhang J.-H., Chen J.-Y. and Li X.-H. (2015) Petrogenesis of Jurassic fractionated I-type granites in Southeast China: Constraints from whole-rock geochemical and zircon U–Pb and Hf–O isotopes. *J. Asian Earth Sci.* **111**, 268–283.

Zhao G. and Cawood P. A. (1999) Tectonothermal evolution of the Mayuan Assemblage in the Cathaysia Block: Implications for Neoproterozoic collision-related assembly of the South China craton. *Am. J. Sci.* **299**, 309–339.

Zhao G. and Guo J. (2012) Precambrian geology of China: Preface. *Precambrian Res.* **222**–**223**, 1–12.

Zhao G., Wilde S. A., Cawood P. A. and Sun M. (2001) Archean blocks and their boundaries in the North China Craton: Lithological, geochemical, structural and P-T path constraints and tectonic evolution. *Precambrian Res.* **107**, 45–73.

Zhao J.-H. and Zhou M.-F. (2007) Neoproterozoic Adakitic Plutons and Arc Magmatism along the Western Margin of the Yangtze Block, South China. *J. Geol.* **115**, 675–689.

Zhao J.-L., Qiu J.-S., Liu L. and Wang R.-Q. (2016) The Late Cretaceous I- and A-type granite association of southeast China: Implications for the origin and evolution of post-collisional extensional magmatism. *Lithos* **240**–**243**, 16–33.

Zhao K.-D., Jiang S.-Y., Chen W.-F., Chen P.-R. and Ling H.-F. (2013) Zircon U–Pb chronology and elemental and Sr–Nd–Hf isotope geochemistry of two Triassic A-type granites in South China: Implication for petrogenesis and Indosinian transtensional tectonism. *Lithos* **160**–**161**, 292–306.

Zhao X., Allen M. B., Whitham A. G. and Price S. P. (1996) Rift-related Devonian sedimentation and basin development in South China. *J. Southeast Asian Earth Sci.* **14**, 37–52.

Zhao X., Liu K., Yu M., Jiang Y., Mao J., Zhou X. and Yu S. (2015) Early Cretaceous I-type granites in the southwest Fujian Province: new constraints on the late Mesozoic tectonic evolution of southeast China. *Isl. Arc* **24**, 359–378.

Zheng J. P., Griffin W. L., Li L. S., O'Reilly S. Y., Pearson N. J., Tang H. Y., Liu G. L., Zhao J. H., Yu C. M. and Su Y. P. (2011) Highly evolved Archean basement beneath the western Cathaysia Block, South China. *Geochim. Cosmochim. Acta* **75**, 242–255.

Zheng J. P., Griffin W. L., O'Reilly S. Y., Pearson N. and Pan Y. (2006) Widespread Archean basement beneath the Yangtze craton. *Geology* **34**, 417–420.

Zheng J. P., O'Reilly S. Y., Griffin W. L., Zhang M., Lu F. and Liu G. (2004) Nature and evolution of Mesozoic-Cenozoic lithospheric mantle beneath the Cathaysia block, SE China. *Lithos* **74**, 41–65.

Zheng W., Mao J., Zhao H., Ouyang H., Zhao C. and Yu X. (2016) Geochemistry, Sr–Nd–Pb–Hf isotopes systematics and geochronological constrains on petrogenesis of the Xishan A-type granite and associated W–Sn mineralization in Guangdong Province, South China. *Ore Geol. Rev.* **88**, 739–752.

Zheng W., Mao J., Zhao H., Zhao C. and Yu X. (2017) Two Late Cretaceous A-type granites related to the Yingwuling W–Sn polymetallic mineralization in Guangdong province, South China: Implications for petrogenesis, geodynamic setting, and mineralization. *Lithos* **274**–**275**, 106–122.

Zheng Y.-F. (2019) Subduction zone geochemistry. *Geosci. Front.* **10**, 1223–1254.

Zheng Y.-F., Zhang S.-B., Zhao Z.-F., Wu Y.-B., Li X.-H., Li Z.-X. and Wu F.-Y. (2007) Contrasting zircon Hf and O isotopes in the two episodes of Neoproterozoic granitoids in South China: Implications for growth and reworking of continental crust. *Lithos* **96**, 127–150.

Zheng Y., Wu R., Wu Y., Zhang S., Yuan H. and Wu F.-Y. (2008) Rift melting of juvenile arc-derived crust: Geochemical evidence from Neoproterozoic volcanic and granitic rocks in the Jiangnan Orogen, South China. *Precambrian Res.* **163**, 351–383.

Zhou G. (1989) The discovery and significance of the northeastern Jiangxi Province ophiolite (NEJXO), its metamorphic peridotite and associated high temperature-high pressure metamorphic rocks. *J. Southeast Asian Earth Sci.* **3**, 237–247.

Zhou G. and Zou H. (1996) Precambrian High-Pressure Metamorphic Rocks within the Collision Zone of the Yangtze and Cathaysia Blocks, China: Jadeite/Glaucophane-Type Facies. *Int. Geol. Rev.* **38**, 87–93.

Zhou J.-C., Wang X.-L. and Qiu J.-S. (2009) Geochronology ofNeoproterozoic mafic rocks and sandstones from northeastern Guizhou, South China: Coeval arc magmatism and sedimentation. *Precambrian Res.* **170**, 27–42.

Zhou M.-F., Yan D.-P., Kennedy A. K., Li Y. and Ding J. (2002) SHRIMP U-Pb zircon geochronological and geochemical evidence for Neoproterozoic arc-magmatism along the western margin of the Yangtze Block, South China. *Earth Planet. Sci. Lett.* **196**, 51–67.

Zhou X. M. and Li W. X. (2000) Origin of Late Mesozoic igneous rocks in Southeastern China: implications for lithosphere subduction and underplating of mafic magmas. *Tectonophysics* **326**, 269–287.

Zhou X. M., Sun T., Shen W., Shu L. S. and Niu Y. (2006) Petrogenesis of Mesozoic granitoids and volcanic rocks in South China: A response to tectonic evolution. *Episodes* **29**, 26–33.

Zhou X. M., Zhou H. B., Yang J. D. and Wang Y. X. (1989) Sm–Nd isochron age of the ophiolite suite in Shexian county, Anhui province and its geological significance. *Chinese Sci. Bull.* **35**, 208–212.

Zhou Z., Ma C., Xie C., Wang L., Liu Y. and Liu W. (2016) Genesis of highly fractionated I-type granites from Fengshun complex: Implications to tectonic evolutions of South China. *J. Earth Sci.* **27**, 444–460.

Zhu K., Li Z., Xu X. and Petrology A. (2014) A Mesozoic Andean-type orogenic cycle in southeastern China as recorded by granitoid evolution. *Am. J. Sci.* **314**, 187–234.

Zhu M., Zhang J. and Yang A. (2007) Integrated Ediacaran (Sinian) chronostratigraphy of South China. *Paleogeography, Paleoclimatology, Paleoecol.* **254**, 7–61.

Zindler A. and Hart S. R. (1986) Chemical Geodynamics. *Annu. Rev. Earth Planet. Sci.* **14**, 493–571.

Appendices

The appendices that accompany this thesis, contain:

Appendix A: Review on the classification, evolution processes and genetic models of granitic rocks

Appendix B: Sample locations

Appendix C: Mineral chemistry

Appendix D: Whole-rock elemental geochemistry

Appendix E: Sr, Nd, Hf and Pb isotope geochemistry

Appendix F: Whole-rock isochron diagrams

Appendix G: Mineral/melt partition coefficients used to calculate fractionation vectors

Appendix A

Review on the classification, evolution processes and genetic models of granitic rocks

1 Granites: classification, evolution processes and genetic models

Granitic rocks or granitoids are felsic plutonic rocks, composed predominantly of feldspar and quartz, being the most abundant igneous rocks in the upper continental crust (e.g. Wedepohl, 1995; Rudnick and Gao, 2003). The formation of granitic rocks have an essential role in shaping the compositional structure of the continental crust, involving the ascent of buoyant, incompatible element-rich silicic magmas that leave behind residues that either reside in the deep crust or are recycled into the upper mantle (Kemp and Hawkesworth, 2003). They occur associated with a wide range of different types of geodynamic settings, ranging from orogenic (subduction-related or continental collision) to anorogenic intraplate settings, and may occur in small volumes at mid-ocean ridges and in ophiolite complexes (e.g. Robin Gill, 2010).

The granitic rocks intrude the upper continental crust as plutons, the fundamental units of granite geology. These are circumscribed magmatic bodies with variable surface outcrop ranging from < 10 km^2 to > 1000 km^2 in size and shape (round, oval, lenticular or tabular; e.g. Myron, 2003; Bouchez et al., 2015). A number of plutons joined together, forming a mosaic of interfering bodies, is called a batholith. The largest identifiable assemblage of related plutons and batholiths is the granite belt or province, which are often related to a particular orogenic phase (Cobbing, 2000).

Despite having general common features, distinctive differences in their mineralogy and chemical composition have potential implications for their derivation, enabling to study the deep inaccessible parts of the Earth (Kemp and Hawkesworth, 2003; Arndt, 2013). This makes the study of granitic rocks crucial to understand the tectono-thermal history of continents and its geodynamic settings. Plus, since granite plutons are often associated with mineralization, the study of their magma evolution processes can also shed some light on the mechanisms responsible for the metal endowment (e.g. Gill, 2010). Because of their diversity, granitic rocks have been the subject of considerable study and controversy; their genesis is highly complex and they may be produced in different ways (Winter, 2001). The causes of such complexity have been attributed to a large number of factors related to the genesis and evolution of granitic magmas and have led to the proposition of different classification schemes for these rocks.

1.1 Classification Schemes

There are many classification schemes for granitic rocks based on a wide range of measurable physical and chemical parameters. The IUGS classification provides a descriptive nomenclature of granitic rocks suggested by Streckeisen (1967, 1974, 1976), attributing the same name to granitic rocks with similar relative proportions of felsic minerals (quartz, plagioclase, and alkaline feldspar) regardless of any genetic implication. This requires the determination of the mode (the percentage of each mineral present, based on volume), which is estimated on the basis of the cumulative area of each mineral type, as seen on the surface of a hand specimen or in a thin section under the microscope (e.g. through the "point counting" technique).

According to the IUGS systematics of igneous rocks (Le Maitre et al., 1989; Le Bas and Streckeisen, 1991), granitic rocks are plutonic rocks with mafic mineral content less than 90%, variable proportions of alkaline feldspar and plagioclase and quartz contents between 20% and 60% (Fig. 1). The predominant mineral phases are plagioclase, quartz, and alkali feldspar. Plagioclase is usually an early and dominant phase, followed by the crystallization of quartz and alkali feldspar. The alkali feldspar commonly occurs as megacrysts and tends to be more abundant in more alkaline rocks. The dominant mafic minerals are amphibole (typically hornblende, although riebeckite or other alkali amphiboles tend to occur in alkali granites) and biotite; these two hydrated phases are considered to be an evidence of the high pressure and H_2O content of the granitic magmas (Gill, 2010; Arndt, 2013). Muscovite is common in aluminous granites, which may also contain trace amounts of garnet, cordierite, sillimanite, or andalusite (e.g. Chappell and White, 2001). Clinopyroxene is rare, but may be present in the more sodic varieties of granites. Fayalitic olivine occurs in some alkaline granitic rocks, and orthopyroxene occurs in high-temperature anhydrous granitic rocks known as charnockites (Le Maitre et al., 2002).

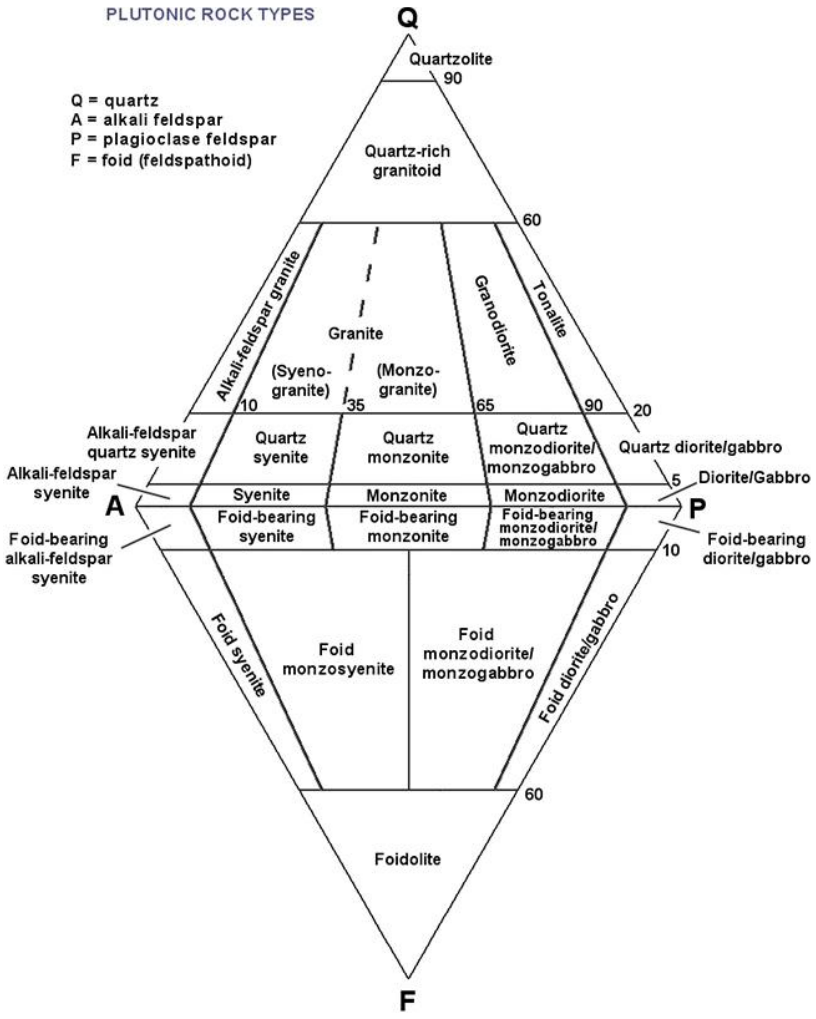

Fig. 1. Classification and nomenclature of the plutonic igneous rocks according to their felsic modal contents when mafic mineral content is less than 90%. Q, quartz; A, alkali feldspar; P, plagioclase; F, feldspathoid, after Le Maitre et al. (1989), from Le Bas & Streckeisen (1991).

Based on mineralogical differences, Tuttle and Bowen (1958) classified granitic rocks as hypersolvus granites and subsolvus granites. This classification takes into consideration whether or not they crystallized under relatively dry low pressure conditions or "wet", higher pressure conditions. Hypersolvus granites crystallization takes place at relatively low water pressures resulting in the formation of a single feldspar (Fig. 2a and b), whereas subsolvus granites reflect higher water percentages resulting in the formation of two distinct types of feldspar (Fig. 2c; Winter, 2001).

At low pressure under dry conditions (Figs. 2a and 2b), the alkali feldspars form a complete solid solution at high temperature, yet at some point, upon slow cooling, they reach the solvus and

exsolve into two feldspars, one rich in albite and the other rich in orthoclase. However, because of the low temperature at which this exsolution process occurs, only single feldspars will occur with a perthitic texture. At higher pressure, under water-saturated conditions (Fig. 2c), the liquidus surface is suppressed and the solvus moves up to intersect the solidus. This results in the crystallization of two alkali feldspar solid solutions, one rich in Or and the another rich in Ab, which will further exsolve on cooling to form perthites (blebs or irregular lamellae of sodic feldspar within potassic alkali feldspar) and anti-perthites (blebs or irregular lamellae of potassic feldspar within sodic alkali feldspar), respectively (e.g. Klein and Philpotts, 2017).

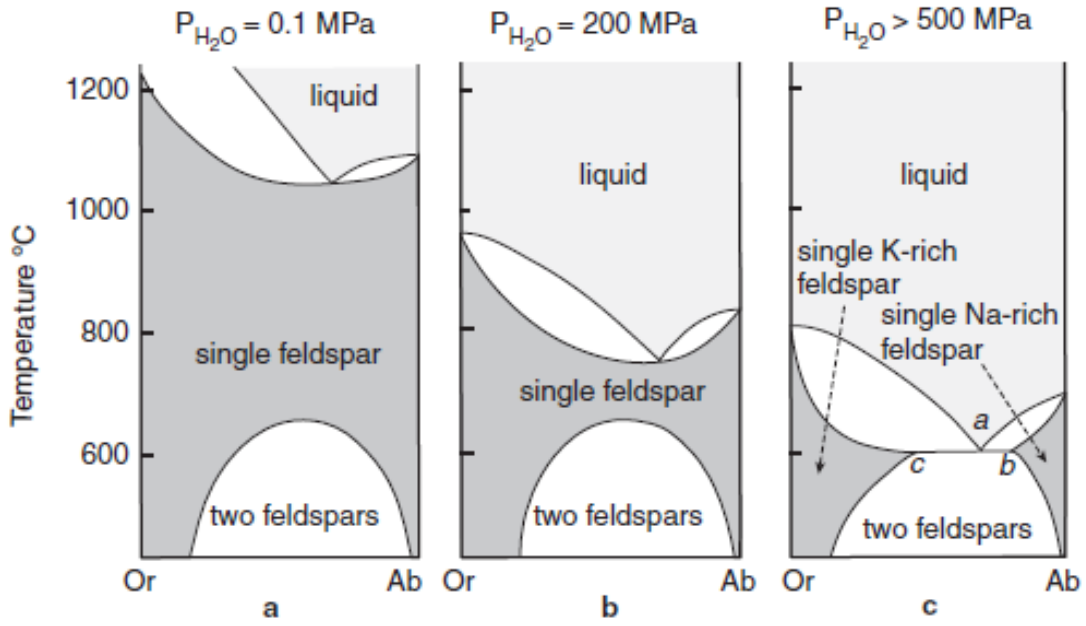

Fig. 2. The albite–K–feldspar system at various H_2O pressures: (a) P_{H2O} = 0.1 MPa; (b) P_{H2O} = 200 MPa; (c) P_{H2O} > 500 Mpa. Shaded areas represent possible single-phase compositions. From Winter (2001).

One way to avoid time-consuming techniques such as slabbing, staining and point-counting (necessary to determine the mode of the rock) is to grind the rocks to powder and analyze them for their major elements. This chemical composition can then be reconstituted in terms of the percentage of minerals composing the rocks by calculating its normative mineralogy. Normative calculations produce an idealized mineralogy of a crystallized melt and are based upon assumptions about the order of mineral formation and known phase relationships of rocks and minerals (e.g. Gill, 2010). Though the CIPW norm is a widely used method for calculating the normative

mineralogy of igneous rocks, the improved granite mesonorm (Mielke and Winkler, 1979) was especially designed for granitic rocks and therefore tends to yield mineral proportions closer to the actual mode of this type of rocks.

The normative amounts of quartz and feldspar can be plotted in the QAP (Fig. 1) or Q'-ANOR (Fig. 3) diagrams. The Q'-ANOR diagram is an empirically derived CIPW normative based equivalent to the modal IUGS classification scheme for granitic rocks.

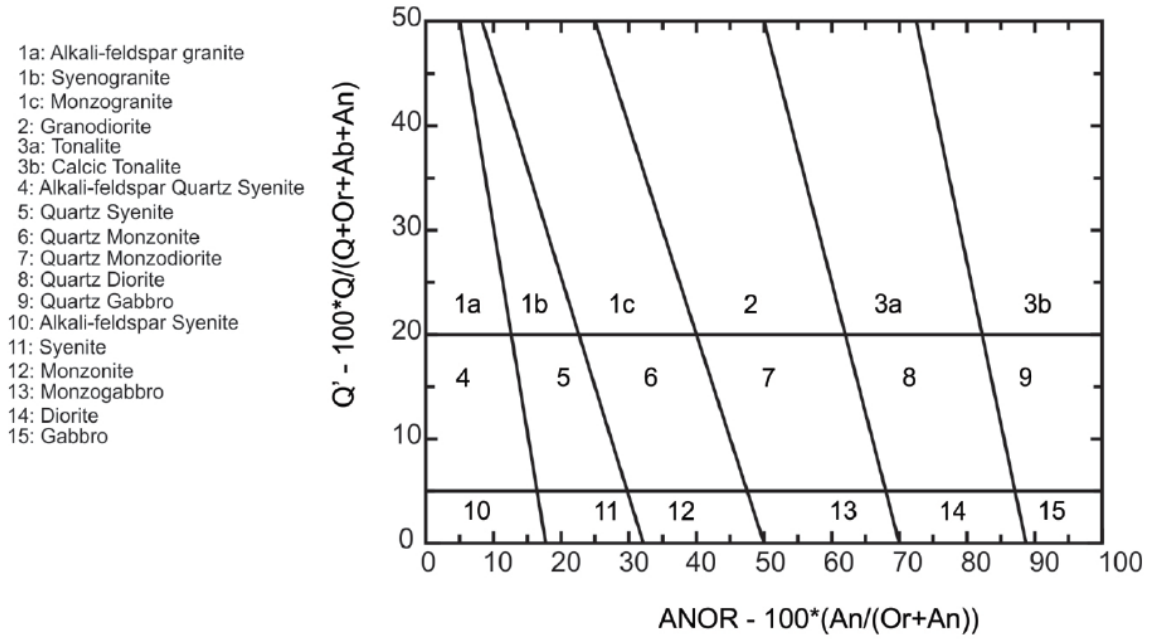

Fig. 3. Q'-ANOR normative composition diagram of Streckeisen & Le Maitre (1979), where Q' = Q/(Q+Or+Ab+An)×100; ANOR = An/(Or+An)×100. Q – Quartz; Or – Orthoclase; Ab – Albite; An – Anorthite.

In terms of major elements, SiO_2 contents of granitic rocks are high (60-75 wt%). While K_2O contents are also high, elements like TiO_2, FeO, MgO and CaO tend to be low, given that they are removed from the magma by fractional crystallization of mafic minerals or calcic plagioclase (e.g. Arndt, 2013) during the early stages of magma differentiation. One of the most common geochemical criteria used to classify granitic rocks is based on the relative proportions of Al_2O_3 vs. CaO, Na_2O and K_2O (Fig. 4). According to Shand (1927), granitic rocks can be classified according to their Aluminous Saturation Index [(ASI = molar Al_2O_3 / (CaO + Na_2O + K_2O)] in: peralkaline granites (ASI << 1, molar Al_2O_3 / (Na_2O+K_2O) < 1); metaluminous granites (ASI < 1); and

peraluminous granites (ASI > 1). The different proportions of these molecules impart a distinct mineralogy to each type of granite (Fig. 4).

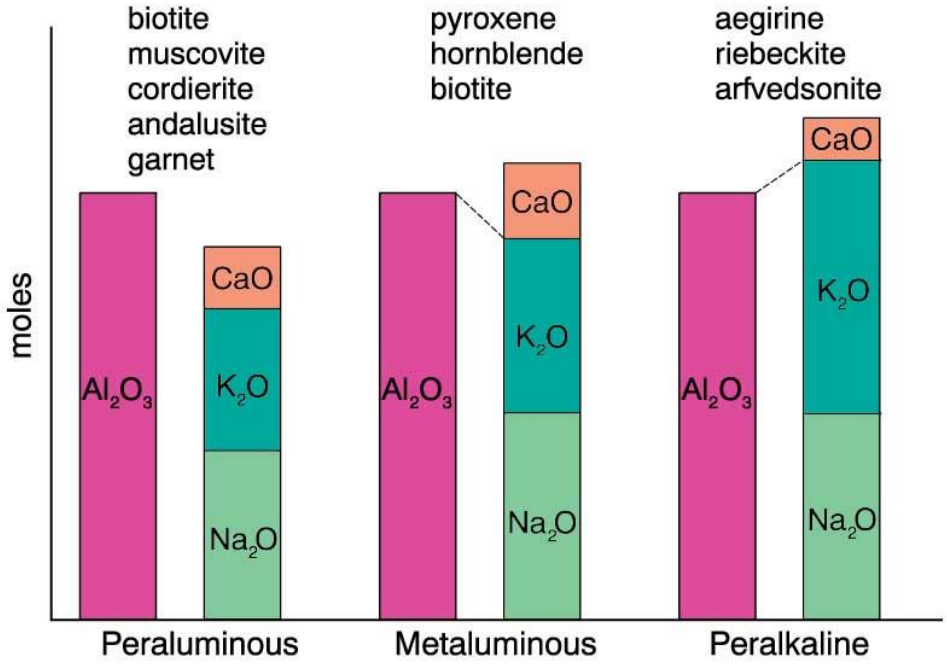

Fig. 4. Alumina saturation classes based on the molar proportions of $Al_2O_3/(CaO+Na_2O+K_2O)$ ("A/CNK") after Shand (1927) and the diagnostic minerals for each type after (Clarke, 1992). From Winter (2001).

Peccerillo and Taylor (1976) devised a method for determining the alkali balance in volcanic rocks, which has been widely used for granitic rocks as well. The K_2O-SiO_2 plot (Fig. 5) subdivides the calc-alkaline suite into high-K and low-K types. Granitic rocks belonging to one or another series may indicate derivation from lithologically distinct sources (e.g. Roberts and Clemens, 1993).

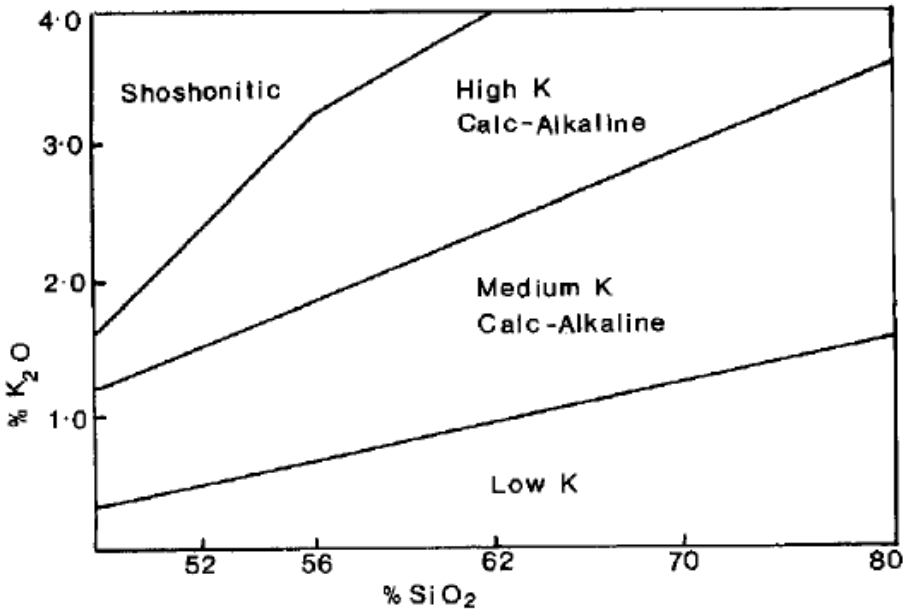

Fig. 5. Alkali discriminant diagram of Peccerillo & Taylor (1976).

Chappell and White (1974) marked the starting point of a genetic classification, which was subsequently developed by other authors and is commonly known as S-I-A-M classification scheme. This type of classification emphasizes the source and geodynamic setting of different types of granitic rocks. When studying the Lachlan Fold Belt (LFB), Chappell and White (1974) identified two different groups of granitic rocks whose distinct features where interpreted as the result of derivation through partial melting of two types of source rock: metasedimentary, originating S-type granites ("S" standing for "sedimentary" or "supracrustal"), and metaigneous, originating I-type granites ("I" standing for "igneous" or "infracrustal"). Later on, White (1979) added another group named M-type granites ("M" standing for "Mantle"), to account for those granitic rocks derived directly from a mantle source or juvenile basaltic crust. Loiselle and Wones (1979) added the last type known as A-type granites ("A" standing for "anorogenic", "alkaline" or "anhydrous"), for those granitic rocks formed in anorogenic settings or derived from an anhydrous source .

S-type granites are strongly peraluminous, relatively potassic, having high silica contents (SiO_2 = 64–77 wt%), low CaO, Na_2O and Sr contents (Chappell and White, 1974; Chappell and White, 1992; Chappell and White, 2001), which are lost when feldspar alters to clay minerals (Arndt, 2013). They have a distinct mineralogy marked by the presence of aluminous phases like

muscovite, cordierite and garnet and normative corundum (Chappell and White, 1974). Often contain metasedimentary xenoliths (Chappell and White, 1974; White and Chappell, 1988). This type of granites usually intrudes in relatively small volumes, especially in subduction zones and continental collision zones (e.g. Gill, 2010; Winter, 2001).

I-type granites are metaluminous to weakly peraluminous, relatively sodic, having a wide range of silica contents (SiO_2 = 56-77 wt%; Chappell and White, 1974; Chappell and White, 1992; Chappell and White, 2001). Hornblende and biotite are typical minerals and they also have normative diopside (Chappell and White, 1974). They commonly contain enclaves or xenoliths of diorite and gabbro or amphibolite (Chappell and White, 1974; Chappell and White, 2001). They usual intrude in large volumes associated with subduction in active continental margins and with lithospheric extension in postcollisional/postorogenic settings (Pearce et al., 1984; Roberts and Clemens, 1993).

The A-type granites are peralkaline, strongly sodic, with high SiO_2 contents (Loiselle and Wones, 1979; Collins et al., 1982; Eby, 1990; King et al., 1997). Their mafic mineralogy is characterized by Fe-rich biotite and alkali pyroxene/amphibole and they have normative diopside ± acmite (e.g. Collins et al., 1982; Whalen et al., 1987). They contain diverse types of xenoliths. Since they are related with non-orogenic settings, they are rarely deformed and are thought to have intruded after the main orogenic event (post-orogenic granites; Eby, 1992). A-type granites may involve diverse genetic processes and have diverse chemical compositions, although their isotopic signatures invariably point to an intraplate setting origin (Whalen et al., 1987; Eby, 1990; Eby, 1992).

The M-type granites result from partial melting of mantle peridotite or of "juvenile" basaltic crust (White, 1979). They include the immature arc plutons and the oceanic plagiogranites present in ophiolites, oceanic crust and in eroded Ocean Island Basalts (OIB; e.g. Winter, 2001). The A- and M-types are much less common than I- and S-types and for this reason do not play a significant role in the formation of continental crust (Arndt, 2013).

However, considering that multiple sources often contribute to the genesis of granitic rocks, in many cases they cannot be said to strictly belong to one S-I-A-M type or another.

Pearce et al. (1984) introduced a geochemical method to characterize the tectonic environment of granitic rocks based on their trace element composition. Four major tectonic environments were

distinguished: ocean ridge granites; volcanic arc granites; within-plate granites; collisional granites. The best discriminators were plots of Nb vs Y, Ta vs Y, Rb vs (Y + Nb) and Rb vs (Y + Ta). This classification scheme is still of wide use and it is considered an important proxy to determine the tectonic environment of granitic rocks

A more comprehensive classification scheme, based primarily on tectonic setting, was proposed by other authors (Barbarin, 1990a; Pitcher, 1997). Fig. 6 shows that the granitic rocks can occur in a wide variety of tectonic settings, from orogenic settings, where compressive tensions and subduction act as the main force, to non-orogenic settings, where extensive forces are responsible for intraplate and rifting magmatism. Granitic rocks can also be formed in a type of transitional setting which has characteristics of the other two, being commonly associated with post-orogenic events.

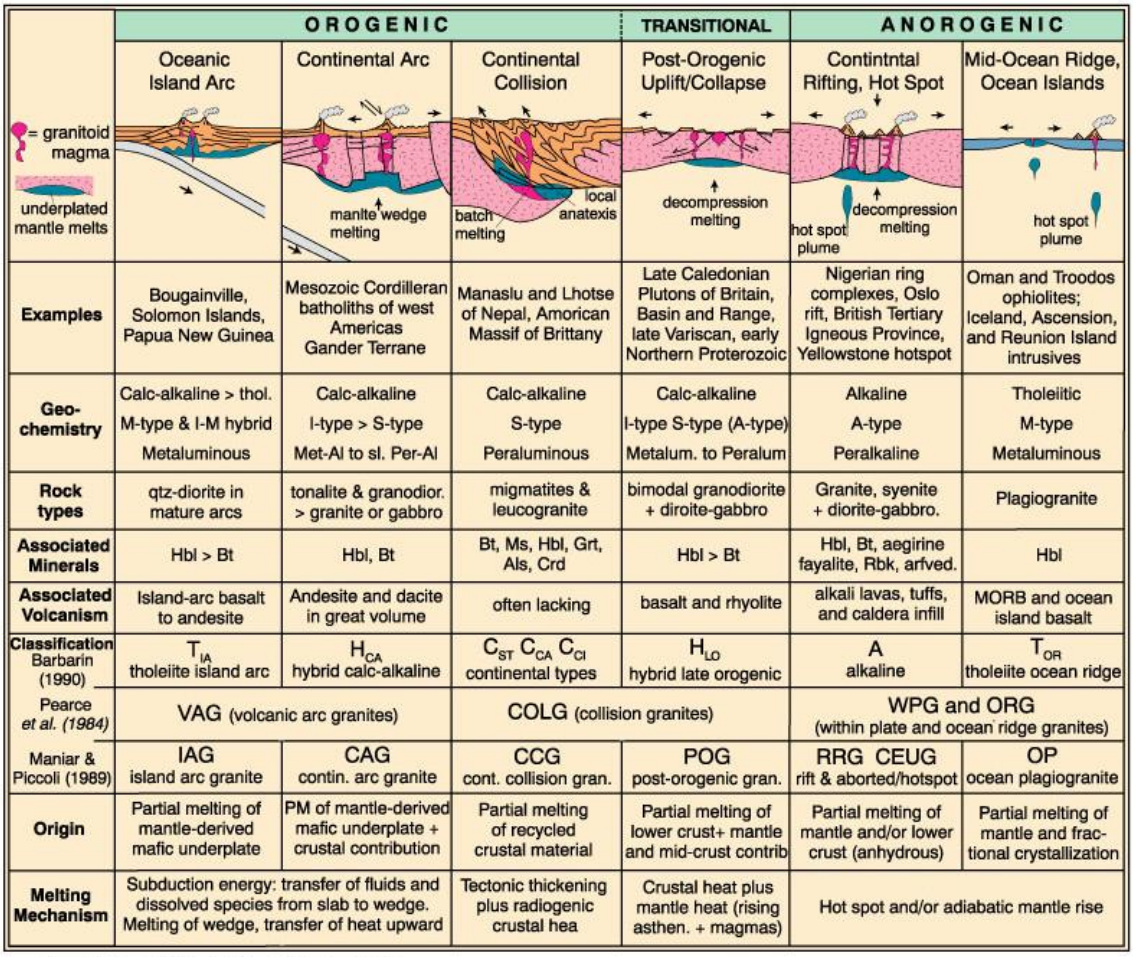

After Pitcher (1983, 1993), Barbarin (1990)

Fig. 6. Classification of granitic rocks based on tectonic setting. From Winter (2001).

Most of these classifications however do not reflect the complexity of granites which results from a wide range of partial melting processes, diversified sources, subsequent magmatic evolution processes and the intrusive or autochthonous nature in various tectonic settings (Barbarin, 1990a; Clarke, 1992). Thus, the application of such schemes to the study of particular granite suites should only serve as a starting point to the understanding of their petrogenesis.

1.2 Genesis processes

Tuttle & Bowen (1958) conducted the first experiments which proved a magmatic origin for granites, by showing that the composition of an average granite coincides with the thermal

minimum NaAlSi308-KAlSi308-Si02-H20 and demonstrating that crystal-liquid equilibria control granite compositions.

S-type granites are mostly generated from recycled upper crust and, as such, do not contribute to the growth of continental crust. I-type granites, on the other hand, are considered to be the building blocks of the continental crust (Kemp and Hawkesworth, 2003; Arndt, 2013). Several petrogenetic models have been proposed for their formation (e.g. Green and Ringwood, 1968; Kemp and Hawkesworth, 2003; Moyen and Martin, 2012): (1) Partial melting of ancient mafic to intermediate lower crust materials followed by fractional crystallization; (2) advanced fractional crystallization of mantle-derived basaltic magmas; (3) partial melting of a hydrated basalt that had been transformed to eclogite or garnet-bearing amphibolite during high-pressure metamorphism; (4) direct melting of (metasomatised) mantle; (5) mixing between partial melts of pre-existing crust and mantle-derived magmas and/or their differentiates. Yet, most of current models for the formation and growth of the continental crust advocate that parental magmas of most granites are generated through the two first processes, i.e., derivation by remelting of infracrustal source rocks (e.g. Chappell and Stephens, 1988; Bryant et al., 1997) or by crystallization of mantle-derived magmas (e.g. Sisson et al., 2005; Annen et al., 2008).

However, many I-type granitic rocks may also incorporate a significant supracrustal (i.e., sedimentary or volcanogenic) source component, as suggested by radiogenic and stable isotope variations (McCulloch and Chappell, 1982) and particularly elevated zircon $\delta^{18}O$ (Kemp et al., 2007). Some models consider that this component is incorporated at depth by interaction between crystallizing mantle-derived magmas and metasedimentary materials (e.g. Kemp et al., 2007), whereas others advocate assimilation of metasedimentary rocks in the middle to upper crust by ascending I-type magmas (e.g. Collins, 1996).

1.3 Chemical variability of granitic rocks

1.3.1 Source influence

The notion that granitic rocks chemically reflect their source forms the basis for many granite classifications (see section 1.1). As mentioned above, Chappell and White (1974; 1992) classified granites into two main categories according to their magma source composition: I-type granites and S-type granites, deriving from melting of igneous and sedimentary sources, respectively. The

source from which granitic magmas derive have important implications for their mineralogy, elemental and isotopic composition. Indeed, it has been suggested that the chemical variation within granitic bodies is mostly controlled by primary or near-source features (e.g. Clemens et al., 2009; Clemens et al., 2011; Clemens and Stevens, 2012). Peritectic minerals, produced from incongruent melting reactions, can be entrained in magmas, determining to a great extent the compositional variations in granites (Stevens et al., 2007). Incremental assembly of magma batches from contrasting sources allows the compositional heterogeneities to be preserved (Coleman et al., 2004; Glazner et al., 2004; Clemens et al., 2009; Clemens et al., 2011).

Elemental and isotopic geochemical data of most S-type granites show that they are not complex mixtures of melts formed from a number of different source materials and suggest sources dominated by feldspathic, aluminous metagreywackes (e.g. Chappell and White, 1974; Chappell and White, 1992; Clemens, 2003). On the other hand, the nature of the source rocks of I-type granites is diverse and complex. For some authors, basalt (of tholeiitic, komatiitic and high-Al compositions) or its metamorphic equivalents (e.g. amphibolite, mafic granulite, or eclogite) are the dominant components in the source of high-volume granitic magmas (Sisson et al., 2005; Moyen and Stevens, 2006). Others suggest that most of I-type protoliths are not mafic igneous rocks but rather arc volcanic rocks of intermediate composition (dacites to andesites), and possibly some relatively mafic granodiorites and tonalites, rich in biotite and hornblende (Roberts and Clemens, 1993; Clemens et al., 2011). It has also been suggested that melting of immature greywackes can form granitic magma with I-type affinity (Frost and Frost, 2014). Another possible and common scenario consists in the mixture of mantle-derived magmas and crustal components (e.g. Keay et al., 1997; Kemp et al., 2007). All of these sources have different compositions, which determine the chemical composition of the primary granitic magmas.

Overall, the isotopic composition of granites can vary between compositions with a strong mantellic signature to typical compositions of old continental crust, though intermediate compositions between these two endmembers are the most common case. This can be seen in the $\varepsilon_{Nd}(t)$ vs. $^{87}Sr/^{86}Sr$ diagram (Fig. 7), where the isotopic compositions of granitic rocks from the LFB (for which the S-I-A-M classification was originally proposed), in Australia, are plotted. Magmas from the depleted mantle (DM) have high Rb/Sr and low Sm/Nd, therefore plotting in the top left quadrant; on the other hand, magmas derived from the continental crust have low Rb/Sr and high Sm/Nd and, if this crust is old, these magmas plot in the lower right quadrant (Fig. 7).

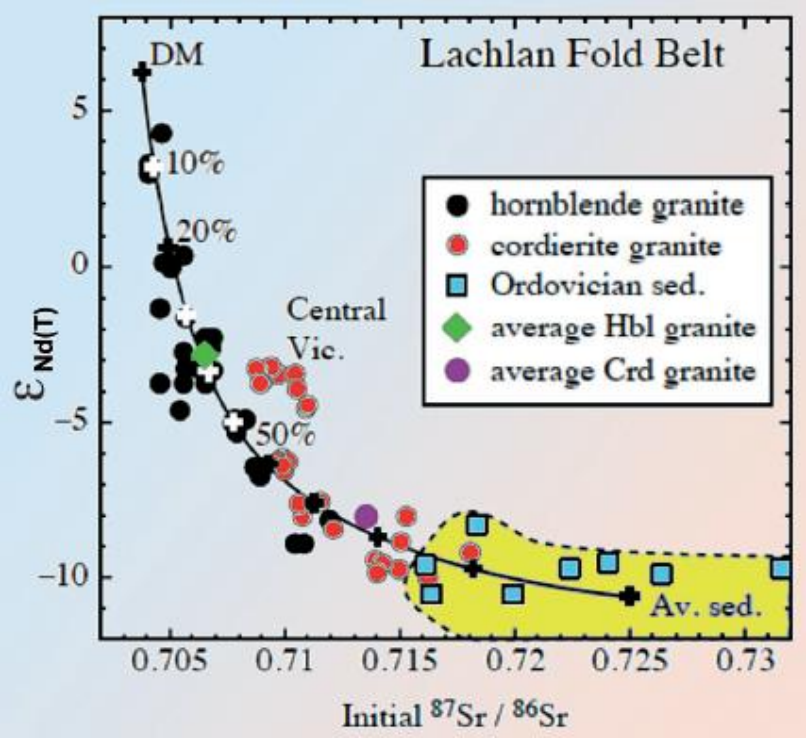

Fig. 7. Isotope data for granites from the Lachlan Fold Belt (LFB), showing that the isotopic compositions of these rocks are consistent with a mixture of juvenile material and continental crust materials in different proportions. DM – depleted mantle; Av. Sed. – average sediments. From Arndt (2013), modified after Kemp and Hawkesworth (2003).

The I-type granites ("hornblende granites") of the LFB are characterized by $\varepsilon_{Nd}(t)$ values ranging from +4 to about -9 and correspondingly low to moderate $^{87}Sr/^{86}Sr$ values. These values indicate a mixed source comprising juvenile material from the mantle and a small proportion of recycled crustal component (Arndt, 2013). On the other hand, S-type granites plot in the crustal field in the bottom right of Fig. 7, typical of magmas derived from sedimentary sources. The presence of the crustal component is manifested more clearly by zircon xenocrysts, which are common in these rocks (e.g., Hawkesworth and Kemp, 2006).

1.3.2 Magma evolution processes

Despite the utility of genetic classification schemes as a way to assess the genetic type of granites, the chemical composition of these rocks is usually more complex than simply reflecting the characteristics of a single uniform source. There may be sources composed of distinct lithologies in the crust and magmas formed through the input of multiple sources (e.g. crustal and mantellic). In addition, a wide range of magmatic differentiation processes can occur and modify

the composition of the primary magmas. Some of the most common magma evolution processes are described below.

1.3.2.1 Magma mixing

Magma mixing is the process by which two contrasting magmas meet and comingle, forming a magma of mixed composition between the two end-members (e.g. Chappell, 1996).

Examples of field evidence for this process are: the presence of mafic microgranular enclaves (MME), chilled margins in a mafic magma at its contact with a felsic one, round and lobate liquid–liquid contacts, net veining with a relatively mobile felsic magma invading a nearly solidified mafic one or late syn-plutonic dykes often disrupted into enclave swarms (Didier and Barbarin, 1991; Hallot et al., 1996). The mechanism and degree of interaction between two dissimilar magmas mainly depend on: 1) thermal energy, reflecting the depth of intrusion and proportion of the hot mafic melt and 2) relative timing of the mafic melt injection into the felsic magma chamber, related to the degree of crystallinity of the latter (Fig. 8; see Barbarin, 2005). Microtextural evidence for multistage crystallization (e.g., dendritic plagioclase, acicular apatite, blade-shaped biotite and quartz/K-feldspar oikocrysts enclosing small quenched crystals), or for exchange of xenocrysts/chemical disequilibria (e.g., amphibole- or pyroxene-rimmed quartz ocelli, rapakivi and antirapakivi feldspars, plagioclase with complex resorption history and discontinuous zoning) is suggestive of magma mixing processes (Hibbard, 1981; Vernon, 1984; Vernon, 1990; Janoušek et al., 2000; Baxter and Feely, 2002; Pankhurst et al., 2011). Compositional mapping obtained through backscatter electron (BSE) or cathodoluminescence (CL) imaging can also reveal complex zoning patterns in minerals, with several episodes of crystallization and resorption (e.g. Pagel et al., 2000; Janoušek et al., 2004).

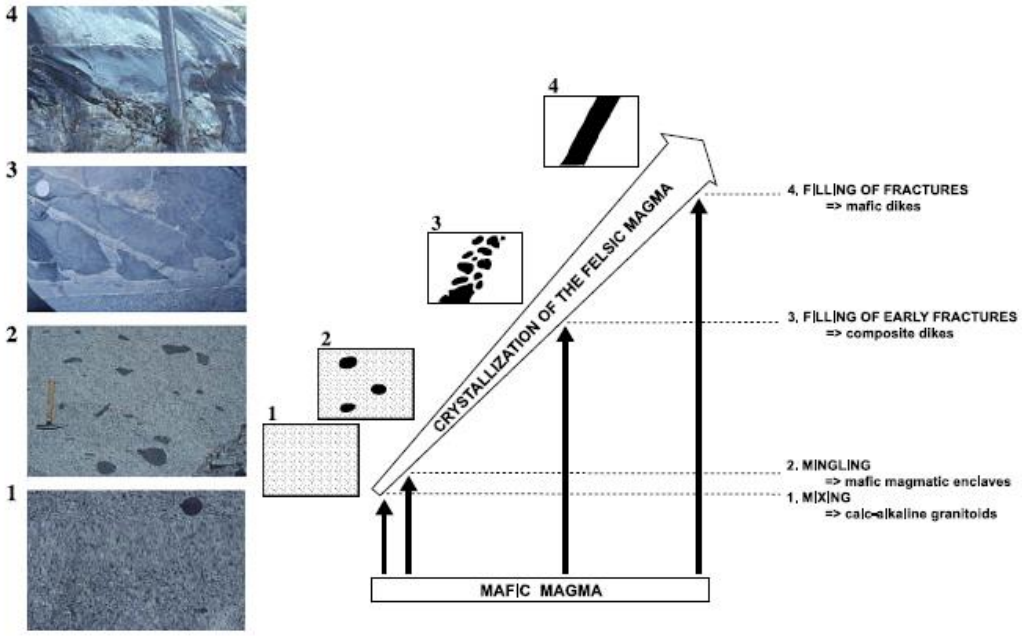

Fig. 8. Variable textures in hybrid rocks resulting from injection of mafic magma at different stages of crystallization of the felsic magma. From Barbarin (2005).

While magma mingling is more likely to occur at more superficial depths where merely mechanical mingling and exchange of earlier formed crystals occur, magma mixing can be a significant process at deeper crustal levels (Barbarin, 2005). However, due to the marked different physical properties of basic and acid magmas (e.g. viscosity contrast; Lesher, 1990), single-stage chemical mixing is not likely to occur. Coexistence of well-mixed regions with poorly homogenized ones (in the form of MME for instance) may result from the chaotic nature of the mixing process (Perugini and Poli, 2000; De Campos et al., 2011; Morgavi et al., 2013).

The scale of each process is not the same. Mixing processes are mainly diffusion-driven and can affect large volumes of magma, producing hybrid rocks (Sparks and Marshall, 1986). Mingling processes, on the other hand, tend to affect small volumes of the magmas, and thus the rocks with end-member compositions have a better chance to be preserved (Janoušek et al., 2006).

The range of compositions shown by liquids resulting from the mixing and homogenization of different proportions of two distinct components can be modeled as binary mixing, using the following equation (e.g. Faure, 1986):

$$C_M = f_1 C_1 + (1 - f_1) C_2 \quad (1)$$

where C_M, C_1 and C_2 are the concentration of element X in the mixed melt (M) and in the components 1 and 2, respectively, while $\boldsymbol{f}_1$ is the proportion of the component 1 in the mix (e.g. if $\boldsymbol{f}$=0.2 there is 20% of component a to 80% of component b in the mixed liquid).

The mixing equation for two end-members, 1 and 2, can also be seen as a mean of isotopic ratios (I_1 and I_2), weighted by their respective mass-fraction in the mixture. Marking the mass fraction of the end-member 1 as $\boldsymbol{f}_1$ (with $\boldsymbol{f}_1 + \boldsymbol{f}_2 = 1$) and respective concentrations C_1, C_2 and C_M (Faure 1986):

$$I_M = I_1 \left(\frac{C_1}{C_M}\right) f_1 + I_2 \left(\frac{C_2}{C_M}\right)(1 - f_1) \qquad 1$$

The combination of two isotopic ratios into a single binary plot is a robust approach in respect to the possible later modification by fractional crystallization or crystal accumulation, providing an insight into the original, open-system generated variation. To model this, two elements X and Y should be considered, as well as their isotopic ratios I^X and I^Y and two end-members (1 and 2), through the following equation (e.g. Janoušek et al., 2006):

$$AI_M^X + BI_M^X I_M^Y + CI_M^Y + D = 0 \qquad 2$$

Where:

$$A = (I^Y)_2 Y_2 X_1 - (I^Y)_1 Y_1 X_2$$

$$B = Y_1 X_2 - Y_2 X_1$$

$$C = (I^X)_1 Y_2 X_1 - (I^X)_2 Y_1 X_2$$

$$D = (I^Y)_1 (I^X)_2 Y_1 X_2 - (I^Y)_2 (I^X)_1 Y_2 X_1$$

Equation 3 is the equation of a hyperbola. The coefficient B can be rearranged, defining:

$$\alpha = \frac{\left(\frac{X}{Y}\right)_2}{\left(\frac{X}{Y}\right)_1} \qquad 3$$

The latter is a measure of the curvature of the hyperbola ($\alpha = 1$ corresponds to a straight line).

1.3.2.2 Fractional Crystallization

Fractional crystallization is the removal of early formed crystals from an originally homogeneous magma (e.g. by gravity crystal settling) so that these crystals are prevented from further reaction with the residual melt (e.g. Wilson, 1989). The removal of crystals changes the composition of the remaining melt, which becomes relatively depleted in some elements and enriched in others, resulting in the precipitation of a sequence of different minerals. As heavy radiogenic isotopes (e.g., Sr, Nd, Pb, Hf) should not be fractionated by equilibrium, closed-system processes such as partial melting and fractional crystallization, the latter will only modify the elemental composition of the evolving magmas (Winter, 2001).

The progressive change of rock compositions in magmatic series is commonly take as an indirect evidence to evolution by fractional crystallization at depth. However, direct evidence (e.g. cumulate layers, phenocrysts in lavas and their oscillatory/continuous zoning patterns) is rare and therefore this process is difficult to constrain with geological data (Janoušek, 2006).

The percentage of fractional crystallization of a certain mineral phase or assemblage necessary to produce the observed compositional spectrum can be modeled using the Rayleigh law, which describes the case where crystals are removed from the melt instantly after crystallization (e.g. Rollinson, 1993). The equation that describes Rayleigh fractional crystallization is:

$$\frac{C_L}{C_0} = F^{(D-1)} \qquad 4$$

where C_0 is the concentration of an element in the initial magma, C_L is the concentration of the same element in the remaining magmatic liquid, F is the remaining melt fraction and D is the partition coefficient between the crystallizing mineral(s) and the magmatic liquid. Equation 5 can be rewritten as:

$$C_L = F^{(D-1)} \times C_0 \qquad 5$$

Equation 6 gives the concentration on an element of known D in the remaining liquid after a certain amount (1-F) of fractional crystallization of a given mineral or mineral assemblage.

1.3.2.3 Crustal assimilation

Crustal assimilation happens when crustal rocks are picked up, incorporated and dissolved into the magma. Except when the material being added has the same chemical composition as the

magma, this process produces a more or less significant change in the chemical (elemental and isotopic) composition of the granitic magma (Clarke, 1992). In the case of mantle-derived magmas, an imprint of crustal assimilation is often isotopically detectable (e.g. Tegner et al., 2005). However, in the case of crustal-derived melts (e.g. granitic) it is often difficult to assess the extent of assimilation processes, as numerous crustal inputs could occur at any point from the source to the level of emplacement. Besides, magmatic evolution commonly involves other processes (e.g. magma mixing) and, therefore, the chemical signatures imposed by the assimilation of crustal materials may be overprinted (Kuritani et al., 2005).

The main evidences for assimilation of country rocks into granitic plutons are the occurrence of host-rock xenoliths as enclaves within the granites (e.g. Clarke et al., 1998; Lackey et al., 2006; Clarke, 2007; Erdmann et al., 2007) and the presence of xenocrysts (from the host-rock) in the mineralogy of granites (e.g. Barbarin, 1990b; Clarke et al., 2005; Clarke, 2007; Wang et al., 2017).

Bulk assimilation would produce some of the same effects as mixing, but it is more complex because of the heat balance involved. In order to assimilate the country rock, enough heat must be provided to first raise the country rock to its solidus temperature where it will begin to melt. Further addition of heat is necessary to change from the solid state to the liquid state (Thompson et al., 2002). The only available heat source is the granitic magma itself. Bowen (1928) pointed out that wall-rock assimilation and fractional crystallization should be considered together, as the heat required for assimilation can be provided by the latent heat of crystallization of the magmas. This led to the proposition of a coupled mechanism known as AFC (Assimilation and Fractional Crystallization; DePaolo, 1981).

The equation that describes the behavior of trace elements during AFC processes was derived by DePaolo (1981) and is given by the following expression:

$$\frac{C_L}{C_0} = f' + \frac{r}{(r - 1 + D)} \times \frac{C_A}{C_0}(1 - f') \qquad 6$$

where $\boldsymbol{C}_L$, C_0 and $\boldsymbol{C}_A$ correspond to the concentration of a trace element in the residual melt, the parental liquid and the assimilant, respectively. D is the bulk distribution coefficient for that same element, r the ratio of the assimilation rate to the ratio of the crystallization rate and $\boldsymbol{f}'$ is given by: $\boldsymbol{f}' = \boldsymbol{F} - (\boldsymbol{r}-\mathbf{1}+\boldsymbol{D})/(\boldsymbol{r}-\mathbf{1})$, where F is the fraction of melt remaining.

The evolution of isotopic ratios during AFC was also described by DePaolo (1981) by the following equation:

$$I_L = I_0 + (I_A - I_0)\left(1 - \frac{C_0}{C_L} \times f'\right) \quad 7$$

where I_L, I_0 and I_A, are the isotopic ratios of the residual melt, of the parental magma and of the assimilant, respectively. C_0 is the concentration of the trace element whose isotopic ratios is being addressed in the parental magma, while C_L is the concentration of that same element in the assimilant.

1.3.2.4 Late-stage fluid/melt and fluid/rock interactions

In general, granitic magmas contain water concentrations of 3–6 wt % and partial pressures of magmatic gases can achieve several hundred bars (Lowenstern, 1994). With an increase of vapor pressure consequent of crystallization, the hydrostatic head of the magma may be exceeded, producing a separate vapor phase at the late stages of their magmatic evolution (Chen and Grapes, 2007). This vapor/fluid phase is highly mobile and large amounts of it can remove and transport significant quantities of chemical elements to other locations, inside or outside of the pluton, leaving marked effects on the chemical composition of the magma left behind (Clarke, 1992). This process is known as volatile stripping and involves the partitioning of elements into the fluid phase and their eventual removal from that part of the magma chamber (e.g. Barnes, 1979; Clarke, 1992; Boily and Williams-Jones, 1994).

Unlike other magmatic rocks, highly evolved granitic magmas are rich in components (e.g. H_2O, Li, B, F, P, and/or Cl), often show non-chondritic Y/Ho and Zr/Hf ratios and "irregular" REE patterns which are sub-divided into four concave-upward segments referred to as "tetrads" (e.g. Masuda and Ikeuchi, 1979; Masuda et al., 1987; Masuda and Akagi, 1989; Bau, 1996; Bau, 1997; Irber, 1999; Monecke et al., 2002). It has been suggested that the combination of these features indicates that non-CHARAC (CHArge-and-RAdius-Controlled) trace element behavior prevails in highly evolved magmatic systems (Bau, 1996). This behavior is attributed to specific physicochemical properties of the magma similar to those that characterize aqueous fluids, suggesting that high-silica magmatic systems are transitional between pure silicate melts and hydrothermal fluids (e.g. Masuda et al., 1987; Bau, 1996; Irber, 1999; Jahn et al., 2001; Monecke et al., 2002; Wu et al., 2004; Monecke et al., 2007). In such transitional systems, non-CHARAC

behavior of high field strength elements (HFSE) is probably due to chemical complexation with a wide variety of ligands such as non-bridging oxygen (e.g. F, B, P, etc.) leading to absolute and relative mineral/melt or mineral/fluid partition coefficients that are highly sensitive to the composition and structure of the magma (Bau, 1996).

Even after the magma has completely solidified, the chemical composition of granites may be further changed. Some examples of subsolidus alteration are: (1) deuteric alteration, i.e., alteration produced by fluids derived from the granitic magma itself (e.g. Neuerburg, 1958; Lee et al., 1995; Duzgoren-Aydin, 2003; Plümper and Putnis, 2009): (2) alteration by externally derived metamorphic or meteoric waters in cases where hydrothermal convection systems extend beyond the contacts of the pluton (e.g. Simon and Hoefs, 1987; Sun and Eadington, 1987); (3) weathering, i.e., alteration at low-temperature (e.g. Koita et al., 2013; Kanamaru et al., 2018).

References

Annen C., Blundy J. D. and Sparks R. S. J. (2008) The sources of granitic melt in Deep Hot Zones. *Trans. R. Soc. Edinburgh, Earth Sci.* **97**, 297–309.

Arndt N. T. (2013) Formation and Evolution of the Continental Crust. *Geochemical Perspect.* **2**, 405–533.

Barbarin B. (1990a) Granitoids: Main petrogenetic classifications in relation to origin and tectonic setting. *Geol. J.* **25**, 227–238.

Barbarin B. (2005) Mafic magmatic enclaves and mafic rocks associated with some granitoids of the central Sierra Nevada batholith, California: Nature, origin, and relations with the hosts. *Lithos* **80**, 155–177.

Barbarin B. (1990b) Plagioclase xenocrysts and mafic magmatic enclaves in some granitoids of the Sierra Nevada Batholith, California. *J. Geophys. Res.* **95**, 17,747-17,756.

Barnes H. L. (1979) *Geochemistry of Hydrothermal Ore Deposits*. 2nd ed., Wiley- Interscience, New York.

Le Bas M. J. and Streckeisen a. L. (1991) The IUGS systematics of igneous rocks. *J. Geol. Soc. London.* **148**, 825–833.

Bau M. (1996) Controls on the fractionation of isovalent trace elements in magmatic and aqueous systems: evidence from Y/Ho, Zr/Hf, and lanthanide tetrad effect - a discussion of the article by M. Bau (1996). *Contrib. to Mineral. Petrol.* **128**, 405–408.

Bau M. (1997) The lanthanide tetrad effect in highly evolved felsic igneous rocks a reply to the comment by Y. Pan. *Contrib. to Mineral. Petrol.* **128**, 409–412.

Baxter S. and Feely M. (2002) Field and Petrographic Evidence for Magma Mixing and Mingling in Granitoids: Examples From the Galway Granite , Connemara , Ireland. *Mineral. Petrol.* **76**, 63–74.

Boily M. and Williams-Jones A. E. (1994) The role of magmatic and hydrothermal processes in the chemical evolution of the Strange Lake plutonic complex, Québec-Labrador. *Contrib. to Mineral. Petrol.* **118**, 33–47.

Bouchez J.-L., Bowden P. and Nédélec A. (2015) *Granites: petrology, structure, geological setting and metallogeny*., Oxford University Press, Oxford, U.K.

Bowen N. L. (1928) *The Evolution of the Igneous Rocks*., Princeton University Press, Princeton.

Bryant C. J., Arculus R. J. and Chappell B. W. (1997) Clarence river supersuite: 250 Ma Cordilleran tonalitic I-type intrusions in eastern Australia. *J. Petrol.* **38**, 975–1001.

De Campos C. P., Perugini D., Ertel-Ingrisch W., Dingwell D. B. and Poli G. (2011) Enhancement of magma mixing efficiency by chaotic dynamics: An experimental study. *Contrib. to Mineral. Petrol.* **161**, 863–881.

Chappell B. W. (1996) Magma mixing and the production of compositional variation within granite suites: Evidence from the granites of southeastern Australia. *J. Petrol.* **37**, 449–470.

Chappell B. W. and Stephens W. E. (1988) Origin of infracrustal (I-type) granite magmas. *Trans. R. Soc. Edinb. Earth Sci.* **79**, 71–86.

Chappell B. W. and White A. J. R. (1992) I- and S-type granites in the Lachlan Fold Belt. *Trans. R. Soc. Edinb. Earth Sci.* **83**, 1–26.

Chappell B. W. and White A. J. R. (2001) Two contrasting granite types: 25 years later. *Aust. J. Earth Sci.* **48**, 489–499.

Chappell B. W. and White A. J. R. (1974) Two contrasting granite types. *Pacific Geol.* **8**, 173–174.

Chen G.-N. and Grapes R. (2007) *Granite Genesis: In Situ Melting and Crustal Evolution*., Elsevier, Netherlands.

Clarke D. B. (2007) Assimilation of xenocrysts in granitic magmas: principles, processes, proxies, and problems. *Can. Mineral.* **45**, 5–30.

Clarke D. B. (1992) *Granitoid Rocks*., Chapman & Hall, New York.

Clarke D. B., Dorais M., Barbarin B., Barker D. A. N., Cesare B., Clarke G., Baghdadi M. E. L., Erdmann S., Gottesmann R., Gaeta M., Vi G. B. M., Neves L. J. P. F., David R. M., Pereira A. J. S. C., Pichavant M., Rapela C. W., Renno A. D., Richards S., Roberts M., Rottura A., Sial A. N., Alejandro J., Visona D., Williamson B. E. N. and Woodard H. H. (2005) Occurrence and Origin of Andalusite in Peraluminous Felsic Igneous Rocks. *J. Petrol.* **46**, 441–472.

Clarke D. B., Henry A. S. and White M. A. (1998) Exploding xenoliths and the absence of "elephants" graveyards' in granite batholiths. *J. Struct. Geol.* **20**, 1335–1343.

Clemens J. D. (2003) S-type granitic magmas — petrogenetic issues, models and evidence. *Earth-Science Rev*. **61**, 1–18.

Clemens J. D., Helps P. A. and Stevens G. (2009) Chemical structure in granitic magmas − a signal from the source? *Earth Environ. Sci. Trans. R. Soc. Edinburgh* **100**, 159–172.

Clemens J. D. and Stevens G. (2012) What controls chemical variation in granitic magmas? *Lithos* **135**, 317–329.

Clemens J. D., Stevens G. and Farina F. (2011) The enigmatic sources of I-type granites: The peritectic connexion. *Lithos* **126**, 174–181.

Cobbing J. (2000) *Lecture Notes Earth Sciences*. eds. S. Bhattacharji, G. M. Friedman, H. J. Neugebauer, and A. Seilacher, Springer, New York.

Coleman D. S., Gray W. and Glazner A. F. (2004) Rethinking the emplacement and evolution of zoned plutons: Geochronologic evidence for incremental assembly of the Tuolumne Intrusive Suite, California. *Geology* **32**, 433–436.

Collins W. J. (1996) Lachlan Fold Belt granitoids: Products of three-component mixing. *Trans. R. Soc. Edinburgh-Earth Sci.* **87**, 171–181.

Collins W. J., Beams S. D., White A. J. R. and Chappell B. W. (1982) Nature and origin of A-type granites with particular reference to southeastern Australia. *Contrib. to Mineral. Petrol.* **80**, 189–200.

DePaolo D. J. (1981) Trace element and isotopic effects of combined wallrock assimilation and fractional crystallization. *Earth Planet. Sci. Lett*. **53**, 189–202.

Didier J. and Barbarin B. (1991) *Enclaves and granite petrology*., Elsevier, Amsterdam.

Duzgoren-Aydin N. S. (2003) Comparative study of weathering signatures in felsic igneous rocks of Hong Kong Comparative study of weathering signatures in felsic igneous rocks of Hong Kong. *Chem. Speciat. Bioavailab.* **14**, 1–18.

Eby G. N. (1992) Chemical subdivision of the A-type granitoids: Petrogenetic and tectonic implications. *Geology* **20**, 641–644.

Eby G. N. (1990) The A-type granitoids: A review of their occurrence and chemical characteristics and speculations on their petrogenesis. *Lithos* **26**, 115–134.

Erdmann S., London D., Morgan VI G. B. and Clarke D. B. (2007) The contamination of granitic magma by metasedimentary country-rock material: An experimental study. *Can. Mineral.* **45**, 43–61.

Faure G. (1986) *Principles of Isotope Geology*. 2nd ed., John Wiley & Sons., New York.

Frost B. R. and Frost C. D. (2014) *Essentials of Igneous and Metamorphic Petrology*. Cambridge University Press, Cambridge.

Gill R. (2010) *Igneous Rocks and Processes: a pratical guide*. Wiley-Blackwell, West Sussex, UK.

Glazner A. F., Bartley J. M., Coleman D. S., Walt G. and Ryan Z. T. (2004) Are plutons assembled over millions of years by amalgamation from small magma chambers? *Gsa Today* **5173**, 4–10.

Green T. H. and Ringwood A. E. (1968) The Genesis of the Calc-Alkaline Igneous Rock Suite. *Contrbutions to Mineral. Petrol.* **18**, 105–162.

Hallot E., Davy P., Auvray B., de Bremond d'Ars J., Martin H. and Van Damme H. (1996) Non-Newtonian effects during injection processes in partially crystallized magmas. *J. Volc. Geotherm. Res.* **71**, 31–44.

Hawkesworth C. J. and Kemp A. I. S. (2006) Using hafnium and oxygen isotopes in zircons to unravel the record of crustal evolution. *Chem. Geol.* **226**, 144–162.

Hibbard M. J. (1981) The Magma Mixing Origin of Mantled Feldspars. *Contrbutions to Mineral. Petrol.* **76**, 158–170.

Irber W. (1999) The lanthanide tetrad effect and its correlation with K/Rb, Eu/Eu*, Sr/Eu, Y/Ho, and Zr/Hf of evolving peraluminous granite suites. *Geochim. Cosmochim. Acta* **63**, 489–508.

Jahn B. M., Wu F., Capdevila R., Martineau F., Zhao Z. and Wang Y. (2001) Highly evolved juvenile granites with tetrad REE patterns: The Woduhe and Baerzhe granites from the Great Xing'an Mountains in NE China. *Lithos* **59**, 171–198.

Janoušek V. (2006) Saturnin , R language script for application of accessory-mineral saturation models in igneous geochemistry. *Geol. Carpathica* **57**, 131–142.

Janoušek V., Braithwaite C. J. R., Bowes D. R. and Gerdes A. (2004) Magma-mixing in the genesis of Hercynian calc-alkaline granitoids: an integrated petrographic and geochemical study of the Sázava intrusion, Central Bohemian Pluton, Czech Republic. *Lithos* **78**, 67–99.

Janoušek V., Farrow C. M. and Erban V. (2006) Interpretation of whole-rock geochemical data in igneous geochemistry: Introducing Geochemical Data Toolkit (GCDkit). *J. Petrol.* **47**, 1255–1259.

Janoušek V., Survey C. G. and Braithwaite C. J. R. (2000) Microstructural and mineralogical evidence for limited involvement of magma mixing in the petrogenesis of a Hercynian high-K calc-alkaline intrusion: The Kozárovice granodiorite, Central Bohemian Pluton, Czech Republic. *Trans. R. Soc. Edinburgh-Earth Sci.* **91**, 15–26.

Kanamaru T., Suganuma Y., Oiwane H., Miura H., Miura M., Okuno J. and Hayakawa H. (2018) The weathering of granitic rocks in a hyper-arid and hypothermal environment: A case study from the Sør-Rondane Mountains, East Antarctica. *Geomorphology* **317**, 62–74.

Keay S., Collins W. J. and McCulloch M. T. (1997) A three-component Sr-Nd isotopic mixing model for granitoid genesis, Lachlan fold belt, eastern Australia. *Geology* **25**, 307–310.

Kemp A. I. S. and Hawkesworth C. J. (2003) Granitic Perspectives on the Generation and Secular Evolution of the Continental Crust. In *Treatise on Geochemistry* pp. 350–410.

Kemp A. I. S., Hawkesworth C. J., Foster G. L., Paterson B. A., Woodhead J. D., Hergt. J. M., Gray C. M. and Whitehouse M. J. (2007) Magmatic and Crustal Differentiation History of Granitic Rocks from Hf-O Isotopes in Zircon. *Science* **315**, 980–983.

King P. L., White A. J. R., Chappell B. W. and Allen C. M. (1997) Characterization and Origin of Aluminous A-type Granites from the Lachlan Fold Belt, Southeastern Australia. *J. Petrol.* **38**, 371–391.

Klein C. and Philpotts A. R. (2017) *Earth Materials Introduction to Mineralogy and Petrology*. 2nd ed., Cambridge University Press.

Koita M., Jourde H., Koffi K. J. P., Silveira K. S. Da and Biaou A. (2013) Characterization of weathering profile in granites and volcanosedimentary rocks in West Africa under humid tropical climate conditions. Case of the Dimbokro Catchment (Ivory Coast). *J. Earth Syst. Sci.* **122**, 841–854.

Kuritani T., Kitagawa H. and Nakamura E. (2005) Assimilation and Fractional Crystallization Controlled by Transport Process of Crustal Melt: Implications from an Alkali Basalt– Dacite Suite from Rishiri Volcano, Japan. *J. Petrol.* **46**, 1421–1442.

Lackey J. S., Valley J. W. and Hinke H. J. (2006) Deciphering the source and contamination history of peraluminous magmas using δ18O of accessory minerals: examples from garnet-bearing plutons of the Sierra Nevada batholith. *Contrib. to Mineral. Petrol.* **151**, 20–44.

Lee M. R., Waldron K. I. M. A. and Parsons I. A. N. (1995) Exsolution and alteration microtextures in alkali feldspar phenocrysts from the Shap granite. *Mineral. Mag.* **59**, 63–78.

Lesher C. E. (1990) Decoupling of Chemical and Isotopic Exchange during Magma Mixing. *Nature* **344**, 235–237.

Loiselle M. C. and Wones D. S. (1979) Characteristics and origin of anorogenic granites. *Geol. Soc. Am. Abstr. with Programs 11* **7**, 468.

Lowenstern J. B. (1994) Dissolved volatile concentrations in an ore-forming magma. *Geology* **22**, 893–896.

Le Maitre R. W., Bateman P., Dudek A., Keller J., Lameyre J., Le Bas M. J., Sabine P. A., Schmid R., Sorensen H., Streckeisen A., Woolley A. R. and Zanettin B. (1989) *A classification of igneous rocks and glossary of terms: Recommendations of the International Union of Geological Sciences Subcommission on the Systematics of Igneous Rocks.*, Blackwell Scientific Publications, Oxford, U.K.

Le Maitre R. W., Streckeisen A., Zanettin B., Le Bas M. J., Bonin B., Bateman P., Bellieni G., Dudek A., Efremova S., Keller J., Lameyre J., Sabine P. A., Schmid R., Sorensen H. and Woolley A. R. (2002) *Igneous Rocks A Classification and Glossary of Terms*. 2nd ed. ed. R. W. Le Maitre, Cambridge University Press, New York.

Masuda A. and Akagi T. (1989) Lanthanide tetrad effect observed in leucogranites from China. *Geochemica Cosmochim. Acta* **23**, 245–253.

Masuda A. and Ikeuchi Y. (1979) Lanthanide tetrad effect observed in marine environment. *Geochem. J.* **13**, 19–22.

Masuda A., Kawakami O., Dohmoto Y. and Takenaka T. (1987) Lanthanide tetrad effects in nature: two mutually opposite types , W and M. *Geochem. J.* **21**, 119–124.

McCulloch M. T. and Chappell B. W. (1982) Nd Isotopic Characteristics of S-Type and I-Type Granites. *Earth Planet. Sci. Lett.* **58**, 51–64.

Mielke P. and Winkler H. G. F. (1979) Eine bessere Berechnung der Mesonorm für granitische Gesteine. *Neu. Jb. Miner. Mh.*, 471—480.

Monecke T., Dulski P. and Kempe U. (2007) Origin of convex tetrads in rare earth element patterns of hydrothermally altered siliceous igneous rocks from the Zinnwald Sn-W deposit, Germany. *Geochim. Cosmochim. Acta* **71**, 335–353.

Monecke T., Kempe U., Monecke J., Sala M. and Wolf D. (2002) Tetrad effect in rare earth element distribution patterns: A method of quantification with application to rock and mineral samples from granite-related rare metal deposits. *Geochim. Cosmochim. Acta* **66**, 1185–1196.

Morgavi D., Perugini D., Campos C. P. De, Ertel-ingrisch W. and Dingwell D. B. (2013) Morphochemistry of patterns produced by mixing of rhyolitic and basaltic melts. *J. Volcanol. Geotherm. Res.* **253**, 87–96.

Moyen J. F. and Martin H. (2012) Forty years of TTG research. *Lithos* **148**, 312–336.

Moyen J. F. and Stevens G. (2006) Experimental constraints on TTG petrogenesis: Implications for archean geodynamics. *Geophys. Monogr. Ser.* **164**, 149–175.

Myron G. B. (2003) *Igenous and Metamorphic Petrology*. 2nd ed., Blackwell Publishers, Malden, MA.

Neuerburg G. J. (1958) Deuteric alteration of some aplite-pegmatites of the Boulder Batholith, Montana, and its possible significance to ore deposition. *Econ. Geol.* **53**, 287–299.

Pagel M., Barbin V., Blanc P. and Ohnenstetter D. (2000) *Cathodoluminescence in geosciences*., Springer, Berlin.

Pankhurst M. J., Vernon R. H., Turner S. P., Schaefer B. F. and Foden J. D. (2011) Contrasting Sr and Nd isotopic behaviour during magma mingling; new insights from the Mannum A-type granite. *Lithos* **126**, 135–146.

Pearce J. A., Harris N. B. W. and Tindle A. G. (1984) Trace element discrimination diagrams for the tectonic interpretation of granitic rocks. *J. Petrol.* **25**, 956–983.

Peccerillo A. and Taylor S. R. (1976) Geochemistry of eocene calc-alkaline volcanic rocks from the Kastamonu area, Northern Turkey. *Contrib. to Mineral. Petrol.* **58**, 63–81.

Perugini D. and Poli G. (2000) Chaotic dynamics and fractals in magmatic interaction processes: a different approach to the interpretation of mafic microgranular enclaves. *Earth Planet. Sci. Lett.* **175**, 93–103.

Pitcher W. S. (1997) *The Nature and Origin of Granite*. 2nd ed., Chapman & Hall, Netherlands.

Plümper O. and Putnis A. (2009) The Complex Hydrothermal History of Granitic Rocks: Multiple Feldspar Replacement Reactions under Subsolidus Conditions. *J. Petrol.* **50**, 967–987.

Roberts M. P. and Clemens J. D. (1993) Origin of high-potassium, calc-alkaline, I-type granitoids. *Geology* **21**, 825–828.

Rollinson H. R. (1993) *Using Geochemical Data: Evaluation, Presentation, Interpretation*., Longman Scientific & Technical, Essex, England.

Rudnick R. L. and Gao S. (2003) Composition of the Continental Crust. In *Treatise on Geochemistry* pp. 1–64.

Shand S. J. (1927) *Eruptive Rocks, Their Genesis, Composition Classification and Their Reaction to Ore-Deposits, with a Chapter on Meteorites*. 1st ed., Thomas Murby and Company, London.

Simon K. and Hoefs J. (1987) Effects of meteoric water interaction on Hercynian granites from the Südschwarzwald, Southwest Germany. *Chem. Geol.* **61**, 253–261.

Sisson T. W., Ratajeski K., Hankins W. B. and Glazner A. F. (2005) Voluminous granitic magmas from common basaltic sources. *Contrib. to Mineral. Petrol.* **148**, 635–661.

Sparks R. S. J. and Marshall L. A. (1986) Thermal and mechanical constraints on mixing between mafic and silicic magmas. *J. Volcanol. Geotherm. Res.* **29**, 99–124.

Stevens G., Villaros A. and Moyen J.-F. (2007) Selective peritectic garnet entrainment as the origin of geochemical diversity in S-type granites. *Geology* **35**, 9–12.

Streckeisen A. L. (1967) Classification and Nomenclature of Igneous Rocks. *Neucs Juhrhuch firer Minerulogie Ahhundlungen* **107**, 144–214.

Streckeisen A. L. (1974) Classification and nomenclature of plutonic rocks. Recommendations of the IUGS subcommission on the systematics of Igneous Rocks. *Geol. Rundschau* **63**, 773–786.

Streckeisen A. L. (1976) To cach plutonic rock its proper name. *Earth Sci. Rev.* **12**, 1–33.

Streckeisen A. and Le Maitre R. W. (1979) A chemical approximation to the modal QAPF classification of the igneous rocks. *Neues Jahrb. fur Mineral. Abteilung*, 169–206.

Sun S.-S. and Eadington P. J. (1987) Oxygen isotope evidence for the mixing of magmatic and meteoric waters during tin mineralization in the Mole Granite, New South Wales, Australia. *Econ. Geol.* **82**, 43–52.

Tegner C., Wilson J. R. and Robins B. (2005) Crustal assimilation in basalt and jotunite: Constraints from layered intrusions. *Lithos* **83**, 299–316.

Thompson A. B., Matile L. and Ulmer P. (2002) Some Thermal Constraints on Crustal Assimilation during Fractionation of Hydrous, Mantle-derived Magmas with Examples from Central Alpine Batholiths. *J. Petrol.* **43**, 403–422.

Tuttle O. F. and Bowen N. L. (1958) Origin of Granite in the Light of Experimental Studies in the System $NaAlSi_3O_8$–$KAlSi_3O_8$–SiO_2–H_2O. In *Geological Society of America Memoirs* pp. 1–146.

Vernon R. H. (1990) Crystallization and hybridism in microgranitoid enclave magmas: Microstructural evidence. *J. Geophys. Res.* **95**, 17849.

Vernon R. H. (1984) Microgranitoid enclaves in granites - Globules of hybrid magma quenched in a plutonic environment. *Nature* **309**, 438–439.

Wang D., Wang X., Cai Y., Chen X., Zhang F. and Zhang F.-F. (2017) Heterogeneous Conservation of Zircon Xenocrysts in Late Jurassic Granitic Intrusions within the Neoproterozoic Jiuling Batholith , South China: a Magma Chamber Growth Model in Deep Crustal Hot Zones. **58**, 1781–1810.

Wedepohl K. H. (1995) The composition of the continental crust. *Geochim. Cosmochim. Acta* **59**, 1217–1232.

Whalen J. B., Currie K. L. and Chappell B. W. (1987) A-type granites: geochemical characteristics, discrimination and petrogenesis. *Contrib. to Mineral. Petrol.* **95**, 407–419.

White A. J. R. (1979) Sources of granite magmas. *Geol. Soc. Am. Abstr. with Programs 11* **7**, 539.

White A. J. R. and Chappell B. W. (1988) Some supracrustal (S-type) granites of the Lachlan Fold Belt. *Earth Environ. Sci. Trans. R. Soc. Edinburgh* **79**, 169–181.

Wilson B. M. (1989) *Igneous Petrogenesis A Global Tectonic Approach*. Chapman & Hall, London.

Winter J. D. (2001) *An Introduction to Igneous and Metamorphic Petrology*. Prentice Hall, New Jersey.

Wu F. Y., Sun D. Y., Jahn B. M. and Wilde S. (2004) A Jurassic garnet-bearing granitic pluton from NE China showing tetrad REE patterns. *J. Asian Earth Sci.* **23**, 731–744.

Appendix B

Sample locations

Appendix C

Mineral chemistry

Table C.1. Electron microprobe standards and detection limits for biotite analysis.

Biotite		
Element	**Standard**	**Detection Limits (ppm)**
Ca	Diopside	11.2
F	Fluorite	0.6
Si	Olivine	0.8
Ti	Rutile	20.4
Na	Jadeite	5.2
Cl	Tugtupite	4.2
K	Sanidine	50.8
Cr	Chromium Oxide	41.6
Mg	Chlorite	7.2
Cs	Thalium Bromide	19.6
Ba	Barite	4
Mn	Bustamite	54.6
Al	Almandine	19.8
Ni	Nickel Silicide	7
Fe	Kaersutite	27.6

Table C.2. Electron microprobe standards and detection limits for feldspar analysis.

Feldspar		
Element	**Standard**	**Detection Limits (ppm)**
Ca	Diopside	4.6
Na	Tugtupite	5.0
Sr	Celestite	0.8
Si	Sanidine	3.0
Ba	Benitoite	6.8
Mg	Olivine	4.0
Ti	Rutile	6.5
K	Sanidine	15.5
Mn	Bustamite	18.9
Al	Pyrope	8.0
Rb	-	0.7
Fe	Almandine	10.1

References

Bruiyn H. de, Van Der Westhuizen W. A. and Schoch A. E. (1983) The estimation of FeO, F and H_2O^+ by regression in microprobe analyses of natural biotite. *J. Trace Microprobe Tech.* **1**, 399–413.

Appendix D

Whole-rock elemental geochemistry

Table D.1. Methods and detection limits of whole-rock elemental analyses.

Analyte	Unit	Detection Limits	Method
Al_2O_3	%	0.01	FUS-ICP
CaO	%	0.01	FUS-ICP
$Fe_2O_3^T$	%	0.01	FUS-ICP
K_2O	%	0.01	FUS-ICP
MgO	%	0.01	FUS-ICP
MnO	%	0.001	FUS-ICP
Na_2O	%	0.01	FUS-ICP
P_2O_5	%	0.01	FUS-ICP
SiO_2	%	0.01	FUS-ICP
TiO_2	%	0.001	FUS-ICP
LOI	%	0.01	FUS-ICP
Total	%	0.01	FUS-ICP
Ba	ppm	1	FUS-ICP
Be	ppm	1	FUS-ICP
Bi	ppm	0.1	FUS-MS
Ce	ppm	0.05	FUS-MS
Cs	ppm	0.1	FUS-MS
Dy	ppm	0.01	FUS-MS
Er	ppm	0.01	FUS-MS
Eu	ppm	0.005	FUS-MS
Ga	ppm	1	FUS-MS
Gd	ppm	0.01	FUS-MS
Ge	ppm	0.5	FUS-MS
Hf	ppm	0.1	FUS-MS
Ho	ppm	0.01	FUS-MS
In	ppm	0.1	FUS-MS
La	ppm	0.05	FUS-MS
Lu	ppm	0.002	FUS-MS
Mo	ppm	2	FUS-MS
Nb	ppm	0.2	FUS-MS
Nd	ppm	0.05	FUS-MS
Pr	ppm	0.01	FUS-MS
Rb	ppm	1	FUS-MS
Sm	ppm	0.01	FUS-MS
Sn	ppm	1	FUS-MS
Sr	ppm	2	FUS-ICP
Ta	ppm	0.01	FUS-MS
Tb	ppm	0.01	FUS-MS

Table D.1 (continued)

Analyte	Unit	Detection Limits	Method
Th	ppm	0.05	FUS-MS
Tl	ppm	0.05	FUS-MS
Tm	ppm	0.005	FUS-MS
U	ppm	0.01	FUS-MS
V	ppm	5	FUS-ICP
Y	ppm	1	FUS-ICP
Yb	ppm	0.01	FUS-MS
Zr	ppm	1	FUS-ICP
Au	ppb	1	INAA
Ag	ppm	0.5	MULT INAA/ TD-ICP
As	ppm	1	INAA
Br	ppm	0.5	INAA
Cd	ppm	0.5	INAA
Co	ppm	0.1	TD-ICP
Cr	ppm	0.5	INAA
Cu	ppm	1	INAA
Hg	ppm	1	TD-ICP
Ir	ppb	1	INAA
Ni	ppm	1	INAA
Pb	ppm	5	TD-ICP
S	%	0.001	TD-ICP
Sb	ppm	0.1	TD-ICP
Sc	ppm	0.01	INAA
Se	ppm	0.5	INAA
W	ppm	1	INAA
Zn	ppm	1	MULT INAA/TD-ICP

Appendix E

Sr, Nd, Hf and Pb isotope geochemistry

Definitions, formulas and reference values used for isotopic calculations

Isotopes are nuclides of a given chemical element having the same atomic number (Z) but different mass numbers (A = Z + N). The isotopic compositions in Table E.1 can be expressed as:

$$^{87}Sr/^{86}Sr = {}^{87}Sr/^{86}Sr_i + {}^{87}Rb/^{86}Sr\left(e^{\lambda t} - 1\right) \quad 1$$

$$^{143}Nd/^{144}Nd = {}^{143}Nd/^{144}Nd_i + {}^{147}Sm/^{144}Nd\left(e^{\lambda t} - 1\right) \quad 2$$

$$^{176}Hf/^{177}Hf = {}^{176}Hf/^{177}Hf_i + {}^{176}Lu/^{177}Hf\left(e^{\lambda t} - 1\right) \quad 3$$

$$^{206}Pb/^{204}Pb = {}^{206}Pb/^{204}Pb_i + {}^{238}U/^{204}Pb\left(e^{\lambda_{238} t} - 1\right) \quad 4$$

$$^{207}Pb/^{204}Pb = {}^{207}Pb/^{204}Pb_i + {}^{235}U/^{204}Pb\left(e^{\lambda_{235} t} - 1\right) \quad 5$$

$$^{208}Pb/^{204}Pb = {}^{208}Pb/^{204}Pb_i + {}^{235}U/^{204}Pb\left(e^{\lambda_{232} t} - 1\right) \quad 6$$

where $^{87}Sr/^{86}Sr$, $^{143}Nd/^{144}Nd$, $^{176}Hf/^{177}Hf$, $^{206}Pb/^{204}Pb$, $^{207}Pb/^{204}Pb$, $^{208}Pb/^{204}Pb$ represent the isotopic ratios at the time of analysis; $^{87}Sr/^{86}Sr_i$, $^{143}Nd/^{144}Nd_i$, $^{176}Hf/^{177}Hf_i$, $^{206}Pb/^{204}Pb_i$, $^{207}Pb/^{204}Pb_i$, $^{208}Pb/^{204}Pb_i$ represent the isotopic ratios at the time of formation of the samples; t represents the time elapsed since the formation of the rock; ʎ is the decay constant (see Table E.2).

Table E.2. Isotope decay schemes and respective decay constants (λ).

Decay Scheme	λ (a^{-1})	References
$^{87}Rb \rightarrow {}^{87}Sr + \beta^- + \bar{\nu} + Q$	1.42 x 10^{-11}	(Minster et al., 1982)
$^{147}Sm \rightarrow {}^{143}Nd + He + Q$	6.54 x 10^{-12}	(Scherer et al., 2001)
$^{176}Lu \rightarrow {}^{176}Hf + \beta^- + \nu + Q$	1.865 x 10^{-11}	(Lugmair and Marti, 1978)
$^{238}U \rightarrow {}^{206}Pb + 8He + 6\beta^- + Q$	1.55125 x 10^{-10}	(Jaffey et al., 1971)
$^{235}U \rightarrow {}^{207}Pb + 7He + 4\beta^- + Q$	9.8485 x 10^{-10}	(Jaffey et al., 1971)
$^{232}Th \rightarrow {}^{208}Pb + 6He + 4\beta^- + Q$	4.9475 x 10^{-11}	(Jaffey et al., 1971)

Note: ν : neutrino; $\bar{\nu}$: antineutrino; β: electron; Q: energy.

The Nd initial ratios are usually represented through the ε notation (parts per 10.000 deviation from the CHUR composition):

$$\varepsilon_{Nd}(t) = \left[\frac{(^{143}Nd/^{144}Nd)_{sample(t)}}{(^{143}Nd/^{144}Nd)_{CHUR(t)}} - 1\right] \times 10000 \qquad 7$$

where CHUR stands for 'chondritic uniform reservoir' and $(^{143}Nd/^{144}Nd)_{CHUR(t)}$ is the value of the ratio in chondrites at time t, which can be calculated as follows:

$$(^{143}Nd/^{144}Nd)_{CHUR(t)} = (^{143}Nd/^{144}Nd)_{CHUR} - (^{147}Sm/^{144}Nd)_{CHUR} \times \left(e^{\lambda t} - 1\right) \qquad 8$$

with $(^{143}Nd/^{144}Nd)_{CHUR} = 0.512638$ (Depaolo and Wasserburg, 1976) and $(^{147}Sm/^{144}Nd)_{CHUR} = 0.1967$ (Jacobsen and Wasserburg, 1980).

A model age is the moment in the past when the Nd isotopic composition of the sample was identical with that of some model reservoir such as the CHUR or the Depleted Mantle (DM). The DM model age (T_{DM}) of a given sample can be calculated by the following equation:

$$T_{DM} = \frac{1}{\lambda} \times \ln\left[1 + \frac{(^{143}Nd/^{144}Nd)_s - (^{143}Nd/^{144}Nd)_{DM}}{(^{147}Sm/^{144}Nd)_s - (^{147}Sm/^{144}Nd)_{DM}}\right] \qquad 9$$

with $(^{143}Nd/^{144}Nd)_{DM} = 0.51315$ and $(^{147}Sm/^{144}Nd)_{DM} = 0.2137$ (Peucat et al., 1989), which correspond to the present ratios in the DM.

Two-stage model ages (T_{DM2}) compensates for effects of possible secondary Sm/Nd fractionation (first having occurred at mantle melting) in course of the intracrustal partial melting. Thus, a model $^{147}Sm/^{144}Nd$ ratio is used, typically that of average continental crust (CC):

$$T_{DM2} = \frac{1}{\lambda} \times \ln\{[1 + (^{143}Nd/^{144}Nd)_s - (^{143}Nd/^{144}Nd)_{DM} - (^{147}Sm/^{144}Nd)_s$$

$$-(^{147}Sm/^{144}Nd)_{CC} \times (e^{\lambda t} - 1)]/(^{147}Sm/^{144}Nd)_{CC} - (^{147}Sm/^{144}Nd)_{DM}\} \quad 10$$

with $(^{143}Nd/^{144}Nd)_{DM}$ = 0.51315 and $(^{147}Sm/^{144}Nd)_{DM}$ = 0.2137 (Peucat et al., 1989); $(^{147}Sm/^{144}Nd)_{CC}$ = 0.118 (Jahn and Condie, 1995).

As in the Sm-Nd system, Lu-Hf data can also be expressed as ε values in terms of compositions at any time t in the past:

$$\varepsilon_{Hf}(t) = \left[\frac{(^{176}Hf/^{177}Hf)_{sample(t)}}{(^{176}Hf/^{177}Hf)_{CHUR(t)}} - 1\right] \times 10.000 \quad 11$$

where $(^{176}Hf/^{177}Hf)_{CHUR(t)}$ is the value of the ratio in chondrites at time t, which can be calculated as follows:

$$(^{176}Hf/^{177}Hf)_{CHUR(t)} = (^{176}Hf/^{177}Hf)_{CHUR} - (^{176}Lu/^{177}Hf)_{CHUR} \times (e^{\lambda t} - 1) \quad 12$$

with $(^{176}Hf/^{177}Hf)_{CHUR}$ = 0.282772 and $(^{176}Lu/^{177}Hf)_{CHUR}$ = 0.0332 (Blichert-Toft and Albarède, 1997).

The Hf model ages can also be calculated for a single-stage model (equation 13) or for a two-stage model (equation 14):

$$T_{DM} = \frac{1}{\lambda} \times \ln\left[1 + \frac{(^{176}Hf/^{177}Hf)_{sample} - (^{176}Hf/^{177}Hf)_{DM}}{(^{176}Lu/^{177}Hf)_{sample} - (^{176}Lu/^{177}Hf)_{DM}}\right] \quad 13$$

$$T_{DM2} = \frac{1}{\lambda} \times \ln\{[1 + (^{176}Hf/^{177}Hf)_s - (^{176}Hf/^{177}Hf)_{DM} - (^{176}Lu/^{177}Hf)_s$$

$$+(^{176}Lu/^{177}Hf)_{CC} \times (e^{\lambda t} - 1)]/[(^{176}Lu/^{177}Hf)_{CC} - (^{176}Lu/^{177}Hf)_{DM}]\} \quad 14$$

with $(^{176}Hf/^{177}Hf)_{DM}$ = 0.28325 and $(^{176}Lu/^{177}Hf)_{DM}$ = 0.0384 (Griffin et al., 2000); $(^{176}Lu/^{177}Hf)_{CC}$ = 0.015 (Griffin et al., 2002) is the average value of the continental crust.

References

Blichert-Toft J. and Albarède F. (1997) The Lu-Hf isotope geochemistry of chondrites and the evolution of the mantle-crust system. *Earth Planet. Sci. Lett.* **148**, 243–258.

Depaolo D. J. and Wasserburg G. J. (1976) Nd Isotopic Variations and Petrogenetic Models. *Geophys. Res. Lett.* **3**, 3–6.

Griffin W. L., Pearson N. J., Belousova E., Jackson S. E., Van Achterbergh E., O'Reilly S. Y. and Shee S. R. (2000) The Hf isotope composition of cratonic mantle: LAM-MC-ICPMS analysis of zircon megacrysts in kimberlites. *Geochim. Cosmochim. Acta* **64**, 133–147.

Griffin W. L., Wang X., Jackson S. E., Pearson N. J., O'Reilly S. Y., Xu X. and Zhou X. (2002) Zircon chemistry and magma mixing, SE China: In-situ analysis of Hf isotopes, Tonglu and Pingtan igneous complexes. *Lithos* **61**, 237–269.

Jacobsen S. B. and Wasserburg G. J. (1980) Sm-Nd isotopic evolution of chondrites. *Earth Planet. Sci. Lett.* **50**, 139–155.

Jaffey A. H., Flynn K. F., Glendenin L. E., Bentley W. C. and Essling A. M. (1971) Precision measurement of half-lives and specific activities of ^{235}U and ^{238}U. *Phys. Rev. C* **4**, 1889–1906.

Jahn B. M. and Condie K. C. (1995) Evolution of the Kaapvaal Craton as viewed from geochemical and Sm-Nd isotopic analyses of intracratonic pelites. *Geochemica Cosmochim. Acta* **59**, 2239–2258.

Lugmair G. W. and Marti K. (1978) Lunar initial ^{143}Nd/^{144}Nd: differential evolution of the lunar crust and mantle. *Earth Planet. Sci. Lett.* **39**, 349–357.

Minster J.-F., Birck J.-L. and Allègre C. J. (1982) Absolute age of formation of chondrites studied by the 87Rb–87Sr method. *Nature* **300**, 414–419.

Peucat J. J., Vidal P., Bernard-Griffiths J. and Condie K. C. (1989) S , Nd, and Pb Isotopic Systematics in the Archean Low- to High-Grade Transition Zone of Southern India: Syn-Accretion vs. Post-Accretion Granulites. *J. Geol.* **97**, 537–550.

Scherer E., Münker C. and Mezger K. (2001) Calibration of the Lutetium-Hafnium Clock. *Science.* **293**, 683–687.

Appendix F

Whole-rock isochron diagrams

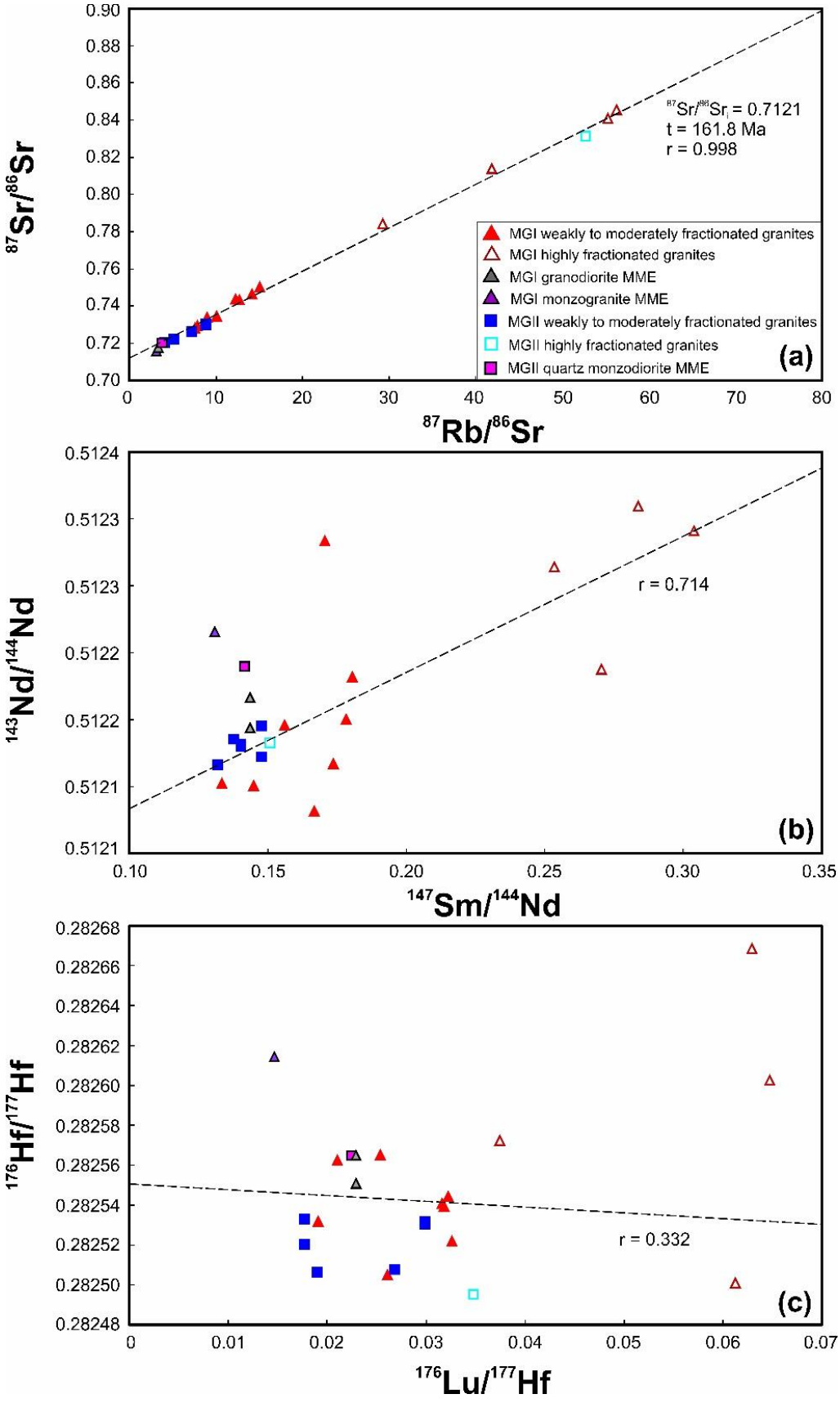
$^{87}Sr/^{86}Sr$
$^{87}Rb/^{86}Sr$
$^{87}Sr/^{86}Sr_i = 0.7121$
t = 161.8 Ma
r = 0.998
MGI weakly to moderately fractionated granites
MGI highly fractionated granites
MGI granodiorite MME
MGI monzogranite MME
MGII weakly to moderately fractionated granites
MGII highly fractionated granites
MGII quartz monzodiorite MME
(a)
$^{143}Nd/^{144}Nd$
$^{147}Sm/^{144}Nd$
r = 0.714
(b)
$^{176}Hf/^{177}Hf$
$^{176}Lu/^{177}Hf$
r = 0.332
(c)

Appendix G

Mineral/melt partition coefficients used to calculate fractionation vectors

Table G.1. Mineral/melt partition coefficients used to calculate fractionation vectors.

Reference	Partition coefficients	
Bea et al. (1994)	D(La/Zrn)	1.30
Bea et al. (1994)	D(Sm/Zrn)	3.79
Bea et al. (1994)	D(Nd/Zrn)	3.35
Bea et al. (1994)	D(Gd/Zrn)	9.21
Bea et al. (1994)	D(Lu/Zrn)	923.00
Bea et al. (1994)	D(Yb/Zrn)	278.00
Bea et al. (1994)	D(Th/Zrn)	22.10
Mahood and Hildreth (1983)	D(La/Aln)	2594.50
Mahood and Hildreth (1983)	D(Sm/Aln)	866.50
Mahood and Hildreth (1983)	D(Nd/Aln)	484.00
Hermann (2002)	D(Gd/Aln)	201.00
Hermann (2002)	D(Lu/Aln)	86.00
Mahood and Hildreth (1983)	D(Yb/Aln)	30.75
Mahood and Hildreth (1983)	D(Th/Aln)	484.00
Yurimoto et al. (1990)	D(La/ Mnz)	3200.00
Yurimoto et al. (1990)	D(Sm/Mnz)	2859.00
Yurimoto et al. (1990)	D(Nd/Mnz)	3726.00
Yurimoto et al. (1990)	D(Gd/Mnz)	2144.00
Yurimoto et al. (1990)	D(Lu/Mnz)	174.00
Yurimoto et al. (1990)	D(Yb/Mnz)	273.00
Stepanov (2012)	D(Th/Mnz)	1294.00
Fujimaki (1986)	D(La/Ap)	14.50
Fujimaki (1986)	D(Sm/Ap)	46.00
Fujimaki (1986)	D(Nd/Ap)	32.80
Fujimaki (1986)	D(Gd/Ap)	43.90
Fujimaki (1986)	D(Lu/Ap)	13.80
Fujimaki (1986)	D(Yb/Ap)	15.40
Dawson and Hinton (2003)	D(Th/Ap)	2.87
Prowatke and Klemme (2005)	D(La/Ttn)	1.88
Prowatke and Klemme (2005)	D(Sm/Ttn)	20.40
Tiepolo et al. (2002)	D(Nd/Ttn)	15.52
Prowatke and Klemme (2005)	D(Gd/Ttn)	18.20
Prowatke and Klemme (2005)	D(Lu/Ttn)	2.38
Tiepolo et al. (2002)	D(Yb/Ttn)	3.27
Prowatke and Klemme (2005)	D(Th/Ttn)	0.15
Bea et al. (1994)	D(La/Grt)	0.10
Bea et al. (1994)	D(Sm/Grt)	0.45
Bea et al. (1994)	D(Nd/Grt)	0.20
Bea et al. (1994)	D(Gd/Grt)	4.95
Bea et al. (1994)	D(Lu/Grt)	525.00
Bea et al. (1994)	D(Yb/Grt)	331.00
Bea et al. (1994)	D(Th/Grt)	0.10
Sisson (1994)	D(La/Hbl)	1.39
Sisson (1994)	D(Sm/Hbl)	9.53
Sisson (1994)	D(Nd/Hbl)	6.95

Table G.1 (continued)

Irving and Frey (1978)	D(Gd/Hbl)	10.00
Irving and Frey (1978)	D(Lu/Hbl)	5.50
Sisson (1994)	D(Yb/Hbl)	4.96
Bacon and Druitt (1988)	D(Th/Hbl)	0.16
Bacon and Druitt (1988)	D(Ba/Hbl)	0.30
Bacon and Druitt (1988)	D(Sr/Hbl)	0.01
Bacon and Druitt (1988)	D(Eu/Hbl)	3.20
Bacon and Druitt (1988)	D(Rb/Hbl)	0.40
Nash and Crecraft (1985)	D(Ba/Pl)	1.52
Nash and Crecraft (1985)	D(Sr/Pl)	15.63
Nash and Crecraft (1985)	D(Eu/Pl)	5.42
Nash and Crecraft (1985)	D(Rb/Pl)	0.11
Nash and Crecraft (1985)	D(Ba/Kfs)	11.45
Nash and Crecraft (1985)	D(Sr/Kfs)	5.40
Nash and Crecraft (1985)	D(Eu/Kfs)	4.45
Nash and Crecraft (1985)	D(Rb/Kfs)	1.75
Bea et al. (1994)	D(Ba/Bt)	23.53
Bea et al. (1994)	D(Sr/Bt)	0.45
Bea et al. (1994)	D(Eu/Bt)	0.05
Bea et al. (1994)	D(Rb/Bt)	6.98

Abbreviations: Kfs – Alkali feldspar; Pl – plagioclase; Bt – biotite; Hbl – hornblende; Zrn – zircon; Ap – apatite; Ttn – titanite; Grt – garnet; Mnz – monazite; Aln – allanite.

References

Bacon C. R. and Druitt T. H. (1988) Compositional evolution of the zoned calcalkaline magma chamber of Mount Mazama, Crater Lake, Oregon. *Contrib. to Mineral. Petrol.* **98**, 224–256.

Bea F., Pereira M. D. and Stroh A. (1994) Mineral/leucosome trace-element partitioning in a peraluminous migmatite (a laser ablation-ICP-MS study). *Chem. Geol.* **117**, 291–312.

Dawson J. B. and Hinton R. W. (2004) Trace-element content and partitioning in calcite, dolomite and apatite in carbonatite, Phalaborwa, South Africa. *Mineral. Mag.* **67**, 921–930.

Fujimaki H. (1986) Partition coefficients of Hf, Zr, and REE between zircon, apatite, and liquid. *Contrib. to Mineral. Petrol.* **94**, 42–45.

Hermann J. (2002) Allanite: Thorium and light rare earth element carrier in subducted crust. *Chem. Geol.* **192**, 289–306.

Irving A. J. and Frey F. A. (1978) Distribution of trace elements between garnet megacrysts and host volcanic liquids of kimberlitic to rhyolitic composition. *Geochim. Cosmochim. Acta* **42**, 771–787.

Mahood G. and Hildreth W. (1983) Large partition coefficients for trace elements in high-silica rhyolites. *Geochim. Cosmochim. Acta* **47**, 11–30.

Nash W. P. and Crecraft H. R. (1985) Partition coefficients for trace elements in silicic magmas. *Geochim. Cosmochim. Acta* **49**, 2309–2322.

Prowatke S. and Klemme S. (2005) Effect of melt composition on the partitioning of trace elements between titanite and silicate melt. *Geochim. Cosmochim. Acta* **69**, 695–709.

Sisson T. W. (1994) Hornblende-melt trace-element partitioning measured by ion microprobe. *Chem. Geol.* **117**, 331–344.

Stepanov A. S. (2012) Monazite control on Th, U and REE redistribution during partial melting: experiment and application to the deeply subducted crust. .

Tiepolo M., Oberti R. and Vannucci R. (2002) Trace-element incorporation in titanite: Constraints from experimentally determined solid/liquid partition coefficients. *Chem. Geol.* **191**, 105–119.

Yurimoto H., Duke E. F., Papike J. J. and Shearer C. K. (1990) Are discontinuous chondrite-normalized REE patterns in pegmatitic granite systems the results of monazite fractionation? *Geochim. Cosmochim. Acta* **54**, 2141–2145.